Bending, Vibration and Vibro-Acoustic Analysis of Composite Sandwich Plates with Corrugated Core

by

Rajesh Kumar Boorle

A dissertation submitted in partial fulfillment
of the requirements for the degree of
Doctor of Philosophy
(Automotive Systems Engineering)
in the University of Michigan-Dearborn
2014

Doctoral Committee:

Professor P.K. Mallick, Chair
Professor Yubao Chen
Professor John Cherng
Associate Professor Hong-Tae Kang

DEDICATION

to my family members, teachers and friends for their kind affection and support during my entire research career

ACKNOWLEDGEMENTS

From the bottom of my heart, I have the immense pleasure of expressing my deep gratitude and sincere thanks to my dissertation committee chair and research supervisor, Prof. P.K. Mallick, for his invaluable knowledge and outstanding support during this research work. I greatly admire his ingeniousness, resourcefulness and devotion to the research. For sure, a word of thanks is not sufficient; given a chance, I would never say no to work for another research program with him.

I would like to thank Prof. John Cherng, Prof. Yubao Chen and Prof. Hong-Tae Kang for serving on my dissertation committee. Their suggestions on the dissertation are deeply acknowledged.

I would also like to express my deep appreciation for the research assistantship provided by CLAMP (Center for Lightweighting Automotive Material Processing) and CEEP (Center for Engineering Education and Practice) during my entire PhD program.

I also take this opportunity to express my profound gratitude to my beloved parents, my family members and relatives for their constant support and having a belief that I sincerely work to excel in my research carrier. My special thanks are for my dear wife Dr. Divya, brother Mr. Srikanth (Charted Accountant, Business Finance Analyst), sister Dr. Sunitha (Henry Ford Hospitals, Detroit, U.S.A) and brother-in-law Dr. Manohar for their encouraging words during the downhearted time in research.

There are many respectable people who have contributed in many ways to make this work a success; I wish to thank them all and offer my prayers.

TABLE OF CONTENTS

LIST OF FIGURES

LIST OF TABLES

ABSTRACT

BENDING, VIBRATION AND VIBRO-ACOUSTIC ANALYSIS OF COMPOSITE SANDWICH PLATES WITH CORRUGATED CORE

by

Rajesh Kumar Boorle

In the current research, a comprehensive study on global and local responses of composite sandwich plates with corrugated core is conducted. The composite is a carbon fiber reinforced epoxy laminate. Two different laminate configurations, $[0/\alpha]_s$ and $[\pm\alpha]_s$, are considered and the fiber orientation angle α is varied. For global bending and vibration analyses, the composite sandwich plate with corrugated core is transformed into an equivalent homogenous orthotropic plate using energy equivalency. Extensional, in-plane shear, bending and twisting and transverse shear stiffness components for the sandwich plate are calculated. Analytical formulation for the equivalent orthotropic plate is developed based on the minimization of energy principle. The effects of sandwich design parameters, such as face thickness, core thickness and pitch, on the global bending and vibration responses are determined. A methodology for local bending analysis is developed using finite element analysis and damage development due to progressively increasing applied pressure load is predicted. Critical buckling behavior of the sandwich plate is also studied. Vibro-acoustic response, which includes of both undamaged and damaged sandwich plates, is determined using boundary element method.

CHAPTER 1

INTRODUCTION

1.1 INTRODUCTION

Sandwich beams and plates offer significant advantages in structural applications because of their higher flexural stiffness per unit weight and higher strength-to-weight ratio compared to monolithic and rib stiffened structures [1], [2]. In general, sandwich constructions exhibit lower bending deflections, higher critical buckling loads, higher natural frequencies and greater transverse load carrying capacity than monolithic structures of equal weight. Due to these advantages, sandwich constructions are used in many aircraft and space structures where weight saving is an important consideration in their design along with high stiffness and high strength.

Sandwich constructions are composed of top and bottom face plates or panels that are separated by a core layer. The faces are in most cases thin panels of aluminum, steel or fiber reinforced composites. The material in the core can be selected from metals, composites, plastics or wood. They are usually designed in such a way that the core carries the shear load and the face plates carry the bending and in-plane loads, resulting in high bending stiffness and resistance to buckling in relation to their weight. Various core topologies can be used for sandwich construction, like aluminum honeycomb, rigid or flexible polymer foam, aluminum foam, solid balsa wood and corrugated or cellular core with a variety of corrugation geometries like sinusoidal, triangular, trapezoidal and rectangular shaped cores.

Among the various options available for the core design, corrugated cores offer excellent opportunity for multi-functional applications when compared with other core designs. Corrugated cores can be designed to provide improved structural integrity, fluid

flow for actively cooled systems, storage space for liquid or pressurized gas, excellent shock resistance, vibration and sound isolation, etc. Corrugated cores are significantly more efficient than foam cores or honeycomb cores, the reason being that under bending loads, foam cores and honeycomb cores deform mainly by shear, whereas corrugated cores deform primarily by axial and bending deformations of their members, which are comparatively much stiffer and stronger load sharing mechanisms between the faces and the core.

A typical corrugated sandwich construction is shown in Figure 1.1. It comprises of a corrugated core and two thin face plates, also called skins, which are bonded or welded to the peaks of the core. Corrugated cores, as shown in Figure 1.2, can be cut and folded into almost any shape or size and they are efficient, low-cost and easy to manufacture. The direction of the corrugation in-line with production is called the machine-direction (MD, x-direction) and the corrugation is oriented in the cross-direction (CD, y-direction), as shown in Figure 1.2. The thickness direction of the sandwich structure is denoted the z-direction. A variety of core shapes and geometries can be designed to provide a range of structural performance under bending, axial compression and other loadings.

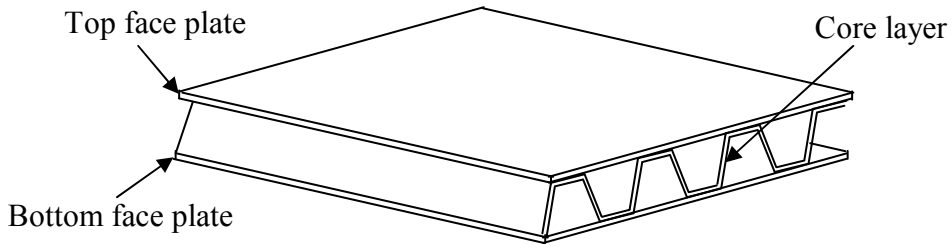

Figure 1.1: Sandwich structure with corrugated core

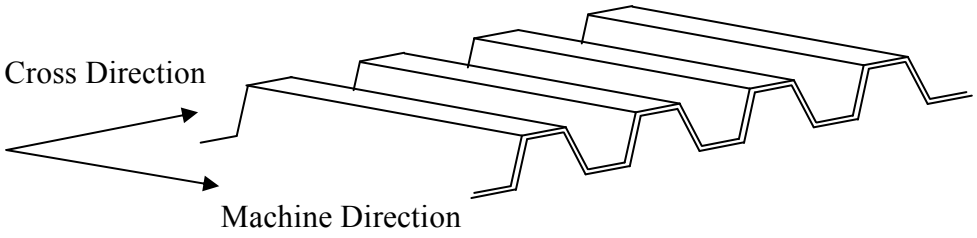

Figure 1.2: Configuration of corrugated core layer

1.2 APPLICATIONS OF CORRUGATED-CORE SANDWICH CONSTRUCTION

Sandwich construction with corrugated core offers greater crash resistance and improved global bending and vibration response when compared to foam cores or honeycomb cores. Applications or potential applications of corrugated-core sandwich construction are briefly described below.

- In automotive, marine and spacecraft applications where conventional monolithic and rib-stiffened structural design for panels, decks, bulkheads and fuselage results in large amount of material being positioned close to the neutral axis, giving them insufficient bending properties and also a relatively large structural height and weight. In such a case, sandwich structure with corrugated core construction can offer high bending stiffness and strength.
- Corrugated-core sandwich construction can be beneficial in automotive body panels and body structures not only because of their high stiffness-to-weight ratio and high strength-to-weight ratio, but also because such a construction can provide high crush resistance under impact conditions and be used for interior heating and cooling channels or for routing cables and electrical harnesses.
- Another challenging application area is the packaging industry, where during the life cycle of a packaging container, it is exposed to various types of loading conditions, such as static loads from packages in a stack during transport and storage, vibration loads during transportation, and shock loads during rough handling and crash. Packaging containers need to be lightweight and also must have high stiffness. Corrugated-core paperboard, shown in Figure 1.3, is commonly used as packaging container material and has high stiffness-to-weight ratio and excellent shock resistance. Whether or not a package will survive the imposed loading condition is crucially dependent on the strength of the corrugated paperboard.

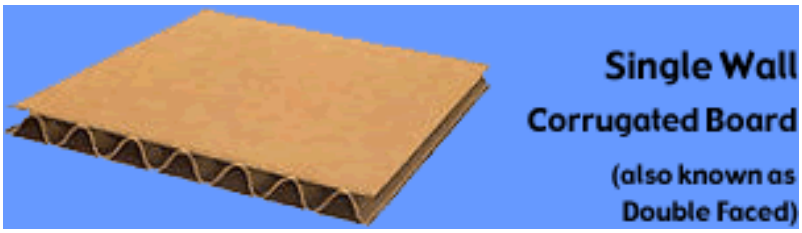

Figure 1.3: Corrugated-core paperboard sandwich of single cells

1.3 LITERATURE REVIEW

Vast majority of the technical literature on sandwich plates and beams involve sandwich construction with a foam core or a honeycomb core [1], [2]. Among the publications involving corrugated core, very few have considered fiber-reinforced composite as the sandwich material. Most of the research studies on corrugated-core sandwich have dealt with the analysis of metallic corrugated-core sandwich panels for vibration control, noise control, shock and impact resistance and energy dissipation. These research studies can be divided into three broad categories: (a) elastic stiffness, (b) maximum load capacity, and (c) energy absorption.

Most of the analytical and numerical work for calculating the effective elastic stiffness terms for corrugated core sandwich plates used homogenization theory and implemented an equivalent thickness plate model. Libove and Hubka [3] were the first to derive equivalent elastic constants for corrugated core sandwich plates using the homogenization theory. Lok and Cheng [4] predicted the bending deflections of truss-core sandwich panels by first calculating their elastic stiffness properties using the homogenization approach. Similarly, Chang et al. [5] used a similar approach to predict the bending behavior of corrugated-core steel sandwich plates with different corrugation angles, core thickness to face thickness ratios and pitch to core depth ratios. Buannic et al. [6] calculated the effective elastic properties for corrugated core sandwich panels using homogenization theory based on asymptotic expansion method. Martinez et al. [7] calculated elastic stiffness terms of corrugated core sandwich plate made of a carbon fiber reinforced epoxy composite. The analytical method involved the use of shear deformable plate theory, but the calculation of transverse shear stiffness values followed the method proposed by Libove and Hubka [3].

Several articles have been published on the elastic and vibration characteristics of corrugated board. For example, Luo et al. [8] calculated bending stiffness of corrugated board. Biancolini [9] and Talbi et al. [10] developed homogenization methods for calculating the elastic stiffness matrix of corrugated cardboards and then implemented it in finite element models to predict their deformation characteristics. Carlsson et al. [11] used the first-shear deformation laminated plate theory to analyze the elastic stiffnesses of corrugated board sandwich panels. They showed that in-plane, bending and twisting stiffnesses are dominated by the face thickness, whereas transverse shear stiffnesses depend strongly on the core shape and the face-to-core bonding. The importance of core shape on transverse shear moduli is further demonstrated by Nordstrand et al. [12]. Lu and Zhu [13] determined the elastic constants of corrugated board panels using lateral compression, three-point bending and simple shear tests. Nordstrand [14], [15] implemented both numerical and experimental methods for stability and collapse analysis of corrugated board panels.

Wicks and Hutchinson [16] considered the minimum weight design of metallic truss-core plates subjected to combinations of bending and transverse shear loads. Based on yielding and buckling failure modes of both face and core members, they developed simple mechanics of materials equations to relate the core design parameters with plate weight per unit area. Using similar approach, Valdevit et al. [17] evaluated the optimal dimensions and minimum weights of corrugated and prismatic diamond core sandwich panels. In another publication, Valdevit et al. [18] conducted an experimental and analytical study on the bending response of steel sandwich panels with corrugated core under both longitudinal and transverse loadings. Panel designs were selected on the basis of failure maps which related face thickness with core thickness based on face yielding, core yielding, face buckling and core buckling. Tian and Lu [19] considered optimum designs of corrugated core sandwich panels and hat-stiffened panels under longitudinal compression for minimum weight. They considered four different failure modes, namely overall buckling, face buckling, core buckling and yielding. From weight standpoint, their analysis showed that sandwich panels with either triangular core or square core are less efficient than hat-stiffened panels. Coté et al. [20] carried out both experimental and analytical investigations to predict out-of-plane compressive, transverse shear and

longitudinal shear responses of corrugated core and diamond core sandwich plates made of stainless steel.

There is potential for reduction in vibration response levels and sound transmission with sandwich structure with corrugated core construction. However, research on vibration and sound transmission of corrugated-core sandwich structure is very limited. El-Raheb [21] predicted frequency response of truss-like periodic panels using an analytical approach and showed the importance of local member vibration. El-Raheb and Wagner [22] extended the analytical approach to determine the sound transmission through similar panels. Ruzzene [23] used spectral finite element method to calculate sound radiation from corrugated sandwich beams with honeycomb core. He also performance of various core configurations and compared their vibration response and sound transmission reduction index.

An overarching conclusion from the literature review is that bending and vibro-acoustic response of corrugated-core sandwich structures used three general methods as shown in Figure 1.4. However, in these studies no accounts have been made of the effect of local responses and damage of the faces and the core as the load on the structure is being increased. This dissertation attempts to provide a systematic study to develop analytical and numerical models for the prediction of bending, vibration and vibro-acoustic response characteristics of corrugated-core composite sandwich plates, implementing appropriate deformation and damage development theories as needed.

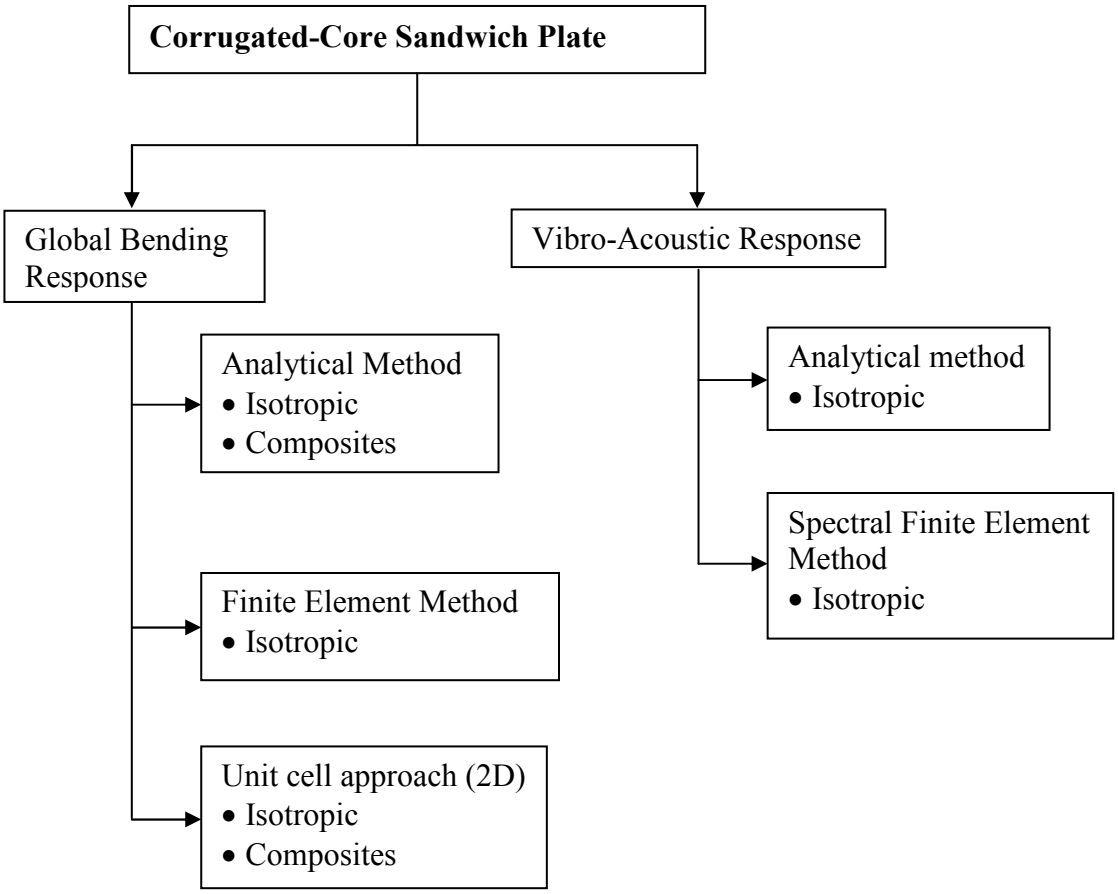

Figure 1.4: Summary of the available literature

1.4 MOTIVATION AND RESEARCH OBJECTIVES

When made of fiber reinforced composite materials, sandwich panels offer attractive weight saving opportunity and a wide range of design solutions in structural applications. Additionally, using a fiber reinforced composite material to manufacture the core topology increases the design space due to their anisotropic nature and unique modes of failure that are different from metals. There are however very few systematic studies addressing the bending, vibration and vibro-acoustic characteristics of fiber reinforced composite sandwich plates and beams with corrugated core.

The current research is undertaken to study the bending, vibration and vibro-acoustic response characteristics of composite sandwich plates with corrugated core of various geometries ranging from triangular to rectangular shapes. The material in both faces and webs in the core is a carbon fiber reinforced composite laminate. Global bending and

vibration responses are first determined analytically using the stiffness of the unit cell. The unit-cell approach is used, since studies have shown that for periodic structures in which there are repeating unit cells connected together, the behavior of the unit cell can be used to predict the behavior of the entire structure [23], [24]. Local bending response and damage development are determined using finite element method and the vibro-acoustic response is determined under both undamaged and damaged conditions using boundary element method.

The specific goals of the current research study are as follows.

- Develop analytical models to determine global static bending and vibration response characteristics of corrugated-core composite sandwich plates
- Conduct a systematic study of the effects of core geometry parameters, such as core thickness, face thickness, pitch and core height, and two different composite laminate constructions on the global bending deflection and resonant frequencies.
- Develop a three-dimensional finite element model of corrugated-core composite sandwich plates using ANSYS, a finite element software, and determine local deformation and damage development characteristics of the faces and the webs under progressively increasing static load.
- Develop a three-dimensional boundary element model using LMS-SYSNOISE, a boundary element software, to determine the structural and acoustic mode shapes and predict the vibro-acoustic characteristics of undamaged and damaged composite sandwich plates with corrugated core.

1.5 ORGANIZATION OF DISSERTATION

In the current research, analytical and numerical models are developed to analyze bending, vibration and vibro-acoustic performance of carbon fiber-reinforced epoxy composite sandwich plates with corrugated core. The dissertation chapters are organized as follows.

1.5.1 Chapter 2: Global Bending Response of Composite Sandwich Plates with Corrugated Core

In the case of global bending analysis of composite sandwich plates with corrugated core, the unit cell which is a repetitive portion of entire sandwich construction is considered. Equivalent extensional, bending, coupling and transverse shear stiffness components of the unit cell are calculated by using the homogenization theory. The analysis is completed using the minimum potential energy approach. Sandwich plates with various corrugation geometries, dimensions and laminate constructions are considered.

1.5.2 Chapter 3: Global Vibration Response of Composite Sandwich Plates with Corrugated Core

Homogenization and equivalent plate model are also used to determine the flexural and longitudinal vibration mode shapes and resonant frequencies of composite sandwich plates with corrugated core. The analysis is conducted using Hamilton's Principle of minimum energy and takes into account both translational and rotary inertias. Various corrugation geometries, dimensions and laminate constructions are also considered

1.5.3 Chapter 4: Local Bending Response of Composite Sandwich Plates with Corrugated Core

For local analysis of composite sandwich plates with corrugated core, a three dimensional finite element model is developed in ANSYS. Buckling analysis is carried out to predict the behavior of each member in the sandwich plate at the critical buckling load. Progressive damage development analysis is carried out by applying increasing pressure load on the top face of the sandwich plate and implementing the maximum stress failure criteria to predict damage.

1.5.4 Chapter 5: Vibro-Acoustic Response of Composite Sandwich Plates with Corrugated Core

For vibro-acoustic analysis, a three-dimensional boundary element model is developed in LMS-SYSNOISE. Both structural and acoustic mode shapes of undamaged and damaged sandwich plates are analyzed. Also, vibro-acoustic response of sandwich

plates with progressively increasing damage is predicted by applying unit surface load on the damaged sandwich plate.

1.5.5 Chapter 6: Conclusions

Conclusions based on global and local analysis of composite sandwich plates with corrugated core are made in this chapter. Future studies are also recommended.

REFERENCES

[1] Zenkert, D., An Introduction to Sandwich Construction, EMAS Publishing, West Midlands, U.K., 1997.

[2] Vinson, J. R., The Behavior of Sandwich Structures of Isotropic and Composite Materials, Technomic Publishing Co., Lancaster, PA, 1999.

[3] Libove, C. and Hubka, RE., "Elastic constants for corrugated core sandwich plates," *Journal of Structural Engineering*, Vol. 122, No. 8, 1951, pp. 958 -966.

[4] Lok, T. S. and Cheng, Q. H., "Elastic stiffness properties and behavior of truss-core sandwich panel," *Journal of Structural Engineering*, Vol. 126, No. 5, 2000, pp. 552 -559.

[5] Chang, W., Ventsel, E., Krauthammer, T., and John, J., "Bending behavior of corrugated-core sandwich plates," *Composite Structures*, Vol. 70, No. 1, 2005, pp. 81-89.

[6] Buannic, N., Cartraud, P. and Quesnel, T., "Homogenization of corrugated core sandwich panels," *Composite Structures*, Vol. 59, 2003, pp. 299-312.

[7] Oscar, A. M., Bhavani V. Sankar, Raphael T. Haftka, and Satish K. Bapanapalli, "Micromechanical Analysis of Composite Corrugated-Core Sandwich Panels for Integral Thermal Protection Systems," *AIAA JOURNAL*, Vol. 45, 2007, pp. 2323-2336

[8] Luo, S., Suhling, J. C., Considine, J. M. and Laufenberg, T. L., "The bending stiffnesses of corrugated board," *Mechanics of Cellulosic Materials*, AMD-Vol. 145/MD-Vol. 36, 1992, pp. 15-26.

[9] Biancolini, M.E., "Evaluation of equivalent stiffness properties of corrugated board," *Composite Structures*, Vol. 69, 2005, pp. 322-328.

[10] Talbi, N., Batti, A., Ayad R. and Guo, Y. Q., "An analytical homogenization model for finite element modeling of corrugated cardboard," *Composite Structures*, Vol. 88, No. 2, 2009, pp. 280-289.

[11] Carlsson, LA., Nordstrand, T. and Westerlind, B., "On the elastic stiffnesses of corrugated core sandwich," *Journal of Sandwich Structures and Materials*, Vol. 3, 2001, pp. 253-267.

[12] Nordstand, T., Carlsson, L. A. and Allen, H.G., "Transverse shear stiffness of structural core sandwich", *Composite Structures*, Vol. 27, 1994, pp. 317-329.

[13] Lu, T. J. and Zhu, G., "The elastic constants of corrugated board panels," *Journal of Composite Materials*, Vol. 35, 2001, pp. 1868-1887.

[14] Nordstrand, T., "Analysis and testing of corrugated board panels into the post-buckling regime," *Composite Structures*, Vol. 63, 2004, pp. 189-99.

[15] Nordstrand, T. and Allansson, A., "Stability and collapse of corrugated board panels, numerical and experimental analysis," *Proceedings of 6th International Conference on Sandwich Structures*, Florida, USA, 2003, pp. 202 -210.

[16] Wicks, N. and Hutchinson, J. W., "Optimal truss plates," *International Journal of Solids and Structures*, Vol. 38, 2001, pp. 5165-5183.

[17] Valdevit, L., Hutchinson, J. W. and Evans, A. G., "Structurally optimized sandwich panels with prismatic cores," *International Journal of Solids and Structures*, Vol. 41, 2004, pp. 5105-5124.

[18] Valdevit, L., Wei, Z., Mercer, C., Zok, F. W. and Evans, A.G., "Structural performance of near optimal sandwich panels with corrugated cores," *International Journal of Solids and Structures*, Vol. 43, 2006, pp. 4888-4905.

[19] Tian, Y. and Lu, T., "Optimal design of compression corrugated panels," *Thin-Walled. Structures*, Vol. 43, 2005, pp. 477-498.

[20] Coté, F., Deshpande, V. S., Fleck, N. A. and Evans, A. G., "The compressive and shear responses of corrugated and diamond lattice materials," *International Journal of Solids and Structure*s, Vol. 43, 2006, pp. 6220-6242.

[21] El-Raheb, M. "Frequency response of a two-dimensional truss like periodic panel," *Journal of the Acoustical Society of America*, Vol. 101, No. 6, 1997, pp. 3457-3465.

[22] El-Raheb, M. and Wagner, P., "Transmission of sound across a truss like periodic panel: 2-D analysis," *Journal of the Acoustical Society of America*, Vol. 102, No. 4, 1997, pp. 2176-2183.

[23] Ruzzene, M., "Vibration and sound radiation of sandwich beams with honeycomb truss core," *Journal of Sound and Vibration*, Vol. 277, 2004, pp. 741–763.

[24] Mead, D. J., "A new method of analyzing wave propagation in periodic structure; applications to periodic Timoshenko beams and stiffened plates," *Journal of Sound and Vibration*, Vol. 104, 1986, pp. 9-27.

CHAPTER 2

GLOBAL BENDING RESPONSE OF COMPOSITE SANDWICH PLATES WITH CORRUGATED CORE

2.1 INTRODUCTION

Several research studies have been published in recent years on the analysis of metallic corrugated-core sandwich panels for vibration control, noise control, shock and impact resistance, and energy dissipation. When made of composite materials, corrugated-core sandwich panels can be even more attractive for structural applications because they offer a wide range of design solutions in addition to weight savings. Using fiber reinforced composites to manufacture the core topologies increases the design space due to their orthotropic nature and the variety of fiber architecture that can be used in making these composites. There are very few studies on the bending and vibration response of fiber reinforced composite sandwich plates with corrugated core.

Most of the analytical and numerical work for calculating the effective stiffness terms for corrugated core sandwich panels used homogenization theory and implemented an equivalent plate model [1-8]. Libove and Hubka [1] suggested that an orthotropic homogeneous plate assumption can be made to analyze the bending response of corrugated sandwich panels, provided they have equivalent elastic constants. They then used force-distortion relationships to derive effective elastic constants for sandwich construction with two parallel faces and a corrugated core, both made of isotropic materials. The effective elastic constants include bending and twisting stiffnesses, transverse shear stiffnesses, stretching and shear moduli and Poison's ratios associated with both bending and stretching.

Fung, Tan, and Lok [2], [3] extended Libove and Hubka's approach to derive the expressions for transverse shear stiffnesses of Z-core and C-core sandwich panels. In a Z-core sandwich panel, the core is made of unidirectional Z-shaped channels, whereas in a C-core sandwich panel, the core is made of unidirectional C-shaped channels. Further, they modeled both sandwich panels as thick orthotropic plates using effective elastic constants and determined their maximum deflections using thick plate formulations.

In another study, Lok and Cheng [4] used the homogeneous equivalent thick plate approach to determine maximum plate deflection of truss-core sandwich panels made of an aluminum alloy. They used both closed-form equations and finite element method for the maximum deflection calculation and found good agreement between the two. The maximum deflection had the lowest value with a triangular truss-core and the highest value with a rectangular truss-core. They also observed that the shear stiffnesses have negligible influence on the maximum deflection if a triangular core is used. On the other hand, sandwich panels with vertical core members have low shear stiffness, which significantly influences their maximum deflection. Lok and Cheng did not conduct a local stress analysis of the sandwich structure and only used effective stiffness equations for isotropic materials.

Chang et al. [5] analyzed the linear elastic bending behavior of a corrugated-core sandwich plate in which an isotropic material, in this case steel, was used for faces and webs. They calculated the elastic constants of a three-dimensional sandwich panel using force-distortion relationship given by Libove and Hubka [1] and used them into an equivalent two-dimensional structurally orthotropic thick plate continuum model. They investigated the effects of several geometric parameters, such as corrugation angle and web-to-face thickness ratio, and two different boundary conditions on the deflection, bending moments and shear forces in the plate subjected to a uniform pressure load.

Wang et al. [6] treated a triangular core aluminum sandwich plate as a three-layered laminated plate in which the triangular core was replaced with an equivalent homogeneous layer. They derived the elastic constants of the equivalent homogeneous layer by applying small-deflection beam theory to the inclined members of the triangular core.

Buannic et al. [7] and Biancolini [8] combined homogenization and finite element methods to determine the deflection of corrugated core sandwich panels. Buannic et al. [7] observed the importance of including transverse shear stiffness in the formulation of the homogeneous plate solution. Biancolini [8] used micromechanical models and energy equivalency in the homogenization process.

Nordstand, Carlsson and Allen [9] analyzed the transverse shear moduli of corrugated core sandwich plates. They observed that the transverse shear modulus normal to the corrugation direction is much smaller and is more sensitive to the corrugation shape than the transverse shear modulus along the corrugation direction. Later, Carlsson, Nordstrand and Westerlind [10] applied the first order shear deformation laminated plate theory to determine the in-plane extensional and shear stiffnesses as well as bending and twisting stiffnesses of corrugated-core sandwich. The authors observed that the bending, twisting, in-plane extensional, and in-plane shear stiffnesses were dominated by the extensional and shear stiffnesses of the face sheets and found reasonable agreements between the calculated and experimental values for corrugated cardboard. However, the measured transverse shear stiffnesses were significantly lower than the calculated values based on the analysis in Ref. [9]. They attributed the discrepancy to the delamination damage and change in the core shape occurring during the manufacturing of corrugated cardboard.

Martinez et al. [11] were the first authors to develop an equivalent plate model for composite corrugated-core sandwich panels using micromechanics approach. As with many previous authors [1-5], they idealized the composite corrugated sandwich plate as an equivalent otthotropic thick-plate continuum. However, unlike the previous works, the material in the faces and the webs was a laminated carbon fiber reinforced epoxy composite. The extensional, flexural and coupling stiffness matrices as well as transverse shear stiffness terms for the equivalent plate were calculated using the strain energy approach. For calculating bending response, which included the maximum deflection and stresses, they implemented higher order shear deformation plate theory and found good agreement with the results obtained by finite element analysis.

In this chapter, composite sandwich plates with corrugated core are analyzed for their global deflections, bending moment and shear force distributions. The sandwich plates consist of repetitive unit cells and each unit cell is constructed of top and bottom faces and two webs connecting the faces. In the present approach, the sandwich plate is first transformed into an equivalent orthotropic plate using the analytical method given by Martinez et al. [11]. The global bending response is then calculated using the minimum potential energy approach. The geometric parameters and laminated construction in the sandwich plate are systematically varied to determine their effects on the global bending response.

The chapter is divided into three major sections: analytical formulations, global deflection, and bending moments and shear forces. The section on analytical formulation starts with the definitions of geometric parameters of a unit cell in the sandwich plate, and then provides the formulations for homogenization and global deflection calculations using minimum potential energy approach. The section on global deflection presents systematic parametric studies on the effects of geometric parameters and explores the importance of transverse shear on the global deflection of homogenized plates. The chapter ends with a description of bending moment and shear force distributions in homogenized plates.

2.2 ANALYTICAL FORMULATIONS

The analysis is performed using a unit cell of the type shown in Figure 2.1. The unit cell is made of two thin faces (indicated as members 1 and 2 in Figure 2.1) and two inclined webs (indicated as members 3 and 4 in Figure 2.1) in the core. The materials in

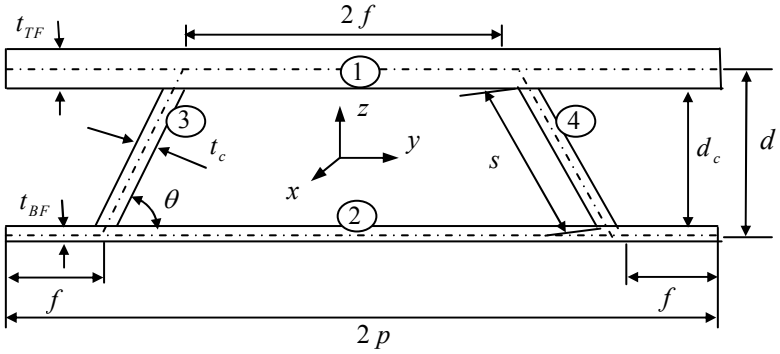

Figure 2.1: Description of the unit cell with unequal face thicknesses

the faces and the webs are fiber reinforced composite laminates. The xyz coordinate system is located at the centroid of the unit cell. The unit cell is aligned with the x-direction. It is symmetric with respect to the xz plane and normal to the corrugation direction is the y-direction.

2.2.1 Geometric Parameters

The geometric parameters of the unit cell that can be independently varied are listed below.

$2p$: pitch of the unit cell

d : face center distance, i.e., center-to-center distance between the top and bottom faces

t_{TF} : top face thickness

t_{BF} : bottom face thickness

t_c : web thickness

θ : web inclination angle

The other useful geometric parameters of the unit cell are as follows.

d_c : core depth, i.e., distance between the faces $= d - \frac{1}{2}t_{TF} - \frac{1}{2}t_{BF}$

s : web length $= \frac{d_c}{\sin\theta}$

f : web location on each side of the bottom face $= \frac{1}{2}\left(p - \frac{d}{\tan\theta}\right)$

For the unit cell considered, the maximum web inclination angle is 90º, which corresponds to $f = 0.5p$ and produces a rectangular core. The minimum web inclination angle is given by $\theta_{\min} = \tan^{-1}\left(\frac{d}{p}\right)$, which corresponds to $f = 0$ and produces a triangular core.

The cross-sectional area A_θ of the unit cell with web inclination angle θ is given by the following equation.

$$A_\theta = 2p\left(t_{TF} + t_{BF}\right) + 2d_c\frac{t_c}{\sin\theta} \qquad (2.1)$$

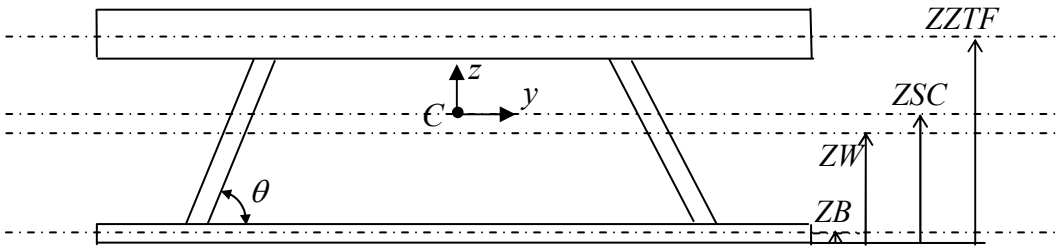

Figure 2.2: Location of the centroidal axis of the unit cell

where, $\theta_{\min} \le \theta \le 90^0$. A_{90} is the cross-sectional area of the unit cell with a rectangular core for which $\theta = 90^o$.

The centroid of the unit cell is located at C, as shown in Figure 2.2.

$$ZSC = \frac{ATP * ZZTF + ABP * ZZBF + 2 * AW * ZW}{ATP + ABP + 2 * AW}$$

$$ZZTF = t_{BF} + d_c + \frac{t_{TF}}{2}$$

$$ZZBF = \frac{t_{BF}}{2}$$

$$ZW = t_{BF} + \frac{d_c}{2}$$

$$ZT = t_{BF} + t_{TF} + d_c$$

where *ATP*: Area of the top face

ABP: Area of the bottom face

AW: Area of the webs

ZZTF-ZSC: Position of the top face from the centroidal y-axis is

ZZBF-ZSC: Position of the bottom face from the centroidal y-axis

ZW-ZSC: Position of the webs' centroid from the centroidal y-axis

If the top and bottom face thickness is the same, i.e., $t_{TF} = t_{BF} = t$, the centroid of the unit

cell is located at (*t/2 + d/2*) from the bottom surface of the unit cell.

2.2.2 Stiffness Matrix for the Face and Core members of the Unit Cell

The face and core members are thin laminated composite plates. The in-plane extensional-shear and out-of-plane bending-twisting responses of laminated plates are governed by the following constitutive relation [12].

$$\begin{bmatrix} N \\ M \end{bmatrix} = \begin{bmatrix} [A] & [B] \\ [B] & [D] \end{bmatrix} \begin{Bmatrix} \varepsilon_\circ \\ \kappa \end{Bmatrix} \tag{2.2}$$

where $[N]$= In-plane force matrix, $[M]$= Bending- twisting moment matrix, $[\varepsilon_\circ]$= Mid-plane strain matrix, $[\kappa]$= Bending-twisting curvature matrix, $[A]$= In-plane extensional-shear stiffness matrix, $[D]$= Bending-twisting stiffness matrix, and $[B]$= Extension-bending coupling matrix.

The elements of $[A]$, $[B]$ and $[D]$ matrices are calculated using the following equation.

$$\begin{aligned} \begin{bmatrix} A_{ij} & B_{ij} & D_{ij} \end{bmatrix} &= \int_{\frac{-t}{2}}^{\frac{t}{2}} \left(\bar{Q}_{ij}^{e}\right)_k \begin{bmatrix} 1 & z & z^2 \end{bmatrix} dz \\ &= \sum_{k=1}^{N} \left(\bar{Q}_{ij}^{e}\right)_k \begin{bmatrix} \left(z_k - z_{k-1}\right) & \dfrac{\left(z_k^2 - z_{k-1}^2\right)}{2} & \dfrac{\left(z_k^3 - z_{k-1}^3\right)}{3} \end{bmatrix} \end{aligned} \tag{2.3}$$

where, $\left(\bar{Q}_{ij}^{e}\right)_k$ is the stiffness matrix elements of the k^{th} lamina, t = laminate thickness, z_k = distance from the mid-plane of the laminate to the top of the k^{th} lamina, z_{k-1} = distance from the mid-plane of the laminate to the top of the $(k-1)^{th}$ lamina and N = number of laminas in the laminate. For a symmetric laminate, [B] = [0].

Deformation $\{D^{(e)}\}$ of each member in the unit cell can be written in terms of deformation of the unit cell $\{D\}^M$ in the following way.

$$\{D\}^{(e)} = [T_D]^{(e)} \{D\}^M \tag{2.4}$$

In Equation (2.4), $[T_D]^{(e)}$ represents the global-to-local co-ordinate transformation matrix for member *e*. Equation (2.4) relates the deformations of the unit cell in the global (x, y) co-ordinate system to the deformations of each member in the unit cell in its local $(\bar{x}, \bar{y})$ co-ordinate system.

Deformation matrix for each member in the unit cell is given as follows.

(i) Top face

$$\begin{Bmatrix} \varepsilon_{xo} \\ \varepsilon_{yo} \\ \gamma_{xyo} \\ \kappa_x \\ \kappa_y \\ \kappa_{xy} \end{Bmatrix}^{(1)} = \begin{bmatrix} 1 & 0 & 0 & (ZZTF - ZSC) & 0 & 0 \\ 0 & 1 & 0 & 0 & (ZZTF - ZSC) & 0 \\ 0 & 0 & 1 & 0 & 0 & (ZZTF - ZSC) \\ 0 & 0 & 0 & 1 & 0 & 0 \\ 0 & 0 & 0 & 0 & 1 & 0 \\ 0 & 0 & 0 & 0 & 0 & 1 \end{bmatrix} \begin{Bmatrix} \varepsilon_{xo} \\ \varepsilon_{yo} \\ \gamma_{xyo} \\ \kappa_x \\ \kappa_y \\ \kappa_{xy} \end{Bmatrix}^{(M)}$$

(ii) Bottom face

$$\begin{Bmatrix} \varepsilon_{xo} \\ \varepsilon_{yo} \\ \gamma_{xyo} \\ \kappa_x \\ \kappa_y \\ \kappa_{xy} \end{Bmatrix}^{(2)} = \begin{bmatrix} 1 & 0 & 0 & -(ZZTF - ZSC) & 0 & 0 \\ 0 & 1 & 0 & 0 & -(ZZTF - ZSC) & 0 \\ 0 & 0 & 1 & 0 & 0 & -(ZZTF - ZSC) \\ 0 & 0 & 0 & 1 & 0 & 0 \\ 0 & 0 & 0 & 0 & 1 & 0 \\ 0 & 0 & 0 & 0 & 0 & 1 \end{bmatrix} \begin{Bmatrix} \varepsilon_{xo} \\ \varepsilon_{yo} \\ \gamma_{xyo} \\ \kappa_x \\ \kappa_y \\ \kappa_{xy} \end{Bmatrix}^{(M)}$$

(iii) Left web

$$\begin{Bmatrix} \varepsilon_{xo} \\ \varepsilon_{yo} \\ \gamma_{xyo} \\ \kappa_x \\ \kappa_y \\ \kappa_{xy} \end{Bmatrix}^{(3)} = \begin{bmatrix} 1 & 0 & 0 & \left((\text{ZT-ZSC-t}_{\text{TF}}) - \bar{y}\sin\theta\right) & 0 & 0 \\ 0 & 0 & 0 & 0 & \cos^2\theta\left((\text{ZT-ZSC-t}_{\text{TF}}) - \bar{y}\sin\theta\right) & 0 \\ 0 & 0 & -\cos\theta & 0 & 0 & -\cos\theta\left((\text{ZT-ZSC-t}_{\text{TF}}) - \bar{y}\sin\theta\right) \\ 0 & 0 & 0 & -\cos\theta & 0 & 0 \\ 0 & 0 & 0 & 0 & -\cos^3\theta - 2\cos\theta\sin^2\theta & 0 \\ 0 & 0 & 0 & 0 & 0 & 1 \end{bmatrix} \begin{Bmatrix} \varepsilon_{xo} \\ \varepsilon_{yo} \\ \gamma_{xyo} \\ \kappa_x \\ \kappa_y \\ \kappa_{xy} \end{Bmatrix}^{(M)}$$

(iv) Right web

$$\begin{Bmatrix} \varepsilon_{xo} \\ \varepsilon_{yo} \\ \gamma_{xyo} \\ \kappa_x \\ \kappa_y \\ \kappa_{xy} \end{Bmatrix}^{(4)} = \begin{bmatrix} 1 & 0 & 0 & \left(\text{(ZT-ZSC-t}_{\text{TF}}\right)-\bar{y}\sin\theta\right) & 0 & 0 \\ 0 & 0 & 0 & 0 & \cos^2\theta\left(\text{(ZT-ZSC-t}_{\text{TF}}\right)-\bar{y}\sin\theta\right) & 0 \\ 0 & 0 & \cos\theta & 0 & 0 & \cos\theta\left(\text{(ZT-ZSC-t}_{\text{TF}}\right)-\bar{y}\sin\theta\right) \\ 0 & 0 & 0 & \cos\theta & 0 & 0 \\ 0 & 0 & 0 & 0 & \cos^3\theta+2\cos\theta\sin^2\theta & 0 \\ 0 & 0 & 0 & 0 & 0 & 1 \end{bmatrix} \begin{Bmatrix} \varepsilon_{xo} \\ \varepsilon_{yo} \\ \gamma_{xyo} \\ \kappa_x \\ \kappa_y \\ \kappa_{xy} \end{Bmatrix}^{(M)}$$

2.2.3 Stiffness Matrix of the Equivalent Plate

Global reaction loads on the equivalent plate are shown in Figure 2.3. The constitutive relation between global reaction loads (in-plane normal/shear forces, transverse shear forces and bending /twisting moment resultants) and global deformations (normal strains, shear strains and curvatures) of the plate [12] is given in Equation (2.5).

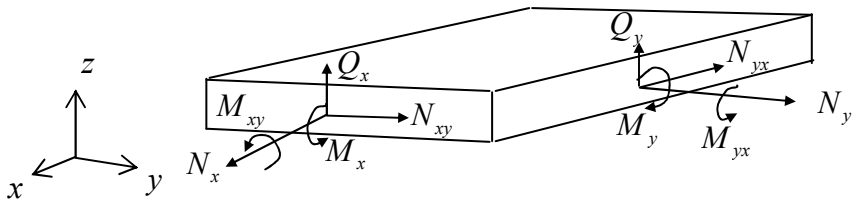

Figure 2.3: In-plane normal and shear forces (N_x, N_y and N_{xy}), transverse shear forces (Q_x and Q_y), bending and twisting moments (M_x, M_y and M_{xy}) on a plate

$$\begin{Bmatrix} N_x \\ N_y \\ N_{xy} \\ Q_y \\ Q_x \\ M_x \\ M_y \\ M_{xy} \end{Bmatrix} = \begin{bmatrix} A_{11} & A_{12} & A_{16} & 0 & 0 & B_{11} & B_{12} & B_{16} \\ A_{12} & A_{22} & A_{26} & 0 & 0 & B_{12} & B_{22} & B_{26} \\ A_{16} & A_{26} & A_{66} & 0 & 0 & B_{16} & B_{26} & B_{66} \\ 0 & 0 & 0 & A_{44} & 0 & 0 & 0 & 0 \\ 0 & 0 & 0 & 0 & A_{55} & 0 & 0 & 0 \\ B_{11} & B_{12} & B_{16} & 0 & 0 & D_{11} & D_{12} & D_{16} \\ B_{12} & B_{22} & B_{26} & 0 & 0 & D_{12} & D_{22} & D_{26} \\ B_{16} & B_{26} & B_{66} & 0 & 0 & D_{16} & D_{26} & D_{66} \end{bmatrix} \begin{Bmatrix} \dfrac{\partial u_0}{\partial x} \\ \dfrac{\partial v_0}{\partial y} \\ \dfrac{\partial u_0}{\partial y}+\dfrac{\partial v_0}{\partial x} \\ \overline{\beta}+\dfrac{\partial w}{\partial y} \\ \overline{\alpha}+\dfrac{\partial w}{\partial x} \\ \dfrac{\partial \overline{\alpha}}{\partial x} \\ \dfrac{\partial \overline{\beta}}{\partial y} \\ \dfrac{\partial \overline{\alpha}}{\partial y}+\dfrac{\partial \overline{\beta}}{\partial x} \end{Bmatrix} \quad (2.5)$$

where [A], [B] and [D] matrices represent the in-plane stiffness, extension-bending coupling stiffness and bending stiffness of the equivalent plate. A_{44} and A_{55} are the transverse shear stiffness components. [$N_{x,\,y,\,xy}$] are the in-plane normal and shear forces, [$Q_{y,\,x}$] are the transverse shear forces, and [$M_{x,\,y,\,xy}$] are the bending and twisting moments. Additionally, u_0, v_0 and w are the mid-plane displacements in the x, y and z directions, respectively, and $\bar{\alpha}$ and $\bar{\beta}$ are the rotations of the transverse normals about the y-axis and x-axis, respectively. The $[A]$, $[B]$ and $[D]$ stiffness elements of the equivalent plate in Equation (2.5) are calculated by equating the total strain energy, U^M, of the equivalent plate to the sum of the strain energies of all four members in the unit cell.

$$\begin{aligned} U^M &= \frac{1}{2}(2p)^2 \left(\{D\}^M\right)^T [K] \{D\}^M \\ &= \sum_{e=1}^{4} U^{(e)} \end{aligned}$$

Following the formulation given in Martinez et al. [11], the stiffness matrix $[K]$ of the equivalent homogenous plate can then be derived as per Equation (2.6) using each member's stiffness matrix $[K]^{(e)}$.

$$\begin{aligned} [K] &= \sum_{e=1}^{4} K^{(e)} \\ &= \frac{1}{2p} \sum_{e=1}^{4} \int_0^L \left(T_D^{(e)}\right)^T [K]^{(e)} \left(T_D^{(e)}\right) d\bar{y} \end{aligned} \tag{2.6}$$

where, the unit cell stiffness matrix $[K]$ contains extensional, bending and bending-extensional coupling matrices in the form given in Equation 2.7.

$$[K] = \begin{bmatrix} A & B \\ B & D \end{bmatrix} \tag{2.7}$$

2.2.4 Transverse Shear Stiffness of the Unit Cell

There are two transverse shear stiffness terms that need to be considered for the unit cell. They are A_{44} and A_{55} corresponding to transverse shear forces Q_y and Q_x

respectively (Figure 2.4). The corresponding shear stress components are τ_{xz} and τ_{yz}, respectively. In this section, formulations are given to calculate both transverse shear stiffness terms using shear strain energy and bending strain energy of the entire unit cell. The formulations were originally derived by Libove and Hubka [1] and were later adopted by several authors in their work [2]-[4] and [11] .

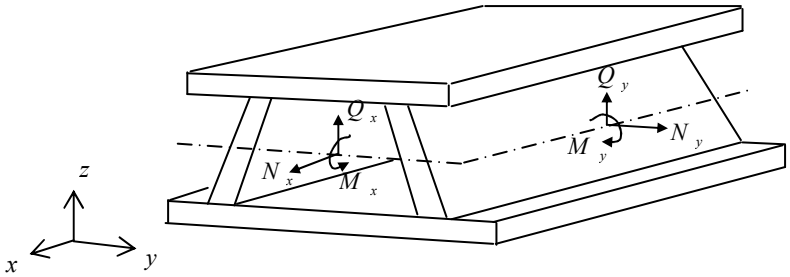

Figure 2.4: Global normal forces, shear forces and bending moments on the unit cell

2.2.4.1 Formulation for A_{44}

It is assumed that the unit cell is subjected to a unit transverse shear force Q_y as shown in Figure 2.5. The moment equilibrium of the unit cell requires the presence of a horizontal force $Y = p/d$ on the faces of the unit cell, which is also shown in Figure 2.5. Under the action of the transverse shear force Q_y and horizontal force Y, the dominant deformation is the bending of the upper and lower faces, which is accompanied by the deformation of the webs as shown in Figure 2.6. Because of symmetry about the xz plane, only half of the unit cell is considered, as shown in Figure 2.6(a). In calculating the transverse shear stiffness term A_{44}, only the strain energy due to bending is considered and the relatively small strain energies due to shear and normal forces are neglected.

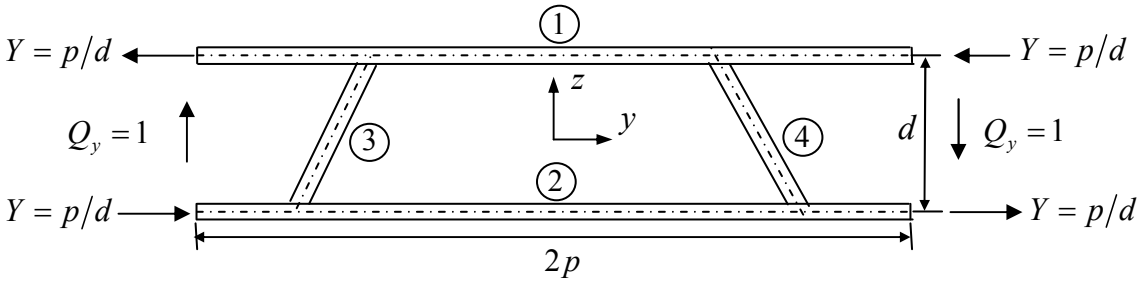

Figure 2.5: Unit transverse shear force and horizontal force for moment equilibrium

The half-unit cell is assumed to be free at A and fixed at D. The fixed support at D prevents rigid-body displacement when the transverse shear force is applied. The web member BE is assumed to fixed at both ends so that it can sustain bending deformation. The unit transverse shear force Q_y is divided into two parts, P acting on the upper face and R acting on the lower face, so that $P + R = 1$. This is shown in Figure 2.6(a). The vertical reaction forces at A and D are represented by F and *(1-F)*, respectively.

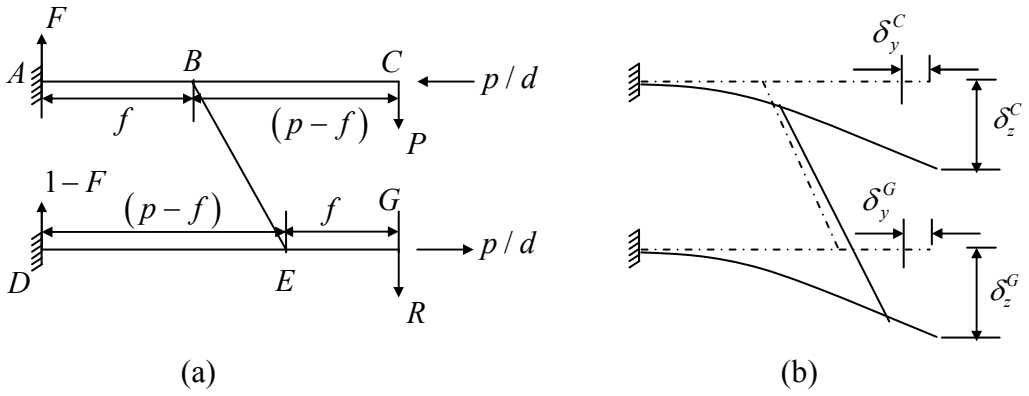

(a) (b)

Figure 2.6: Half unit cell of corrugated core panel with deflection

Since bending is the major deformation mode of the top and bottom faces as well as the right web, only the bending strain energy is considered here, which is given by Equation (2.8).

$$U_S = \frac{1}{2} D_{11}^{\prime(1)} \left[\int_0^f M_{AB}^2(y)\,dy + \int_0^{p-f} M_{BC}^2(y)\,dy \right] + \frac{1}{2} D_{11}^{\prime(2)} \left[\int_0^{p-f} M_{DE}^2(y)\,dy + \int_0^f M_{EG}^2(y)\,dy \right] + \frac{1}{2} D_{11}^{\prime(4)} \int_0^s M_{BE}^2(\bar{y})\,d\bar{y} \tag{2.8}$$

where, the moment equations for all elements in the half unit cell are given as

$$\begin{aligned}
M_{AB}(\bar{y}) &= F\bar{y} && 0 \le \bar{y} \le f \\
M_{BC}(\bar{y}) &= P\bar{y} && 0 \le \bar{y} \le p - f \\
M_{DE}(\bar{y}) &= (1-F)\,\bar{y} && 0 \le \bar{y} \le p - f \\
M_{EG}(\bar{y}) &= R\bar{y} && 0 \le \bar{y} \le f \\
M_{BE}(\bar{y}) &= F(f + \bar{y}\cos\theta) + P(p - f - \bar{y}\cos\theta) - \frac{p}{d}\bar{y}\sin\theta && 0 \le \bar{y} \le s
\end{aligned} \tag{2.9}$$

Using Castigliano's theorem [13], displacements and rotations are calculated by taking the first partial derivative of the total strain energy with respect to the force in the direction of the displacement, i.e., $\delta_i = \frac{\partial U_i}{\partial P_i}$

Displacement equations of the half-unit cell due to unit Q_y are

$$\delta_y^C = -\frac{1}{3} D_{11}'^{(4)} \left(F\cos\theta - (1-R)\cos\theta - \frac{p\sin\theta}{d} \right) s^3 \sin\theta - \frac{1}{2} D_{11}'^{(4)} \left(Ff + (1-R)(p-f) \right) s^2 \sin\theta$$

$$\delta_y^G = -\frac{1}{2} D_{11}'^{(2)} d (1-F)(p-f)^2$$

$$= -\frac{1}{2} D_{11}'^{(2)} d (1-F) \left(\frac{p}{2} + \frac{d}{2\tan\theta} \right)^2$$

$$\delta_z^G = D_{11}'^{(2)} \left((1-F)(p-f)^2 \left(\frac{1}{3}(p-f)^2 - \frac{1}{2}p \right) + \frac{1}{3} R f^3 \right)$$

$$= D_{11}'^{(2)} \left((1-F) \left(\frac{p}{2} + \frac{d}{2\tan\theta} \right)^2 \left(\frac{1}{3} \left(\frac{p}{2} + \frac{d}{2\tan\theta} \right) - \frac{1}{2}p \right) + \frac{1}{3} R \left(\frac{p}{2} - \frac{d}{2\tan\theta} \right)^3 \right)$$

Shear strain for half unit cell is given as $\gamma_y = \frac{\delta_y}{d} + \frac{\delta_z}{p}$

where, $\delta_y = \delta_y^C + \delta_y^G$ and vertical deflection $\delta_z = \delta_z^C = \delta_z^G$. Since Q_y is assumed to be 1N/m, the transverse shear stiffness A_{44} is obtained as follows.

$$A_{44} = \frac{Q_y}{\gamma_y} = \frac{1}{\frac{\delta_y}{d} + \frac{\delta_z}{p}} = \frac{1}{\frac{\left(\delta_y^C + \delta_y^G\right)}{d} + \left(\frac{\delta_z}{p} \right)} \tag{2.10}$$

2.2.4.2 Formulation for A_{55}

Shear stresses in the webs due to shear force Q_x are determined by considering the force equilibrium of an element of length Δx of the unit cell shown in Figure 2.7. Since the transverse shear stress in the faces is very small, its contribution to total shear strain energy for the entire unit cell is neglected and only the contributions of the web members are considered.

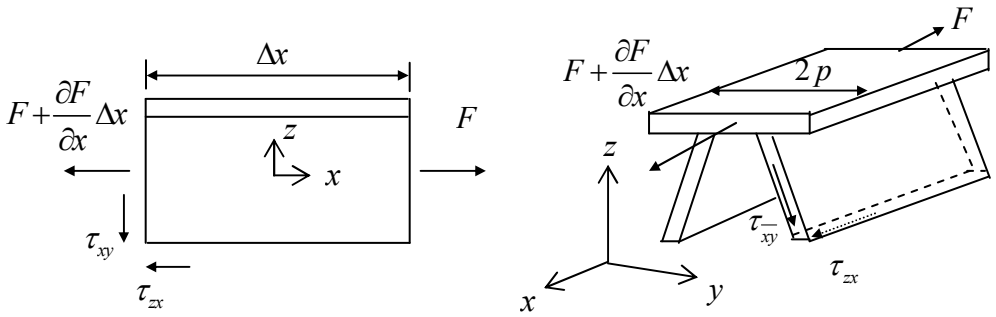

(a) (b)

Figure 2.7: Stresses acting in the x-direction on element of the unit cell

The force equilibrium equation in the x-direction can be written as

$$\left(F+\frac{\partial F}{\partial x}\Delta x-F\right)+2\left[\tau_{zx}\Delta x\left(\frac{t_c}{\sin\theta}\right)\right]=0$$

$$2\tau_{zx}\left(\frac{t_c s}{d}\right)=-\frac{\partial F}{\partial x} \qquad \because \ \sin\theta=\frac{d}{s}$$

since $\tau_{zx}=\tau_{\bar{x}\bar{y}}\sin\theta$ and the forces in the x-direction are a summation of forces on the top face and both left and right webs, the force equilibrium equation transforms to

$$2\left[\tau_{\bar{x}\bar{y}}\sin\theta\left(\frac{t_c s}{d}\right)\right]=-\frac{\partial}{\partial x}\left[N_{\bar{x}}^{(1)}(2p)+\int_0^{\bar{s}}N_{\bar{x}}^{(3)}d\bar{y}+\int_0^{\bar{s}}N_{\bar{x}}^{(4)}d\bar{y}\right] \tag{2.11}$$

In Equation (2.11), the normal forces on members 1, 3 and 4 (top face, left web and right web, respectively) can be written in terms of respective extensional stiffness and mid-plane strain as $N_{\bar{x}}^{(1)}=A_{11}^{(1)}\varepsilon_{x_0}^{(1)}$, $N_{\bar{x}}^{(3)}=A_{11}^{(3)}\varepsilon_{x_0}^{(3)}$ and $N_{\bar{x}}^{(4)}=A_{11}^{(4)}\varepsilon_{x_0}^{(4)}$. The mid-plane strains are given in terms of the bending moment M_x as $\varepsilon_{x_0}^{(1)}=\frac{d}{2}D_{11}'M_x$ and $\varepsilon_{x_0}^{(3)}=\varepsilon_{x_0}^{(4)}=\left(\frac{d}{2}-\bar{y}\sin\theta\right)D_{11}'M_x$. Substituting for N_x in terms of bending moment M_x and noting that $\partial M_x/\partial x=Q_x$, Equation (2.11) can be rewritten to obtain shear stress as

$$\tau_{\overline{xy}}(\overline{y}) = -Q_x\left(\frac{d}{2st_c\sin\theta}\right)\left[pdA_{11}^{(1)}D'_{11}\left(\frac{d}{2}\overline{y} - \frac{\overline{y}^2}{2}\sin\theta\right)\right] \tag{2.12}$$

Shear stress $\tau_{\overline{xy}}$ calculated in Equation (2.12) is then used to calculate to shear strain energy which is given below.

$$U_s = \frac{t_c}{p}\int_0^s \frac{1}{2}\frac{\left(\tau_{\overline{xy}}\right)^2}{G_{\overline{xy}}}d\overline{y} = \frac{Q_x^2}{2A_{55}} \tag{2.13}$$

In Equation (2.13), the right hand side is the expression for shear strain energy in terms of the transverse shear force Q_x and effective shear modulus G_{xy}. Using the equality relationship between the two shear strain energy expressions given in Equation (2.13), A55 can be determined as

$$A_{55} = \frac{1}{2\left[\frac{t_c}{p}\int_0^s \frac{1}{2}\frac{\left(\left(\frac{d}{2st_c\sin\theta}\right)\left[pdA_{11}^{(1)}D'_{11}\left(\frac{d}{2}\overline{y} - \frac{\overline{y}^2}{2}\sin\theta\right)\right]\right)^2}{G_{\overline{xy}}}d\overline{y}\right]} \tag{2.14}$$

2.2.5 Formulation for Global Bending Response using Minimum Potential Energy

In this research, a flat corrugated sandwich plate of dimensions (*a* x *b*) is considered. The plate is simply supported on all four edges and is subjected to a uniform pressure load p_o on its top surface. The plate has a unidirectional corrugation in the y-direction as shown in Figure 2.1. Based on the approach described in the previous sections, the stiffness elements of an equivalent homogenous orthotropic plate are calculated using Equations (2.6), (2.10) and (2.12). To calculate the global bending response of the equivalent plate, the minimum potential energy approach is used.

The potential energy (Π) of a plate subjected to external loads is the difference of the total strain energy (*U*) stored in the plate and the work done (*W*) by the applied external loads. The total strain energy of the plate under static loading can be expressed as the sum of four strain energies integrated over the entire plate, U_S-strain energy due to

stretching, U_B-strain energy due to bending, U_{TS}-strain energy due to transverse shearing, U_{BS}-strain energy due to bending-stretching coupling.

$$U = U_S + U_B + U_{TS} + U_{BS} \tag{2.15}$$

U_S, strain energy due to stretching, is given as

$$U_S = \frac{1}{2}\int_A \left\{ \begin{array}{l} A_{11}\left(\frac{\partial u_0}{\partial x}\right)^2 + 2A_{12}\frac{\partial u_0}{\partial x}\frac{\partial v_0}{\partial y} + 2A_{16}\frac{\partial u_0}{\partial x}\left(\frac{\partial u_0}{\partial y} + \frac{\partial v_0}{\partial x}\right) \\ + A_{22}\left(\frac{\partial v_0}{\partial y}\right)^2 + 2A_{26}\frac{\partial v_0}{\partial y}\left(\frac{\partial u_0}{\partial y} + \frac{\partial v_0}{\partial x}\right) + A_{66}\left(\frac{\partial u_0}{\partial y} + \frac{\partial v_0}{\partial x}\right)^2 \end{array} \right\} dA$$

U_B, strain energy due to bending, is given as

$$U_B = \frac{1}{2}\int_A \left\{ \begin{array}{l} D_{11}\left(\frac{\partial \overline{\alpha}}{\partial x}\right)^2 + 2D_{12}\frac{\partial \overline{\beta}}{\partial y}\frac{\partial \overline{\alpha}}{\partial x} + D_{22}\left(\frac{\partial \overline{\beta}}{\partial y}\right)^2 + D_{66}\left(\frac{\partial \overline{\alpha}}{\partial y} + \frac{\partial \overline{\beta}}{\partial x}\right)^2 \\ +2D_{16}\frac{\partial \overline{\alpha}}{\partial x}\left(\frac{\partial \overline{\alpha}}{\partial y} + \frac{\partial \overline{\beta}}{\partial x}\right) + 2D_{26}\frac{\partial \overline{\beta}}{\partial y}\left(\frac{\partial \overline{\alpha}}{\partial y} + \frac{\partial \overline{\beta}}{\partial x}\right) \end{array} \right\} dA$$

U_{TS}, strain energy due to transverse shearing, is given as

$$U_{TS} = \frac{1}{2}\int_A \left\{ A_{44}\left(\overline{\beta} + \frac{\partial w}{\partial y}\right)^2 + A_{55}\left(\overline{\alpha} + \frac{\partial w}{\partial x}\right)^2 + 2A_{45}\left(\overline{\beta} + \frac{\partial w}{\partial y}\right)\left(\overline{\alpha} + \frac{\partial w}{\partial x}\right) \right\} dA$$

U_{BS}, strain energy due to bending-stretching coupling, is given as

$$U_{BS} = \int_A \left\{ \begin{array}{l} B_{11}\frac{\partial u_0}{\partial x}\frac{\partial \overline{\alpha}}{\partial x} + B_{12}\left[\frac{\partial u_0}{\partial x}\frac{\partial \overline{\beta}}{\partial y} + \frac{\partial v_0}{\partial y}\frac{\partial \overline{\alpha}}{\partial x}\right] \\ +B_{16}\left[\frac{\partial u_0}{\partial x}\left(\frac{\partial \overline{\alpha}}{\partial y} + \frac{\partial \overline{\beta}}{\partial x}\right) + \left(\frac{\partial u_0}{\partial y} + \frac{\partial v_0}{\partial x}\right)\frac{\partial \overline{\alpha}}{\partial x}\right] + B_{22}\frac{\partial v_0}{\partial y}\frac{\partial \overline{\beta}}{\partial y} \\ +B_{26}\left[\frac{\partial v_0}{\partial y}\left(\frac{\partial \overline{\alpha}}{\partial y} + \frac{\partial \overline{\beta}}{\partial x}\right) + \left(\frac{\partial u_0}{\partial y} + \frac{\partial v_0}{\partial x}\right)\frac{\partial \overline{\beta}}{\partial y}\right] + B_{66}\left[\left(\frac{\partial u_0}{\partial y} + \frac{\partial v_0}{\partial x}\right) + \left(\frac{\partial \overline{\alpha}}{\partial y} + \frac{\partial \overline{\beta}}{\partial x}\right)\right] \end{array} \right\} dA$$

Total potential energy is obtained by integrating over the entire plate. Thus,

$$\Pi = \iint_A (U - W)\ dA$$

In terms of displacement and rotational components, the potential energy of the plate, is given as

$$\Pi = \int_A \left\{ \begin{array}{l} \frac{A_{11}}{2}\left(\frac{\partial u_0}{\partial x}\right)^2 + A_{12}\frac{\partial u_0}{\partial x}\frac{\partial v_0}{\partial y} + A_{16}\frac{\partial u_0}{\partial x}\left(\frac{\partial u_0}{\partial y} + \frac{\partial v_0}{\partial x}\right) + \frac{A_{22}}{2}\left(\frac{\partial v_0}{\partial y}\right)^2 + A_{26}\frac{\partial v_0}{\partial y}\left(\frac{\partial u_0}{\partial y} + \frac{\partial v_0}{\partial x}\right) \\ + \frac{A_{66}}{2}\left(\frac{\partial u_0}{\partial y} + \frac{\partial v_0}{\partial x}\right)^2 + \frac{A_{44}}{2}\left(\overline{\beta} + \frac{\partial w}{\partial y}\right)^2 + \frac{A_{55}}{2}\left(\overline{\alpha} + \frac{\partial w}{\partial x}\right)^2 + A_{45}\left(\overline{\beta} + \frac{\partial w}{\partial y}\right)\left(\overline{\alpha} + \frac{\partial w}{\partial x}\right) \\ + B_{11}\frac{\partial u_0}{\partial x}\frac{\partial \overline{\alpha}}{\partial x} + B_{12}\left[\frac{\partial u_0}{\partial x}\frac{\partial \overline{\beta}}{\partial y} + \frac{\partial v_0}{\partial y}\frac{\partial \overline{\alpha}}{\partial x}\right] + B_{16}\left[\frac{\partial u_0}{\partial x}\left(\frac{\partial \overline{\alpha}}{\partial y} + \frac{\partial \overline{\beta}}{\partial x}\right) + \left(\frac{\partial u_0}{\partial y} + \frac{\partial v_0}{\partial x}\right)\frac{\partial \overline{\alpha}}{\partial x}\right] \\ + B_{22}\frac{\partial v_0}{\partial y}\frac{\partial \overline{\beta}}{\partial y} + B_{26}\left[\frac{\partial v_0}{\partial y}\left(\frac{\partial \overline{\alpha}}{\partial y} + \frac{\partial \overline{\beta}}{\partial x}\right) + \left(\frac{\partial u_0}{\partial y} + \frac{\partial v_0}{\partial x}\right)\frac{\partial \overline{\beta}}{\partial y}\right] \\ + B_{66}\left[\left(\frac{\partial u_0}{\partial y} + \frac{\partial v_0}{\partial x}\right) + \left(\frac{\partial \overline{\alpha}}{\partial y} + \frac{\partial \overline{\beta}}{\partial x}\right)\right] + \frac{D_{11}}{2}\left(\frac{\partial \overline{\alpha}}{\partial x}\right)^2 + \frac{D_{12}}{2}\frac{\partial \overline{\beta}}{\partial y}\frac{\partial \overline{\alpha}}{\partial x} + \frac{D_{22}}{2}\left(\frac{\partial \overline{\beta}}{\partial y}\right)^2 \\ + \frac{D_{66}}{2}\left(\frac{\partial \overline{\alpha}}{\partial y} + \frac{\partial \overline{\beta}}{\partial x}\right)^2 + D_{16}\frac{\partial \overline{\alpha}}{\partial x}\left(\frac{\partial \overline{\alpha}}{\partial y} + \frac{\partial \overline{\beta}}{\partial x}\right) + D_{26}\frac{\partial \overline{\beta}}{\partial y}\left(\frac{\partial \overline{\alpha}}{\partial y} + \frac{\partial \overline{\beta}}{\partial x}\right) - p * w \end{array} \right\} dA \quad (2.16)$$

The general solutions for the displacement and rotational components of a plate with dimensions $(a \times b)$, in the x-y directions under simply supported boundary conditions on all edges are assumed as

$$\begin{aligned} u_0(x,y) &= \sum_{m=1}^{M}\sum_{n=1}^{N} U_{mn} \sin\left(\frac{m\pi x}{a}\right)\cos\left(\frac{n\pi y}{b}\right) \\ v_0(x,y) &= \sum_{m=1}^{M}\sum_{n=1}^{N} V_{mn} \cos\left(\frac{m\pi x}{a}\right)\sin\left(\frac{n\pi y}{b}\right) \\ w(x,y) &= \sum_{m=1}^{M}\sum_{n=1}^{N} W_{mn} \sin\left(\frac{m\pi x}{a}\right)\sin\left(\frac{n\pi y}{b}\right) \\ \overline{\alpha}(x,y) &= \sum_{m=1}^{M}\sum_{n=1}^{N} RTX_{mn} \cos\left(\frac{m\pi x}{a}\right)\sin\left(\frac{n\pi y}{b}\right) \\ \overline{\beta}(x,y) &= \sum_{m=1}^{M}\sum_{n=1}^{N} RTY_{mn} \sin\left(\frac{m\pi x}{a}\right)\cos\left(\frac{n\pi y}{b}\right) \end{aligned} \quad (2.17)$$

The general expression for the applied uniform pressure load p_0 on the plate with dimensions $a \times b$, in the $x - y$ directions is assumed as

$$p_0(x,y) = \sum_{m=1}^{M}\sum_{n=1}^{N} p_{mn} \sin\left(\frac{m\pi x}{a}\right)\sin\left(\frac{n\pi y}{b}\right) \tag{2.18}$$

where $p_{mn} = \dfrac{16p_0}{(\pi^2 mn)}$ for m = 1, 3,…, M and n = 1, 3, …., N combinations and $P_{mn} = 0$ for other combinations of m and n.

The five unknown Fourier coefficients in Equation (2.17), namely U_{mn}, V_{mn}, $W_{mn,}$ RTX_{mn} and RTY_{mn}, are calculated using the principle of minimum potential energy, which is written as

$$\delta(\Pi) = 0$$

where, δ(Π) represents partial differentiation of Πwith respect to each unknown Fourier coefficient. Thus,

$$\frac{\partial(\Pi)}{\partial Umn} = 0, \frac{\partial(\Pi)}{\partial Vmn} = 0, \frac{\partial(\Pi)}{\partial Wmn} = 0, \frac{\partial(\Pi)}{\partial RTXmn} = 0 \text{ and } \frac{\partial(\Pi)}{\partial RTYmn} = 0$$

For the deflection response, the partial differentiations result in five independent equations for each m and n combination. By using MATLAB symbolic variables, a code is written for the above formulation and solutions were obtained for U_{mn}, V_{mn}, $W_{mn,}$ RTX_{mn} and RTY_{mn}. The displacement and rotational components are then calculated using Equation (2.17). Convergence is checked using sufficient number of terms in Equation (2.17). The MATLAB codes are presented in Appendix A.

After the displacement and rotational components are calculated using Equation (2.17), the bending moments and shear forces are calculated using Equation (2.5). More specifically,

$$M_x = D_{11}\frac{\partial\bar{\alpha}}{\partial x} + D_{12}\frac{\partial\bar{\beta}}{\partial y} + D_{16}\left(\frac{\partial\bar{\alpha}}{\partial y} + \frac{\partial\bar{\beta}}{\partial x}\right) + B_{11}\frac{\partial u_0}{\partial x} + B_{12}\frac{\partial v_0}{\partial y} + B_{16}\left(\frac{\partial u_0}{\partial y} + \frac{\partial v_0}{\partial x}\right)$$

$$M_y = D_{12}\frac{\partial \bar{\alpha}}{\partial x} + D_{22}\frac{\partial \bar{\beta}}{\partial y} + D_{26}\left(\frac{\partial \bar{\alpha}}{\partial y} + \frac{\partial \bar{\beta}}{\partial x}\right) + B_{12}\frac{\partial u_0}{\partial x} + B_{22}\frac{\partial v_0}{\partial y} + B_{26}\left(\frac{\partial u_0}{\partial y} + \frac{\partial v_0}{\partial x}\right)$$

$$Q_y = A_{44}\left(\bar{\beta} + \frac{\partial w}{\partial y}\right) \tag{2.19}$$

$$Q_x = A_{55}\left(\bar{\alpha} + \frac{\partial w}{\partial x}\right)$$

2.3 GLOBAL DEFLECTIONS

In this section, several case studies are presented to demonstrate the use of the potential energy formulation developed in Section 2.2.5 for the global deflections of composite sandwich plates with corrugated core. The material in the faces and the webs is a carbon fiber reinforced epoxy composite laminate with the basic elastic properties [11] as $E_{11} = 138$ GPa, $E_{22} = 9$ GPa, $\nu_{12} = 0.3$, and $G_{12} = 6.9$ GPa. It is assumed that each layer in the laminate is of equal thickness. A square plate of 640 mm in length and 640 mm in width is considered. The plate is simply supported on all four edges and is subjected to a uniformly distributed load p_0 of 1 N/m^2 on its top surface.

The first four case studies in this section will consider the effects of varying geometric parameters, such as web inclination angle (θ), web thickness (t_c), pitch ($2p$) and face center distance (d) , on the maximum deflection. The laminate construction in these case studies has a stacking sequence of $[0/90]_s$, which is a symmetric laminate with four layers of equal thickness. The 0 and 90º layers in this laminate are oriented in the x- and y-directions, respectively. The effect of laminate construction is considered in the final case study in which two different four-layered symmetric laminates are selected, namely $[0/\alpha]_s$ and $[\pm\alpha]_s$, where α is the fiber orientation angle with respect to the longitudinal axis (x) of the plate. Since the laminates are symmetric about their mid-plane, $[B] = [0]$.

In all five case studies, the cross-sectional area of the unit cell, and therefore, its mass is maintained constant so that the effects of the geometric parameters and laminate construction can be directly compared.

2.3.1 Case Study 1: $[0/90]_s$ Laminates, $t_{TF} = t_{BF} = t_c = t \leq 1$ mm, $p = d = 80$ mm

This case study is undertaken to validate the energy formulation given in Section 2.2.5. The results of the case study are compared with the results given by Martinez et al. [11] who used a shear deformable plate theory to solve for the global plate deflection. The approach developed in the current work is based on minimum potential energy.

In this case study, the unit cell dimensions p and d are assumed to be 80 mm each, and the face plate and web thicknesses are assumed to be equal, i.e. $t_{TF} = t_{BF} = t_C = t$. The web inclination angle is varied from $\theta_{\min} = 45°$ to $\theta_{\max} = 90°$ to investigate the effect of web inclination angle on the global bending response of composite sandwich plates of equal cross-sectional area. Since the pitch, $2p$, is 160 mm, the plate has four unit cells in the y-direction. The calculated extensional, bending and transverse shear stiffness terms of the equivalent plate with web inclination angle $\theta = 90°$, i.e., a rectangular core, and $t_{TF} = t_{BF} = t_C = 1$ mm are listed in Table 2.1.

Table 2.1: Extensional, bending and transverse shear stiffness terms for $\theta = 90°$, $[0/90]_s$ laminates $t_{TF} = t_{BF} = t_c = t \leq 1$ mm, $p = d = 80$ mm

Extensional Stiffness (N/m)	A_{11}	A_{12}	A_{22}	A_{66}	A_{16}	A_{26}
	2.208E8	5.431E6	1.478E8	1.38E7	0	0
Bending Stiffness (N.m)	D_{11}	D_{12}	D_{22}	D_{66}	D_{16}	D_{26}
	2.745E5	0.87E5	2.365E5	0.22E5	0	0
Transverse Shear Stiffness (N/m)	A_{44}			A_{55}		
	15707.09			6.76E6		

The cross-sectional area, A_{90}, of this unit cell is 478 mm^2. For the other plates with web inclination angle θ lower than 90º, the cross-sectional area A_θ is assumed to be equal to A_{90}. In order to maintain the same cross-sectional area of the unit cell at various web inclination angles, the thickness t is varied using Equation (2.20), which is obtained by setting $A_\theta = A_{90}$ in Equation (2.1). In Equation (2.20), $p = 80$ mm, $d = 80$ mm and $A_{90} = 478$ mm^2. The variation of t with web inclination angle θ for constant cross-sectional area is shown graphically in Figure 2.8. The smallest thickness is 0.0875 mm at

$\theta = 45^{o}$, i.e., for the triangular core, and the highest thickness is 1 mm at $\theta = 90^{o}$ for the rectangular core.

$$A_\theta = A_{90}$$

$$\Rightarrow 2p\left(t_{TF} + t_{BF}\right) + 2\left(\frac{d_c}{\sin\theta}\right)t_c = A_{90}$$

$$\Rightarrow 2p\left(t_{TF} + t_{BF}\right) + \frac{2}{\sin\theta}\left(d - \frac{1}{2}t_{TF} - \frac{1}{2}t_{BF}\right)t_c = A_{90} \qquad (2.20)$$

$$where\ t_{TF} = t_{BF} = t_c = t \text{ and } A_{90} = 478\ mm^2$$

$$\therefore 4pt + \frac{2(d-t)t}{\sin\theta} = 478$$

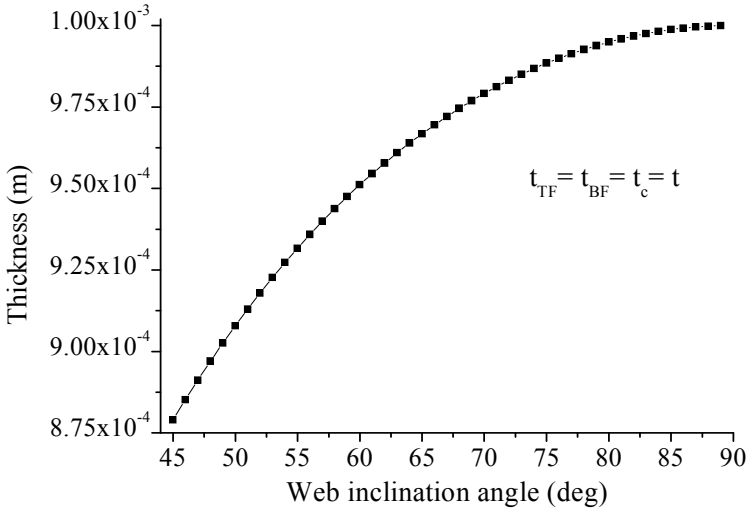

Figure 2.8: Thickness of members in unit cells with cross-sectional area of 478 mm^2, but with different web inclination angles

In Figure 2.9, the extensional stiffness terms are shown for web inclination angle θ varying from 45° to 90°. A_{11} is constant and A_{22} increases slightly with increasing web inclination angle. The effect of web inclination angle on A_{11}, A_{12} and A_{66} is also small.

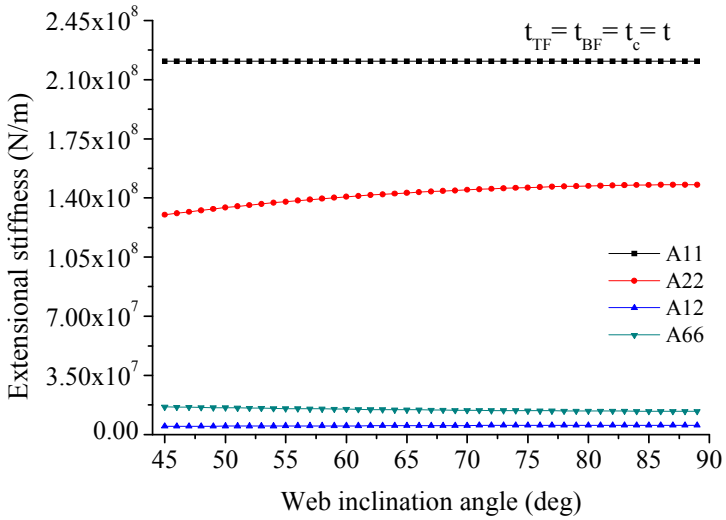

Figure 2.9: Extensional stiffness terms for varying web inclination angle

In Figure 2.10, transverse shear stiffness terms are shown. The transverse shear stiffness A_{44} is significantly lower than the transverse shear stiffness A_{55}. Also, it is observed that A_{44} has the highest value at $\theta = \theta_{min} = 45°$, i.e., for the triangular core, and decreases rapidly to a near-constant value at $\theta > 55°$. A_{55}, on the other hand, has its lowest value at $\theta = 45°$ and increases with increasing web inclination angle. Its highest value is at $\theta = 90^{\circ}$, i.e., for the rectangular core.

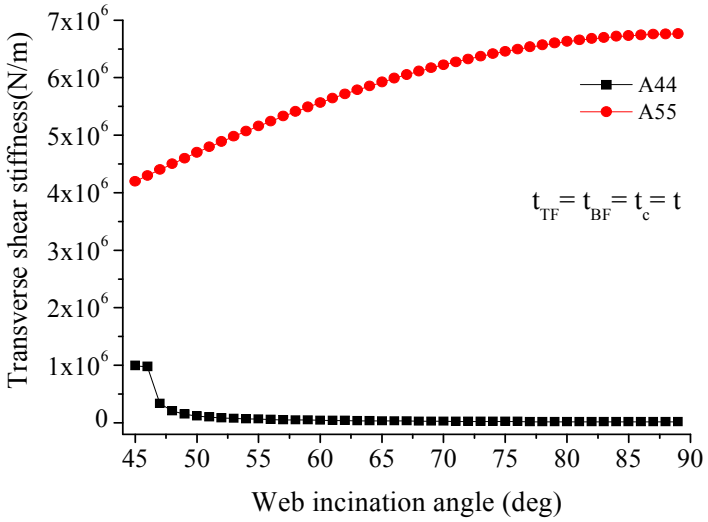

Figure 2.10: Transverse shear stiffness terms for varying web inclination angle

Flexural stiffness terms are shown in Figure 2.11. Both D_{11} and D_{22} increase slightly with increasing web inclination angle, mainly due to increase in thickness; but the web inclination angle has no effect on D_{12} and D_{66}. The highest D_{11} and D_{22} occur at $\theta = 90^{\circ}$, i.e., for a rectangular core.

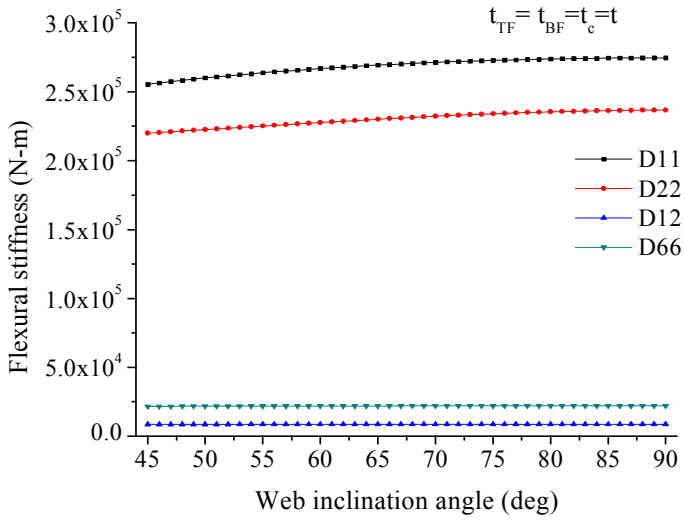

Figure 2.11: Flexural stiffness terms for varying web inclination angle

In Figure 2.12, the global deflection response of a sandwich plate with 45º web inclination angle is shown for a uniformly distributed load of 1 N/m^2 on its top surface. The maximum deflection occurs at the center of the plate and has a magnitude of 1.7x10^{-8} m. In Figure 2.13, the maximum deflection of the sandwich plate is shown as a function of the web inclination angle θ for a uniformly distributed load p_o of 1 N/m^2. The results are in good agreement with Martinez et al. [9] who used a shear deformable plate theory to determine the maximum deflection. It can be noted in this figure that the highest maximum deflection occurs at 48^o web inclination angle and the lowest maximum deflection occurs at 90º web inclination angle, i.e., for the rectangular core. Also, the maximum deflection for the triangular core is higher than that for the rectangular core.

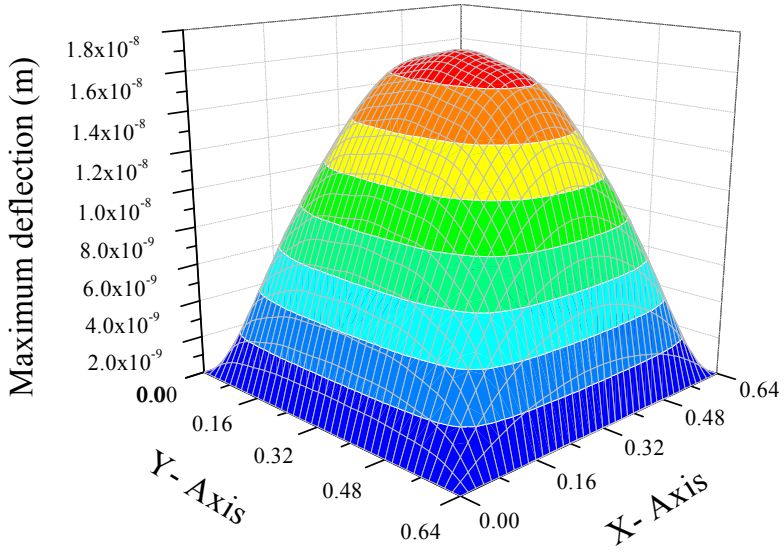

Figure 2.12: Global defection of the sandwich plate corresponding to 45º web inclination angle and under a uniform pressure load of 1 N/m^2

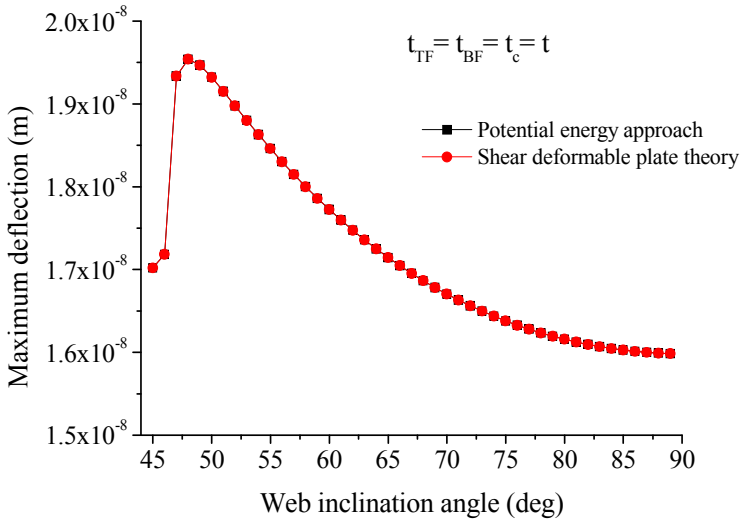

Figure 2.13: Maximum deflection of sandwich plates with various web inclination angles and with a uniform pressure load of 1 N/m^2

Figure 2.14 shows the rotations of the transverse normals, $\bar{\alpha}$ and $\bar{\beta}$, as a function of web inclination angle θ. It can be seen that $\bar{\alpha}$, which represents the rotation of the transverse normal to the y-axis, increases rapidly from a negative value at θ = 45º to a positive value at θ > 47º and then increases slowly to its maximum positive value at θ = 90º. On the other hand, $\bar{\beta}$, representing the rotation of the transverse normal to the x-

axis, starts with a negative value at $\theta = 45^{\circ}$ and becomes increasingly negative as the web inclination angle is increased. Since both $\bar{\alpha}$ and $\bar{\beta}$ influence the plate deflection, their effects are additive from $\theta = 45^{\circ}$ and $\theta = 48^{\circ}$, which is the reason for increase in the maximum plate deflection between these two web inclination angles. For $\theta > 48^{\circ}$, $\bar{\alpha}$ and $\bar{\beta}$ have opposite effects on the plate deflection, which is the reason for decreasing value of the maximum plate deflection between $\theta = 45^{\circ}$ and 90°.

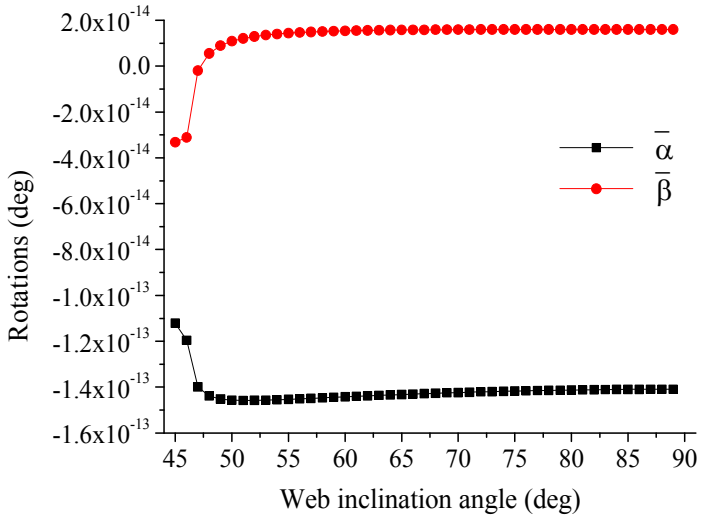

Figure 2.14: Maximum values of rotations $\bar{\alpha}$ and $\bar{\beta}$ of equivalent plate models of varying web inclination angle

2.3.2 Case Study 2: $[0/90]_s$ Laminates, Effects of Web and Face Thickness, $p = d = 80$ mm

Case study 2 is divided into two parts. In the first part, Case Study 2.1, the web thickness is varied while maintaining the face thickness at 1 mm. In the second part, Case Study 2.2, the web thickness is maintained constant at 1 mm, while the face thickness is varied. In both cases, $p = d = 80$ mm and the maximum face thickness is 1 mm when $\theta = 90^{\circ}$. To maintain a constant cross-sectional area of 478 mm^2, which is equal to $A_{90^{\circ}}$, the web thickness in Case Study 2.1 is varied using the relationship: $t_c = t_{90^{\circ}} \sin\theta$. In Case Study 2.2, the face thickness is varied using the relationship given by $t = (478 \sin\theta - 160)/(320 \sin\theta - 2)$. A comparison of the variation of web thickness and

face thickness with web inclination angle θ for both case studies is given in Figure 2.15. In Case Study 2, t_c at $\theta = 90^o$ is the same as that in Case Study 1.

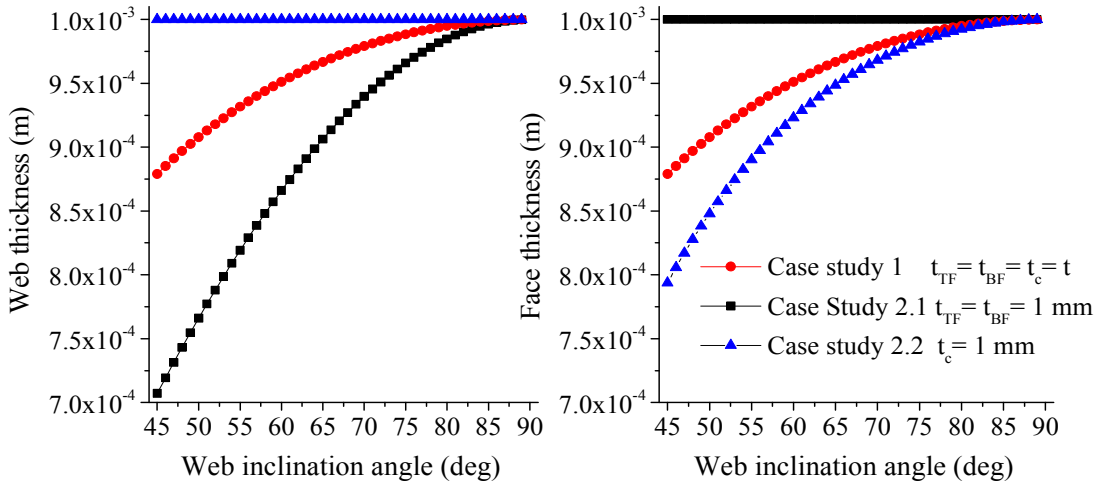

Figure 2.15: Comparison of member thickness for varying web inclination angle

In Figure 2.16, extensional stiffness terms are given for Case Study 2.1 and it is observed that web inclination angle has very little effect on the extensional stiffness matrix terms. Since extensional stiffness terms depend on the cross-sectional area, which is the same in both case studies, the extensional stiffness values are also the same in both case studies.

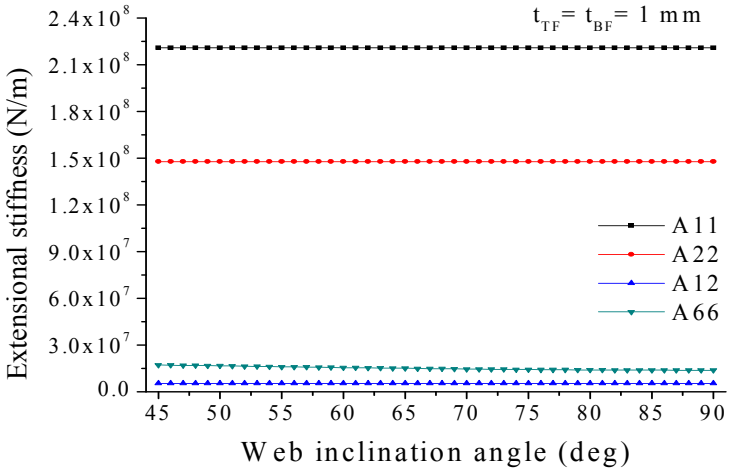

Figure 2.16: Extensional stiffness terms for varying web inclination angle in Case Study 2.1

In Figure 2.17, transverse shear stiffness terms are plotted for Case Study 2.1. The effect of web inclination angle θ on A_{44} and A_{55} is similar to that shown in Figure 2.10; however, A_{55} is lower for the case when the web and face thicknesses are not equal (i.e., in Case Study 2.1) than when they are equal (i.e., in Case Study 1).

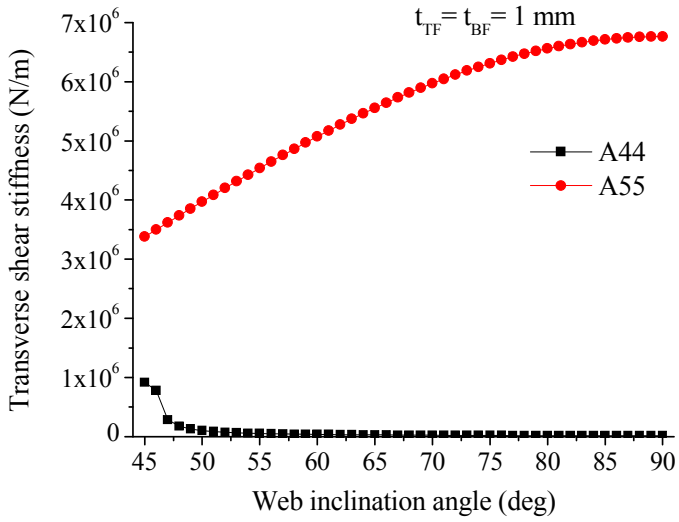

Figure 2.17: Transverse shear stiffness terms for varying web inclination angle in Case Study 2.1

In Figure 2.18, flexural stiffness terms are given for Case Study 2.1. There is no significant change in D_{11}, D_{12} and D_{66} terms, but D_{22} shows a slightly decreasing trend with increasing web inclination angle. For the same face center distance (d), the flexural stiffness terms depend on the face thickness, which is 1 mm for all web inclination angles in Case Study 2.1 and, except for $\theta = 90^{\circ}$, is lower than 1 mm in Case Study 1. This is the reason for higher flexural stiffness terms in Case Study 2.1 than in Case Study 1.

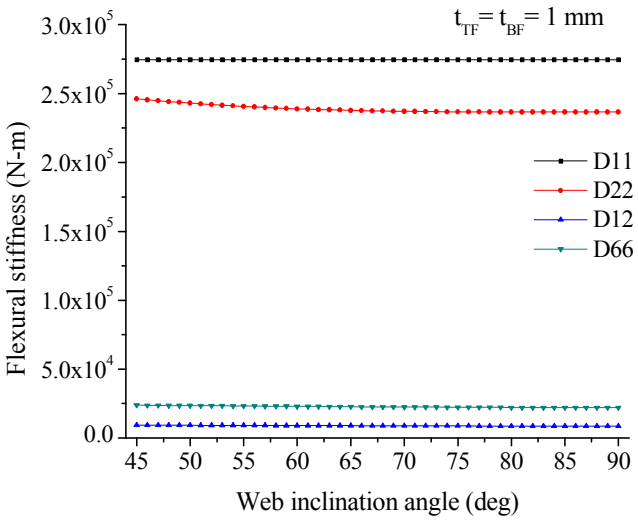

Figure 2.18: Flexural stiffness terms for varying web inclination angle in Case Study 2.1

In Figure 2.20, maximum deflections of equivalent plates are plotted for varying web inclination angles for Case Study 1, Case Study 2.1 and Case Study 2.2. In each case, the maximum deflection reaches the peak value at 48° web inclination angle and then decreases to the lowest value at 90° web inclination angle. The maximum deflections in Case Study 2 are higher than the maximum deflection in Case Study 1 for all web inclination angles less than 90°. The difference in maximum deflections of the two case studies in Case Study 2 is very small, which indicates that the influence of face thickness (Case Study 2.2) on the maximum deflection is much smaller than that of the web thickness (Case Study 2.1). Flexural stiffness terms D_{11} and D_{22} are higher in Case Study 2.1, but transverse shear stiffness terms A_{44} and A_{55} are lower. The higher maximum deflection in Case Study 2.2 compared to Case Study 1 is due to lower flexural stiffness D_{11} and D_{22}. The higher maximum deflection in Case Study 2.1 compared to Case Study 1 is due to lower A_{44} and A_{55}, which causes higher shear deformations as evidenced by the higher values of rotational components (Figure 2.19) in Case Study 2.1. Thus, for equal cross-sectional area (i.e., for equal mass), equal thickness for the faces and the webs provide lower deflection, and therefore, higher overall bending stiffness for the plate.

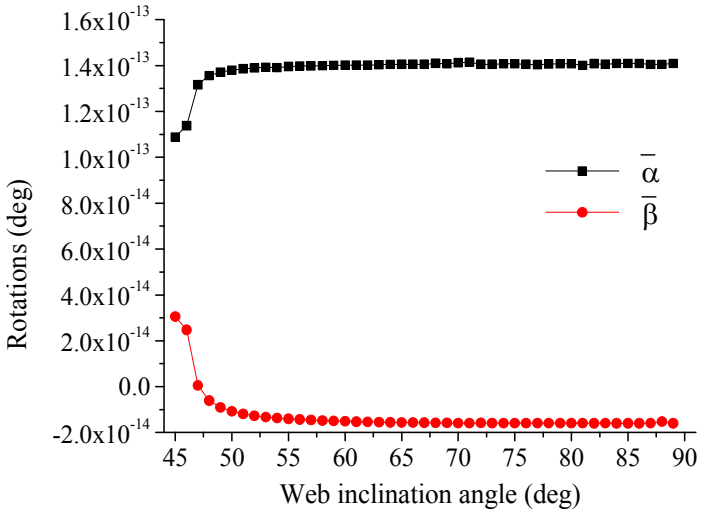

Figure 2.19: Maximum rotation $\bar{\alpha}$ and $\bar{\beta}$ of sandwich plates of varying web inclination angle in Case Study 2.1

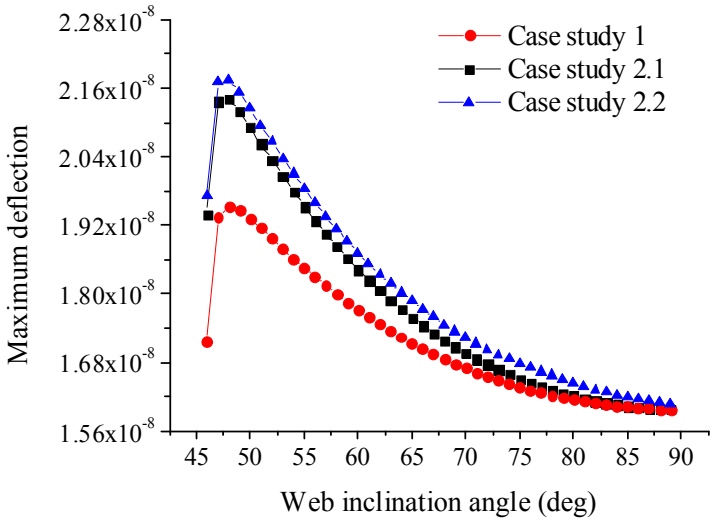

Figure 2.20: Comparison of maximum deflections of sandwich plates for varying web inclination angles

Transverse deflections in Case Study 2.1 are investigated further by considering their values normal to the corrugation direction (i.e., in the y-direction of the plate) at three different locations in the length direction, namely at x = 0.16 m, 0.32 m and 0.48 m (Figure 2.21). Transverse deflections at these three locations are plotted in Figure 2.22 for y = 0 to y = 0.64 m. It is seen that for θ = 45º, i.e., the triangular core, transverse deflection shows a smooth increase from both sides of the plate (i.e., y = 0 and 0.64 m) to

the maximum value at y = 0.32 m. For other web inclination angles, the deflection curves, except near the ends, show wavy characteristics and multiple peaks. The waviness increases as the web inclination angle θ is increased. The transverse deflection patterns for $\theta = 45°, 48°$ and $90°$ are elaborated using three dimensional depictions, as shown in Figure 2.23.

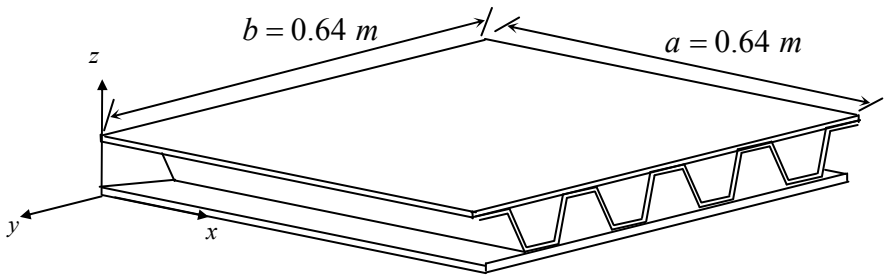

Figure 2.21: Locations for transverse deflection curves in (a), (b) and (c)

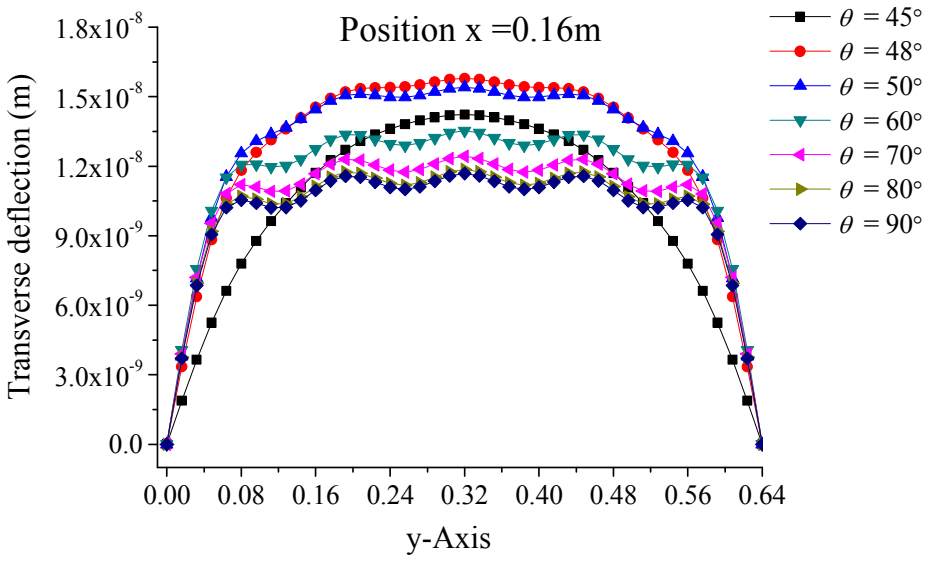

(a)

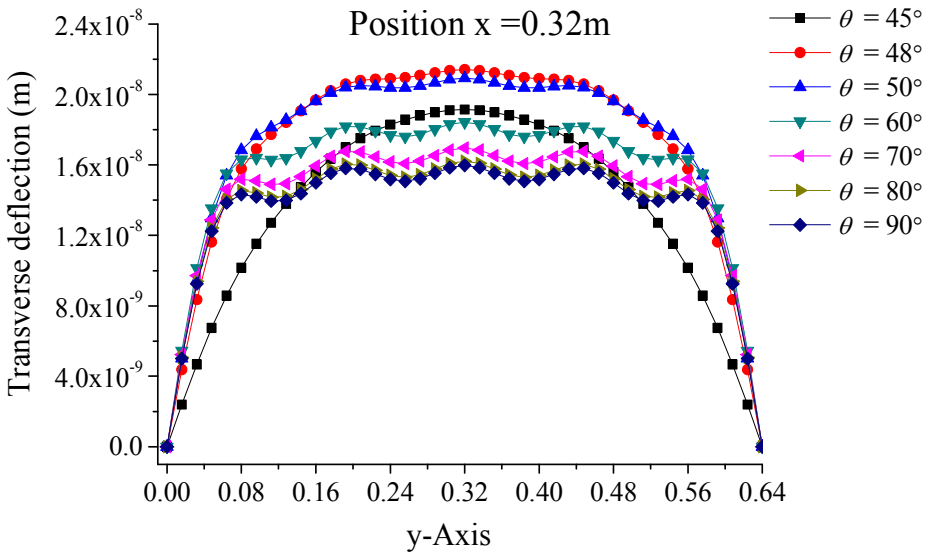

(b)

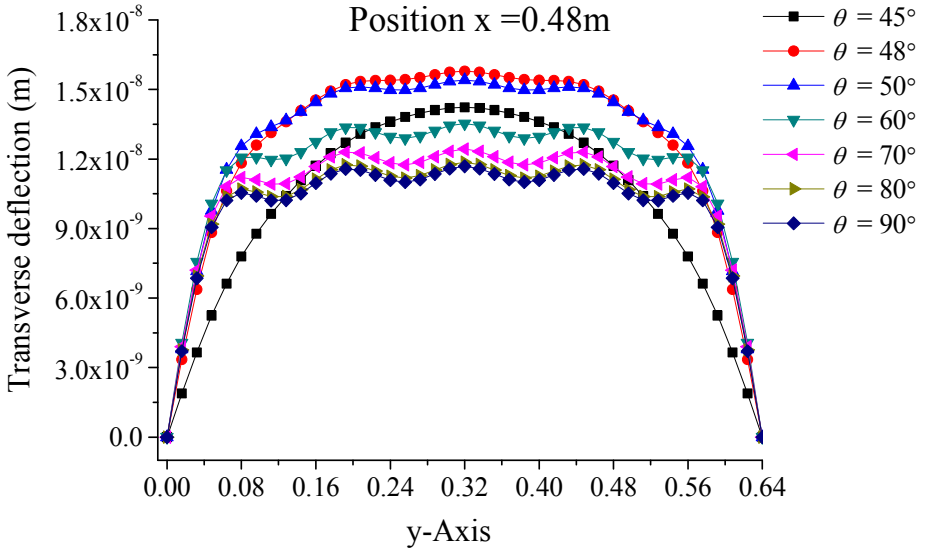

(c)

Figure 2.22: Transverse deflections normal to the corrugation direction at x = 0.16, 0.32 and 0.48 m in Case Study 2.1

(a) θ = 45º

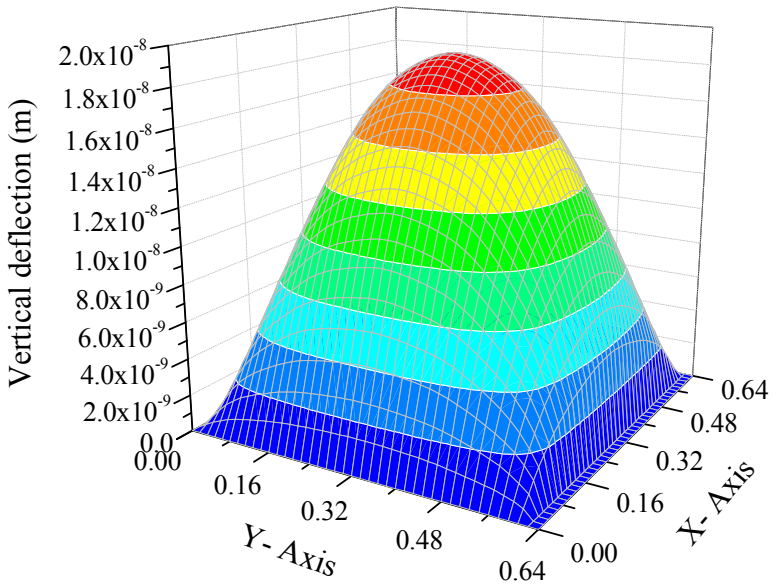
Vertical deflection (m)
2.0x10-8
1.8x10-8
1.6x10-8
1.4x10-8
1.2x10-8
1.0x10-8
8.0x10-9
6.0x10-9
4.0x10-9
2.0x10-9
0.0
0.00
0.16
0.32
0.48
0.64
Y- Axis
0.64
0.48
0.32
0.16
0.00
X- Axis

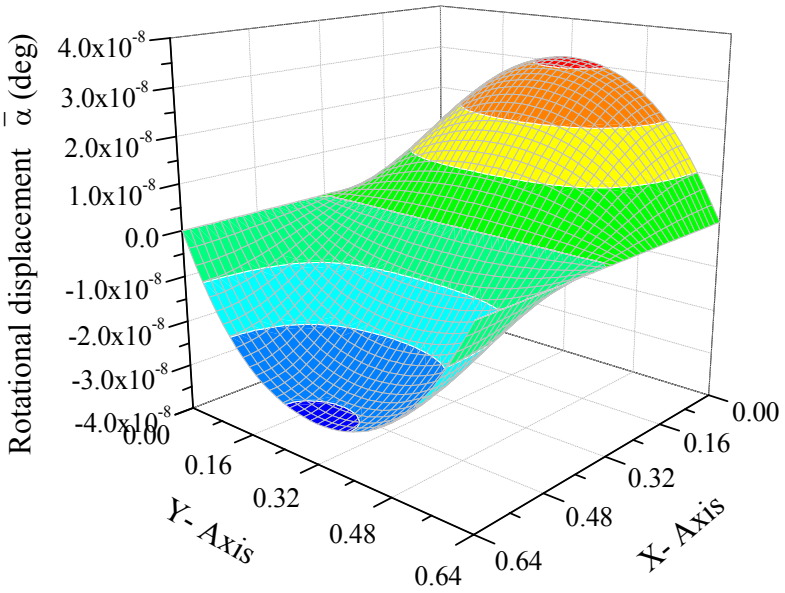
Rotational displacement $\bar{\alpha}$ (deg)
4.0x10-8
3.0x10-8
2.0x10-8
1.0x10-8
0.0
-1.0x10-8
-2.0x10-8
-3.0x10-8
-4.0x10-8
0.00
0.16
0.32
0.48
0.64
Y- Axis
0.00
0.16
0.32
0.48
0.64
X- Axis

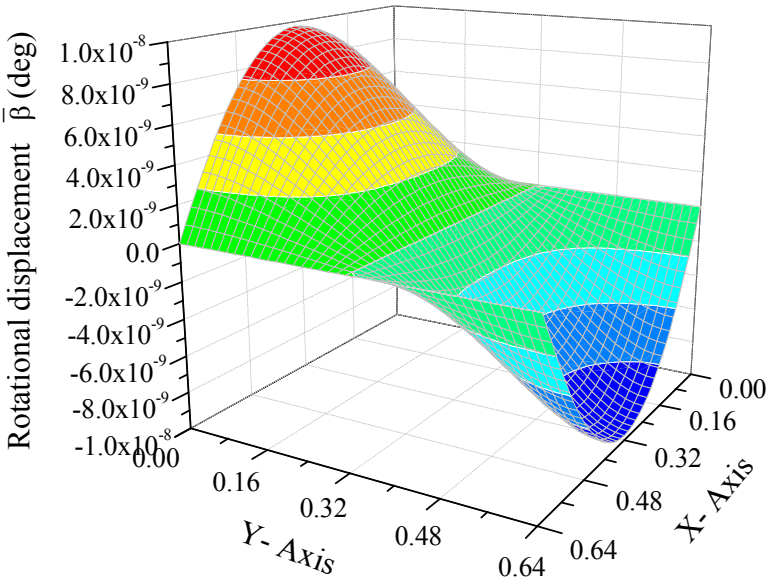
Rotational displacement $\bar{\beta}$ (deg)
1.0x10-8
8.0x10-9
6.0x10-9
4.0x10-9
2.0x10-9
0.0
-2.0x10-9
-4.0x10-9
-6.0x10-9
-8.0x10-9
-1.0x10-8
0.00
0.16
0.32
0.48
0.64
Y- Axis
X- Axis

(b) θ = 48º

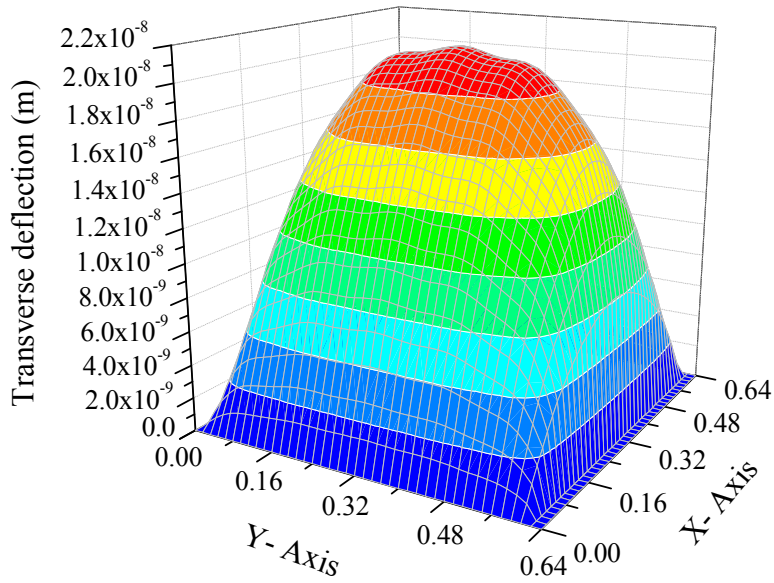
Transverse deflection (m)
2.2x10-8
2.0x10-8
1.8x10-8
1.6x10-8
1.4x10-8
1.2x10-8
1.0x10-8
8.0x10-9
6.0x10-9
4.0x10-9
2.0x10-9
0.0
0.00
0.16
0.32
0.48
0.64
Y- Axis
X- Axis

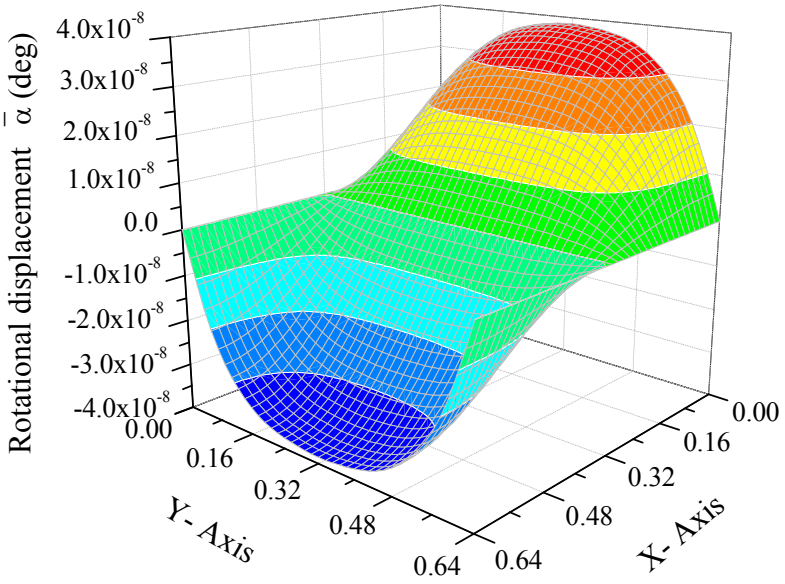
Rotational displacement $\bar{\alpha}$ (deg)
4.0x10-8
3.0x10-8
2.0x10-8
1.0x10-8
0.0
-1.0x10-8
-2.0x10-8
-3.0x10-8
-4.0x10-8
0.00
0.16
0.32
0.48
0.64
Y- Axis
0.00
0.16
0.32
0.48
0.64
X- Axis

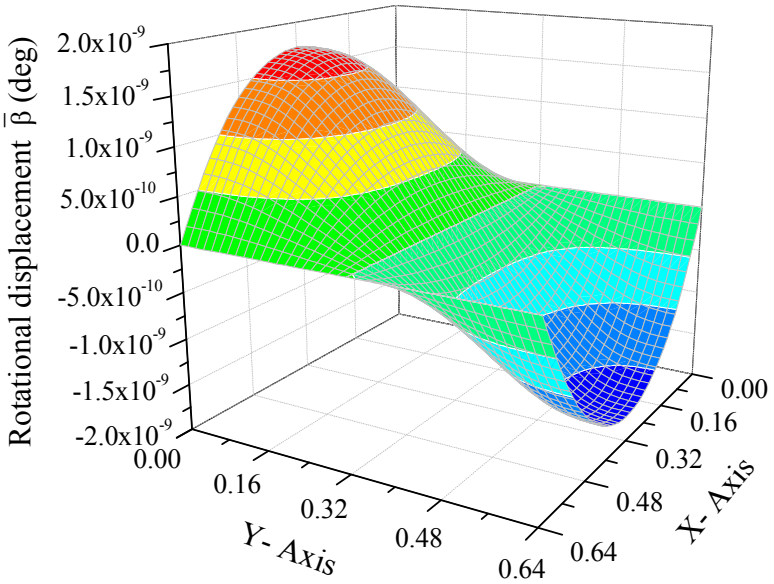
Rotational displacement $\bar{\beta}$ (deg)
2.0x10-9
1.5x10-9
1.0x10-9
5.0x10-10
0.0
-5.0x10-10
-1.0x10-9
-1.5x10-9
-2.0x10-9
0.00
0.16
0.32
0.48
0.64
Y- Axis
0.00
0.16
0.32
0.48
0.64
X- Axis

(c) $\theta = 90^{o}$

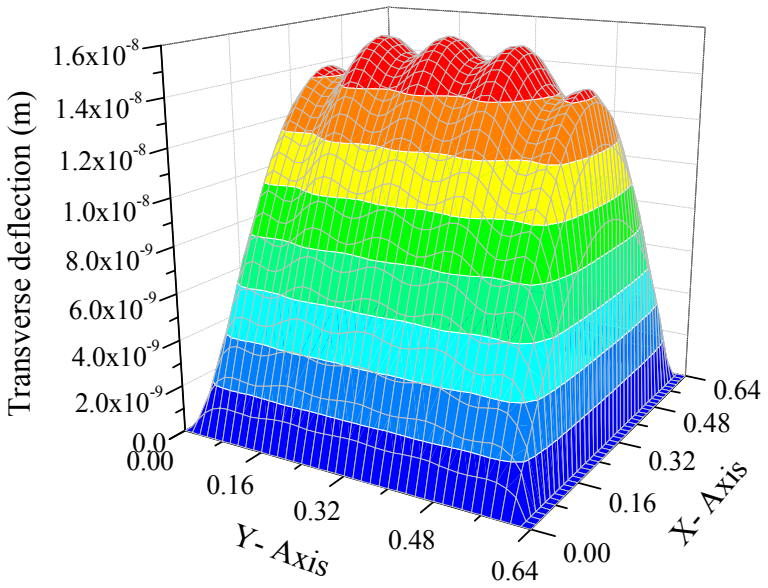
Transverse deflection (m)
1.6x10-8
1.4x10-8
1.2x10-8
1.0x10-8
8.0x10-9
6.0x10-9
4.0x10-9
2.0x10-9
0.0
0.00
0.16
0.32
0.48
0.64
Y- Axis
0.64
0.48
0.32
0.16
0.00
X- Axis

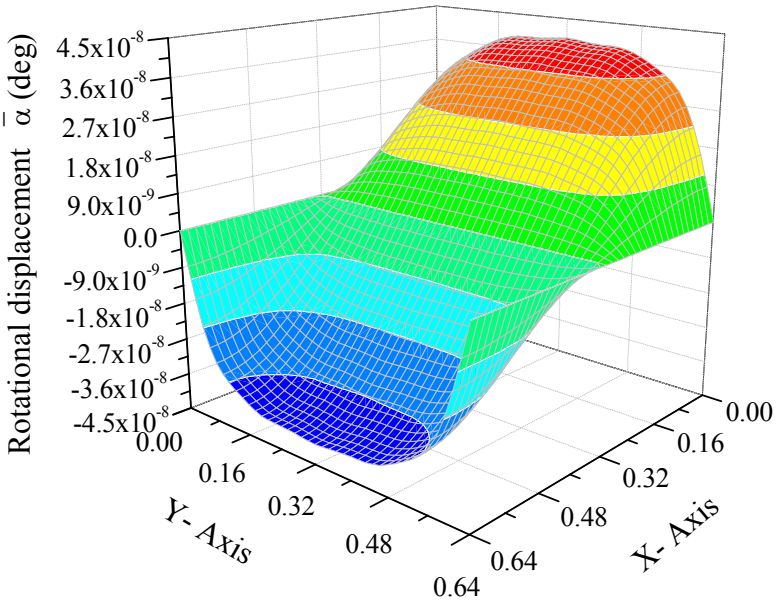
Rotational displacement $\bar{\alpha}$ (deg)
4.5x10-8
3.6x10-8
2.7x10-8
1.8x10-8
9.0x10-9
0.0
-9.0x10-9
-1.8x10-8
-2.7x10-8
-3.6x10-8
-4.5x10-8
0.00
0.16
0.32
0.48
0.64
Y- Axis
0.00
0.16
0.32
0.48
0.64
X- Axis

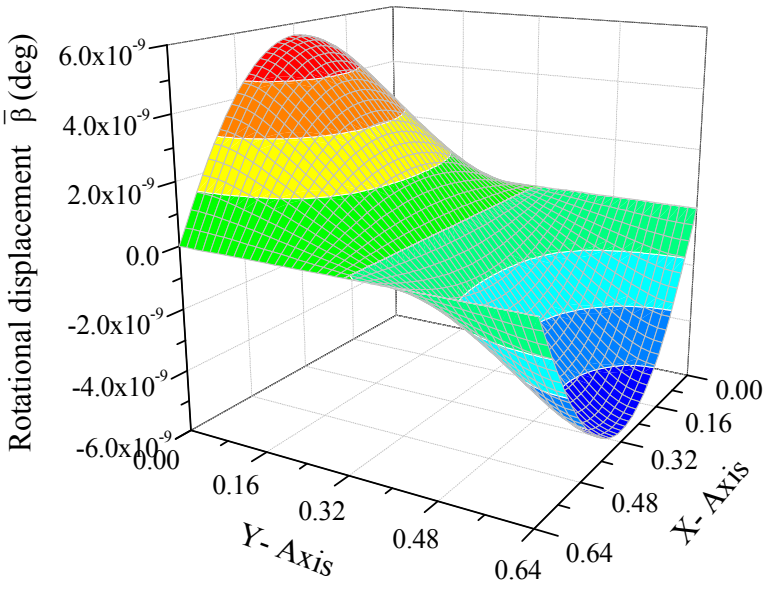

Figure 2.23: Three-dimensional depiction of transverse deflection and rotational displacement patterns for web inclination angle $\theta = 45^{\circ}$, 48° and 90° in Case Study 2.1

2.3.3 Case Study 3: $[0/90]_S$ Laminates, $t_{TF} = t_{BF} = 1$ mm, $t_c \leq 1$ mm, $d = 80$ mm, $p = 20, 40, 80, 160$ and 320 mm

In this case study, the principal geometric parameter of interest is the pitch, $2p$. A parametric case study is conducted to predict the global deflection response of composite sandwich plates with constant cross-sectional area, but varying pitch ($2p$) and web inclination angle (θ). The face thickness (t_f) and face center distance (d) are maintained at 1 mm and 80 mm, respectively. Five different pitch values are considered 40, 80, 160, 320 and 640 mm. The corresponding p/d ratios are 0.25, 0.5, 1.0, 2.0 and 4.0, and since the plate dimension b normal to the corrugation direction is 640 mm, the corresponding numbers of unit cells in the plate are 16, 8, 4, 2 and 1, respectively. In this case study, the minimum possible web inclination θ_{min} decreases with increasing p/d ratio, which is shown in Figure 2.24. For $p = 80$ mm, θ_{min} is 45°, but as p is changed from 20 mm to 320 mm, θ_{min} reduces from 75.96° to 14.04° . To maintain a constant cross-sectional area of 478 mm^2, the web thickness (t_c) is calculated as a function of web inclination angle θ using Equation (2.21).

$$4p + 158\frac{t_c}{\sin\theta} = 478 \tag{2.21}$$

The variation of t_c with θ for each value of p is shown in Figure 2.25. It can be noted that to maintain a constant cross-sectional area, web thickness t_c is higher for higher p. For example, at $\theta = 90^o$, t_c is 0.25 mm for p = 20 mm and 4 mm for p = 320 mm, which is 16 times higher than the former.

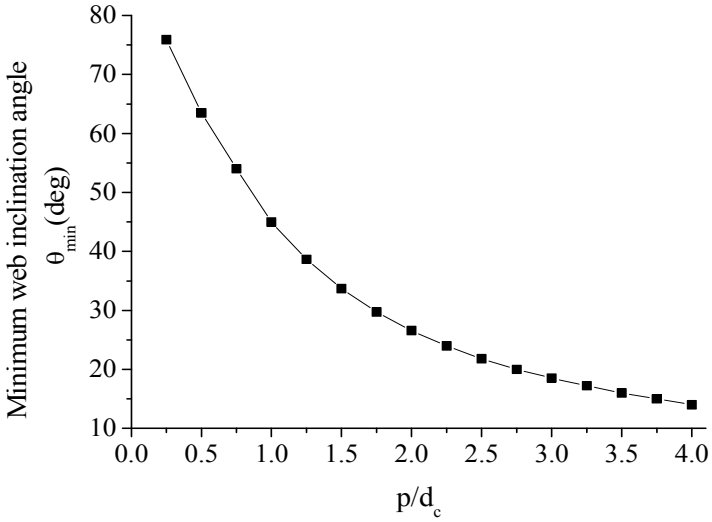

Figure 2.24: Minimum possible web inclination θ_{min} for varying pitch

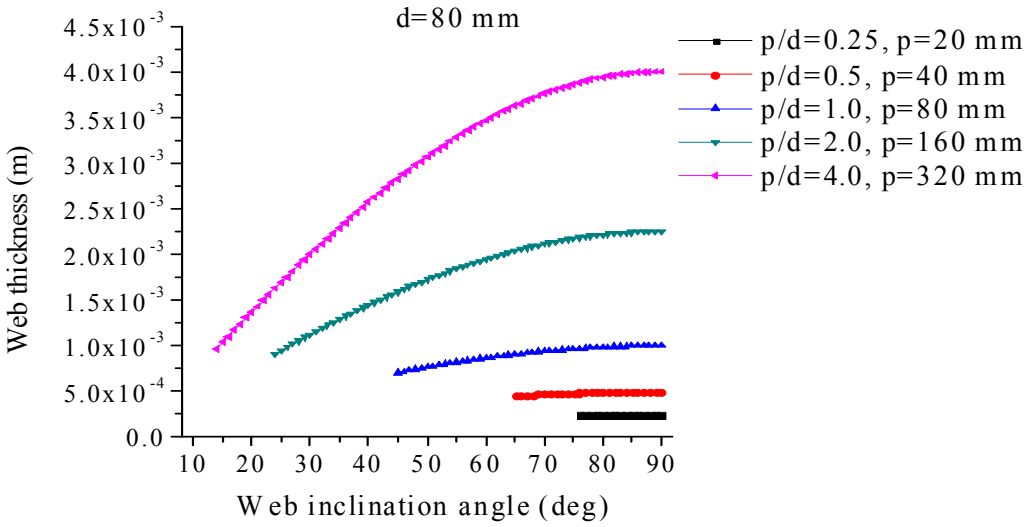

Figure 2.25: Web thickness for varying pitch and web inclination angle

Extensional stiffness A_{11} and A_{22} with varying web inclination angle for different values of p are shown in Figure 2.26. It is observed that they are constant for all values of p and web inclination angles, due to constant cross-sectional area of the composite sandwich plates. Flexural stiffness as D_{11} and D_{22} for different p and varying web inclination angles are given in Figure 2.27. It is observed that D_{11} is a constant. D_{22} decreases as web inclination angle is increased, but it does not depend on p. Flexural stiffness D_{12} and D_{66} for different p and varying web inclination angle are given in Figure 2.28. It is observed that both D_{12} and D_{66} decrease as the web inclination angle is increased, but they do not depend on p.

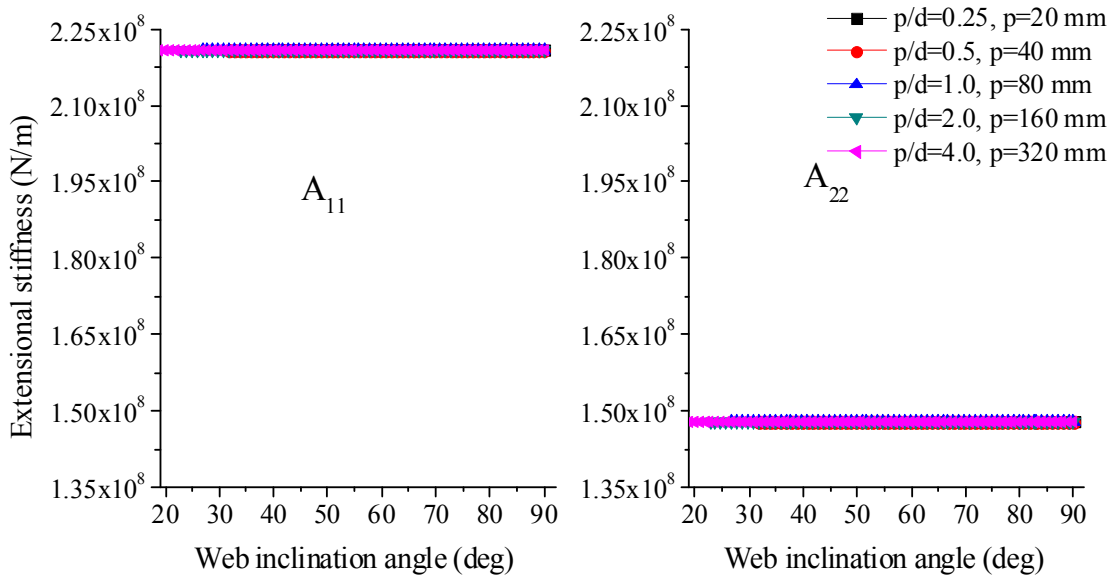

Figure 2.26: Extensional stiffness terms A_{11} and A_{22} of sandwich plates with varying pitch and web inclination angle

Variations of transverse shear stiffness components, A_{44} and A_{55}, with varying web inclination angle are shown in Figure 2.29 for different values of p. It is observed for all values of p, A_{44} decreases with increasing web inclination angle after the initial maximum value at θ_{min}. A_{55}, on the other hand, increases with increasing web inclination angle and does not depend on p. The maximum A_{44} is also seen to be dependent on p. At p = 20 mm, the maximum A_{44} is 160 times higher than that at p = 320 mm. At p = 20 mm, the web thickness t_c is much smaller and there are 16 unit cells in the plate. At p = 320 mm, the web thickness t_c is much larger and there is only one unit cell in the plate. Thus, the

higher maximum value of A_{44} at p = 20 mm is principally due to larger number of unit cells.

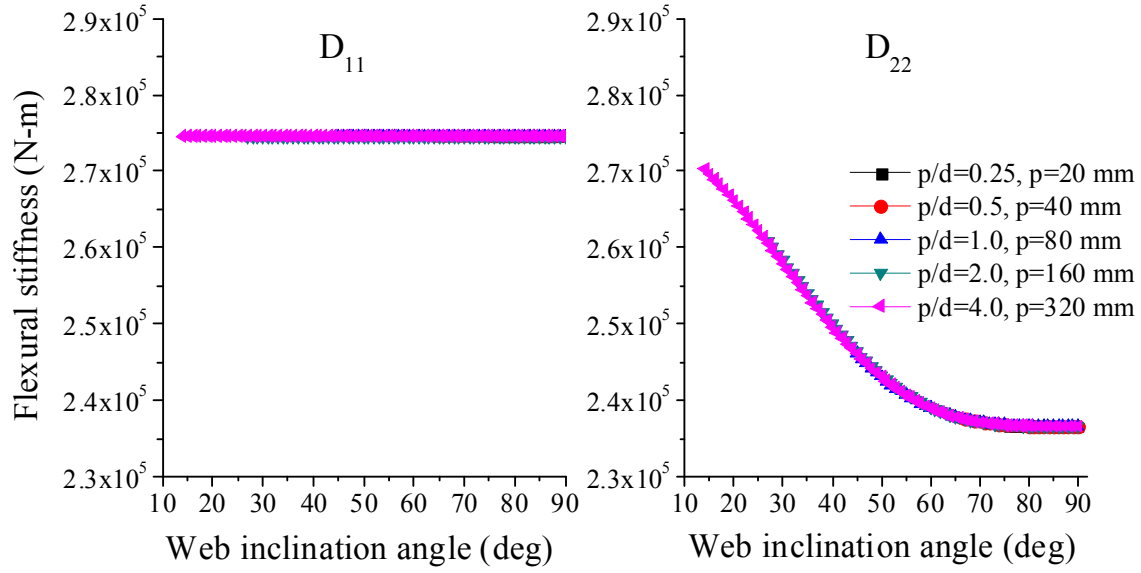

Figure 2.27: Flexural stiffness terms D_{11} and D_{22} of sandwich plates with varying pitch and web inclination angle

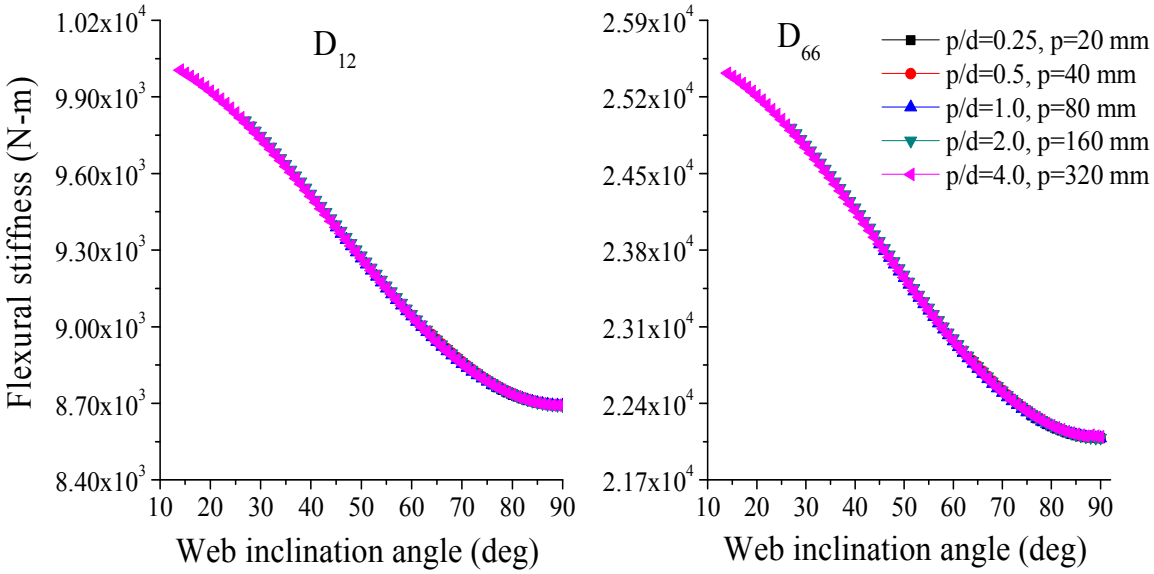

Figure 2.28: Flexural stiffness terms D_{12} and D_{66} of sandwich plates with varying pitch and web inclination angle

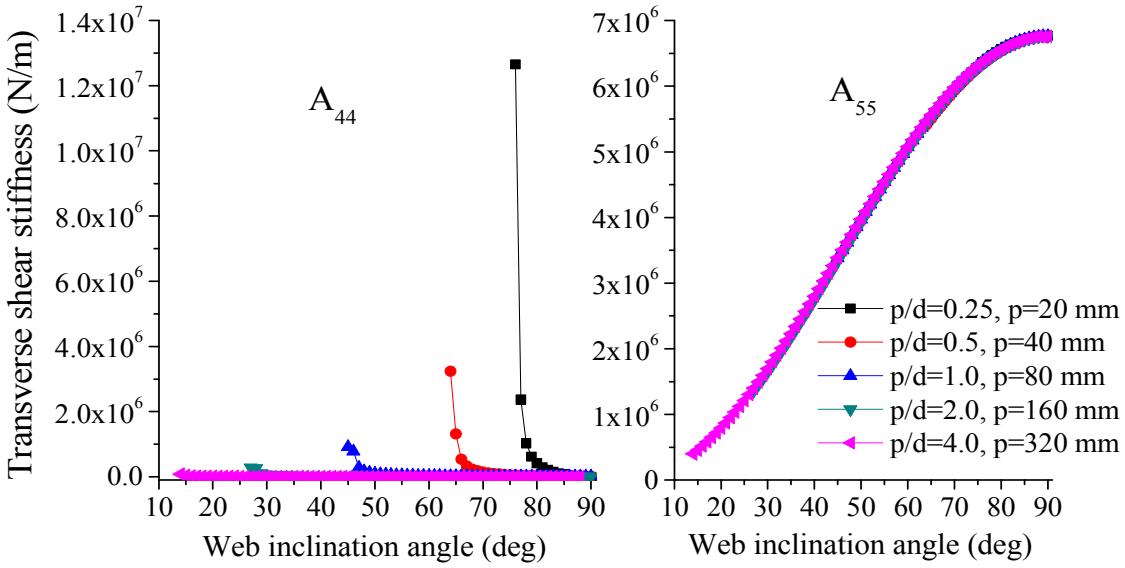

Figure 2.29: Transverse shear stiffness terms A_{44} and A_{55} of sandwich plates with varying pitch and web inclination angle

Maximum deflection of sandwich plates with varying web inclination angle for different p/d ratios is given in Figure 2.30. It is observed that the maximum deflection of the sandwich plate with p = 20 mm has the smallest value at the minimum web inclination angle of 75.96º, i.e., for the triangular core, and increases to a larger value as the web inclination angle is increased to 90º, i.e., for the rectangular core. On the other hand, for p = 320 mm, the maximum deflection has the highest value at the minimum web inclination angle of 14.04º, i.e., for the triangular core and decreases steadily as the web inclination angle is increased to 90º. The maximum deflection at θ = 90º, i.e., for a rectangular core, is the same for all values of p. Higher maximum deflection with higher p can be attributed to lower A_{44} as p is increased.

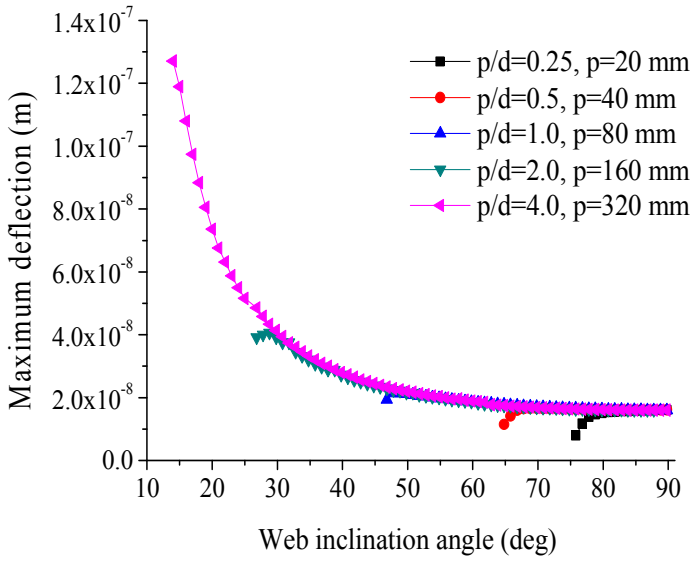

Figure 2.30: Maximum deflection of sandwich plates with varying pitch and web inclination angle

2.3.4 Case Study 4: $[0/90]_S$ Laminates, $t_{TF} = t_{BF} = 1$ mm, $t_c \leq 1$ mm, $p = 80$ mm, $d = 20, 40, 60, 80$ mm

In this case study, the effect of face center distance (d) on the maximum deflection is predicted for composite sandwich plates with constant cross sectional area. The face thickness (t_f) and pitch ($2p$) are maintained constant at 1 mm and 160 mm, respectively. The face center distance d is changed from 20 mm to 80 mm in steps of 20 mm. To maintain a constant cross sectional area of 478 mm^2, the web thickness (t_c) is varied as a function of the web inclination angle θ for each value of d. The equation for web thickness as a function of web inclination angle and face center distance is given in Equation (2.22) and plotted in Figure 2.31. It should be noted that in this case study, p is a constant; but as d is decreased, p/d increases, and therefore, the minimum web inclination angle θ_{min} decreases.

$$A_\theta = 2p\left(t_{TF} + t_{BF}\right) + 2\left(d - \frac{t_{TF} + t_{BF}}{2}\right)\frac{t_c}{\sin\theta}$$

where $t_{TF} = t_{BF} = 1mm$, p=80mm and $A_\theta = A_{90} = 478mm^2$

$$\Rightarrow 2*80*(1+1) + 2\left(d - \frac{1+1}{2}\right)\frac{t_c}{\sin\theta} = 478$$

$$\Rightarrow 2(d-1)\frac{t_c}{\sin\theta} = 158$$
$$\therefore t_c = \frac{79\sin\theta}{2(d-1)} \tag{2.22}$$

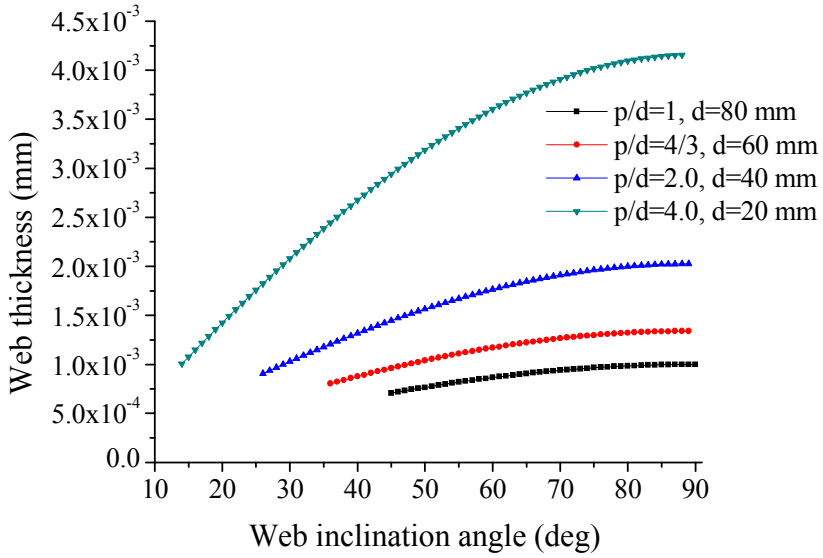

Figure 2.31: Web thickness for varying face center distance and web inclination angle

Extensional stiffness elements A_{11} and A_{22} of sandwich plates with varying web inclination angle and face center distance are given in Figure 2.32, and as before, they are constant for all d and θ due to a constant cross sectional area of the sandwich plates. The variation of bending stiffness elements with d and θ is shown in Figure 2.33. All four bending stiffness elements, D_{11}, D_{22}, D_{12} and D_{66} increase with face center distance. While D_{11} is not affected by θ, D_{22}, D_{12} and D_{66} decrease with increasing θ. The effect of θ on these three bending stiffness elements increases with increasing d. Transverse shear stiffness eleements A_{44} and A_{55} of sandwich plates with varying web inclination angle and face center distance are given in Figure 2.35. It is observed that A_{44} is an order of magnitude higher at θ_{min} (i.e., for the triangular core) compared to its value at $\theta = 90^{o}$ (i.e., for the rectangular core). At θ close to θ_{min}, A_{44} increases rapidly with decreasing θ and the maximum A_{44} increases with decreasing d. At higher θ, A_{44} is not affected by d. The transverse shear stiffness A_{55} increases with increasing θ, but is not affected by d.

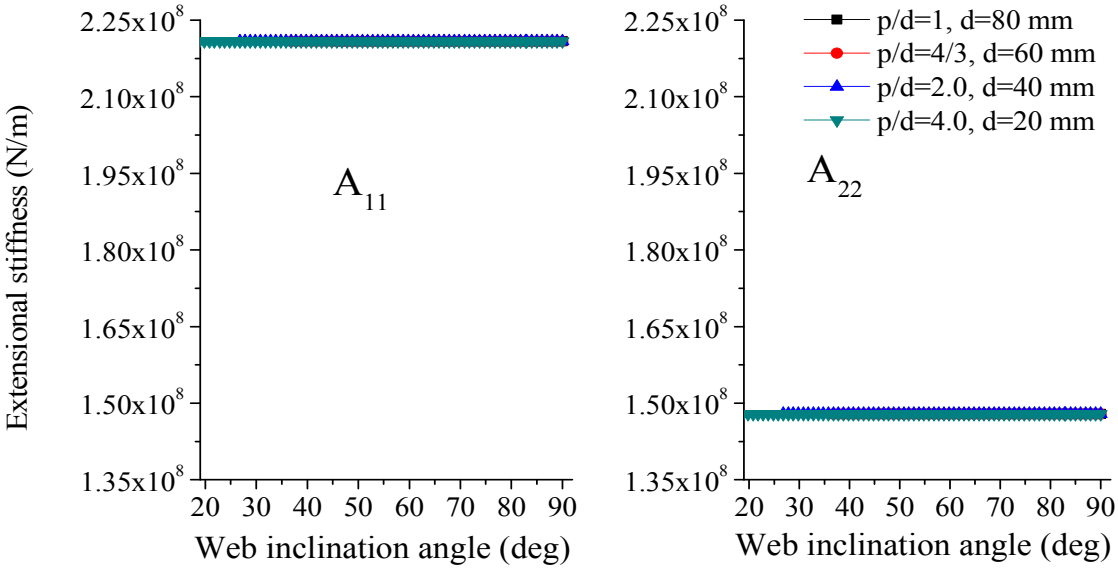

Figure 2.32: Extensional stiffness terms A_{11} and A_{22} of sandwich plates for varying face center distance and web inclination angle

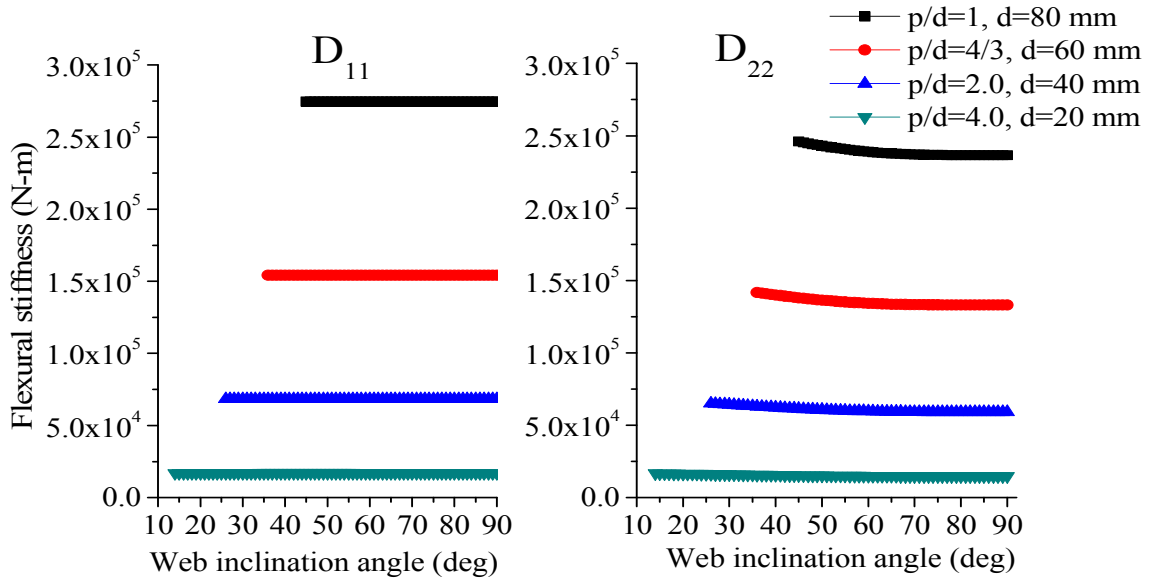

Figure 2.33: Flexural stiffness terms D_{11} and D_{22} of sandwich plates for varying face center distance and web inclination angle

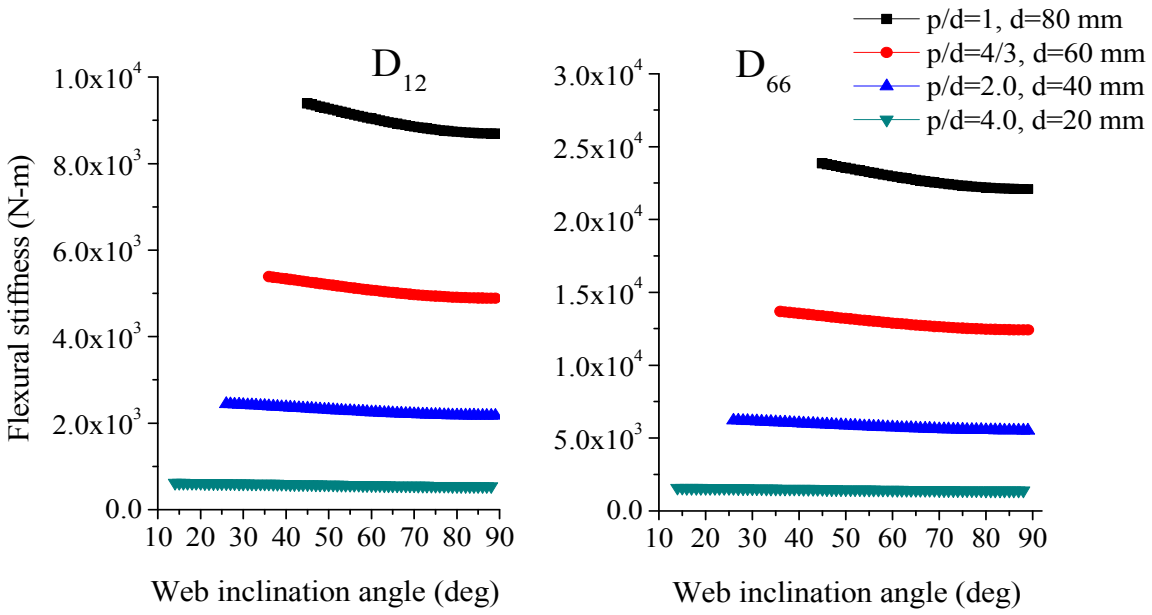

Figure 2.34: Flexural stiffness terms D_{12} and D_{66} of sandwich plates for varying face center distance and web inclination angle

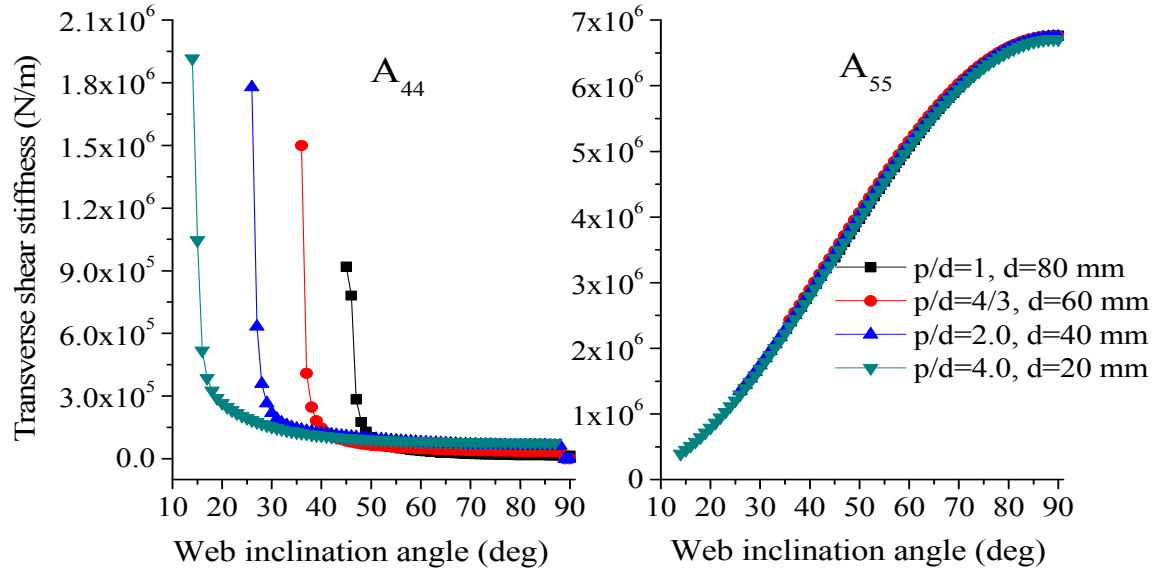

Figure 2.35: Transverse shear stiffness terms A_{44} and A_{55} of sandwich plates for varying face center distance and web inclination angle

The effect of face center distance *d* on maximum deflection of sandwich plates is shown in Figure 2.36. It is observed that maximum deflection increases with decreasing *d*, which is primarily due to decreasing bending stiffness with decreasing *d*. For each face

center distance, maximum deflection first increases with increasing θ, and after reaching the highest value at a θ close to θ_{min}, it then decreases slowly to a lower value at $\theta = 90^{\circ}$. The highest maximum deflection occurs at $\theta = 48^{\circ}$ for $d = 80$ mm, $\theta = 42^{\circ}$ for $d = 60$ mm, $\theta = 32^{\circ}$ for $d = 40$ mm and $\theta = 20^{\circ}$ for 20 mm. The initial rapid increase in maximum deflection appears to be the effect of A_{44}, which decreases rapidly as θ is increased from θ_{min} toward higher values of θ.

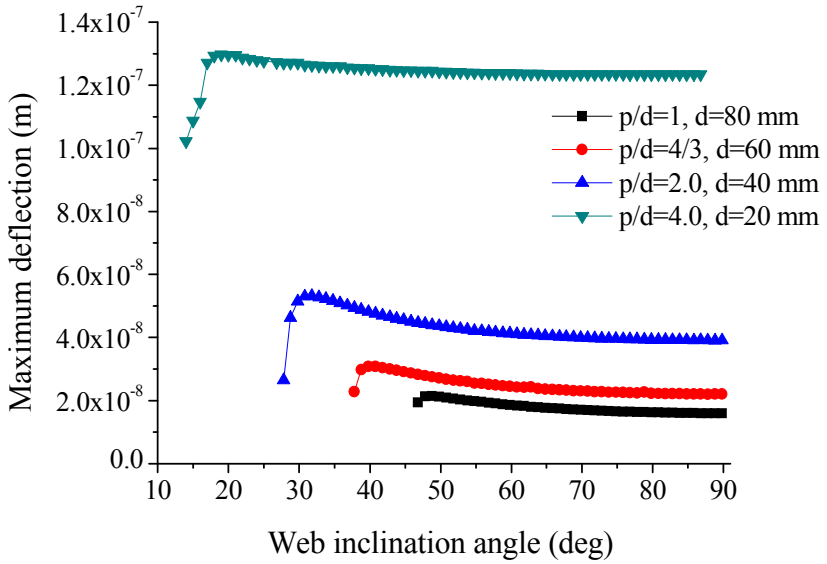

Figure 2.36: Maximum deflection of sandwich plates for varying face center distance and web inclination angle

2.3.5 Case Study 5: Effect of Laminate Construction, $(0/\alpha)_S$ and $(\pm\alpha)_S$ Laminates, $t_{TF} = t_{BF} = 1$ mm, $t_c \leq 1$ mm, $p = d = 80$ mm

The previous case studies were performed with a $(0/90)_s$ laminate construction. In this case study, two different 4-layered symmetric laminate constructions are considered for both faces and webs, namely $(0/\alpha)_s$ and $(\pm\alpha)_s$. The fiber orientation angle α is varied from 0º to 90º in steps of 15º. Thus, for example, when $\alpha = 15^{\circ}$, the construction of the $(0/15)_s$ laminate is $(0/15/15/0)$ and the construction of the $(\pm 15)_s$ laminate is $(15/-15/-15/15)$. The $(0/\alpha)_s$ laminates contain 0º fibers on the outside

layers, while the $(\pm\alpha)_s$ laminates contain fibers at $+\alpha$ orientations on the outside layers. The composite sandwich construction in this case study is the same as in Case Study 2.1, i.e., $p = d = 80$ mm, face thickness $t_{TF} = t_{BF} = t_f = 1$ mm, and since the cross sectional area is maintained constant at 478 mm^2, $t_c = t \sin\theta$. The variation of the core thickness with web inclination angle θ is shown in Figure 2.15.

Flexural stiffness elements D_{11}, D_{22} and D_{12} of the sandwich plates for varying web inclination angle and fiber orientation angle are shown in Figure 2.37 and Figure 2.40. It is observed in Figure 2.37 that for both $(0/\alpha)_s$ and $(\pm\alpha)_s$ laminate constructions, D_{11} decreases with increasing fiber orientation angle and is not influenced by the web inclination angle. The highest and the lowest D_{11} occur with $\alpha = 0°$ and $\alpha = 90°$ respectively. Also, due to the presence of 0º fibers in $(0/\alpha)_s$ laminates, D_{11} for these laminates is greater than that for the $(\pm\alpha)_s$ laminates. Figure 2.38 shows that for both $(0/\alpha)_s$ and $(\pm\alpha)_s$ laminate constructions, D_{22} increases from its minimum value at $\alpha = 0°$ to its maximum value at $\alpha = 90°$. The slightly decreasing trend of D_{22} with increasing web inclination angle can also be seen in Figure 2.38. D_{22} for the $(\pm\alpha)_s$ laminates is higher than D_{22} for the $(0/\alpha)_s$ laminates. Flexural stiffness D_{12}, given in Figure 2.39, also shows a slightly decreasing trend with increasing web inclination angle. The highest D_{12} with each laminate construction occurs when α = 45º and the lowest occurs when α is either 0º or 90º. D_{12} for the $(\pm\alpha)_s$ laminates is higher than D_{12} for the $(0/\alpha)_s$ laminates. The variation of D_{66} with both web inclination angle and fiber orientation angle is shown in Figure 2.40 and it is similar to that observed for D_{12}.

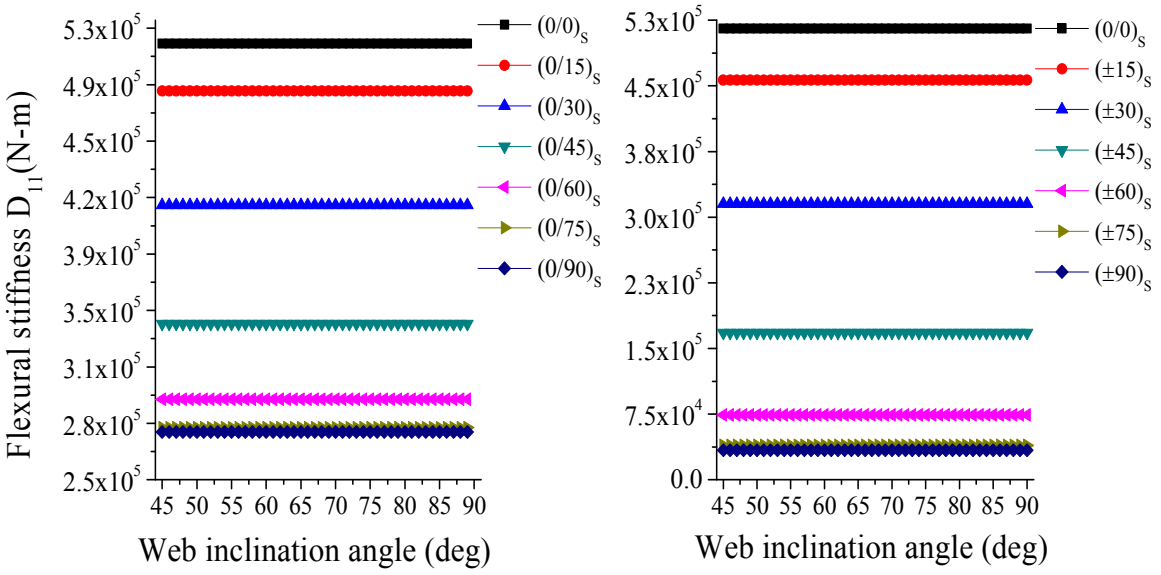

Figure 2.37: Flexural stiffness D_{11} of sandwich plates with varying web inclination and fiber orientation angles for $(0/\alpha)_s$ and $(\pm\alpha)_s$ laminate constructions

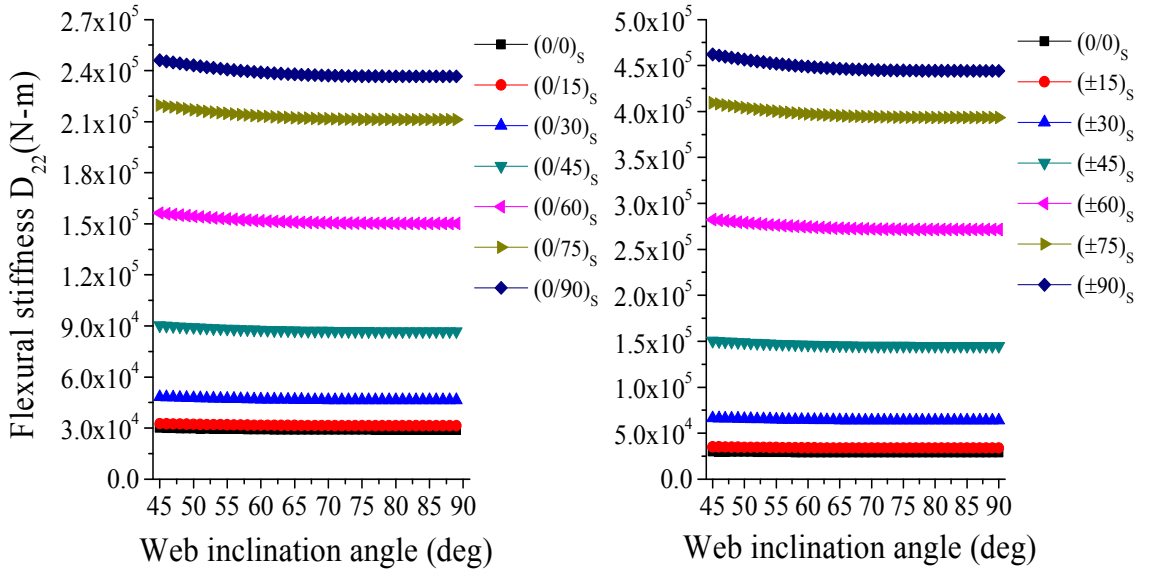

Figure 2.38: Flexural stiffness D_{22} of sandwich plates with varying web inclination and fiber orientation angles for $(0/\alpha)_s$ and $(\pm\alpha)_s$ laminate constructions

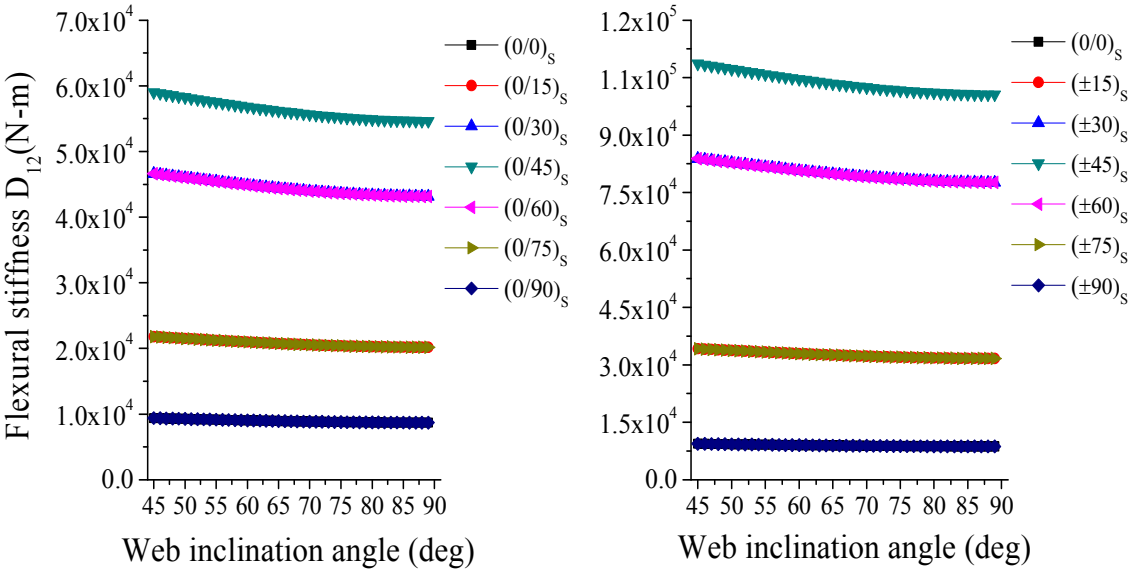

Figure 2.39: Flexural stiffness D_{12} of sandwich plates with varying web inclination and fiber orientation angles

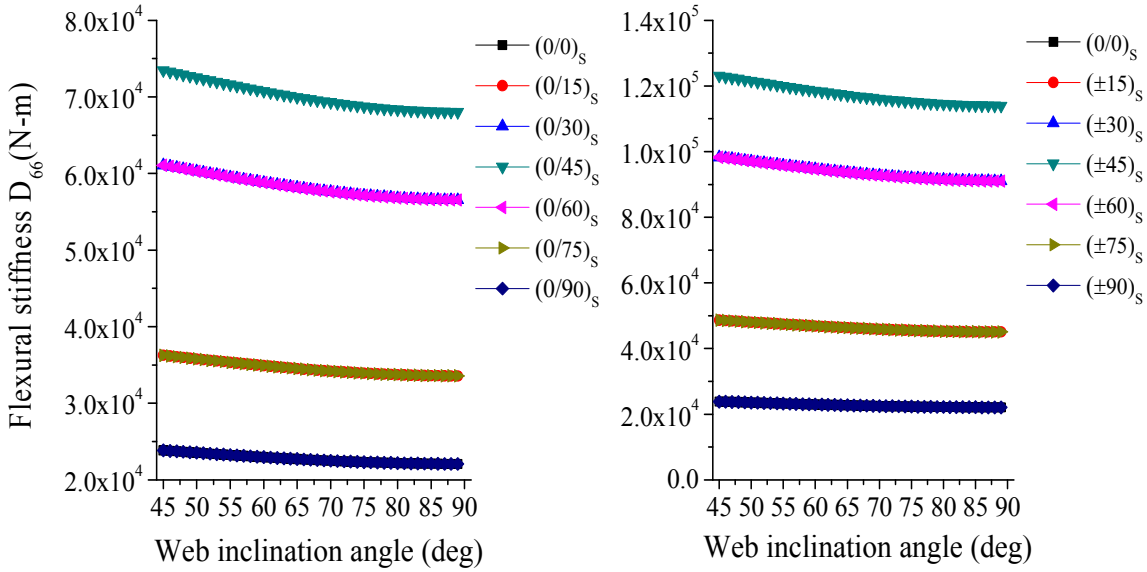

Figure 2.40: Flexural stiffness D_{66} of sandwich plates with varying web inclination and fiber orientation angles

Transverse shear stiffness A_{44} of the sandwich plate for varying web inclination angle and fiber orientation angle are given in Figure 2.41. In the case of $(0/\alpha)_s$ laminate construction, there is not much influence of fiber orientation angle on transverse shear

stiffness A_{44}, and with an increase in web inclination angle, A_{44} decreases from its maximum value at $\theta = 45°$ to its minimum value at $\theta = 90°$. In the case of $(\pm\alpha)_s$ laminate construction, A_{44} also has its highest value at the minimum web inclination angle, but now fiber orientation angle shows a much greater influence on A_{44}. At the minimum web inclination angle, the higher the fiber orientation angle, the lower is the value of A_{44}. As the web inclination angle approaches 90º, the effect of fiber orientation angle on A_{44} becomes very small.

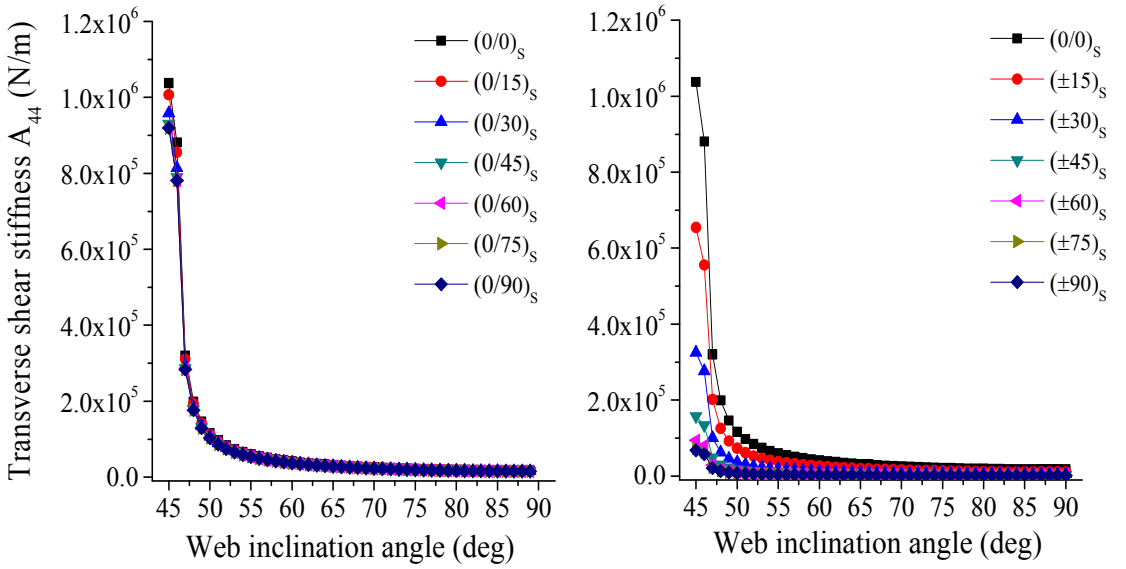

Figure 2.41: Transverse shear stiffness A_{44} of sandwich plates with varying web inclination and fiber orientation angles for $(0/\alpha)_s$ and $(\pm\alpha)_s$ laminate constructions

Transverse shear stiffness A_{55} of the sandwich plate for varying web inclination angle and fiber orientation angle are given in Figure 2.42. For both $(0/\alpha)_s$ and $(\pm\alpha)_s$ laminate constructions, A_{55} increases with increasing web inclination angle. For both laminates, fiber orientation angle has a significant effect on A_{55}. The lowest A_{55} is observed at α = 0 and 90º and the highest A_{55} is observed at α = 45º. A_{55} has equal values at α = 15 and 75º as well as at α = 30 and 60º.

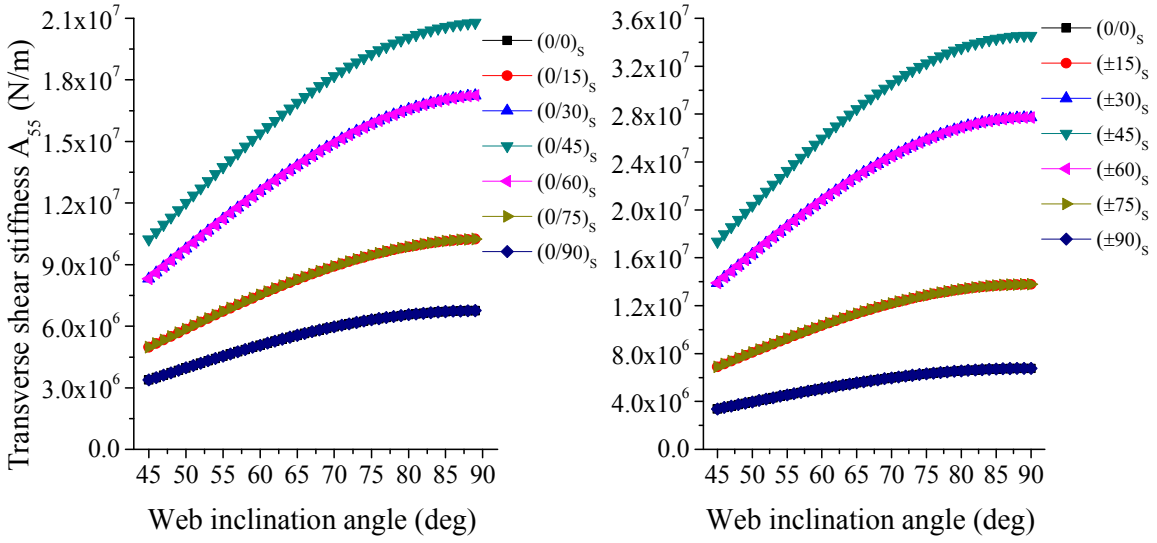

Figure 2.42: Transverse shear stiffness A_{55} of sandwich plates with varying web inclination and fiber orientation angles for $(0/\alpha)_s$ and $(\pm\alpha)_s$ laminate constructions

Maximum deflections of sandwich plates with varying web inclination angle are given in Figure 2.43. In each case, the maximum deflection reaches a peak value at a web inclination angle of 48° and then decreases to the lowest value at the 90º web inclination angle. For both laminate constructions, the maximum deflection occurs with $\alpha = 90º$. For the $(0/\alpha)_s$ laminates, the lowest maximum deflection occurs when α = 30º and for the $(\pm\alpha)_s$ laminates, the lowest maximum deflection occurs when $\alpha = 15º$.

Maximum deflections and rotational components α and β of the $(0/\alpha)_s$ and $(\pm\alpha)_s$ laminates are compared in Figure 2.44 for web inclination angles 45, 48 and 90º. At α greater than 30º, the $(\pm\alpha)_s$ laminates have much higher deflections and rotations than the $(0/\alpha)_s$ laminates. For both laminates, the maximum deflection exhibits a valley and then increases as α is increased from 0 to 90º. The maximum value of the rotational component $\bar{\alpha}$ increases with α for both laminates, but it is significantly higher for the $(\pm\alpha)_s$ laminates than for the $(0/\alpha)_s$ laminates at α greater than 30º. For both laminates, the maximum value of the rotational component $\bar{\beta}$ has the lowest value at α = 0º and exhibits a peak at $\alpha = 45º$. Maximum $\bar{\beta}$ at $\alpha = 45º$ is significantly higher for the $(\pm\alpha)_s$ laminates than for the $(0/\alpha)_s$ laminates.

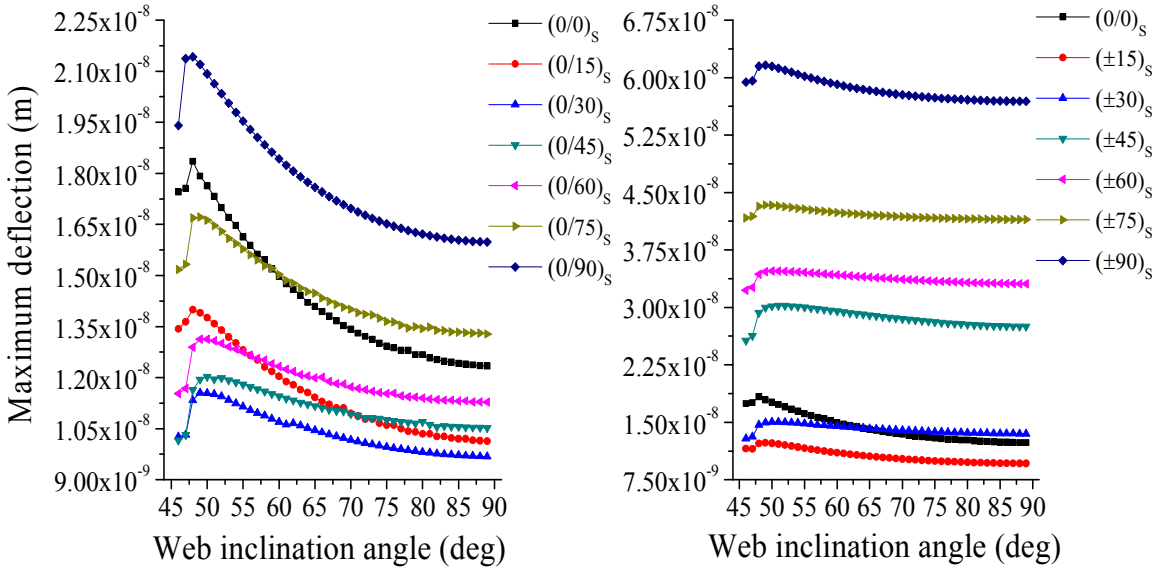

Figure 2.43: Maximum deflection of sandwich plates with varying web inclination and fiber orientation angles for $(0/\alpha)_s$ and $(\pm\alpha)_s$ laminate constructions

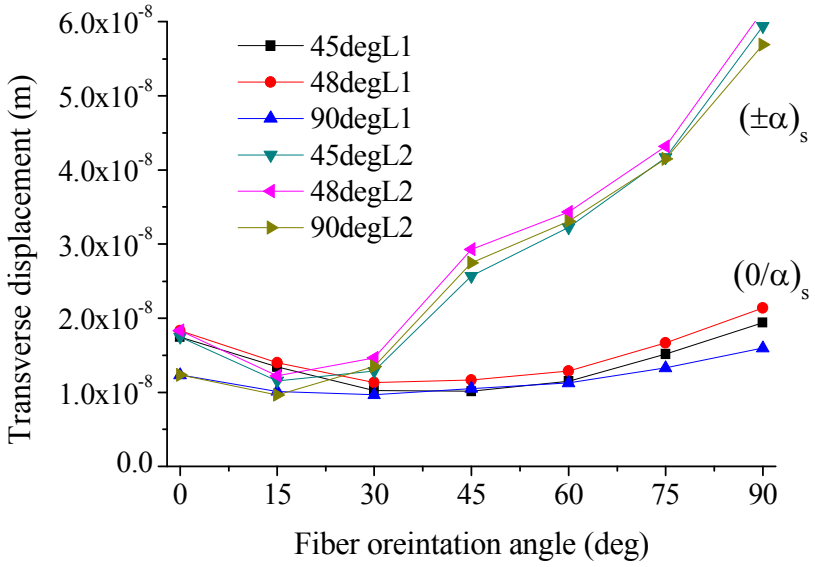

(a)

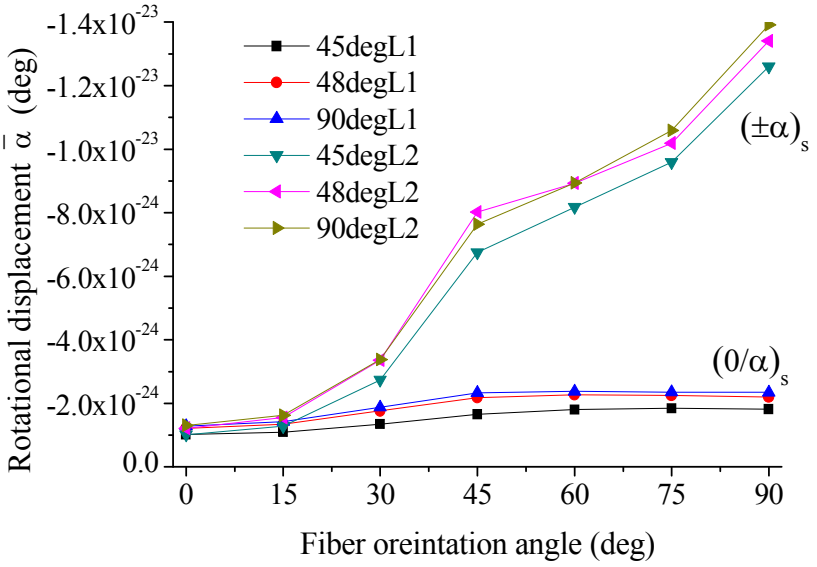

(b)

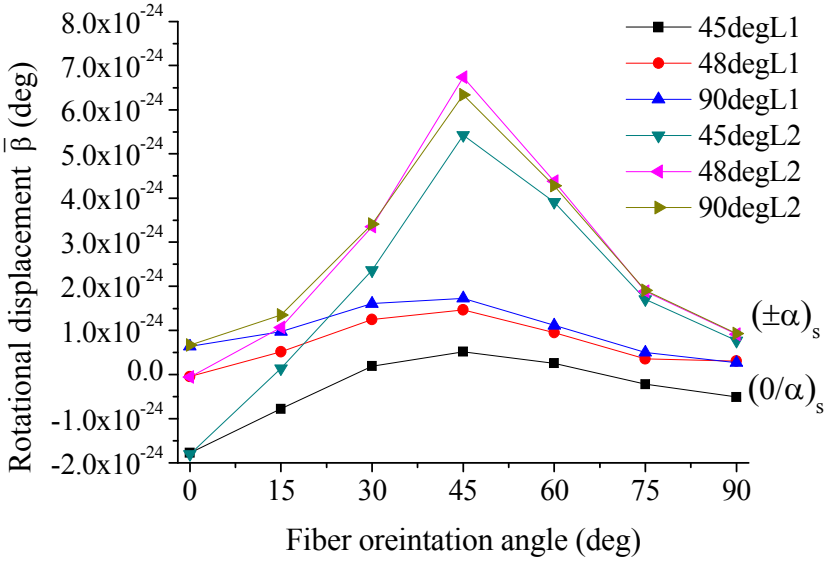

(c)

Figure 2.44: Maximum deflection and rotational components $\bar{\alpha}$ and $\bar{\beta}$ of sandwich plates with varying web inclination angles and fiber orientation angles in the laminate construction

2.4 BENDING MOMENTS AND TRANSVERSE SHEAR FORCES

The constitutive equation relating normal force, transverse shear force and bending moment resultants to normal strains, shear strains and curvatures is given in Equation 2.19. Since [B] = [0] and both D_{16} and D_{26} = 0 for the sandwich plates considered here, it can be simplified to obtain bending moments, M_x and M_y, and transverse shear forces, Q_x and Q_y, as shown in Equation (2.23). It is used for calculating the bending moment and shear force distributions in the sandwich plates. The deflection w and rotation components $\bar{\alpha}$ and $\bar{\beta}$ are calculated using the minimum potential energy approach as mentioned in Section 2.2.

$$
\begin{aligned}
M_x &= D_{11}\frac{\partial \bar{\alpha}}{\partial x} + D_{12}\frac{\partial \bar{\beta}}{\partial y} \\
M_y &= D_{12}\frac{\partial \bar{\alpha}}{\partial x} + D_{22}\frac{\partial \bar{\beta}}{\partial y} \\
Q_x &= A_{44}\left(\bar{\beta} + \frac{\partial w}{\partial y}\right) \\
Q_x &= A_{55}\left(\bar{\alpha} + \frac{\partial w}{\partial x}\right)
\end{aligned}
\qquad (2.23)
$$

2.4.1 $(0/90)_s$ Laminate, $t_{TF} = t_{BF} = 1$ mm, $t_c \leq 1$ mm, $p = d = 80$ mm

Figure 2.45 shows three-dimensional representations of bending moments M_x and M_y and Figure 2.46 shows three-dimensional representations of transverse shear forces Q_x and Q_y in the plate for the web inclination angle θ = 48º. The laminate construction in both faces and webs in the sandwich construction is $(0/90)_s$. The geometric parameters for the unit cell are $t_{TF} = t_{BF} = 1$ mm, $t_c = 1$ mm, and $p = d = 80$ mm. The transverse loading acting on the plate is a distributed pressure of 1 N/m^2. It can be observed from Figure 2.45 that M_x has a positive value throughout the plate and its maximum value, 4.36 x 10^{-2} N-m, is at the center of the plate. M_y, on the other hand, has positive values near the ends of the width of the plate, but is negative away from the ends. The maximum positive and negative values of M_y are 3.9 x 10^{-4} N-m and 3.6 x 10^{-4} N-m, respectively. Thus, the maximum value of M_x is two orders of magnitude higher than the maximum value of M_y. This is due to the fact that the plate is more resistant to bending in

the direction of the corrugation than in the transverse direction. As Figure 2.46 shows, the transverse shear force Q_x is zero at $y = 0$ and at $y = b$. The transverse shear force Q_y is maximum (positive) at $y = 0$ and minimum (negative) at $y = b$.

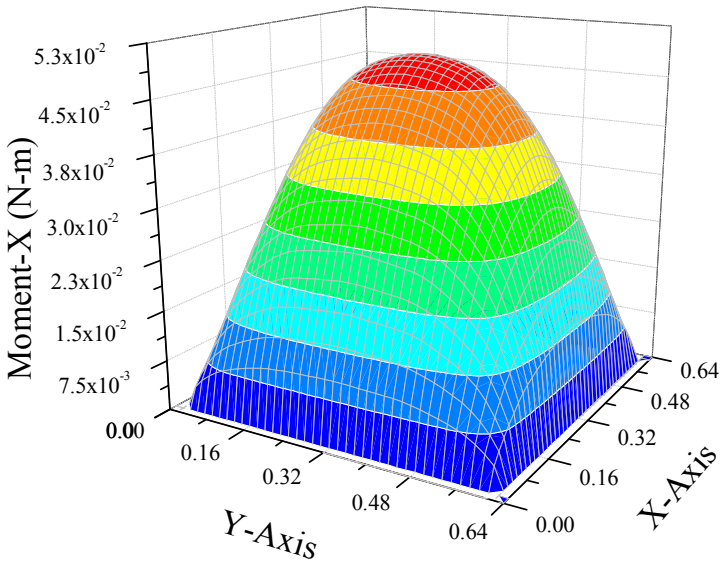

(a) Bending moment M_x

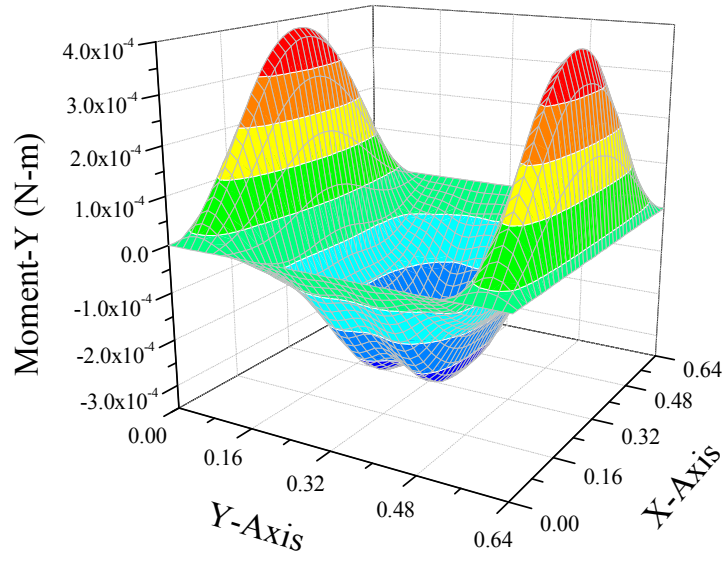

(b) Bending moment My

Figure 2.45: Bending moment distributions for 48º web inclination angle

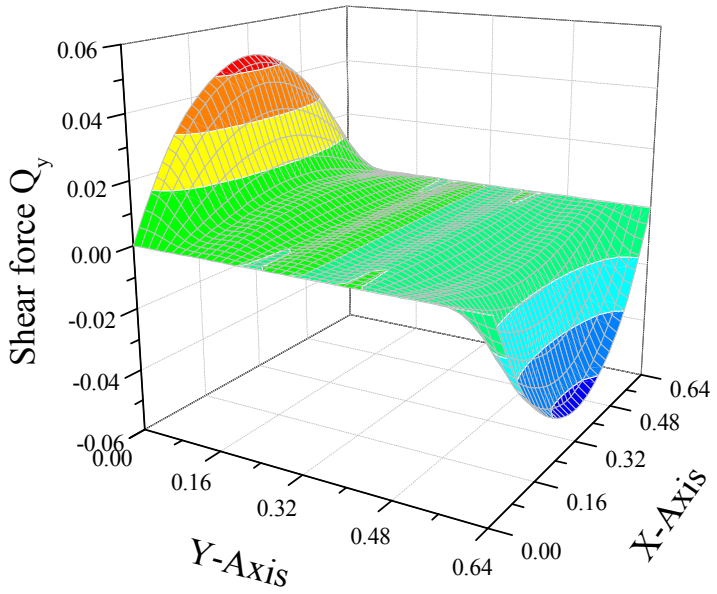

(a) Shear force Q_y

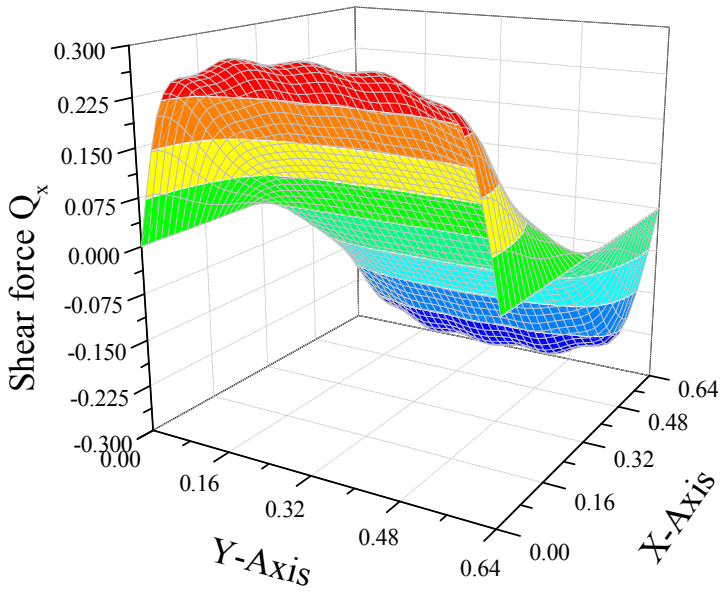

(b) Shear force Q_x

Figure 2.46: Transverse shear force distributions for 48º web inclination angle

The variations of M_x, M_y, Q_x and Q_y across the corrugation direction at the mid-length (i.e., x = 0.32 m) of the plate are shown for different web inclination angles in Figure 2.47 and Figure 2.48. It can be observed in Figure 2.47 that M_x is positive for all web inclination angles. The lowest and highest M_x are observed for θ = 45 and 90º, respectively. M_y is positive for θ = 45º and only near the ends for θ = 48º; but for all other web inclination angles, M_y is negative across the entire width direction of the plate. The highest and lowest M_y are observed for θ = 45º and 90º, respectively. The highest Q_y occurs at the ends of the plate (Figure 2.48).

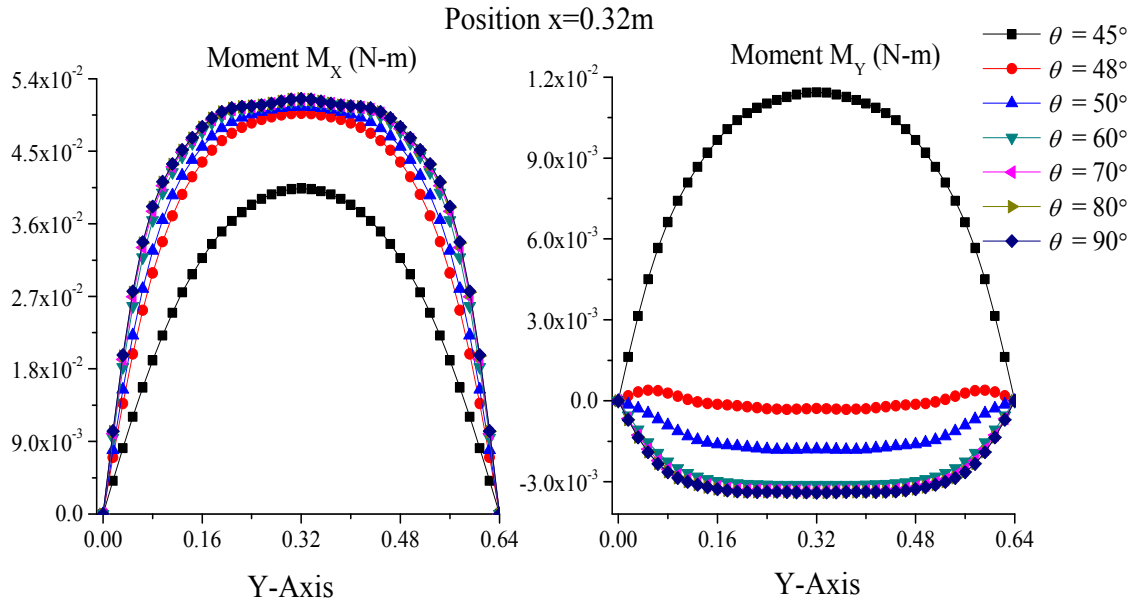

Figure 2.47: Bending moments M_x and M_y calculated for different web inclination angles

The presence of positive M_x and negative M_y has been observed by Chang et al. [5] in their analysis of corrugated-core sandwich plates in which steel was the material for the faces and the webs. They also observed that the magnitude of maximum M_x is significantly higher than that of M_y. A positive M_x creates tension on the bottom surface and compression on the top surface of the plate, whereas a negative M_y creates compression on the bottom surface and tension on the top surface. Since both are acting simultaneously, their combined effect is reflected in the variation of deflection pattern observed in Section 2.3.

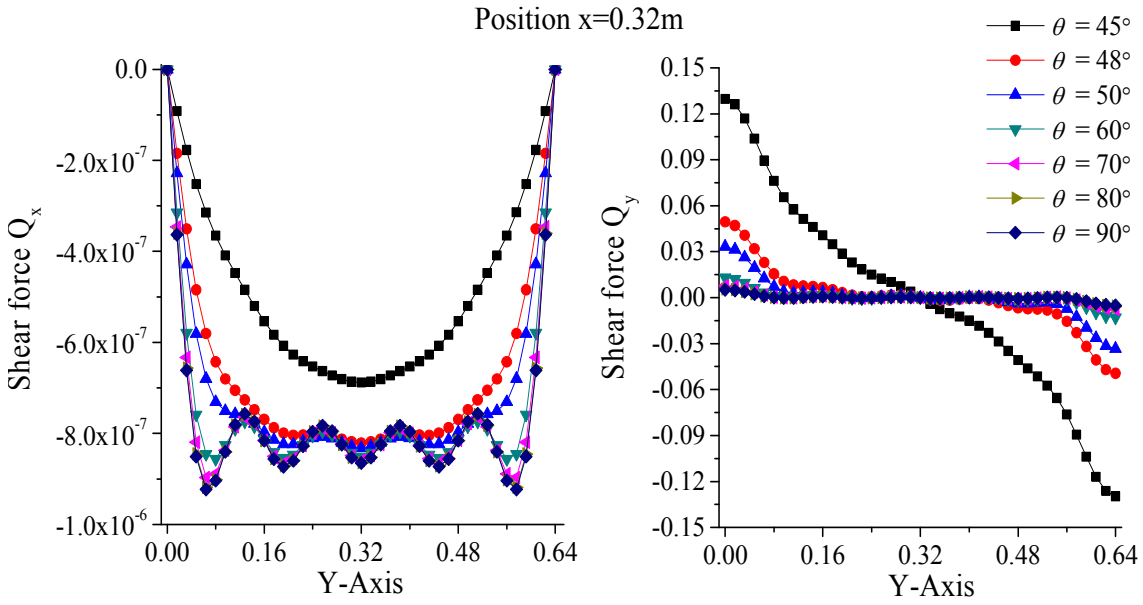

Figure 2.48: Shear forces Q_x and Q_y calculated for different web inclination angles

2.4.2 Effect of Pitch, $(0/90)_s$ Laminate, $t_{TF} = t_{BF} = 1$ mm, $t_c \leq 1$ mm, $d = 80$ mm $p = 20$, 40, 80, 160 and 320 mm

In this section, the effects of pitch on the bending moment and shear force distributions are plotted for the sandwich plates with triangular and rectangular cores. The laminate construction in the faces and webs is $(0/90)_s$. The material and the unit cell geometry are the same as in Case Study 3 in Section 2.3.3. Five different pitch ($2p$) values are considered. As noted before, since the plate has a fixed width of 640 mm, the number of unit cells in the plate decreases as the pitch is increased. For the rectangular core, $\theta = 90°$ for all p/d ratios, and as shown in Figure 2.24, for the triangular core (which corresponds to the minimum web inclination angle), the web inclination angle decreases with increasing p/d ratio. Also, since the cross-sectional area is maintained constant at 478 mm^2, the core thickness increases with increasing web inclination angle as well as p/d ratio. The thickness variation plot is shown in Figure 2.25.

For the triangular core (Figure 2.49), both M_x and M_y have positive values. M_x increases with increasing pitch, but M_y decreases with increasing pitch. Both transverse shear forces increase with increasing pitch. For the rectangular core (Figure 2.50), there is

no effect of pitch on M_x and there is only a small effect on M_y. Similarly, there is no effect of pitch on Q_x and the effect of pitch on Q_y is very similar to that on M_y.

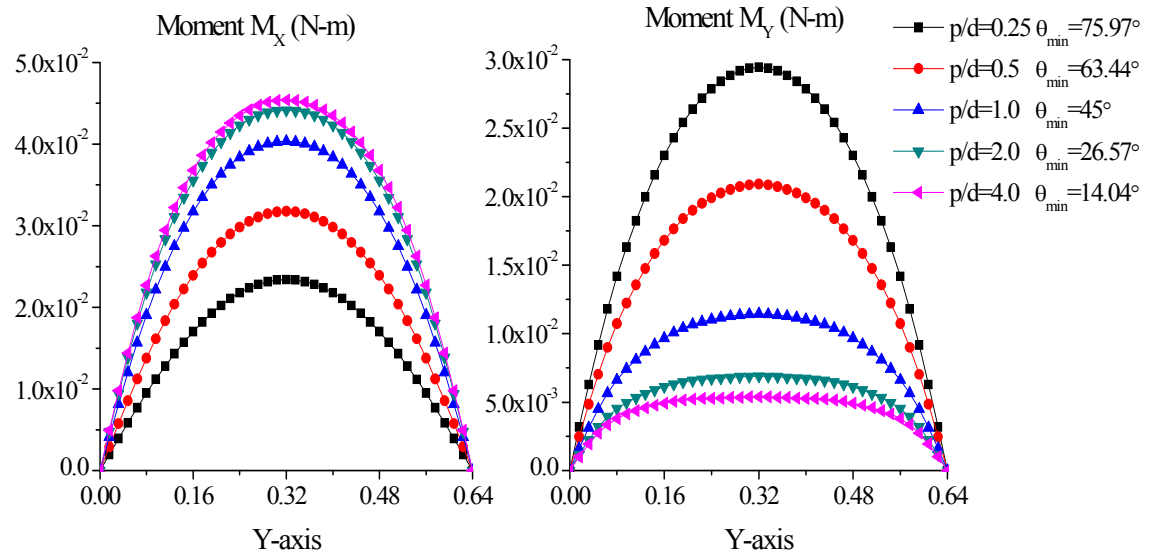

(a) Moment distributions

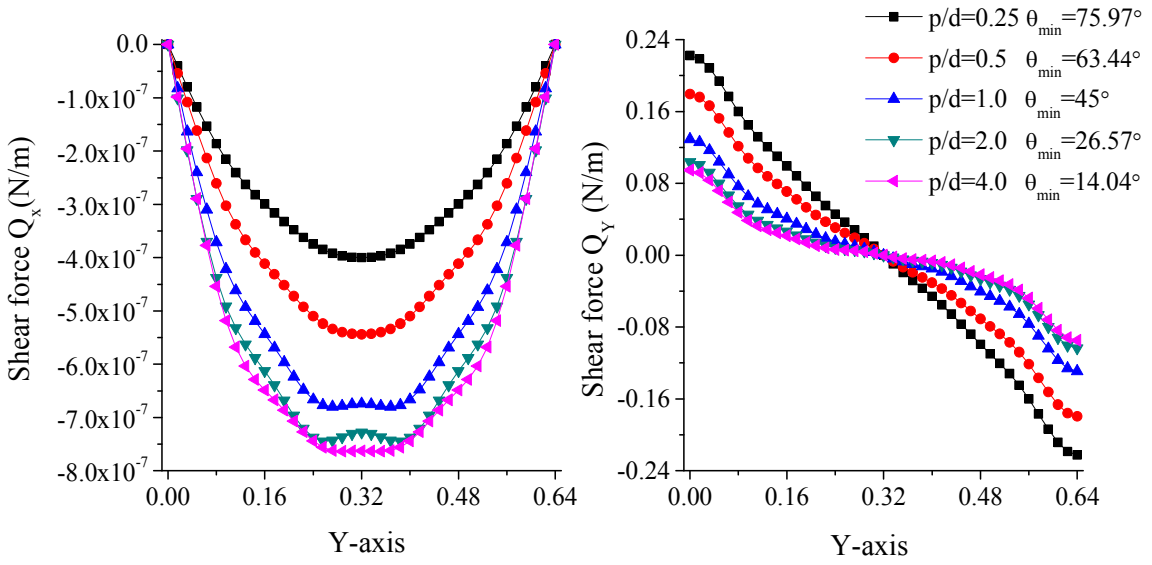

(b) Shear force distributions

Figure 2.49: Bending moment and shear force variations across the corrugation direction at the mid-length of the equivalent plate (x = 0.32 m). The core is triangular. The web inclination angles are shown in the figure

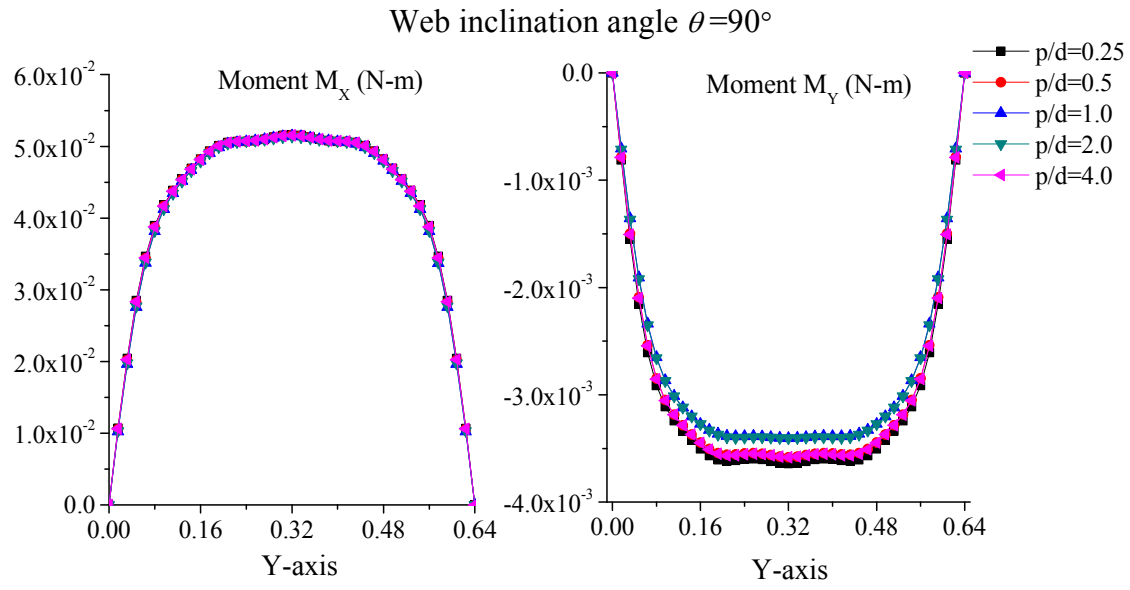

(a) Moment distributions

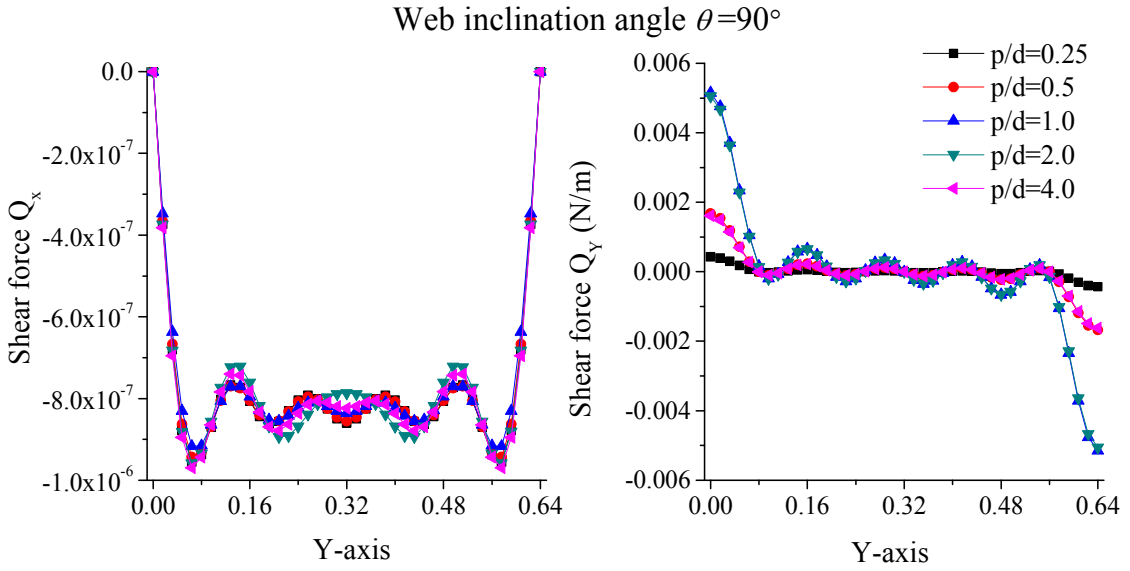

(b) Shear force distributions

Figure 2.50: Bending moment and shear force variation across the corrugation direction at the mid-length of the equivalent plate (x = 0.32 m). The core is rectangular (θ = 90º).

To understand the effect of pitch on the bending moments, each component of the bending moment equations given in Equation (2.23) is further examined. At the minimum

web inclination angle, the higher the pitch, the higher are the flexural stiffness components D_{12}, D_{22} and D_{66}, but D_{11} is the same for all pitches. However, as shown in Figure 2.51, $D_{11}\frac{\partial\bar{\alpha}}{\partial x}$ increases with increasing pitch, whereas $D_{22}\frac{\partial\bar{\beta}}{\partial y}$ decreases with increasing pitch. The other two components $D_{12}\frac{\partial\bar{\alpha}}{\partial y}$ and $D_{12}\frac{\partial\bar{\beta}}{\partial y}$ do not vary much with increasing pitch. At $\theta = 90°$, all four flexural stiffness components have the same values at all pitches, and as shown in Figure 2.52, the components of the bending moments M_x and M_y also do not vary much with increasing pitch.

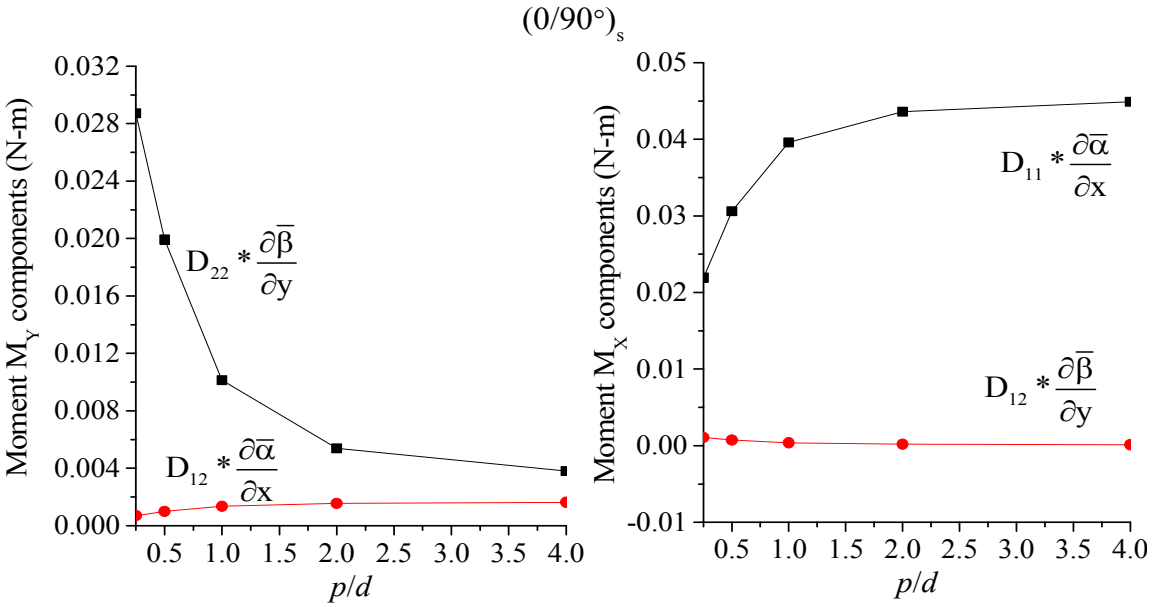

Figure 2.51: Components of M_x and M_y as a function of p/d for the case of minimum web inclination angle. The laminate construction is $(0/90)_s$ and d = 80 mm.

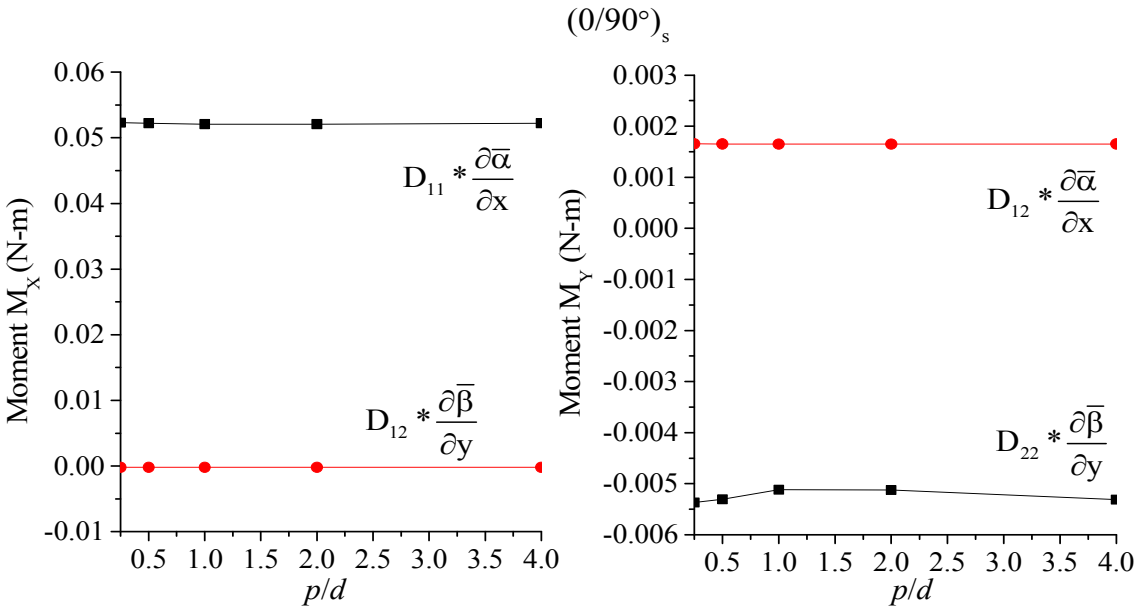

Figure 2.52: Components of M_x and M_y as a function of p/d for the case of rectangular webs ($\theta = 90°$). The laminate construction is $(0/90)_s$ and $d = 80$ mm

2.4.3 Effect of Laminate Construction: $(0/\alpha)_s$ and $(\pm\alpha)_s$ Laminates

In this section, bending moment and shear force distribution plots are presented for $(0/\alpha)_s$ and $(\pm\alpha)_s$ laminate constructions in the corrugated-core sandwich plate. The material and unit cell dimensions are the same as in Case Study 2.1 presented in Section 2.3.2. For all of the plots, the x-distance is 0.32 m, i.e., at the mid-length of the plate and the distributions are shown across the corrugation direction, i.e., the y-direction. Since the cross-sectional area is maintained constant at 478 mm^2, the core thickness increases as the web inclination angle θ is increased from the minimum value of 45° (triangular core) to the maximum value of 90° (rectangular core). The variation in thickness as a function of web inclination angle is shown in Figure 2.15. The bending moment and shear force distribution plots are shown in Figure 2.53 to Figure 2.60, for $\theta = 45°$, 48° and 90°. In addition to 45° and 90°, which represent the minimum and maximum web inclination angles, the 48° web inclination angle is selected since it represents the web inclination angle at which transverse displacement has the maximum value as shown in Figure 2.20.

As can be observed in Figure 2.53 to Figure 2.56, the effect of fiber orientation angle α on M_x, M_y, Q_x and Q_y in $(0/\alpha)_s$ laminates is relatively small. On the other hand, Figure 2.57 and Figure 2.58 show that α has significant effects on both M_x and M_y in $(\pm\alpha)_s$ laminate constructions. However, as with the $(0/\alpha)_s$, Q_x and Q_y are unaffected by change in α. To illustrate the effects of α in these two laminates, the M_x and M_y values at y = 0.32 m or the mid-width of the plate are plotted in Figure 2.61. For the $(\pm\alpha)_s$ laminate constructions, both M_x and M_y increase with α from α = 0º to 30º, then they decrease from α = 30 to 60º, and finally, they increase from α = 60º to 90º. The highest and lowest M_x are observed for the $(\pm30)_s$ and $(\pm60)_s$ laminates, respectively. M_y is positive for α = 0º, 15º and 30º and negative for α = 45º, 60º, 75º and 90º. The highest and lowest M_y also occur with the $(\pm30)_s$ and $(\pm60)_s$ laminates, respectively. For the $(0/\alpha)_s$ laminate constructions, much smaller variation in either M_x or M_y occurs with α. One reason for this is the presence of 0º fibers in the $(0/\alpha)_s$, which, being in the outer layers, provides the major resistance to bending.

To investigate the variations of M_x and M_y with fiber orientation angle α, their components, namely $D_{11}\frac{\partial\bar{\alpha}}{\partial x}$, $D_{12}\frac{\partial\bar{\beta}}{\partial y}$, $D_{12}\frac{\partial\bar{\alpha}}{\partial y}$ and $D_{22}\frac{\partial\bar{\beta}}{\partial y}$, are plotted as a function of α in Figure 2.62 to Figure 2.65. Comparing Figures 2.62 and 2.64 with Figures 2.63 and 2.65, it can be seen the components of M_x do not vary much with α for the $(0/\alpha)_s$ laminates, but the components of M_x for the $(\pm\alpha)_s$ laminates first increase and then decrease as α is increased, with the peaks observed at α = 45º On the other hand, the components of M_y for both laminate constructions show considerable variation with increasing α.

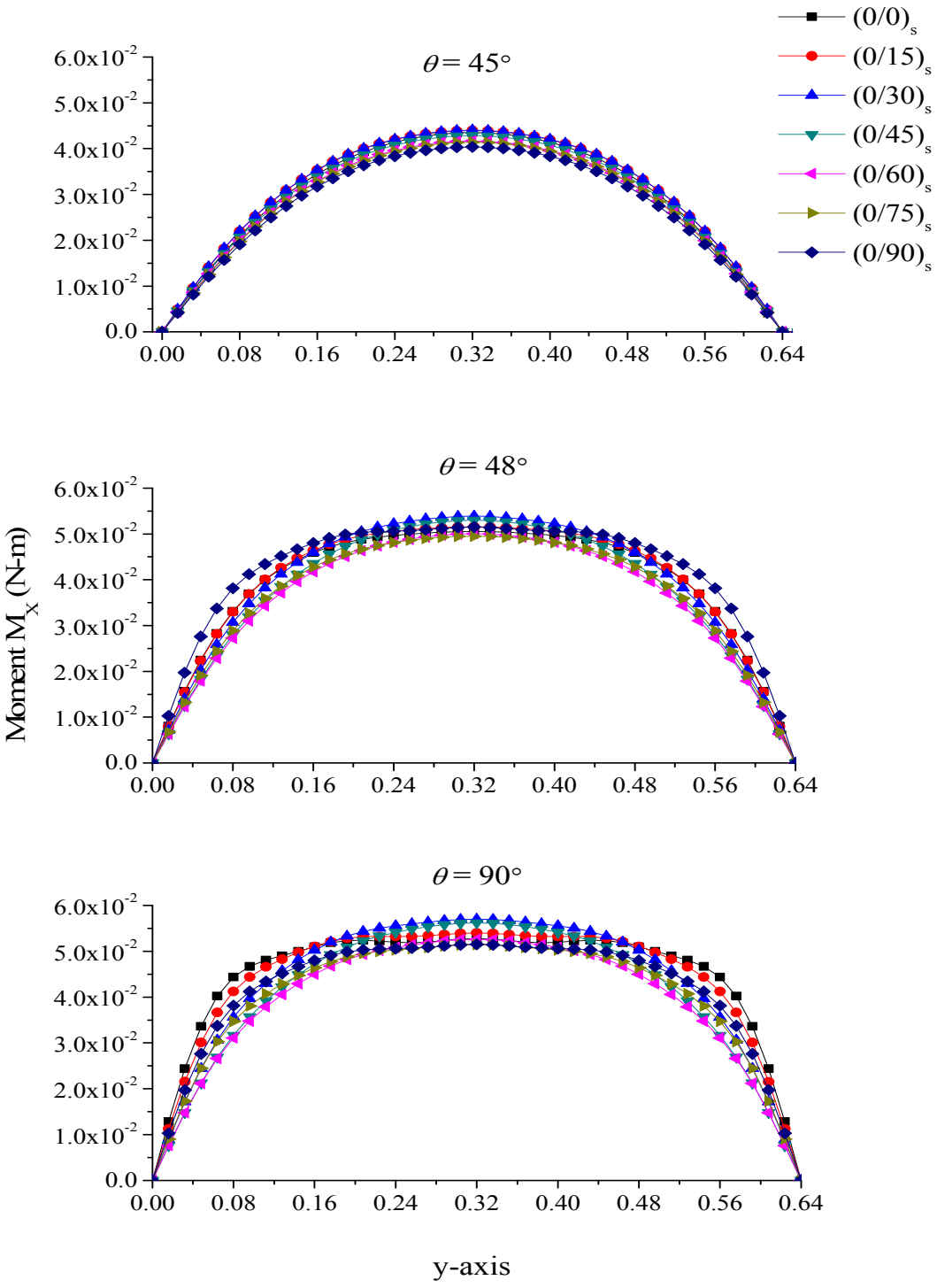

Figure 2.53: Bending moment M_x distribution at mid-length in the width direction of sandwich plates with web inclination angles $\theta = 45°$, 48° and 90° and laminate construction $(0/\alpha)_s$

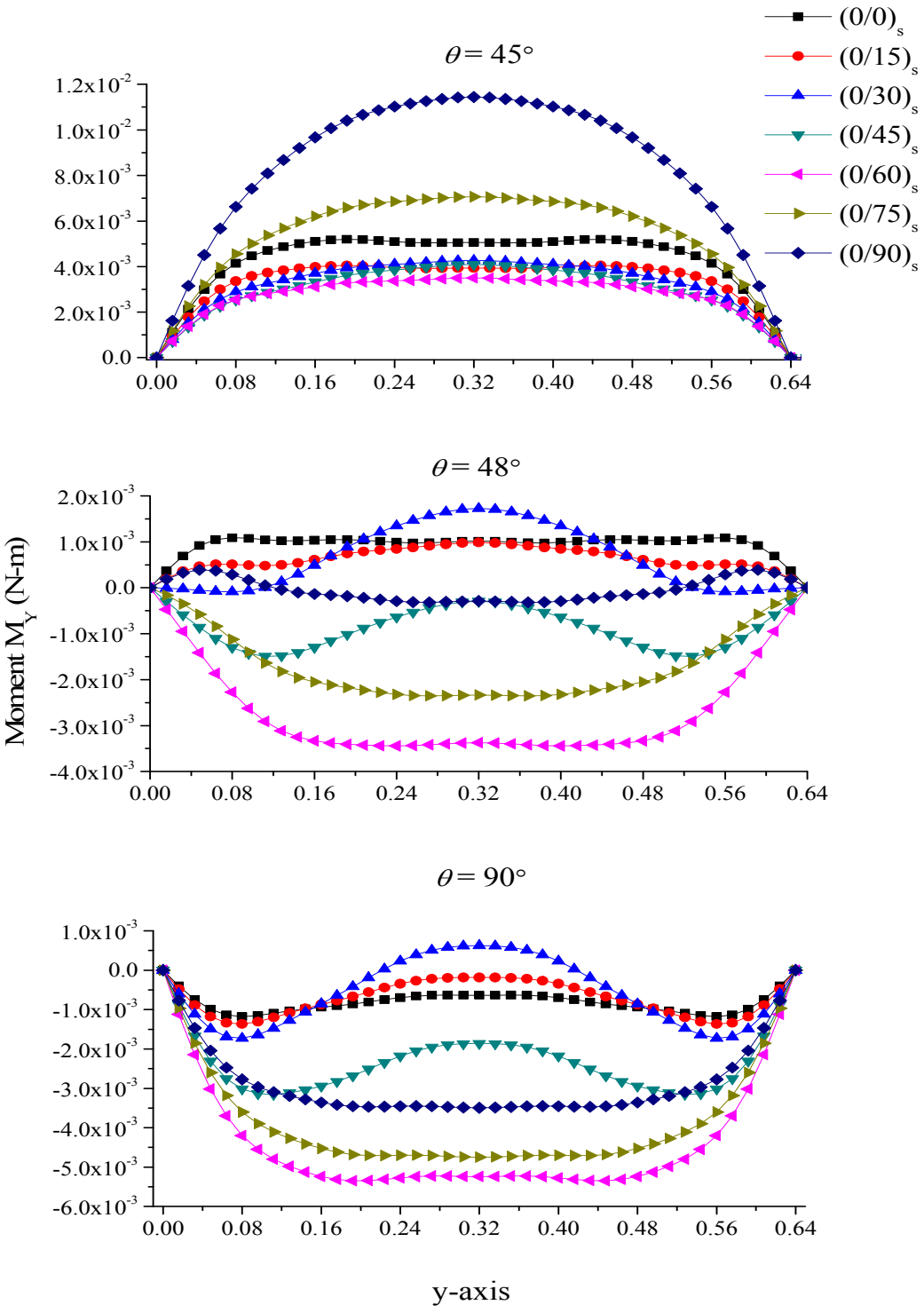

Figure 2.54: Bending moment M_y distribution at mid-length in the width direction of sandwich plates with web inclination angles $\theta = 45°$, 48° and 90° and laminate construction $(0/\alpha)_s$

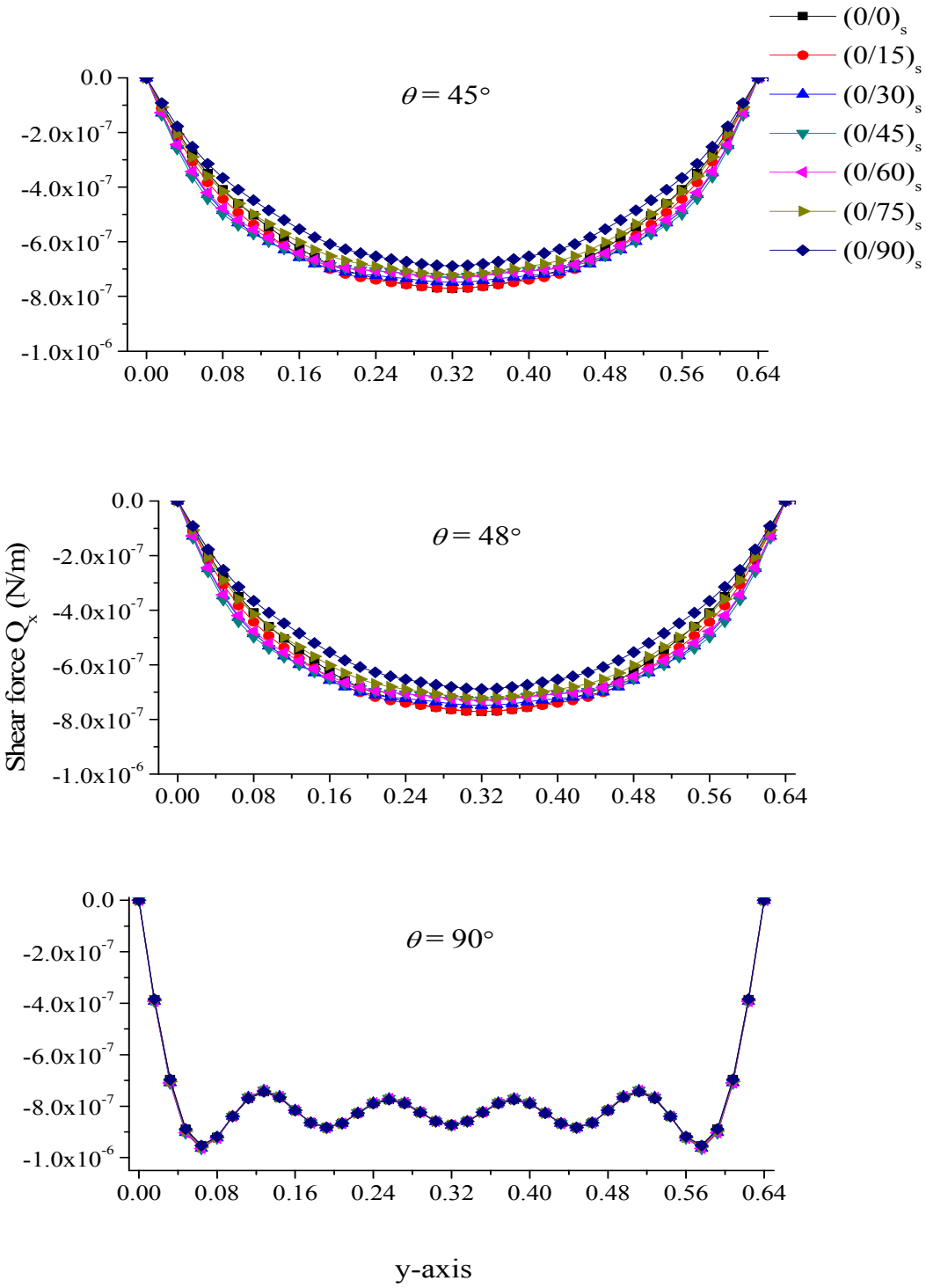

Figure 2.55: Shear force Q_x distribution at mid-length in the width direction of sandwich plates with web inclination angles θ = 45º, 48º and 90º and laminate construction $(0/\alpha)_s$

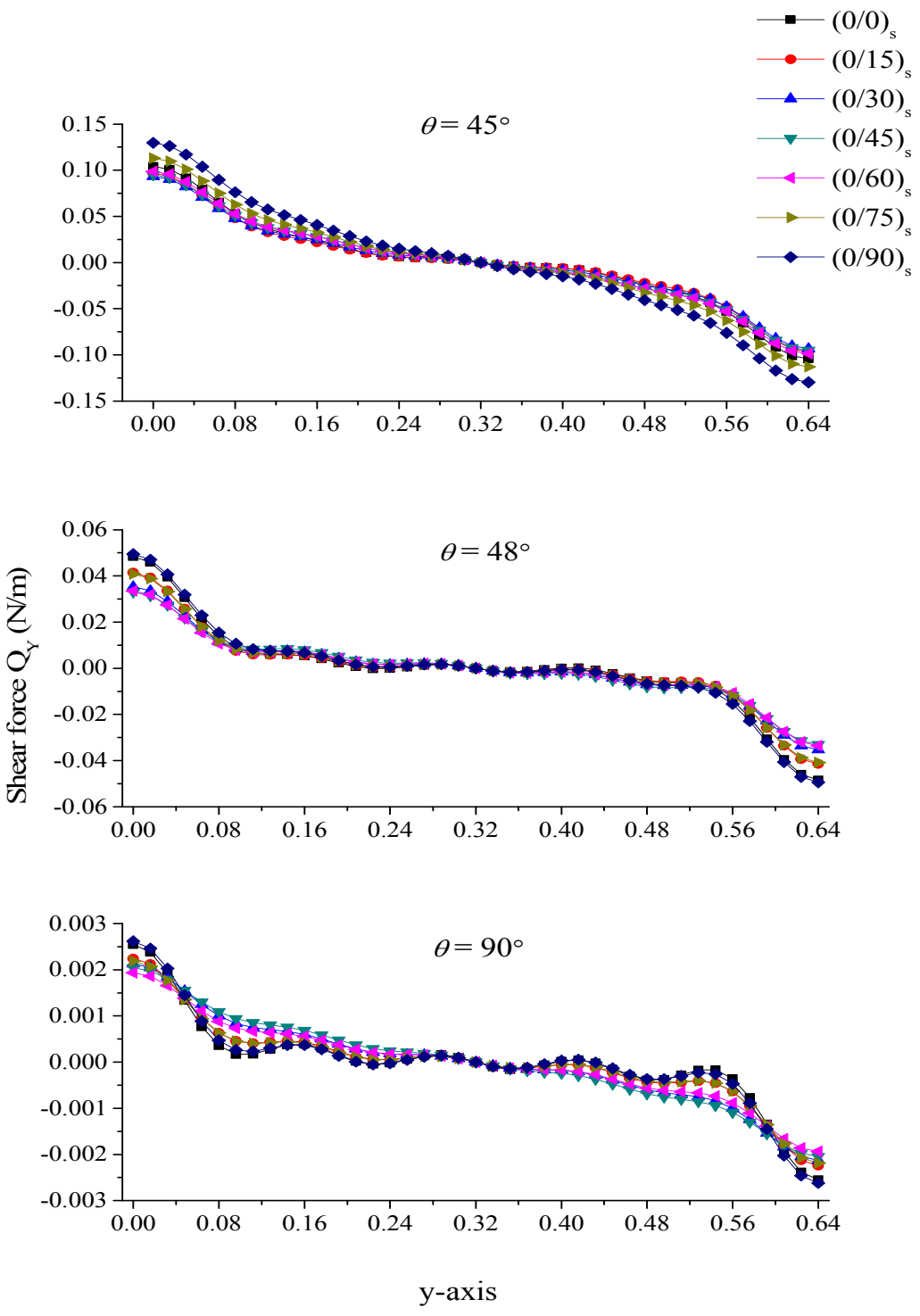

Figure 2.56: Shear force Q_y distribution at mid-length in the width direction of sandwich plates with web inclination angles θ = 45º, 48º and 90º and laminate construction $(0/\alpha)_s$

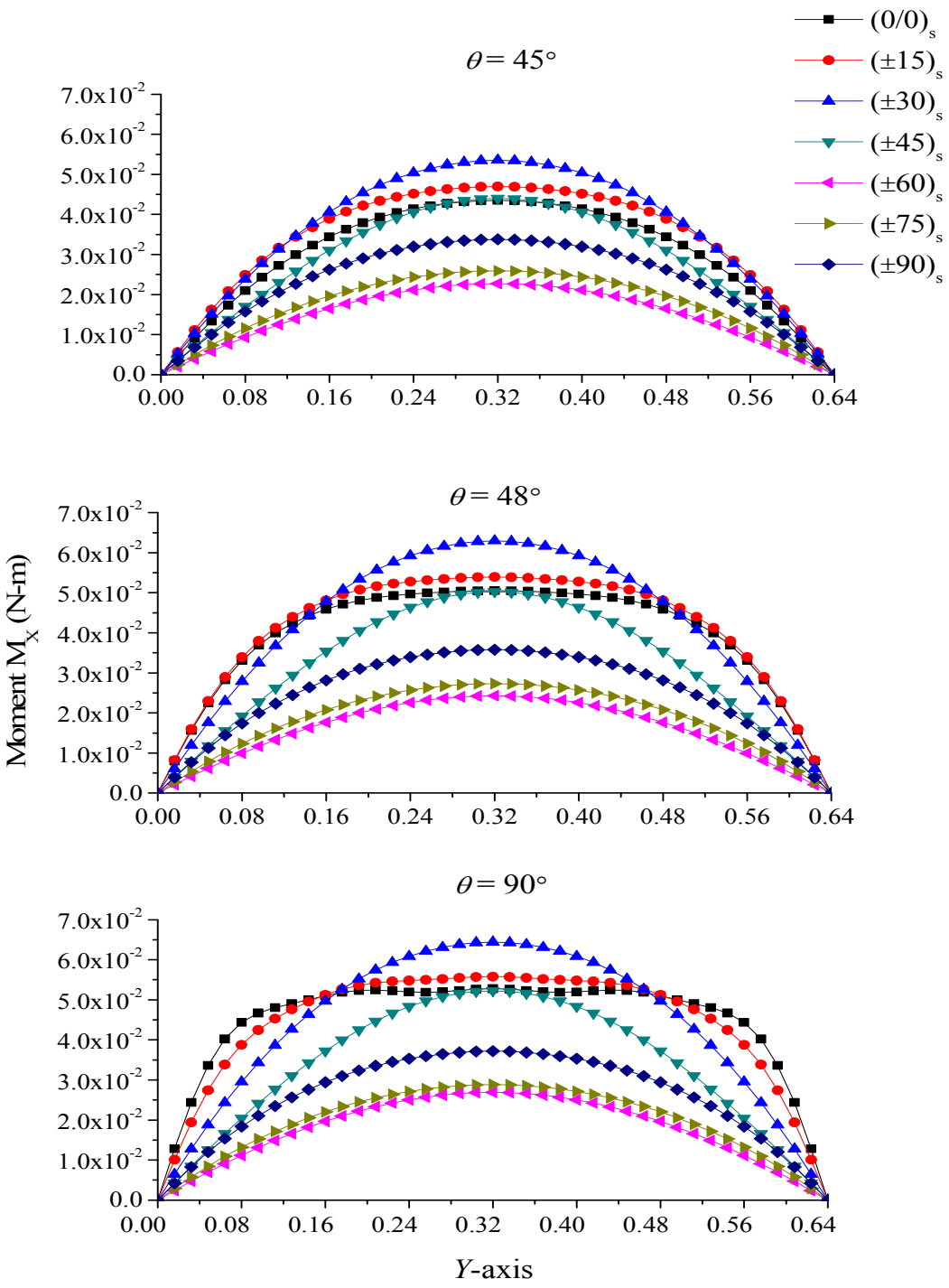

Figure 2.57: Bending moment M_x distribution at mid-length in the width direction of sandwich plates with web inclination angles $\theta = 45^\circ$, 48° and 90° and laminate construction $(\pm\alpha)_s$

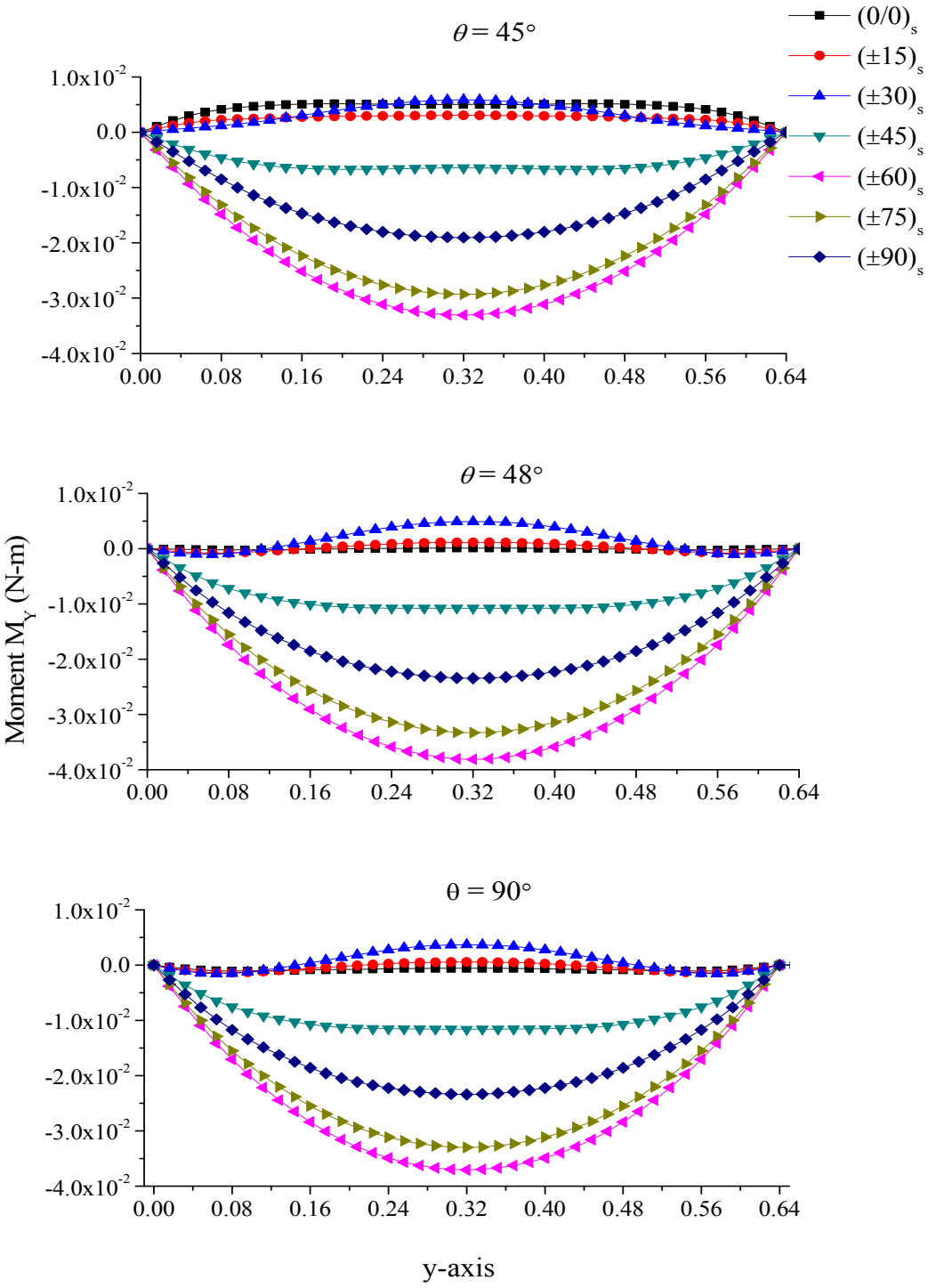

Figure 2.58: Bending moment M_y distribution at mid-length in the width direction of sandwich plates with web inclination angles $\theta = 45^o$, 48^o and 90^o and laminate construction $(\pm\alpha)_s$

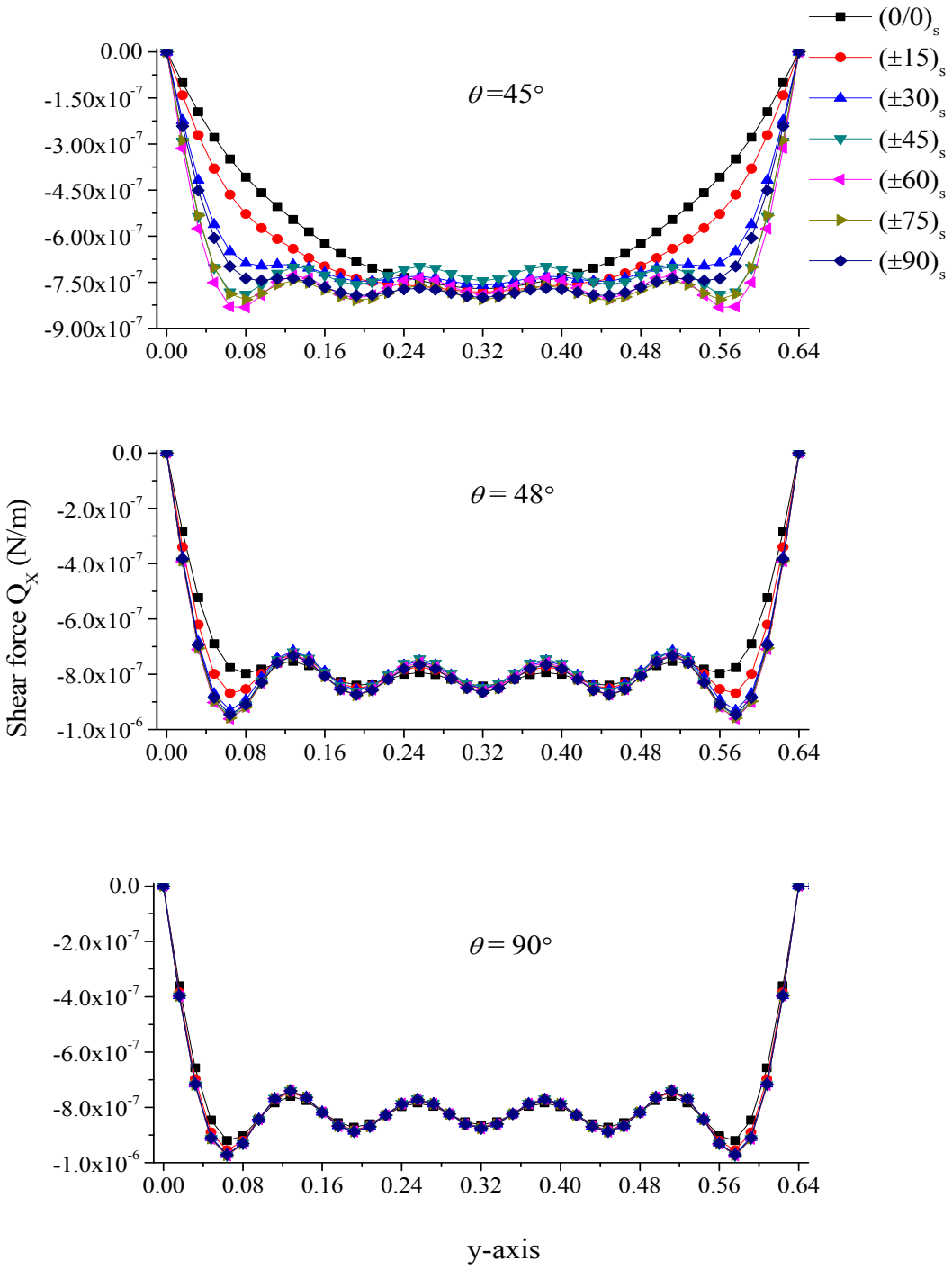

Figure 2.59: Shear force Q_x distribution at mid-length in the width direction of sandwich plates with web inclination angles θ = 45º, 48º and 90º and laminate construction $(\pm\alpha)_s$

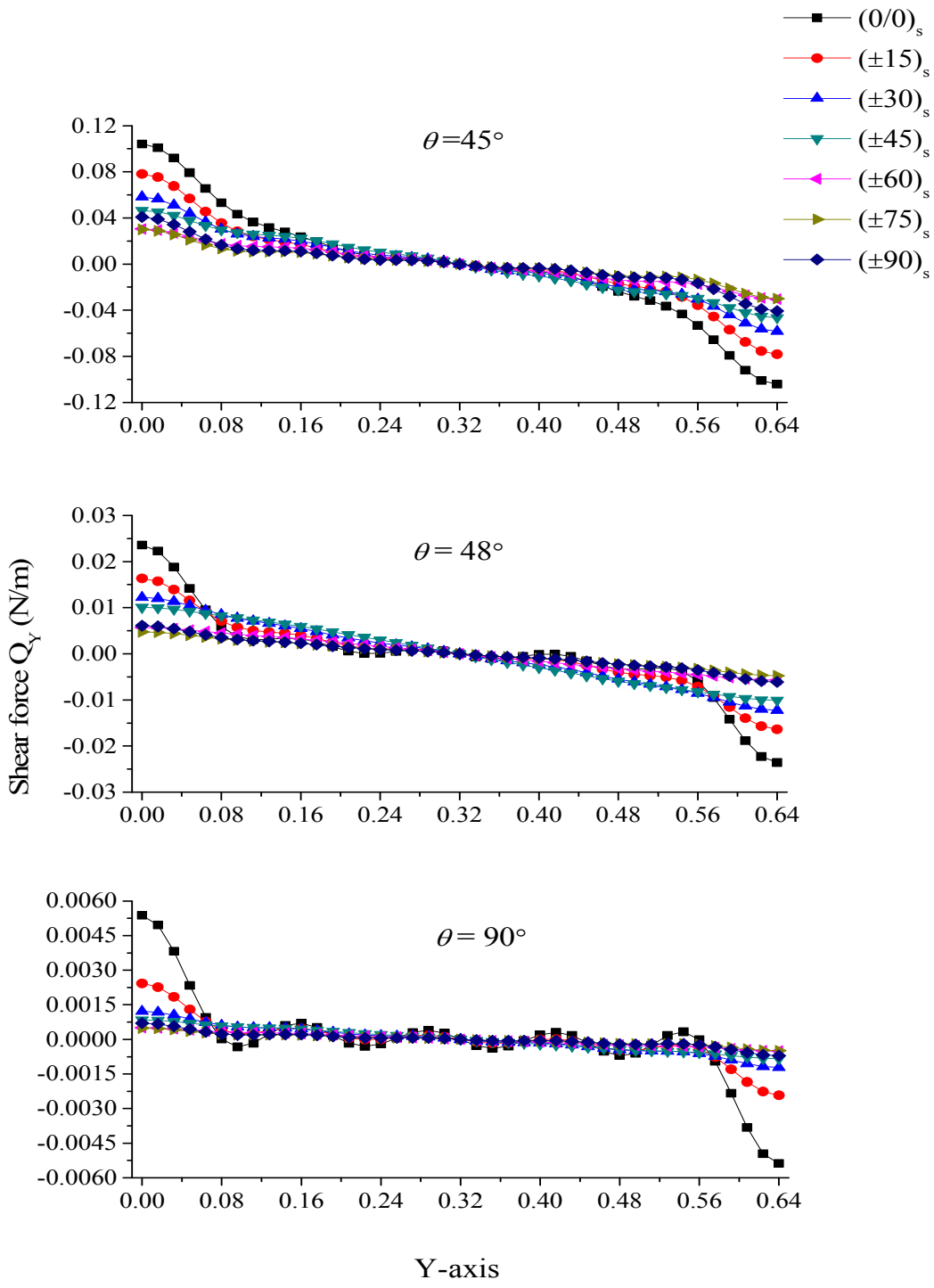

Figure 2.60: Shear force Q_y distribution at mid-length in the width direction of sandwich plates with web inclination angles θ = 45º, 48º and 90º and laminate construction $(\pm\alpha)_s$

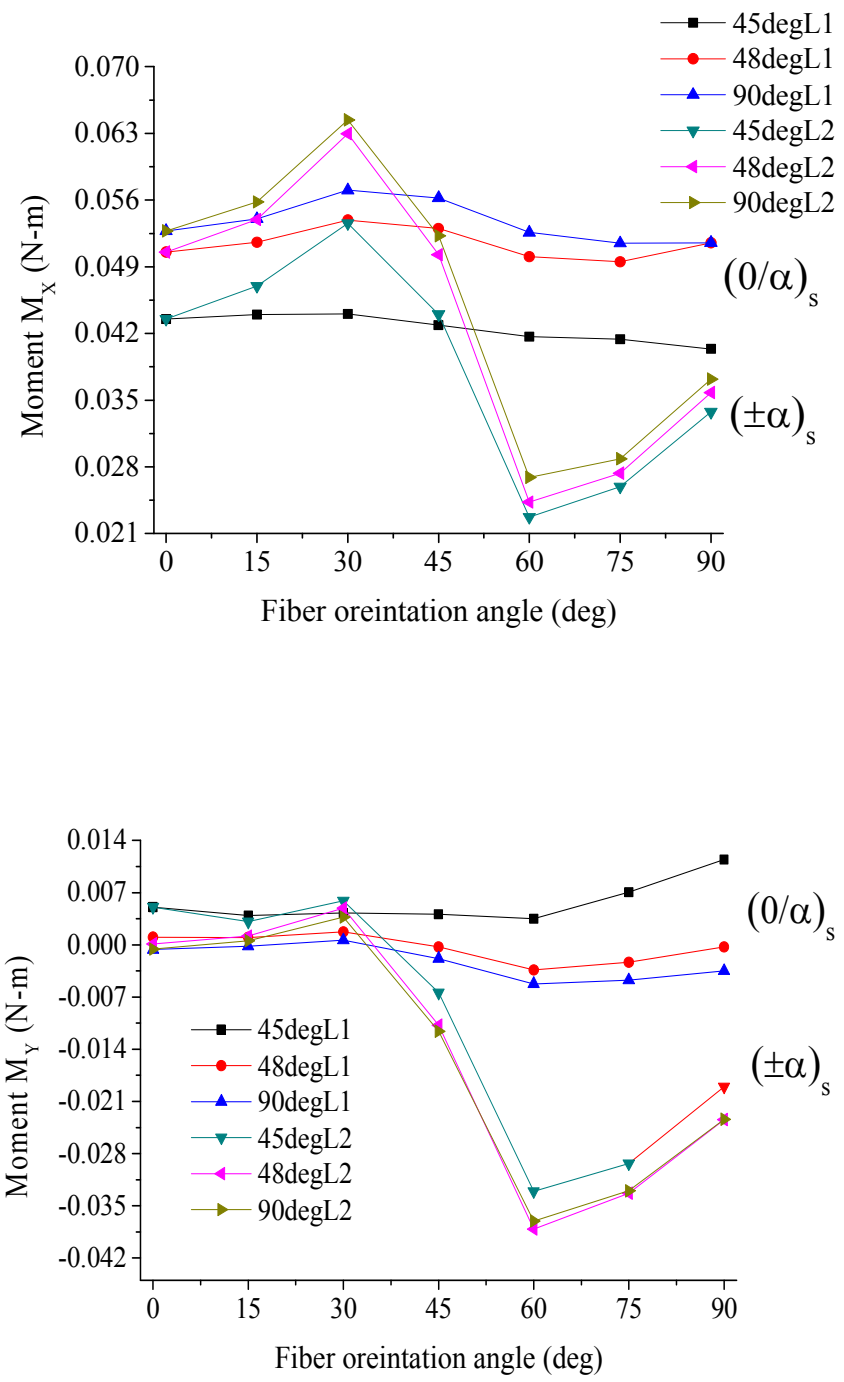

Figure 2.61: Effects of fiber orientation angle α on M_x and M_y at web inclination angles 45º, 48º and 90º. For these plots, $x = y = 0.32$ m and the pressure load = 1 N/m^2.

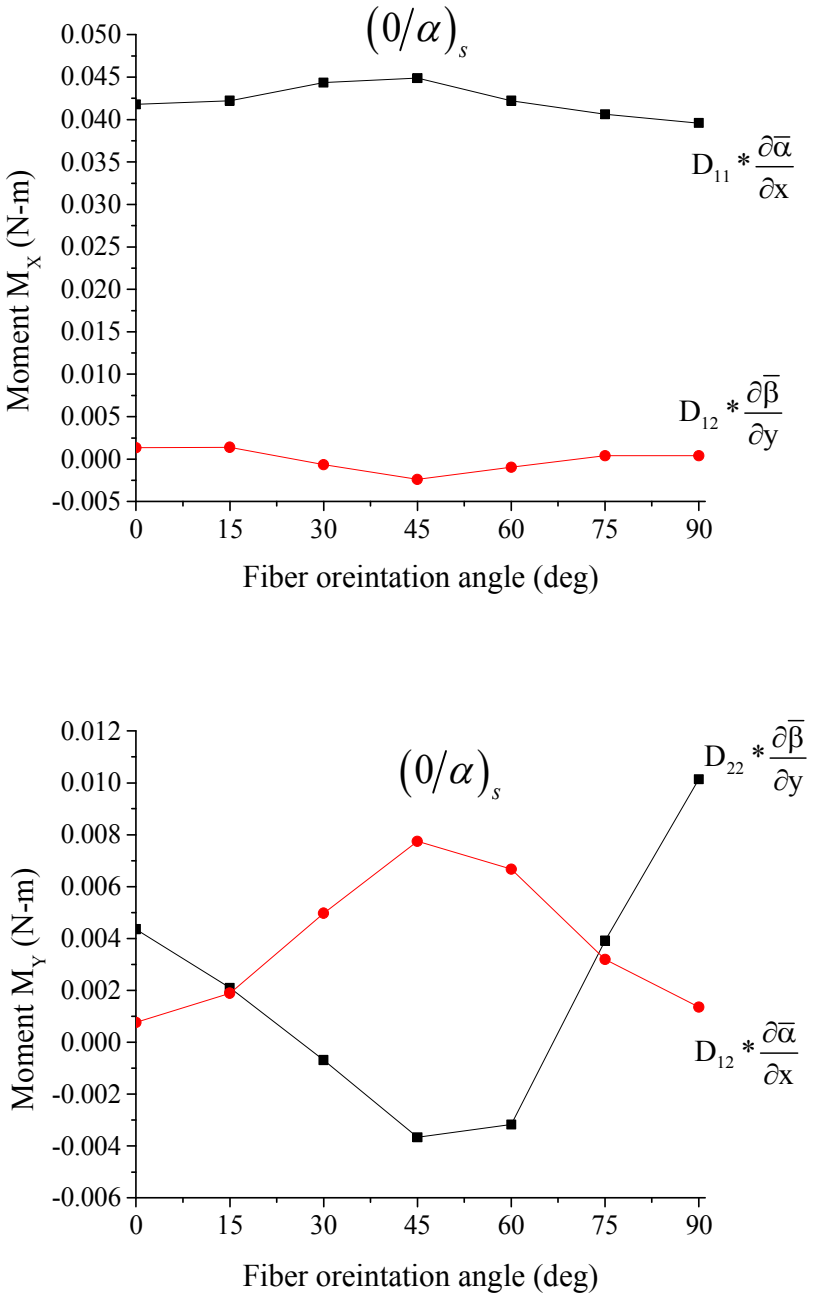

Figure 2.62: Components of M_x and M_y as a function of fiber orientation angle α for the case of triangular webs ($\theta = 45°$) with laminate construction $(0/\alpha)_s$

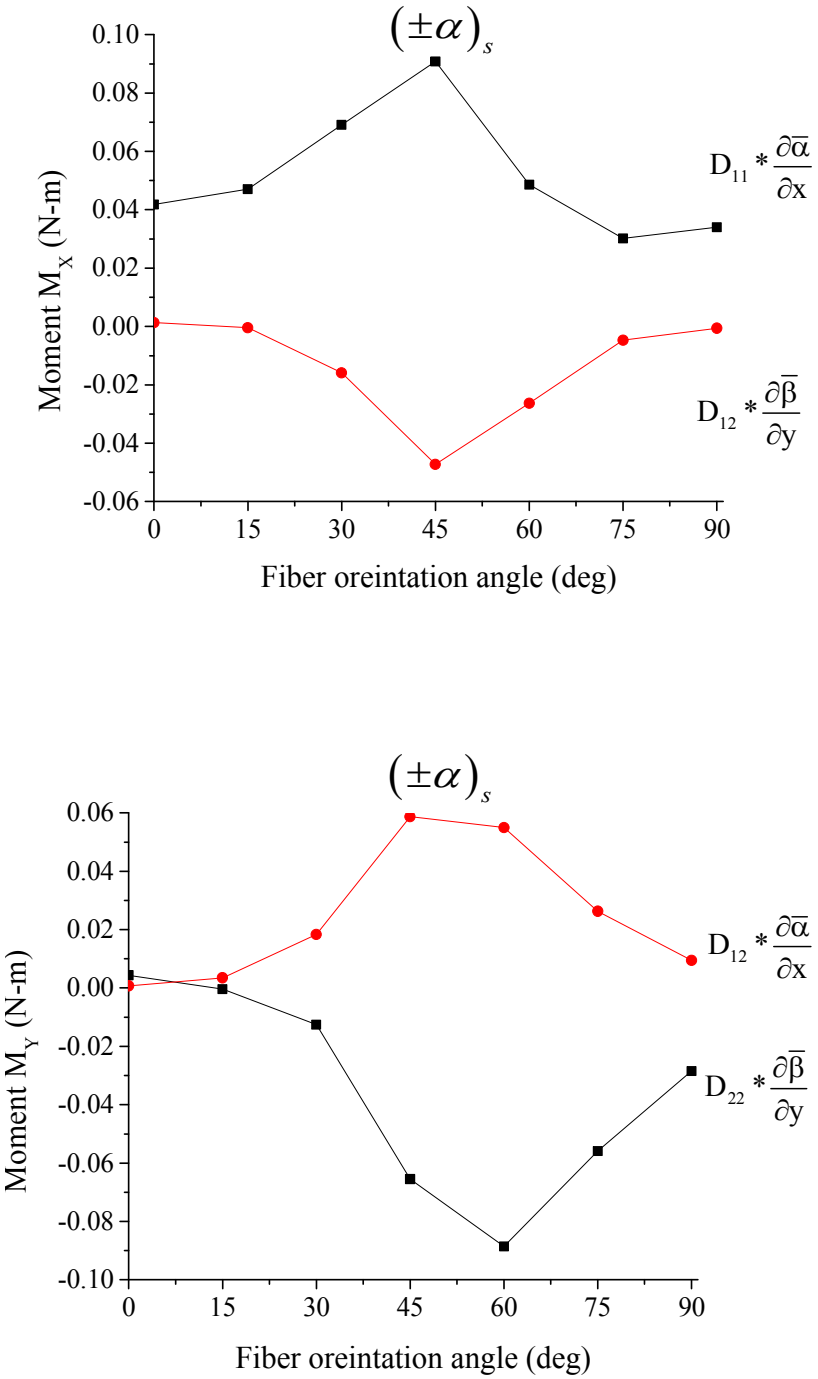

Figure 2.63: Components of M_x and M_y as a function of fiber orientation angle α for the case of triangular webs (θ = 45º) with laminate construction $(\pm\alpha)_s$

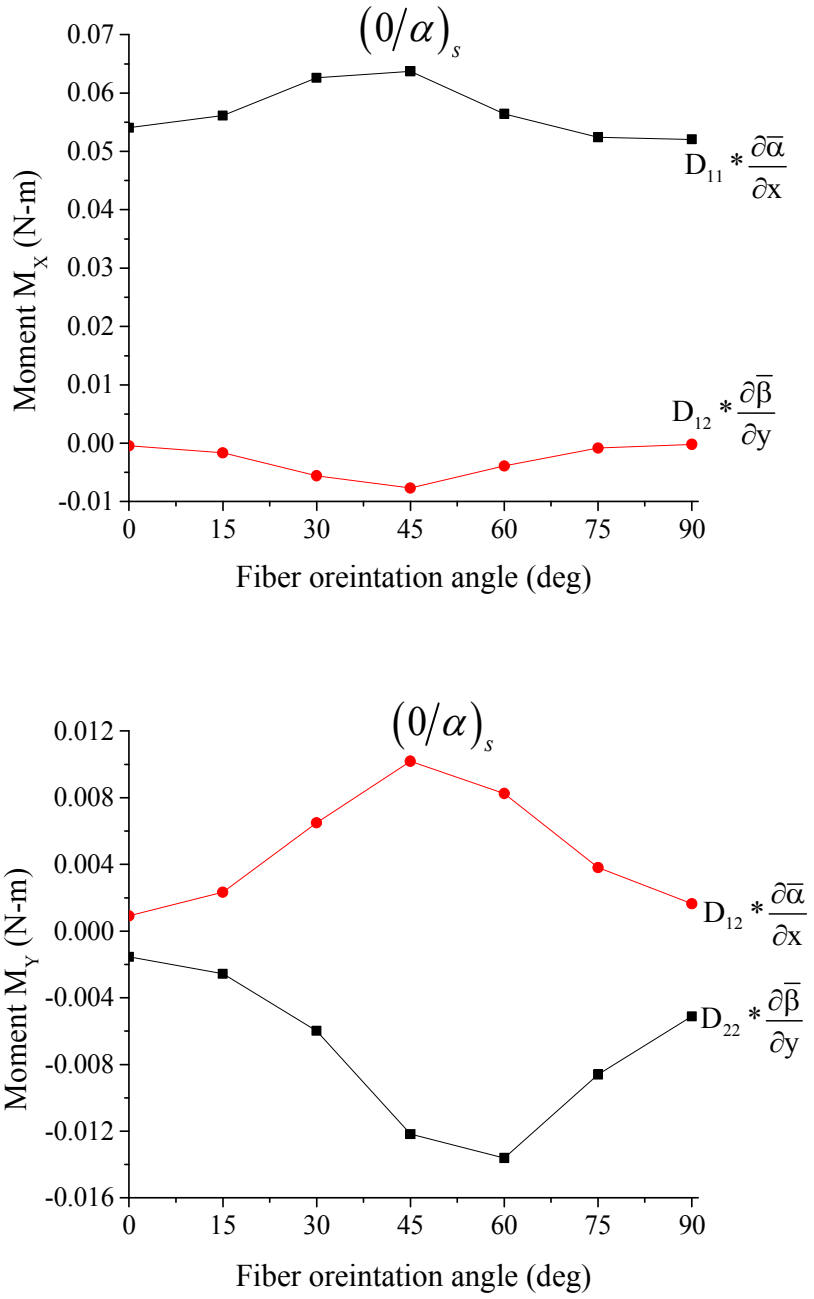

Figure 2.64: Components of M_x and M_y as a function of fiber orientation angle α for the case of triangular webs (θ = 90º) with laminate construction $(0/\alpha)_s$

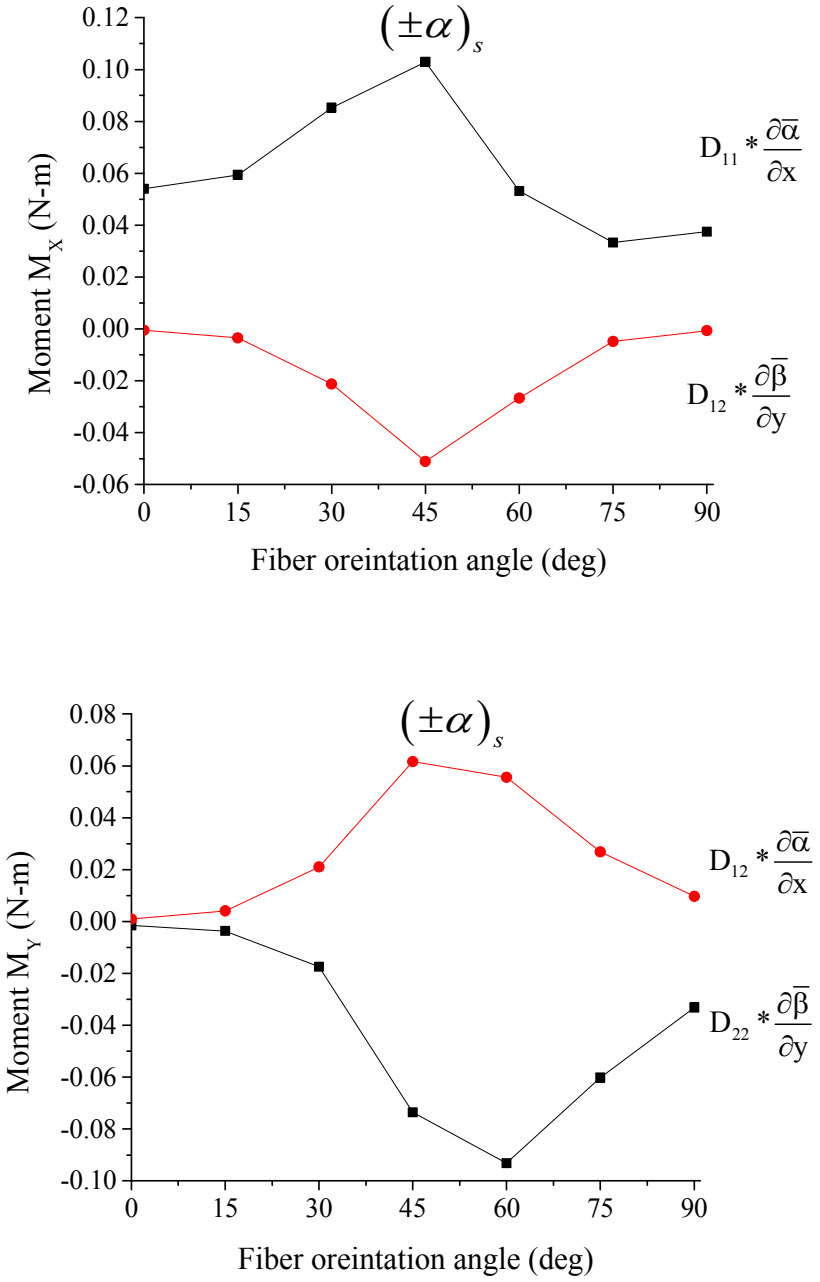

Figure 2.65: Components of M_x and M_y as a function of fiber orientation angle α for the case of triangular webs (θ = 90º) with laminate construction $(\pm\alpha)_s$

2.5 CONCLUSIONS

In this chapter, global bending response of composite sandwich plates with a unidirectional corrugated core is studied in terms of the transverse deflections, rotations of transverse normals, bending moment and shear force distributions. Both the face and web materials of the sandwich plate are made of symmetric carbon fiber reinforced composite laminates. The sandwich plate is first transformed into an equivalent orthotropic plate using strain energy equivalency. The global response is then determined using the minimum potential energy approach. The energy formulations include not only the extensional, in-plane shear, bending and twisting stiffness components, but also the transverse shear stiffness components, which are deemed to have important contributions to the global response of sandwich structures with relatively flexible core.

The effects of geometric parameters, such as face thickness, web thickness, web inclination angle, pitch and face center distance, on the global response of the sandwich plates with $[0/90]_s$ laminates in the faces and the webs are systematically determined. The effects of laminate construction on the global response are also determined by considering two different laminate constructions, namely $[0/\alpha]_s$ and $[\pm\alpha]_s$, for the faces and the webs. The fiber orientation angle α in the laminates is varied between 0 and 90^o. In all cases, the cross-sectional area, and hence the mass was maintained at a constant value so that direct comparison can be made between the effects of various geometric parameters and laminate constructions.

The following observations are made regarding the effects of geometric parameters.

1. The maximum deflection of the sandwich plates depends on the web inclination angle with its largest value occurring at a web inclination angle at or closer to the triangular core. The maximum deflection has the lowest value at web inclination angle of 90^o, i.e., for the rectangular core.
2. The maximum deflection depends on the core thickness relative to the face thickness; however, the effect of core thickness is greater that the effect of face

thickness. The maximum deflection is higher when the core thickness is lower than the face thickness compared to when both core and face thicknesses are the same.

3. Pitch influences the highest maximum deflection, which occurs at or near the web inclination angle close to that of a triangular core. The lowest maximum deflection which occurs with a rectangular core is not influenced by the pitch, since increase in pitch is accompanied with increase in core thickness.
4. The maximum deflection decreases with increasing face center distance, which is principally due to the decrease in the flexural stiffness components.

The following observations are made regarding the effects of laminate construction in the faces and webs.

1. The maximum transverse deflection of the sandwich plates is significantly higher with $[\pm\alpha]_s$ laminate construction than with $[0/\alpha]_s$ laminate construction at fiber orientations angles higher than 30^o. The largest difference in maximum deflections occurs at fiber orientation angle of 90^o. For the $[\pm\alpha]_s$ laminate construction, the lowest maximum deflection occurs at a fiber orientation angle of 15^o, i.e., with the $[\pm 15]_s$ laminate. For the $[0/\alpha]_s$ laminate construction, the lowest maximum deflection occurs at a fiber orientation angle of 30^o, i.e., with the $[0/30]_s$ laminate. The difference in maximum deflections of the two types of laminate construction can be attributed mainly to the transverse normal rotation influenced by the transverse shear stiffness A_{55}.
2. The fiber orientation angle α has a relatively small effect on bending moments and shear forces in the sandwich plates with the $[0/\alpha]_s$ laminate construction; but its influence is significant with the $[\pm\alpha]_s$ laminate construction.

The most important observation made in this chapter are related to the transverse shear stiffness components A_{44} and A_{55} corresponding to transverse shear components Q_y and Q_x, respectively. Since the corrugation is oriented in the x-direction, A_{44} is much lower than A_{55}, and because of lower A_{44}, its contribution to the global deflection is higher than A_{55}.

REFERENCES

[1] Libove, C. and Hubka, RE., "Elastic constants for corrugated core sandwich plates," *Journal of Structural Engineering*, Vol. 122, No. 8, 1951, pp. 958 -966.

[2] Fung, T.C., K.H. Tan and T.S. Lok., "Elastic constants for Z-core sandwich panels", *Journal of Structural engineering*, vol. 120, 1994, pp. 3046-3054.

[3] Fung, T.C., K.H. Tan and T.S. Lok., "Shear stiffness D_{Qy} for C-core sandwich panels," *Journal of Structural engineering*, Vol. 122, 1996, pp. 958-967.

[4] Lok, T.S. and Cheng, Q.H., "Elastic stiffness properties and behavior of truss-core sandwich panel," *Journal of Structural Engineering*, Vol. 126, No. 5, 2000, pp. 552 -559.

[5] Chang, W., Ventsel, E., Krauthammer, T., and John, J., "Bending behavior of corrugated-core sandwich plates," *Composite Structures*, Vol. 70, No. 1, 2005, pp. 81-89.

[6] Wang, H. X., and Chung, S.W., "Equivalent elastic constants of truss core sandwich plates" *Journal of Pressure Vessel Technology*, Vol. 133, 2011, pp. 473-479.

[7] Buannic, N., Cartraud, P. and Quesnel, T., "Homogenization of corrugated core sandwich panels," *Composite Structures*, Vol. 59, 2003, pp. 299-312.

[8] Biancolini, M.E., "Evaluation of equivalent stiffness properties of corrugated board," *Composite Structures*, Vol. 69, 2005, pp. 322-328.

[9] Nordstrand, T.N., Allen, H.G. and Carlsson, L.A., "Transverse shear stiffnesses of structural core sandwich," *Composite Structures*, Vol. 27, 1994, pp. 317-329.

[10] Carlsson, LA., Nordstrand, T. and Westerlind, B., "On the elastic stiffnesses of corrugated core sandwich," *Journal of Sandwich Structures and Materials*, Vol. 3, 2001, pp. 253-267.

[11] Martinez, O. A., Sankar, B. V., Haftka, R.T., and Bapanapalli, S. K., "Micromechanical analysis of composite corrugated-core sandwich panels for integral thermal protection systems," *AIAA JOURNAL*, Vol. 45, 2007, pp. 2323-2336.

[12] Mallick, P. K., Fiber-Reinforced Composites, 3rd Edition, CRC Press, Boca Raton, FL, 2009.

[13] Gere, J.M. and Timoshenko, S. P., Mechanics of Materials, 2nd Edition, Wadsworth, Inc., Belmont, CA, 1984.

CHAPTER 3

GLOBAL FREE VIBRATION RESPONSE OF COMPOSITE SANDWICH PLATES WITH CORRUGATED CORE CONSTRUCTION

3.1 INTRODUCTION

Sandwich plates are used in many applications in which resistance to vibration is a desirable design goal. Many publications exist on the free vibration analysis of sandwich plates with either foam core or honeycomb core [1-5]. Most of these publications dealt with flexural vibrations of sandwich plates using either analytical or finite element methods. Free vibration analysis of corrugated core sandwich plates is relatively few. Lok and Cheng [6] studied the free vibration characteristics of a fully-clamped truss-core sandwich panel in which both the skin and the core material is an aluminum alloy. They first transformed the corrugated sandwich panel into an equivalent homogeneous plate and then used the energy method to determine its natural frequencies. They also verified that their analytical solution agrees well with both two-dimensional and three-dimensional finite element results. In another study, Lok and Cheng [7] considered the dynamic transient response of a fully-clamped aluminum truss-core sandwich panel subjected to a step load function uniformly applied on its top surface. Here also the approach was to transform the sandwich panel to an equivalent homogeneous plate and then use the energy approach to determine the peak center deflection. Lou et al. [8] investigated the free vibration characteristics of stainless steel sandwich beams with pyramidal truss core. They transformed the lattice truss structure to a continuous homogeneous material and calculated the natural frequencies of the homogeneous plate under simply supported boundary conditions.

Free flexural vibration response of laminated composite beams and plates has been considered by many investigators [9-14]. In these investigations, Hamilton's

principle of minimizing total energy is used to determine the natural frequencies and mode shapes. For laminated composite plates, the effect of transverse shear deformation has been taken into account for using various shear deformable theories [13-14]. Compared to free flexural vibrations, there are very few publications on free in-plane vibrations of composite plates. The first publication on the free in-plane vibration of composite plates was due to Woodcock et al. [15] who studied the effect of fiber orientation angle on the in-pane natural frequencies of single-layered composite plates. Later, Lorenzo [16] determined the free in-plane natural frequencies of single-layered generally-orthotropic laminate and symmetrically laminated composite plates with clamped and free boundary conditions.

In this chapter, free flexural and extensional vibration responses of composite sandwich plates with corrugated construction are studied. For the composite face pates and webs, the first order shear deformation is assumed. Shear deformation of the core and rotary inertia of the faces and webs are also considered. Vibration responses are determined in terms of natural frequencies and mode shapes. Various core configurations ranging from triangular core to rectangular core are considered. The laminate constructions in the faces and the webs are $(\pm\alpha)_s$ and $(0/\alpha)_s$. The fiber orientation angle α in these laminates is varied to determine its effect on the natural frequencies. The effects of geometric parameters, such as face and web thickness, pitch and face center distance, are also examined.

3.2 ANALYTICAL FORMULATION

Hamilton's principle is applied in this study to develop the analytical formulation for the determination of global free vibration response of composite sandwich plates with corrugated core. According to this principle, the vibratory motion of a plate is governed by the minimization of the following Hamiltonian integral.

$$H = \int (T - U + W)dt \tag{3.1}$$

where, T is the kinetic energy of the plate, U is the elastic strain energy of the plate and W is the work done by the external loads acting on the plate. The kinetic energy of the plate includes both translational and rotary inertia components, both of which are considered in

this research. The minimization of the Hamiltonian integral H is obtained by taking the time derivative of Equation (3.1) and setting it equal to zero, i.e.,

$$\delta(H) = 0 \tag{3.2}$$

In this research, the corrugated-core sandwich plate is first transformed into an equivalent homogenous plate. The expression for elastic strain energy, U, of the equivalent plate was developed in Chapter 2. For free vibration analysis, there are no external loads; therefore, the work done W is zero. The kinetic energy term has both translational and rotational components, which are developed in the following section.

3.2.1 Kinetic Energy of the Sandwich Plate

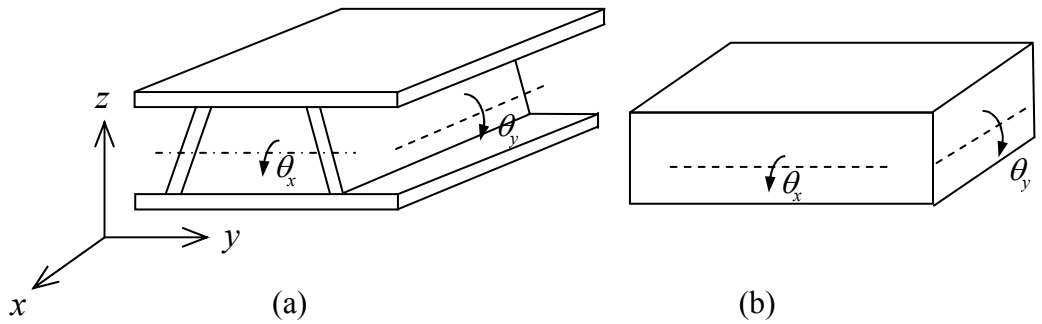

Figure 3.1: (a) Unit cell and (b) Equivalent homogenous plate

The total kinetic energy of the sandwich plate can be expressed as the sum of translational and rotational kinetic energies as given in Equation 3.3.

$$T = T_{translational} + T_{rotational} \tag{3.3}$$

In the calculation of translational kinetic energy, three translational degrees of freedom u, v and w are considered.

$$T_{translational} = \frac{1}{2}\int_{\Omega}\left\{P\left[\left(\frac{\partial u}{\partial t}\right)^2 + \left(\frac{\partial v}{\partial t}\right)^2 + \left(\frac{\partial w}{\partial t}\right)^2\right]\right\}dxdy$$

where, normal inertia P of the entire unit cell is the sum of normal inertia of each individual member in the unit cell as given below.

$$P = \rho\left(\frac{\left((a*b*t_{TF})+(a*b*t_{BF})+n*(a*s*t_c)\right)}{(a*b)}\right)$$

$$P = \rho\left(t_{TF}+t_{BF}+\frac{nst_c}{b}\right)$$

where, a and b = length and width of the plate

ρ = density of the material

n = number of webs in the unit cell

t_{TF} = thickness of the top face

t_{BF} = thickness of the bottom face

t_c = thickness of the webs

Rotational kinetic energy of sandwich construction for equivalent thick plate model is given as

$$T_{Eq} = \frac{1}{2}\int_{\Omega}\left\{\left[J_{Eq}\left(\frac{\partial\bar{\alpha}}{\partial t}\right)^2 + J_{Eq}\left(\frac{\partial\bar{\beta}}{\partial t}\right)^2\right]\right\}dxdy$$

where, $J_{Eq} = \rho_{Eq}\frac{d_c^3}{12}$ is the rotary inertia and equivalent density is given as $\rho_{Eq} = \frac{\rho\left(t_{TF}+t_{BF}+\frac{nst_c}{b}\right)}{d}$, calculated based on equivalent plate model given in Figure 3.1.

3.2.2 Calculation of Elastic Strain Energy of the Plate

The total elastic strain energy of the plate can be expressed as the sum of four strain energies as given in Equation (3.4).

$$U = U_S + U_B + U_{TS} + U_{BS} \tag{3.4}$$

where,

U_S, strain energy due to stretching, is given as

$$U_S = \frac{1}{2}\int_A \left\{ \begin{array}{l} A_{11}\left(\frac{\partial u_0}{\partial x}\right)^2 + 2A_{12}\frac{\partial u_0}{\partial x}\frac{\partial v_0}{\partial y} + 2A_{16}\frac{\partial u_0}{\partial x}\left(\frac{\partial u_0}{\partial y}+\frac{\partial v_0}{\partial x}\right) \\ +A_{22}\left(\frac{\partial v_0}{\partial y}\right)^2 + 2A_{26}\frac{\partial v_0}{\partial y}\left(\frac{\partial u_0}{\partial y}+\frac{\partial v_0}{\partial x}\right) + A_{66}\left(\frac{\partial u_0}{\partial y}+\frac{\partial v_0}{\partial x}\right)^2 \end{array} \right\} dA$$

U_B, strain energy due to bending, is given as

$$U_B = \frac{1}{2}\int_A \left\{ \begin{array}{l} D_{11}\left(\frac{\partial \overline{\alpha}}{\partial x}\right)^2 + 2D_{12}\frac{\partial \overline{\beta}}{\partial y}\frac{\partial \overline{\alpha}}{\partial x} + D_{22}\left(\frac{\partial \overline{\beta}}{\partial y}\right)^2 + D_{66}\left(\frac{\partial \overline{\alpha}}{\partial y}+\frac{\partial \overline{\beta}}{\partial x}\right)^2 \\ +2D_{16}\frac{\partial \overline{\alpha}}{\partial x}\left(\frac{\partial \overline{\alpha}}{\partial y}+\frac{\partial \overline{\beta}}{\partial x}\right) + 2D_{26}\frac{\partial \overline{\beta}}{\partial y}\left(\frac{\partial \overline{\alpha}}{\partial y}+\frac{\partial \overline{\beta}}{\partial x}\right) \end{array} \right\} dA$$

U_{TS}, strain energy due to transverse shearing is given as

$$U_{TS} = \frac{1}{2}\int_A \left\{ A_{44}\left(\overline{\beta}+\frac{\partial w}{\partial y}\right)^2 + A_{55}\left(\overline{\alpha}+\frac{\partial w}{\partial x}\right)^2 + 2A_{45}\left(\overline{\beta}+\frac{\partial w}{\partial y}\right)\left(\overline{\alpha}+\frac{\partial w}{\partial x}\right) \right\} dA$$

and, U_{BS}, strain energy due to bending and stretching coupling, is given as

$$U_{BS} = \int_A \left\{ \begin{array}{l} B_{11}\frac{\partial u_0}{\partial x}\frac{\partial \overline{\alpha}}{\partial x} + B_{12}\left[\frac{\partial u_0}{\partial x}\frac{\partial \overline{\beta}}{\partial y} + \frac{\partial v_0}{\partial y}\frac{\partial \overline{\alpha}}{\partial x}\right] \\ +B_{16}\left[\frac{\partial u_0}{\partial x}\left(\frac{\partial \overline{\alpha}}{\partial y}+\frac{\partial \overline{\beta}}{\partial x}\right) + \left(\frac{\partial u_0}{\partial y}+\frac{\partial v_0}{\partial x}\right)\frac{\partial \overline{\alpha}}{\partial x}\right] + B_{22}\frac{\partial v_0}{\partial y}\frac{\partial \overline{\beta}}{\partial y} \\ +B_{26}\left[\frac{\partial v_0}{\partial y}\left(\frac{\partial \overline{\alpha}}{\partial y}+\frac{\partial \overline{\beta}}{\partial x}\right) + \left(\frac{\partial u_0}{\partial y}+\frac{\partial v_0}{\partial x}\right)\frac{\partial \overline{\beta}}{\partial y}\right] + B_{66}\left[\left(\frac{\partial u_0}{\partial y}+\frac{\partial v_0}{\partial x}\right) + \left(\frac{\partial \overline{\alpha}}{\partial y}+\frac{\partial \overline{\beta}}{\partial x}\right)\right] \end{array} \right\} dA$$

In Equation (3.4), A_{ij}, B_{ij} and D_{ij} are extensional, extension-bending and bending stiffness terms of the homogenized plate with equivalent stiffness properties as the sandwich plate. These terms are derived in Chapter 2.

3.2.3 Calculation of Global Vibration Response using Hamilton's Principle

Following Equation (3.1) and substituting for T and U as given in Equation (3.3) and (3.4), respectively, the Hamiltonian integral can be written as

$$H=\int_A \left\{ \begin{array}{l} \frac{A_{11}}{2}\left(\frac{\partial u_0}{\partial x}\right)^2+A_{12}\frac{\partial u_0}{\partial x}\frac{\partial v_0}{\partial y}+A_{16}\frac{\partial u_0}{\partial x}\left(\frac{\partial u_0}{\partial y}+\frac{\partial v_0}{\partial x}\right)+\frac{A_{22}}{2}\left(\frac{\partial v_0}{\partial y}\right)^2+A_{26}\frac{\partial v_0}{\partial y}\left(\frac{\partial u_0}{\partial y}+\frac{\partial v_0}{\partial x}\right) \\ +\frac{A_{66}}{2}\left(\frac{\partial u_0}{\partial y}+\frac{\partial v_0}{\partial x}\right)^2+\frac{A_{44}}{2}\left(\bar{\beta}+\frac{\partial w}{\partial y}\right)^2+\frac{A_{55}}{2}\left(\bar{\alpha}+\frac{\partial w}{\partial x}\right)^2+A_{45}\left(\bar{\beta}+\frac{\partial w}{\partial y}\right)\left(\bar{\alpha}+\frac{\partial w}{\partial x}\right) \\ +B_{11}\frac{\partial u_0}{\partial x}\frac{\partial \bar{\alpha}}{\partial x}+B_{12}\left[\frac{\partial u_0}{\partial x}\frac{\partial \bar{\beta}}{\partial y}+\frac{\partial v_0}{\partial y}\frac{\partial \bar{\alpha}}{\partial x}\right]+B_{16}\left[\frac{\partial u_0}{\partial x}\left(\frac{\partial \bar{\alpha}}{\partial y}+\frac{\partial \bar{\beta}}{\partial x}\right)+\left(\frac{\partial u_0}{\partial y}+\frac{\partial v_0}{\partial x}\right)\frac{\partial \bar{\alpha}}{\partial x}\right] \\ +B_{22}\frac{\partial v_0}{\partial y}\frac{\partial \bar{\beta}}{\partial y}+B_{26}\left[\frac{\partial v_0}{\partial y}\left(\frac{\partial \bar{\alpha}}{\partial y}+\frac{\partial \bar{\beta}}{\partial x}\right)+\left(\frac{\partial u_0}{\partial y}+\frac{\partial v_0}{\partial x}\right)\frac{\partial \bar{\beta}}{\partial y}\right]+B_{66}\left[\left(\frac{\partial u_0}{\partial y}+\frac{\partial v_0}{\partial x}\right)+\left(\frac{\partial \bar{\alpha}}{\partial y}+\frac{\partial \bar{\beta}}{\partial x}\right)\right] \\ +\frac{D_{11}}{2}\left(\frac{\partial \bar{\alpha}}{\partial x}\right)^2+\frac{D_{12}}{2}\frac{\partial \bar{\beta}}{\partial y}\frac{\partial \bar{\alpha}}{\partial x}+\frac{D_{22}}{2}\left(\frac{\partial \bar{\beta}}{\partial y}\right)^2+\frac{D_{66}}{2}\left(\frac{\partial \bar{\alpha}}{\partial y}+\frac{\partial \bar{\beta}}{\partial x}\right)^2+D_{16}\frac{\partial \bar{\alpha}}{\partial x}\left(\frac{\partial \bar{\alpha}}{\partial y}+\frac{\partial \bar{\beta}}{\partial x}\right) \\ +D_{26}\frac{\partial \bar{\beta}}{\partial y}\left(\frac{\partial \bar{\alpha}}{\partial y}+\frac{\partial \bar{\beta}}{\partial x}\right)+P\left[\left(\frac{\partial u}{\partial t}\right)^2+\left(\frac{\partial v}{\partial t}\right)^2+\left(\frac{\partial w}{\partial t}\right)^2\right]+\frac{1}{2}\left[J_{Eq}\left(\frac{\partial \bar{\alpha}}{\partial t}\right)^2+J_{Eq}\left(\frac{\partial \bar{\beta}}{\partial t}\right)^2\right]-p^*w \end{array} \right\} dA \quad (3.5)$$

There are no external loads when free vibration is considered. Thus, the last term in Equation (3.5), which represents the work done by the external loads, is equal to zero.

The general solutions for translational displacement components u, v, w and rotational components $\bar{\alpha}$ and $\bar{\beta}$ under simply supported boundary conditions on all edges are assumed by Fourier series given in Equation 3.6.

$$\begin{aligned} u_0(x,y) &= \sum_{m=1}^{M}\sum_{n=1}^{N} U_{mn}\sin\left(\frac{m\pi x}{a}\right)\cos\left(\frac{n\pi y}{b}\right)e^{i\omega t} \\ v_0(x,y) &= \sum_{m=1}^{M}\sum_{n=1}^{N} V_{mn}\cos\left(\frac{m\pi x}{a}\right)\sin\left(\frac{n\pi y}{b}\right)e^{i\omega t} \\ w(x,y) &= \sum_{m=1}^{M}\sum_{n=1}^{N} W_{mn}\sin\left(\frac{m\pi x}{a}\right)\sin\left(\frac{n\pi y}{b}\right)e^{i\omega t} \\ \bar{\alpha}(x,y) &= \sum_{m=1}^{M}\sum_{n=1}^{N} RTX_{mn}\cos\left(\frac{m\pi x}{a}\right)\sin\left(\frac{n\pi y}{b}\right)e^{i\omega t} \\ \bar{\beta}(x,y) &= \sum_{m=1}^{M}\sum_{n=1}^{N} RTY_{mn}\sin\left(\frac{m\pi x}{a}\right)\cos\left(\frac{n\pi y}{b}\right)e^{i\omega t} \end{aligned} \quad (3.6)$$

In Equation (3.6) there are five unknown Fourier coefficients, which are calculated using the principle of minimum total energy as given in Equation 3.7.

$$\delta(H) = 0 \tag{3.7}$$

which leads to partial differentiations with respect to the unknown Fourier coefficients as given in Equation 3.8.

$$\frac{\partial(H)}{\partial Umn} = 0,\ \frac{\partial(H)}{\partial Vmn} = 0,\ \frac{\partial(H)}{\partial Wmn} = 0,\ \frac{\partial(H)}{\partial RTXmn} = 0,\ \frac{\partial(H)}{\partial RTYmn} = 0 \tag{3.8}$$

By using MATLAB symbolic variables, a code has been written to solve the five equations in Equation 3.8 for the five unknowns. The MATLAB code is given in Appendix A3.

3.3 FLEXURAL MODES

Based on the above formulation, global free vibration response characteristics of sandwich composite plates with corrugated core are determined and presented here for four case studies. The unit cell in the corrugated sandwich plate is shown in Figure 3.2. It is assumed that the top and bottom faces have the same thickness so that $t_{TF} = t_{BF} = t_F$ The geometric parameters considered in this study are face center distance (d), pitch ($2p$), face thickness (t_F) and web thicknesses (t_c). The web inclination angle, which depends on these parameters, varies from $\theta_{\min}$ for the triangular core to $\theta_{\max}$= 90º for the rectangular core. The material in the faces and the webs is a four-layered symmetric carbon fiber

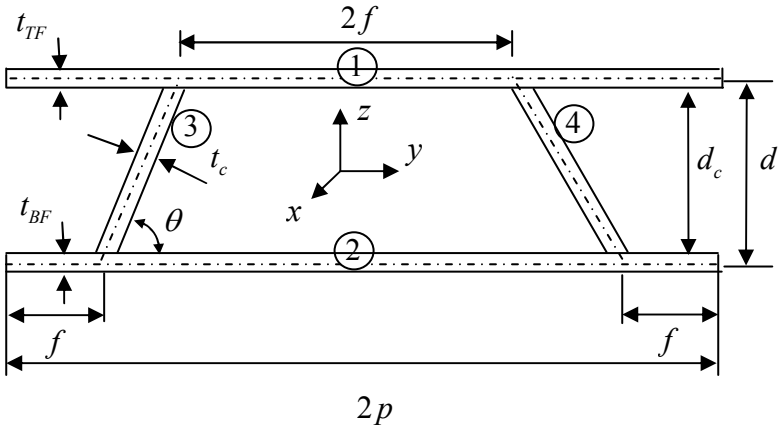

Figure 3.2: Unit cell in a corrugated-core sandwich plate

reinforced epoxy composite laminate. The basic properties of the composite material are $E_{11} = 138$ GPa, $E_{22} = 9$ GPa, $\nu_{12} = 0.3$, $G_{12} = 6.9$ GPa and $\rho = 1700$ kg/m^3. A square plate of 640 mm in length and 640 mm in width is considered. The plate is simply supported on all four edges. In all case studies, the cross-sectional area of the sandwich plate is maintained constant so that the effects of the geometric variables and laminate construction can be directly compared. The four case studies considered here are as follows.

(a) Case Study 1: Both faces and webs have the same thickness, i.e. $t_{TF} = t_{BF} = t_c = t$. The pitch is 160 mm and the depth is 80 mm, so that $p/d = 1$.

(b) Case study 2: Face thickness is 1 mm, i.e., $t_{TF} = t_{BF} = 1$ mm, but the web thickness, t_c, is varied. The pitch is 160 mm and the depth is 80 mm, so that $p/d = 1$.

(c) Case study 3: Face thickness is 1 mm, i.e., $t_{TF} = t_{BF} = 1$ mm, but the web thickness, t_c, is varied. The depth is 80 mm, but the pitch is varied from 40 to 640 mm at five different levels so that $p/d = 0.25$, 0.5, 1, 2 and 4.

(d) Case Study 4: Face thickness is 1 mm, i.e., $t_{TF} = t_{BF} = 1$ mm, but the web thickness, t_c, is varied. The pitch is 160 mm, but the depth is varied from 20 to 80 mm at five different levels so that $p/d = 1$, 1.33, 2 and 4.

The effect of laminate construction is considered in the first two case studies. Two different four-layered symmetric laminates are selected, namely $(0/\alpha)_s$ and $(\pm\alpha)_s$, where α is the fiber orientation angle with respect to the longitudinal axis (x) of the plate. The fiber orientation angle is varied from 0 to 90º in steps of 15º to observe the effect of fiber orientation angle on the free vibration response of corrugated-core sandwich plates. In the third and fourth case studies, the laminate constructions are $(0/90)_s$ and $(\pm 90)_s$.

3.3.1 Flexural Mode Shapes

Figure 3.3 shows the global flexural mode shapes of sandwich plates in which the web inclination angle θ = 90º, $t_{TF} = t_{BF} = t_c = 1$ mm, $p = d = 80$ mm, and the laminate construction is $(0/90)_s$. Similar mode shapes are observed for other sandwich plates. In the case of m = 1 and n = 1, we can observe the first flexural mode, which is also the fundamental mode. It consists of a single half sine wave in both x and y directions. In the

case of m = 1 and n = 2, we can observe a full sine wave in the x-direction and two half sine waves in the y-direction. Higher order mode shapes corresponding to several other m and n combinations are also shown in Figure 3.3.

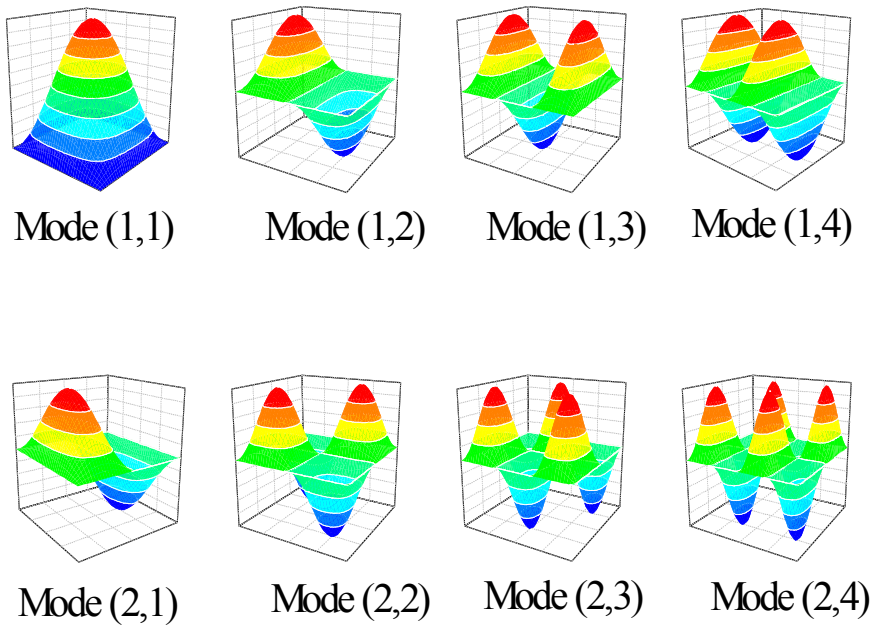

Figure 3.3: Flexural modes shapes of sandwich plates

3.3.2 Case Study 1: $t_{TF} = t_{BF} = t_c = t$ and $p = d = 80$ mm

In Case Study 1, the face and web thicknesses are assumed to be equal, i.e., $t_{TF} = t_{BF} = t_C = t$ and the unit cell dimensions p and d are assumed to be 80 mm each. Since the pitch, $2p$, is 160 mm and the plate width is 640 mm, the plate contains four unit cells. The cross-sectional area of the unit cell with rectangular core, i.e., A_{90}, is 478 mm^2. For the other plates with web inclination angle lower than 90^o, the cross-sectional area A_θ is assumed to be equal to A_{90}. In order to maintain the same cross-sectional area of the

unit cell at various web inclination angles, the thickness t is varied using Equation (2.10) given in Chapter 2, which is obtained by setting $A_0 = A_{90}$.

3.3.2.1 Stiffness Terms

Stiffness terms of the sandwich plates with web inclination angle $\theta = 45°$, $48°$ and $90°$ for different fiber orientation angles in the $(\pm\alpha)_s$ laminate construction are given in Figure 3.4. Both flexural stiffness D_{11} and transverse shear stiffness A_{44} decrease with increasing α, whereas flexural stiffness D_{22} increases with increasing α. On the other hand, flexural stiffness D_{12} and D_{66} as well as transverse shear stiffness A_{55} increase with increasing α from a minimum value at $\alpha = 0°$ to a maximum value at $\alpha = 45°$, and then decrease to the minimum value at $\alpha = 90°$.

It can also be noted in Figure 3.4 that the web inclination angle θ has a very small influence on D_{11}, D_{22}, D_{12} and D_{66}. On the other hand, θ has a large influence on A_{44} as it is increased from 45 to 48^o. The influence of θ on A_{55} is also very significant, but only between θ equal to 48 and 90^o. The difference between A_{44} values for $\theta = 45^o$ and 90^o is the largest when $\alpha = 0^o$, while the difference between A_{55} values for $\theta = 45^o$ and 90^o is the largest when $\alpha = 45^o$.

Figure 3.5 shows the variation of stiffness terms with increasing fiber orientation angle α for the $(0/\alpha)_s$ laminate construction, which is similar that observed in Figure 3.4 for the $(\pm\alpha)_s$ laminate construction. Both D_{11} and A_{44} decrease with increasing α, whereas D_{22} increases with increasing α. However, unlike the $(\pm\alpha)_s$ laminates, the reduction in A_{44} with increasing α is relatively small. The other stiffness terms, such as D_{12}, D_{66} and A_{55} decrease with increasing α. Comparing Figures 3.4 and 3.5, it can be observed that both D_{11} and A_{44} are higher for $(0/\alpha)_s$ laminates compared to $(\pm\alpha)_s$ laminates, but D_{22}, D_{12}, D_{66} and A_{55} are lower for the $(0/\alpha)_s$ laminates compared to the $(\pm\alpha)_s$ laminates. This is due to the presence of 0^o layers on the top and bottom surfaces of the $(0/\alpha)_s$ laminates.

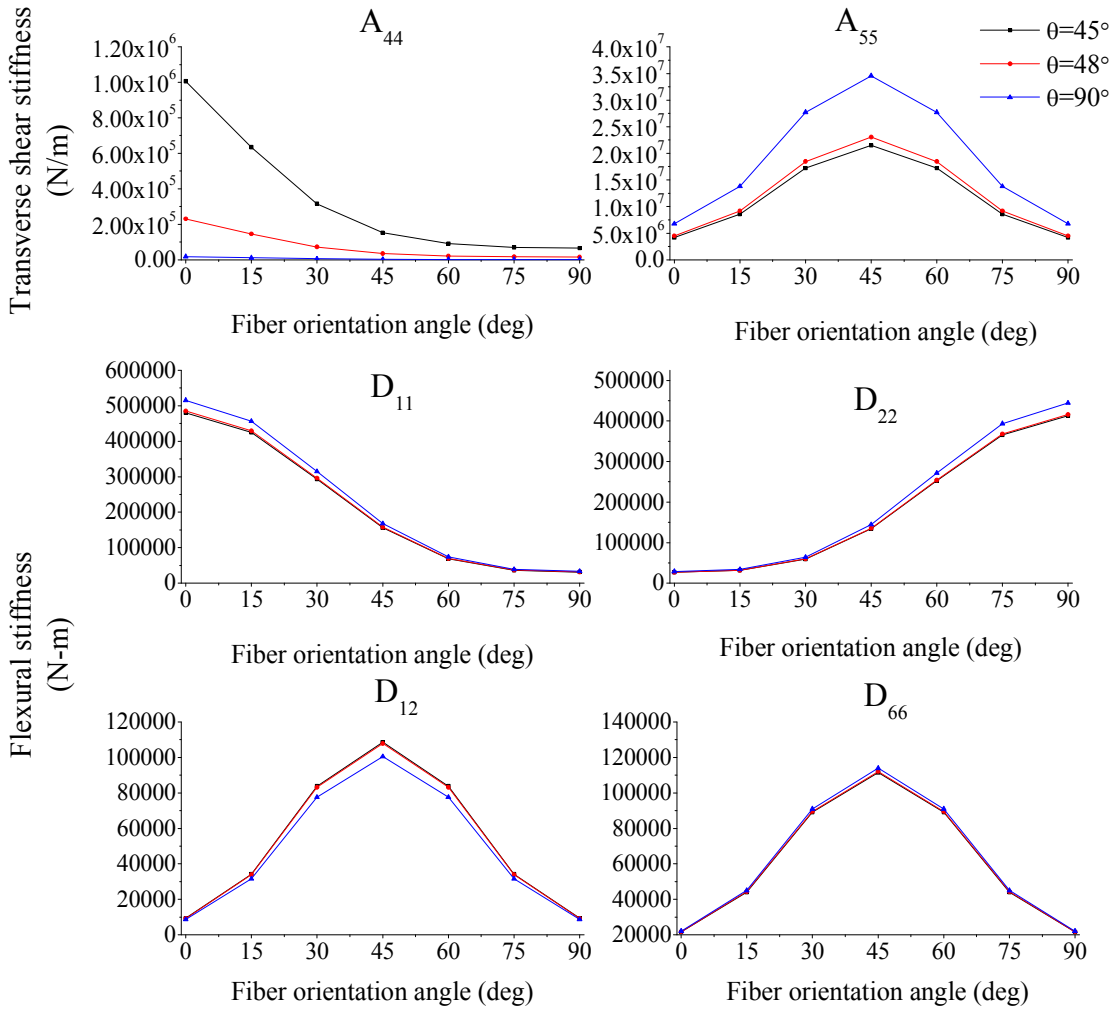

Figure 3.4: Stiffness terms for the sandwich plates with web inclination angles $\theta = 45^{\circ}$, 48º and 90º and $(0/\alpha)_s$ laminate construction

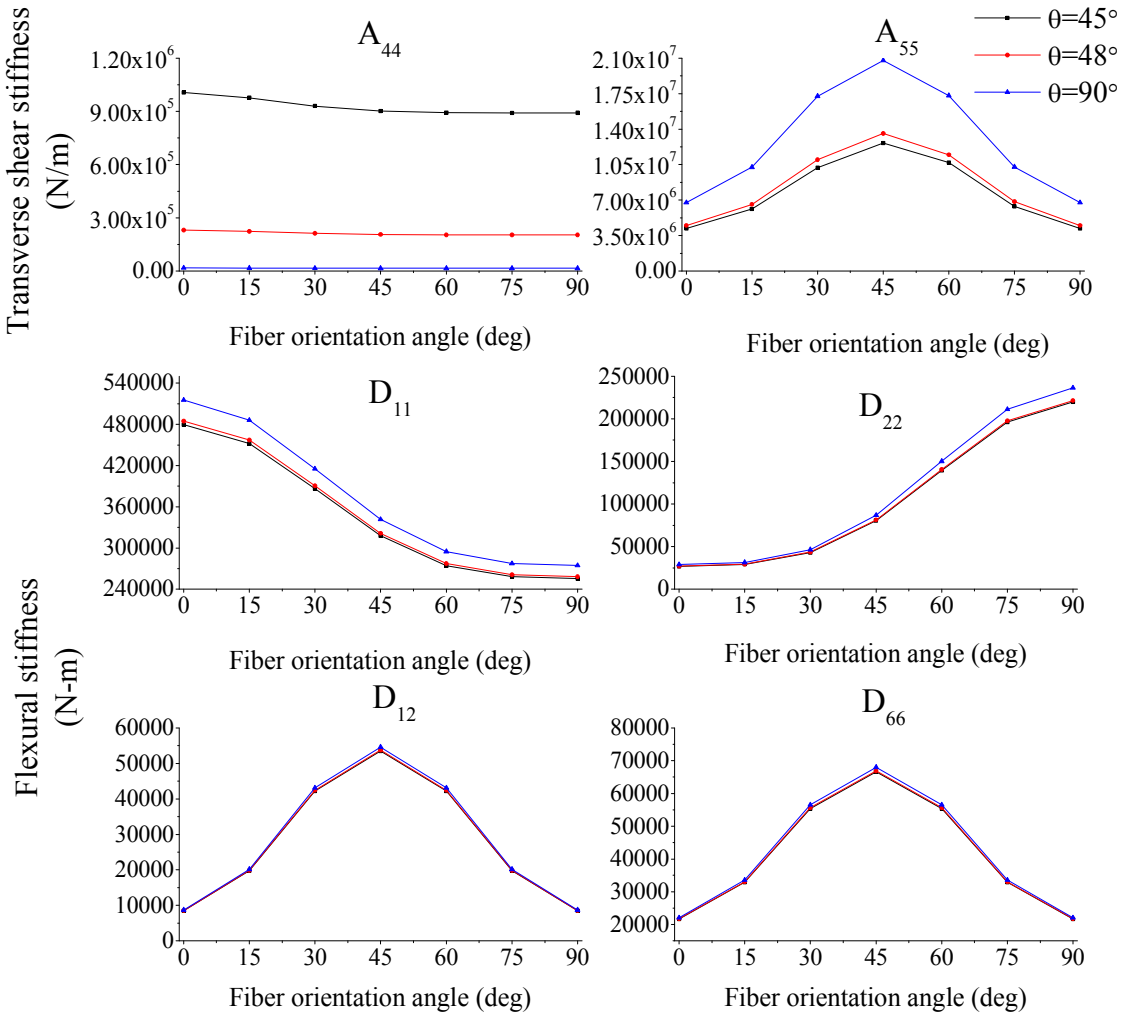

Figure 3.5: Stiffness terms for the sandwich plates with web inclination angles θ = 45º, 48º and 90º and $(\pm\alpha)_s$ laminate construction

3.3.2.2 Natural Frequencies

(a) $(\pm\alpha)_s$ laminates in faces and webs

Natural frequencies of sandwich plates in (1,1) flexural mode are plotted in Figure 3.6 as a function of web inclination angle θ. It is observed that for each fiber orientation angle, (1,1) natural frequency has the maximum value at $\theta = 46°$ and the minimum value at $\theta = 48°$. For $\theta = 48°$ to 90°, it increases with increasing web inclination angle. Figure 3.6 also shows that the (1, 1) flexural frequencies have their

highest values when $\alpha = 15°$, i.e., with the $(\pm 15)_s$ laminate, and the lowest values when $\alpha = 90°$, i.e. with the $(\pm 90)_s$ laminate.

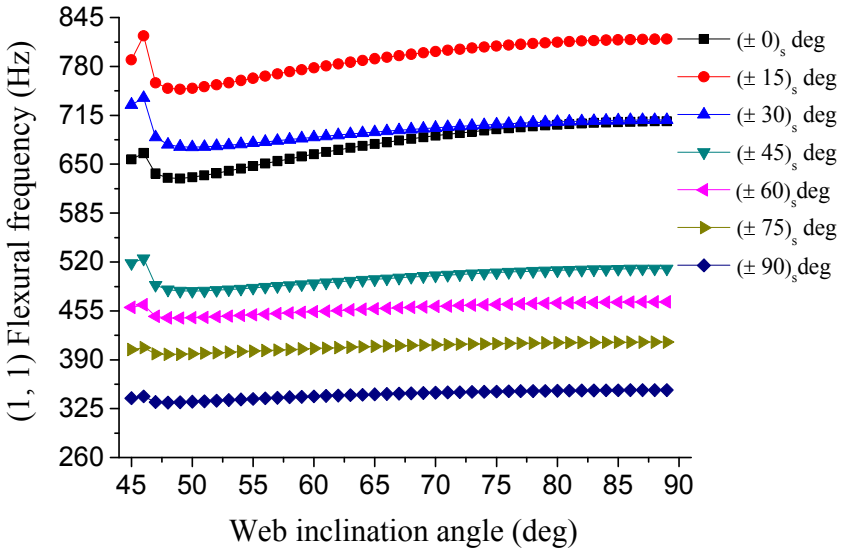

Figure 3.6: Natural frequencies of sandwich plates with $(\pm\alpha)_s$ laminate construction in faces and webs in (1, 1) flexural mode

Natural frequencies in flexural modes (1,*n*) with web inclination angles $\theta = 45°$, 48° and 90° are plotted in Figure 3.7 as a function of fiber orientation angle α. At θ = 45°, the natural frequency at lower flexural modes, such as (1,1) and (1,2), increases slightly as α is increased from 0 to 15°; but at α > 15°, it decreases with increasing α. At higher flexural modes, the natural frequency does not show a peak; instead it decreases with increasing α as it is increased from 0 to 90°. For web inclinations 48 and 90°, natural frequency at all flexural modes first increases with increasing α, reaches the highest value at α = 45° and then decreases. It is also noteworthy that at α = 0°, natural frequencies for different flexural modes are closer to each other when the web inclination angle is 90° and are spread over a large range when the web inclination angle is 45°.

Natural frequencies at flexural modes (2, *n*) of sandwich plates with web inclination $\theta = 45°$, 48° and 90° are shown in Figure 3.8. For these modes, a peak in

natural frequencies is observed at $\alpha = 45°$ for all three web inclination angles. Here also, at $\alpha = 0^o$, natural frequencies at different flexural modes are closer to each other when the web inclination angle is 90^o and are spread over a large range when the web inclination angle is 45^o.

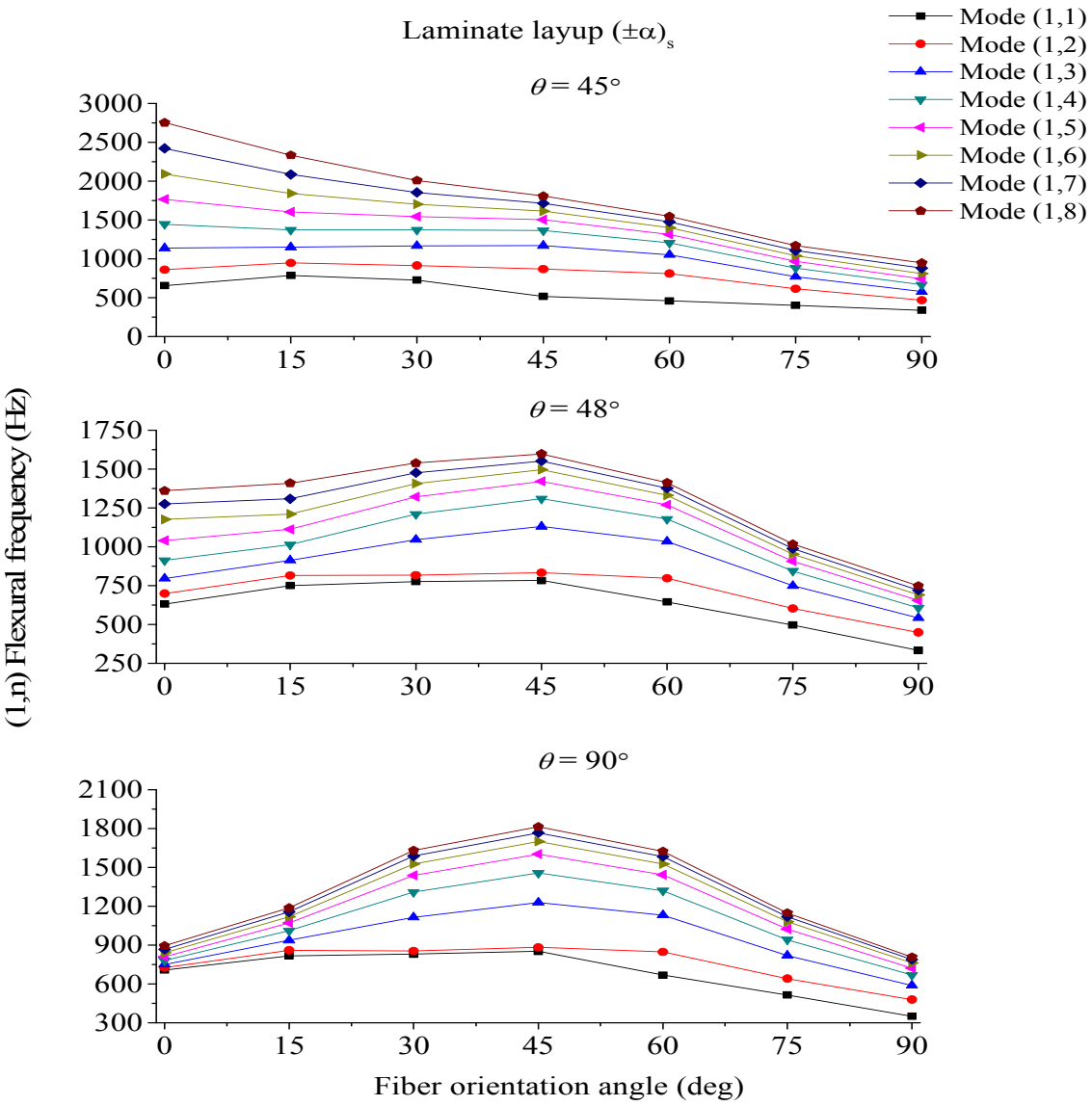

Figure 3.7: Natural frequencies of sandwich plates in (1,*n*) flexural modes. The laminate construction in both faces and webs is $(\pm\alpha)_s$ and the web inclination angles are 45º (top), 48º (middle) and 90º (bottom)

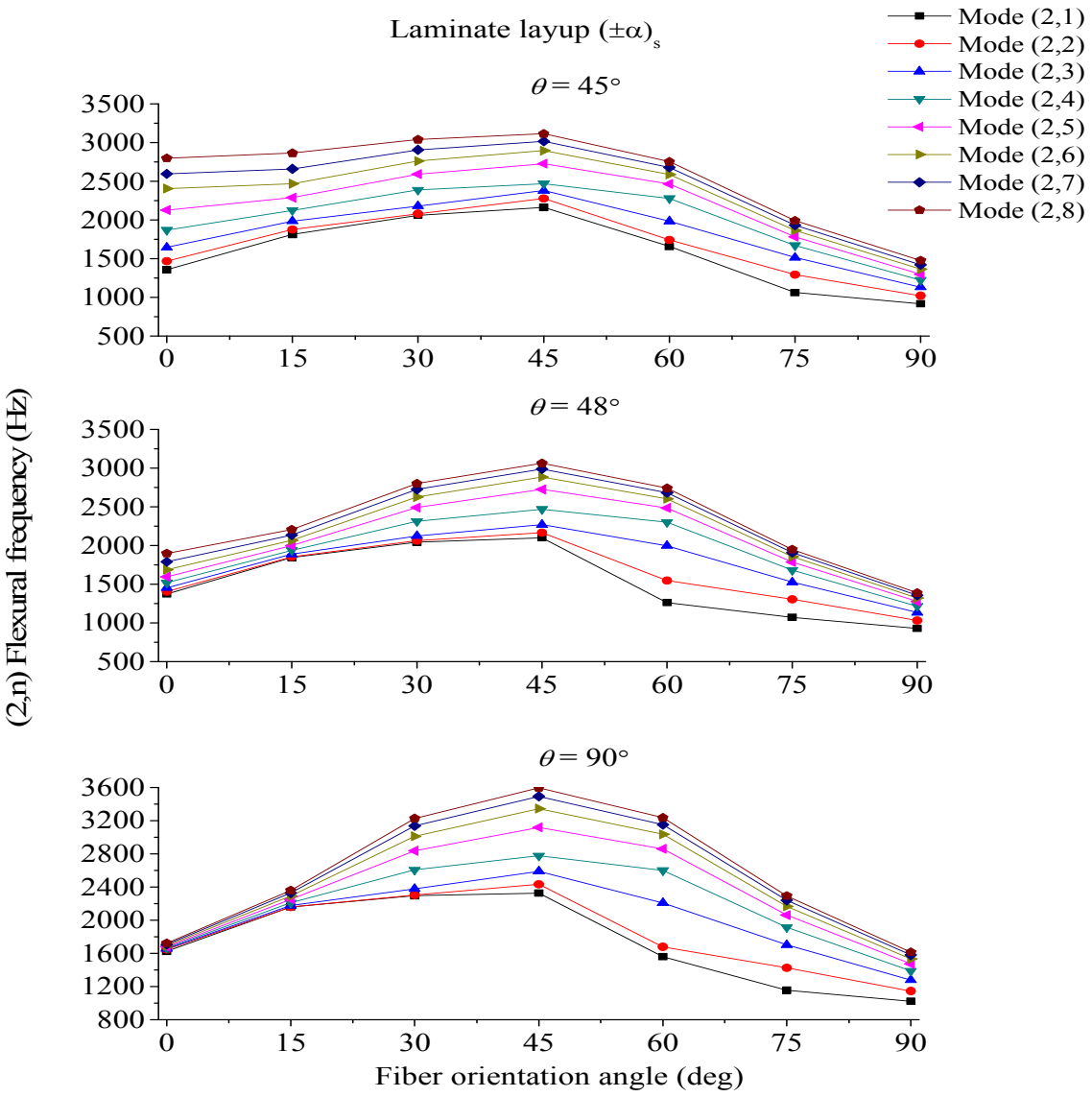

Figure 3.8: Natural frequencies of sandwich plates in (2, *n*) flexural modes. The laminate construction in both faces and webs is $(\pm\alpha)_s$ and the web inclination angles are 45º (top), 48º (middle) and 90º (bottom)

(b) $(0/\alpha)_s$ laminates in faces and webs

Natural frequencies in flexural mode (1,1) of sandwich plates made of $(0/\alpha)_s$ laminates in the faces and webs are plotted in Figure 3.9 as a function of web inclination angle θ. As with $(\pm\alpha)_s$ laminates, the (1,1) natural frequencies have the maximum value

at $\theta = 46°$ and the minimum value at $\theta = 48°$. As for the effect of fiber orientation angle α, natural frequency in (1,1) flexural mode increases with increase in α until the maximum value is reached at $\alpha = 30°$ and then decreases to a minimum value at fiber orientation angle $\alpha = 90°$.

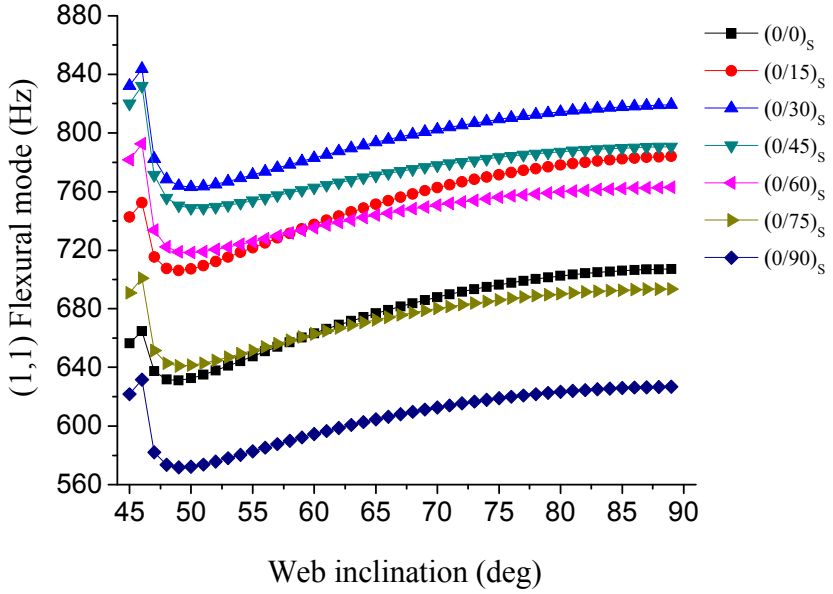

Figure 3.9: Natural frequencies of sandwich plates with $(0/\alpha)_s$ laminate construction in faces and webs in (1, 1) flexural mode

Natural frequencies in flexural modes (1,*n*) and (2,*n*) of sandwich plates with web inclination angles $\theta = 45°$, 48° and 90° are plotted in Figure 3.9 and Figure 3.10, respectively, as a function of fiber orientation angle α. It is observed that for all three web inclination angles, natural frequencies increase with increasing α, reach a peak, which for most modes is at $\alpha = 45°$, and then decrease with increasing α. The natural frequencies in various modes are closer to each other for $\theta = 90^o$ than for $\theta = 45$ and 48^o.

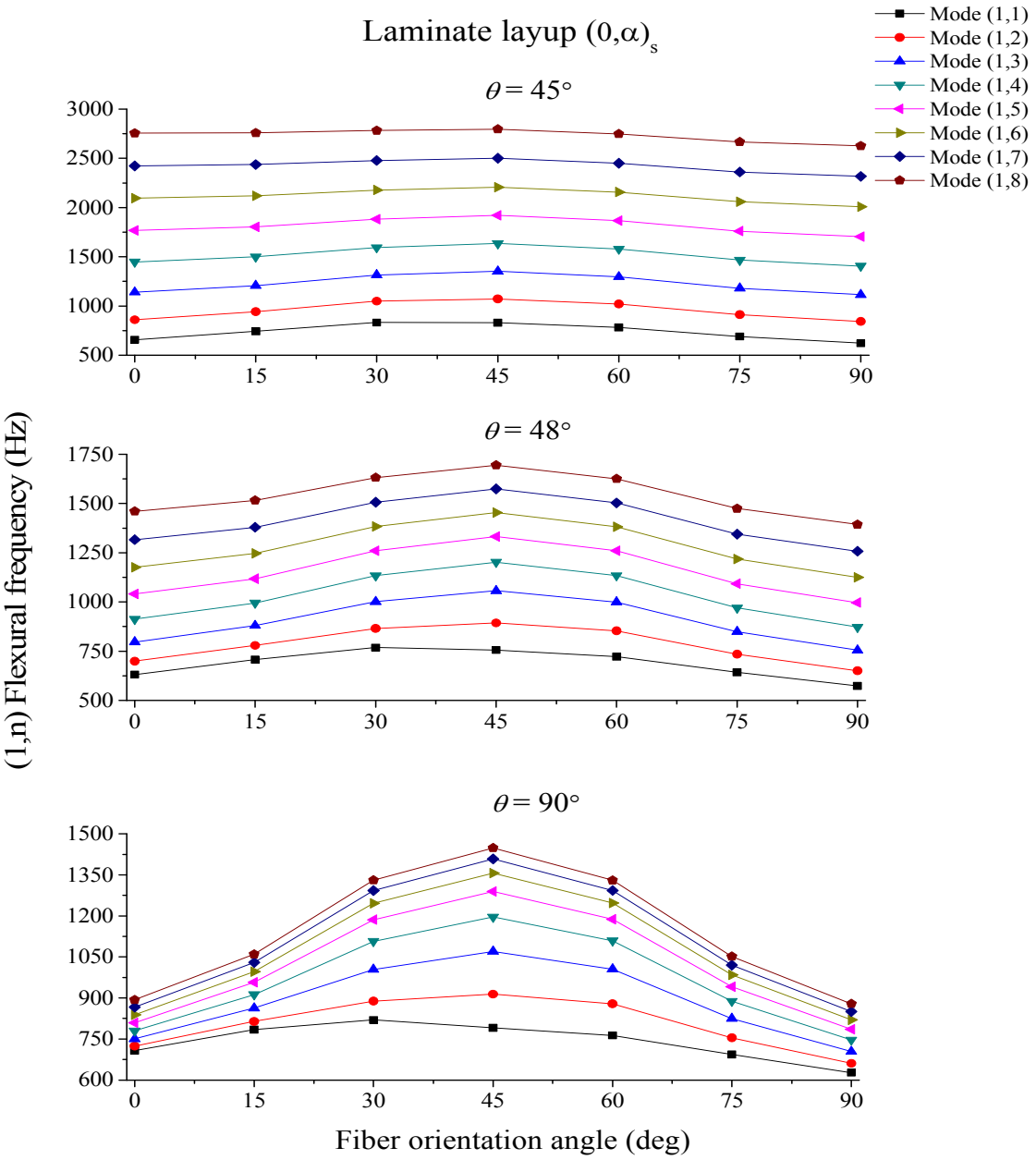

Figure 3.10: Natural frequencies of sandwich plates in (1, *n*) flexural modes. The laminate construction in both faces and webs is $(0/\alpha)_s$ and the web inclination angles are 45º (top), 48º (middle) and 90º (bottom)

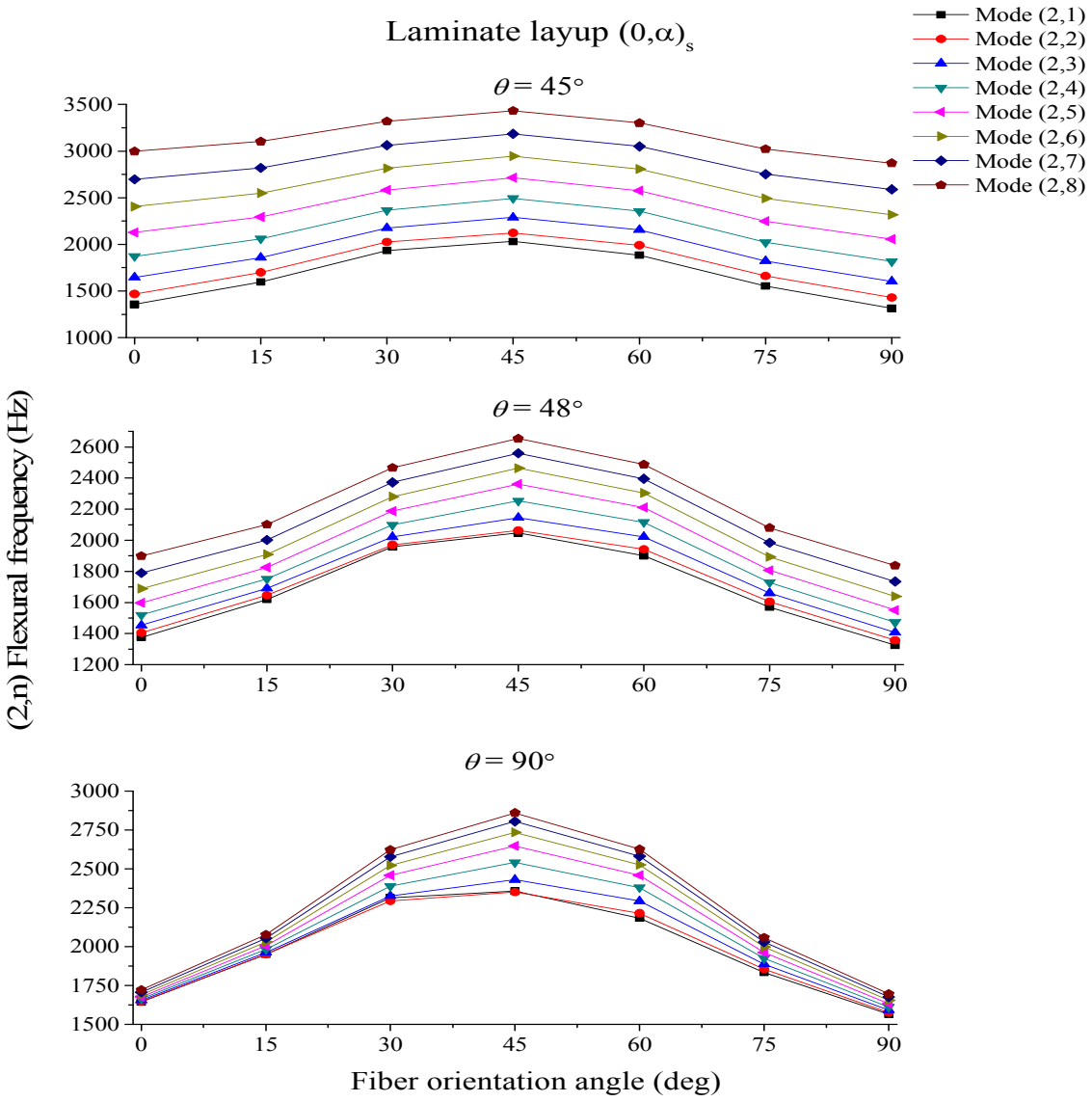

Figure 3.11: Natural frequencies of sandwich plates in (2, *n*) flexural modes. The laminate construction in both faces and webs is $(0/\alpha)_s$ and the web inclination angles are 45º (top), 48º (middle) and 90º (bottom)

3.3.3 Case Study 2: $t_{TF} = t_{BF} = 1$ mm, $t_c \leq 1$ mm and $p = d = 80$ mm

In Case Study 1, the web thickness was assumed to be equal to the face thickness. In this case study, $t_{TF} = t_{BF} = 1$ mm, and as in Case Study 1, $p = d = 80$ mm; but the web thickness is varied using the relationship $t_c = t_{90^\circ} \sin\theta$ to maintain a constant cross-sectional area of 478 mm^2. As the web inclination angle is varied from 45^o to 90^o, the

web thickness increases from its lowest value of 0.707 mm to its highest value of 1 mm. As shown in Figure 2.15 in Chapter 2, except for $\theta = 90^o$, the web thickness in Case Study 2 is lower than that in Case Study 1.

3.3.3.1 Stiffness terms

Stiffness terms of sandwich plates with laminate constructions $(\pm\alpha)_s$ and $(0/\alpha)_s$ in the faces and webs are shown in Figure 3.12 and Figure 3.13, respectively. The web inclination angles in these figures are 45, 48 and 90^o. The variation of stiffness terms with fiber orientation angle is similar to that shown in Figure 3.4 and Figure 3.5 for Case Study 1. However, in Case Study 2, the face thickness is 1 mm for all sandwich plates, whereas in Case Study 1, the face thickness is lower than 1 mm for all but the rectangular core (with $\theta = 90^o$). A comparison of stiffness terms listed in Table 3.1 and shows that for $\theta = 45$ and 48^o, D_{11}, D_{22}, D_{12} and D_{66} are higher for Case Study 2. For $\theta = 90^o$, D_{11}, D_{22}, D_{12} and D_{66} are the same for both case studies. For $\theta = 45$ and 48^o, the transverse shear stiffness A_{55} is greater for Case Study 1, except at $\theta = 90^o$ where A_{55} has the same value for both case studies. The other shear stiffness, A_{44}, has a higher value for Case Study 2 at $\theta = 45^o$, but a lower value at $\theta = 48^o$. At $\theta = 90^o$, A_{44} has the same value for both case studies.

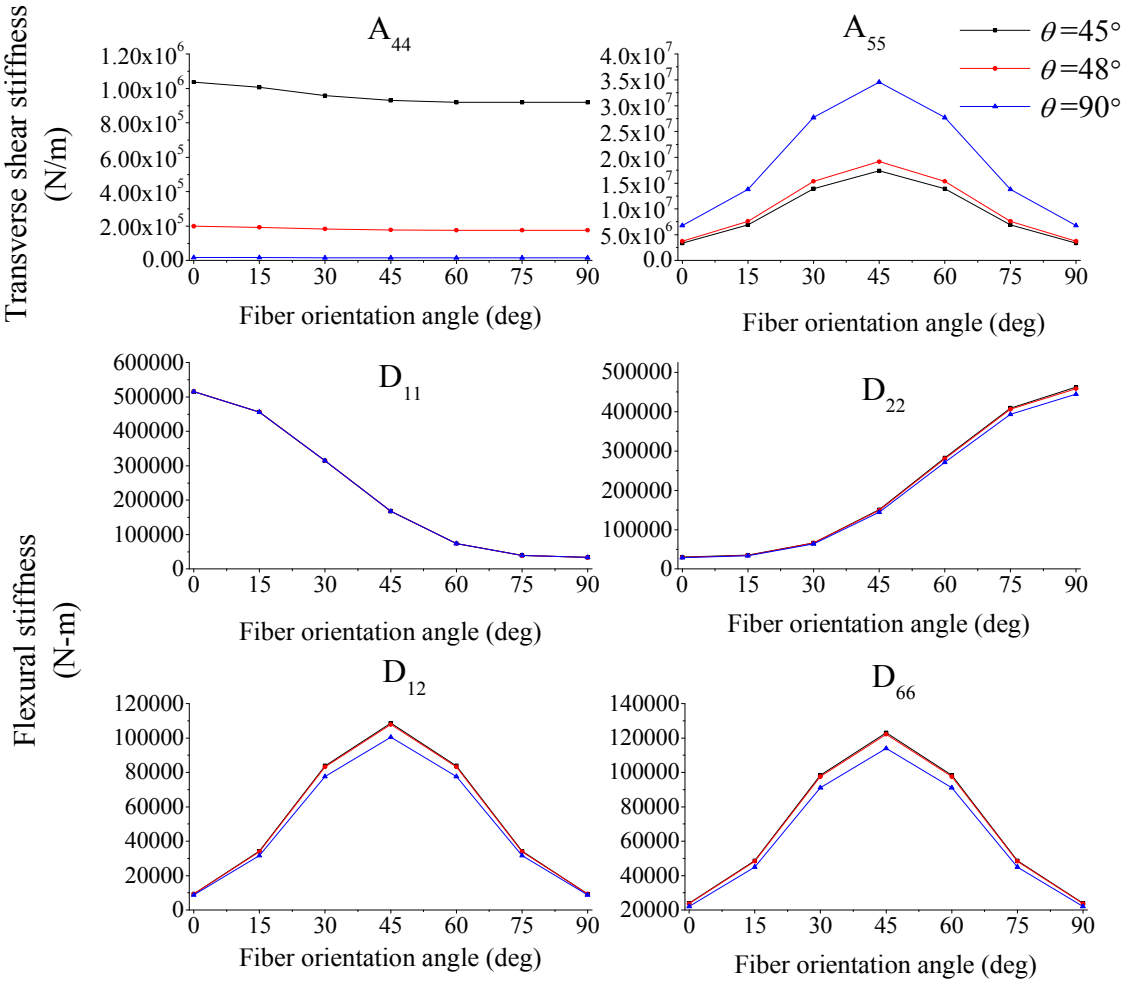

Figure 3.12: Stiffness terms for the sandwich plates with web inclination angles θ = 45º, 48º and 90º and $(0/\alpha)_s$ laminate construction

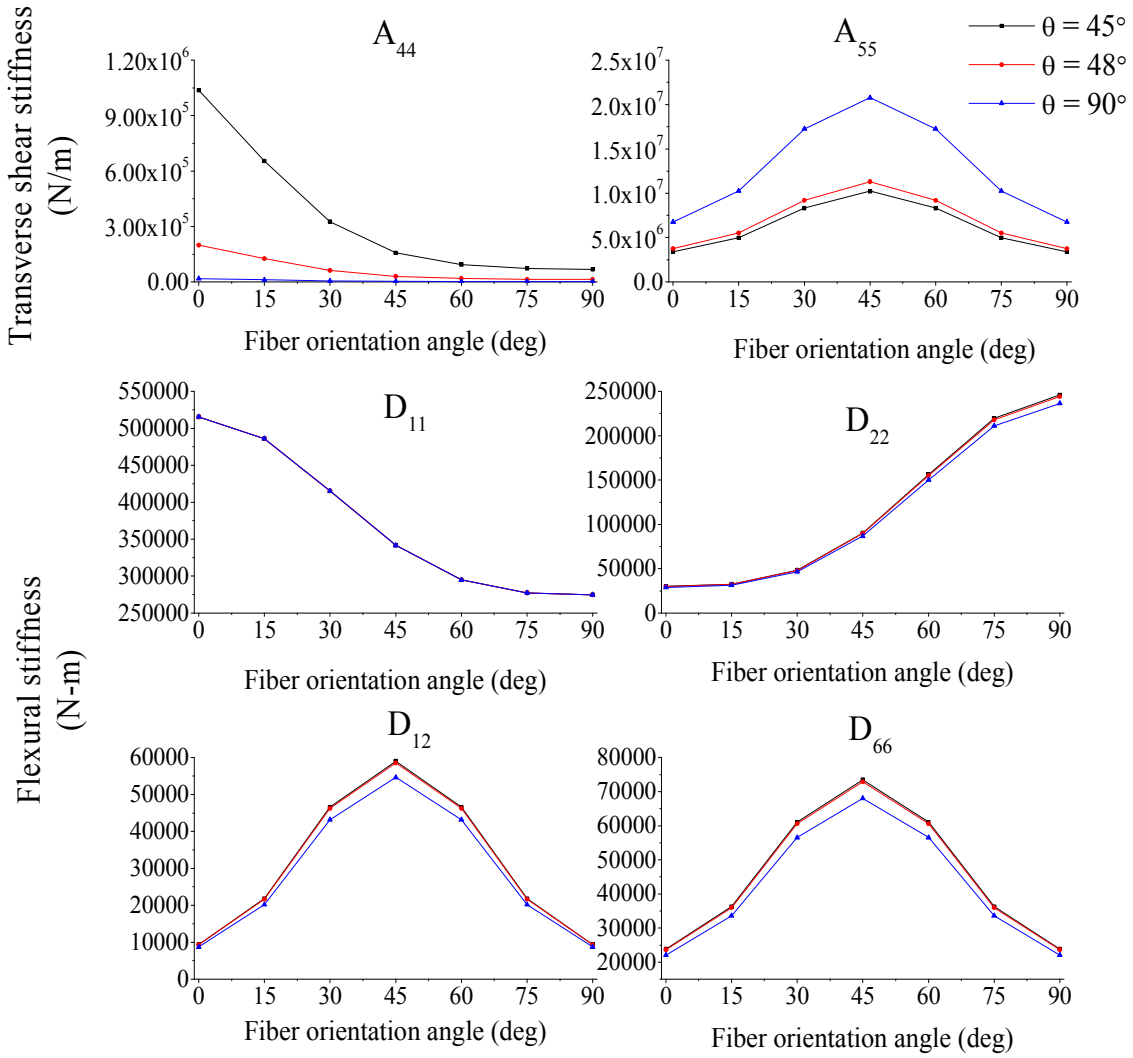

Figure 3.13: Stiffness terms for the sandwich plates with web inclination angles θ = 45º, 48º and 90º and $(\pm\alpha)_s$ laminate construction

Table 3.1: Comparison of stiffness terms of sandwich plates in Case Studies (CS) 1 and 2 with $(\pm\alpha)_s$ laminate construction

(1)	(2)	D_{11} (1E5) (N-m)		D_{22} (1E5) (N-m)		D_{12} (1E4) (N-m)		D_{66} (1E4) (N-m)	
α	θ	CS 1	CS 2	CS 1	CS 2	CS 1	CS 2	CS 1	CS 2
	45	4.79	5.15	2.69	3.01	0.93	0.93	0.21	0.23
	48	4.84	5.15	2.71	2.99	0.93	0.93	0.21	0.23
0	90	5.15	5.15	2.89	2.89	0.86	0.86	0.22	0.22
	45	4.24	4.56	3.14	3.51	0.34	0.34	0.44	0.48
	48	4.29	4.56	3.16	3.49	0.33	0.33	0.44	0.48
15	90	4.56	4.56	3.38	3.38	0.31	0.31	0.45	0.45
	45	2.93	3.15	5.93	6.64	0.83	0.83	0.89	0.98
	48	2.96	3.15	5.97	6.59	0.83	0.83	0.89	0.97
30	90	3.15	3.15	6.38	6.38	0.77	0.77	0.90	0.90
	45	1.56	1.67	1.34	1.50	1.08	1.08	1.11	1.20
	48	1.57	1.67	1.35	1.49	1.07	1.07	1.12	1.22
45	90	1.67	1.67	1.44	1.44	1.00	1.00	1.13	1.13
	45	6.89	7.41	2.52	2.82	0.83	0.83	0.89	0.98
	48	6.97	7.41	2.54	2.80	0.83	0.83	0.89	0.97
60	90	7.41	7.41	2.71	2.71	0.77	0.77	0.90	0.90
	45	3.65	3.92	3.65	4.09	0.34	0.34	0.44	0.48
	48	3.69	3.92	3.68	4.06	0.33	0.33	0.44	0.48
75	90	3.92	3.92	3.93	3.93	0.31	0.31	0.45	0.45
	45	3.12	3.36	4.12	4.62	0.93	0.93	0.21	0.23
	48	3.16	3.36	4.15	4.58	0.93	0.93	0.21	0.23
90	90	3.36	3.36	4.44	4.44	0.86	0.86	0.22	0.22

(1) α = Fiber Orientation Angle (in degrees)

(2) θ = Web Inclination Angle (in degrees)

A_{11} (1E8) (N/m)		A_{22}(1E8) (N/m)		A_{44} (1E6) (N/m)		A_{55}(1E7) (N/m)	
CS 1	CS 2	CS 1	CS 2	CS 1	CS 2	CS 1	CS 2
4.15	4.15	1.01	1.04	0.41	0.33	0.159	1.81
4.15	4.15	0.23	0.19	0.45	0.37	0.162	1.81
4.15	4.15	0.017	0.017	0.67	0.67	0.181	1.81
3.67	3.67	0.63	1.01	0.85	0.69	0.186	2.11
3.67	3.67	0.14	0.19	0.91	0.76	0.190	2.11
3.67	3.67	0.011	0.017	1.38	1.38	0.211	2.11
2.53	2.53	0.31	0.95	1.72	1.39	0.351	3.99
2.53	2.53	0.72	0.18	1.85	1.53	0.358	3.99
2.53	2.53	0.005	0.016	2.77	2.77	0.399	3.99
1.35	1.35	1.52	0.92	2.15	1.74	0.795	9.04
1.35	1.35	0.34	0.17	2.30	1.92	0.811	9.04
1.35	1.35	0.002	0.015	3.46	3.46	0.904	9.04
0.59	0.59	0.91	0.91	1.72	1.39	1.49	1.70
0.59	0.59	0.20	0.17	1.85	1.53	1.52	1.70
0.59	0.59	0.001	0.015	2.77	2.77	1.70	1.70
0.31	0.31	0.70	0.91	0.85	0.69	2.16	2.46
0.31	0.31	0.16	0.17	0.91	0.76	2.21	2.46
0.31	0.31	0.001	0.015	1.38	1.38	2.46	2.46
0.27	0.27	0.65	0.91	0.41	0.33	2.44	2.78
0.27	0.27	0.15	0.17	0.45	0.37	2.49	2.78
0.27	0.27	0.001	0.015	0.67	0.67	2.78	2.78

Table 3.2: Comparison of stiffness terms of sandwich plates in Case Studies 1 and 2 with $(0/\alpha)_s$ laminate construction

(1)	(2)	D_{11}(1E5) (N-m)		D_{22}(1E5) (N-m)		D_{12}(1E4) (N-m)		D_{66}(1E4) (N-m)		A_{44}(1E6) (N/m)		A_{55}(1E7) (N/m)	
α	θ	CS 1	CS 2	CS 1	CS 2	CS 1	CS 2	CS 1	CS 2	CS 1	CS 2	CS 1	CS 2
	45	4.79	5.15	0.26	0.30	0.85	0.93	2.16	2.38	1.01	1.04	0.41	0.33
	48	4.84	5.15	0.27	0.29	0.85	0.93	2.17	2.36	0.23	0.19	0.45	0.37
0	90	5.15	5.15	0.28	0.28	0.86	0.86	2.20	2.20	0.017	0.017	0.67	0.67
	45	4.52	4.86	0.29	0.32	1.97	2.17	3.28	3.62	0.97	0.65	0.61	0.49
	48	4.57	4.86	0.29	0.32	1.98	2.16	3.30	3.59	0.22	0.12	0.65	0.55
15	90	4.86	4.86	0.31	0.31	2.01	2.01	3.35	3.35	0.017	0.011	1.03	1.03
	45	3.86	4.15	0.43	0.48	4.22	4.66	5.53	6.10	0.92	0.32	1.02	0.83
	48	3.90	4.15	0.43	0.48	4.24	4.62	5.56	6.05	0.21	0.062	1.10	0.92
30	90	4.15	4.15	0.46	0.47	4.31	4.31	5.65	5.65	0.016	0.005	1.72	1.72
	45	3.17	3.41	0.80	0.90	5.34	5.90	6.66	7.34	0.90	0.15	1.26	1.02
	48	3.21	3.41	0.81	0.89	5.37	5.85	6.69	7.29	0.20	0.030	1.36	1.13
45	90	3.41	3.41	0.86	0.86	5.46	5.46	6.80	6.80	0.015	0.002	2.08	2.08
	45	2.74	2.94	1.39	1.56	4.22	4.66	5.53	6.10	0.89	0.93	1.07	0.83
	48	2.77	2.94	1.40	1.55	4.24	4.62	5.56	6.05	0.20	0.018	1.15	0.92
60	90	2.94	2.94	1.50	1.50	4.31	4.31	5.65	5.65	0.015	0.001	1.73	1.72
	45	2.58	2.77	1.96	2.19	1.97	2.17	3.28	3.62	0.89	0.72	0.63	0.49
	48	2.60	2.77	1.97	2.17	1.98	2.16	3.30	3.59	0.20	0.13	0.68	0.55
75	90	2.77	2.77	2.11	2.11	2.01	2.01	3.35	3.35	0.015	0.001	1.03	1.03
	45	2.55	2.74	2.19	2.46	0.85	0.93	2.16	2.38	0.89	0.67	0.42	0.33
	48	2.58	2.74	2.21	2.44	0.85	0.93	2.17	2.36	0.20	0.12	0.45	0.37
90	90	2.74	2.74	2.36	2.36	0.86	0.86	2.20	2.20	0.001	0.001	0.67	0.67

(1) α = Fiber Orientation Angle (in degrees)

(2) θ = Web Inclination Angle (in degrees)

3.3.3.2 Natural Frequencies

For Case Study 2, the variations of natural frequencies with web inclination angle as well as fiber orientation angle are shown in Figure 3.14 to Figure 3.18. They are similar to the ones observed for Case Study 1. However, due to differences in stiffness between Case Study 1 and Case Study 2, the values of natural frequencies are different.

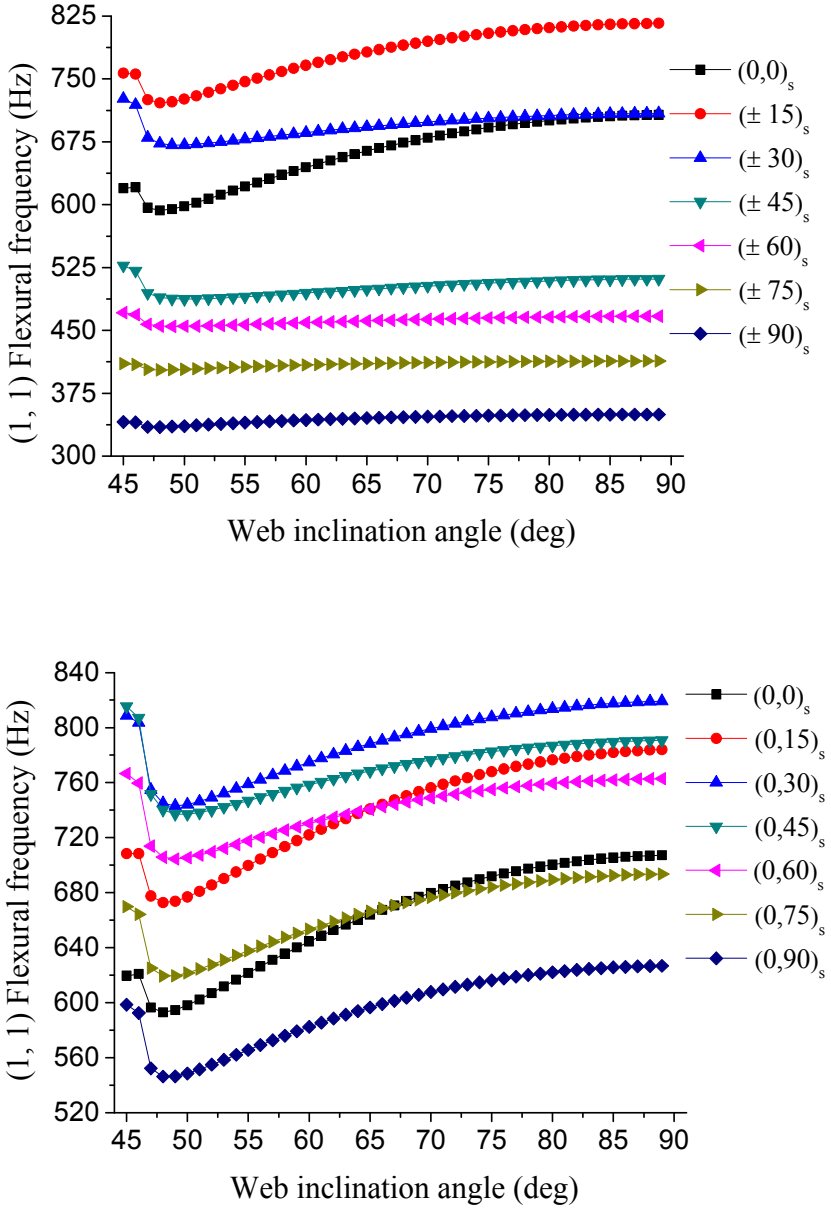

Figure 3.14 : Natural frequencies in (1, 1) flexural mode for sandwich plates with $(0/\alpha)_s$ (top) and $(\pm\alpha)_s$ (bottom) laminate construction in faces and webs

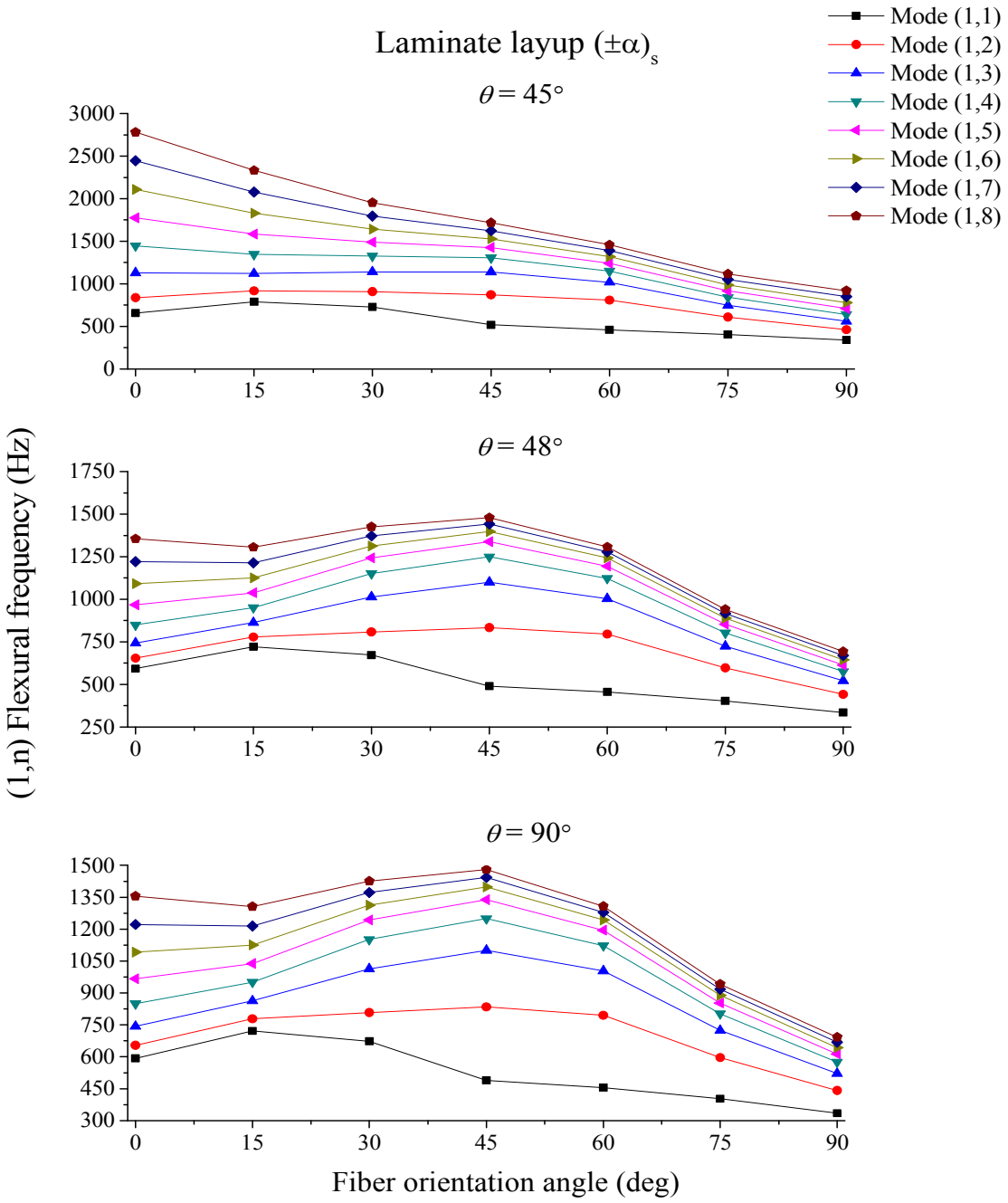

Figure 3.15: Flexural mode (1, n) of sandwich construction with web inclination θ = 45º, 48º and 90º for different fiber orientation angle

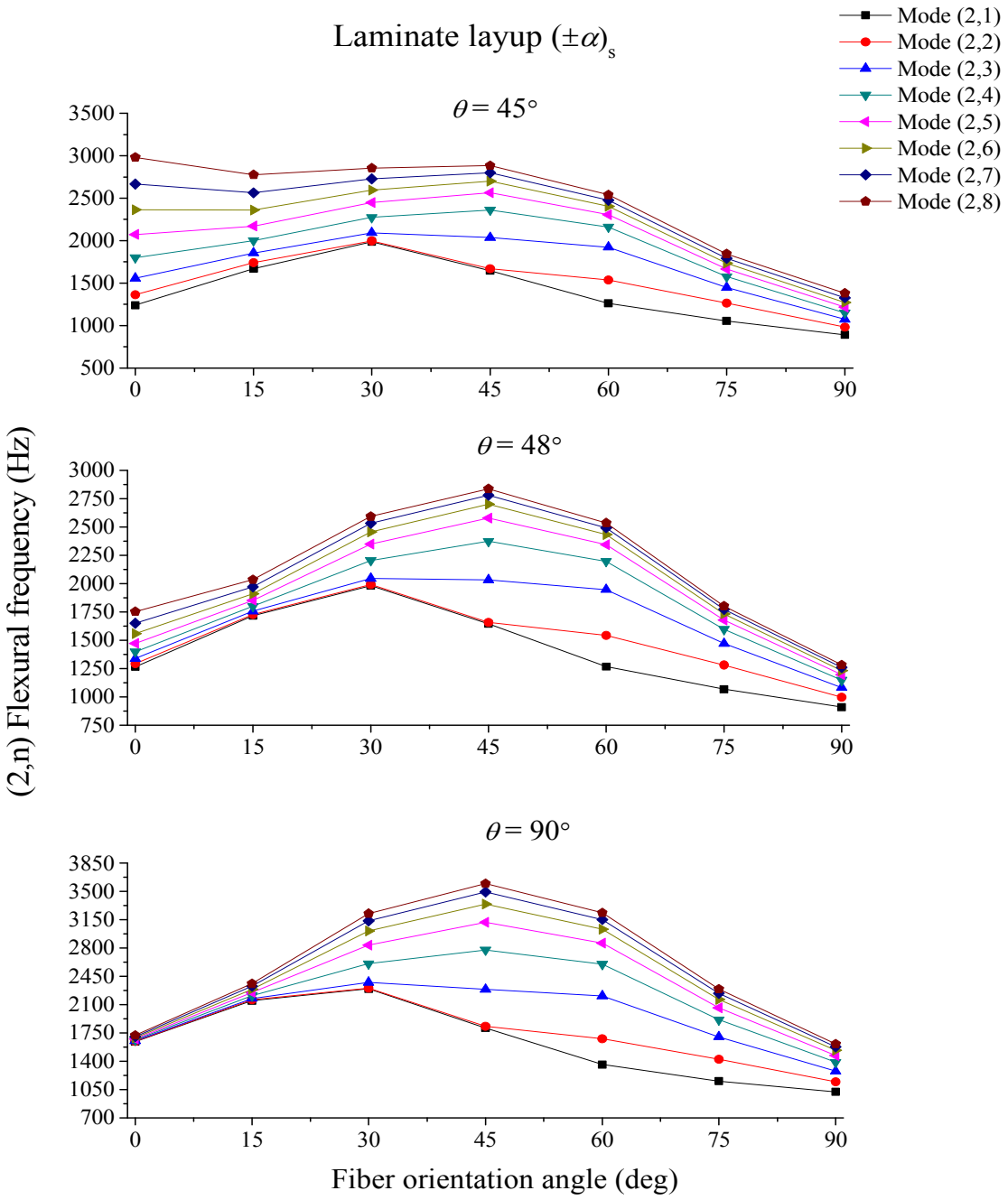

Figure 3.16: Flexural mode (2, n) of sandwich construction with web inclination θ = 45º, 48º and 90º for different fiber orientations

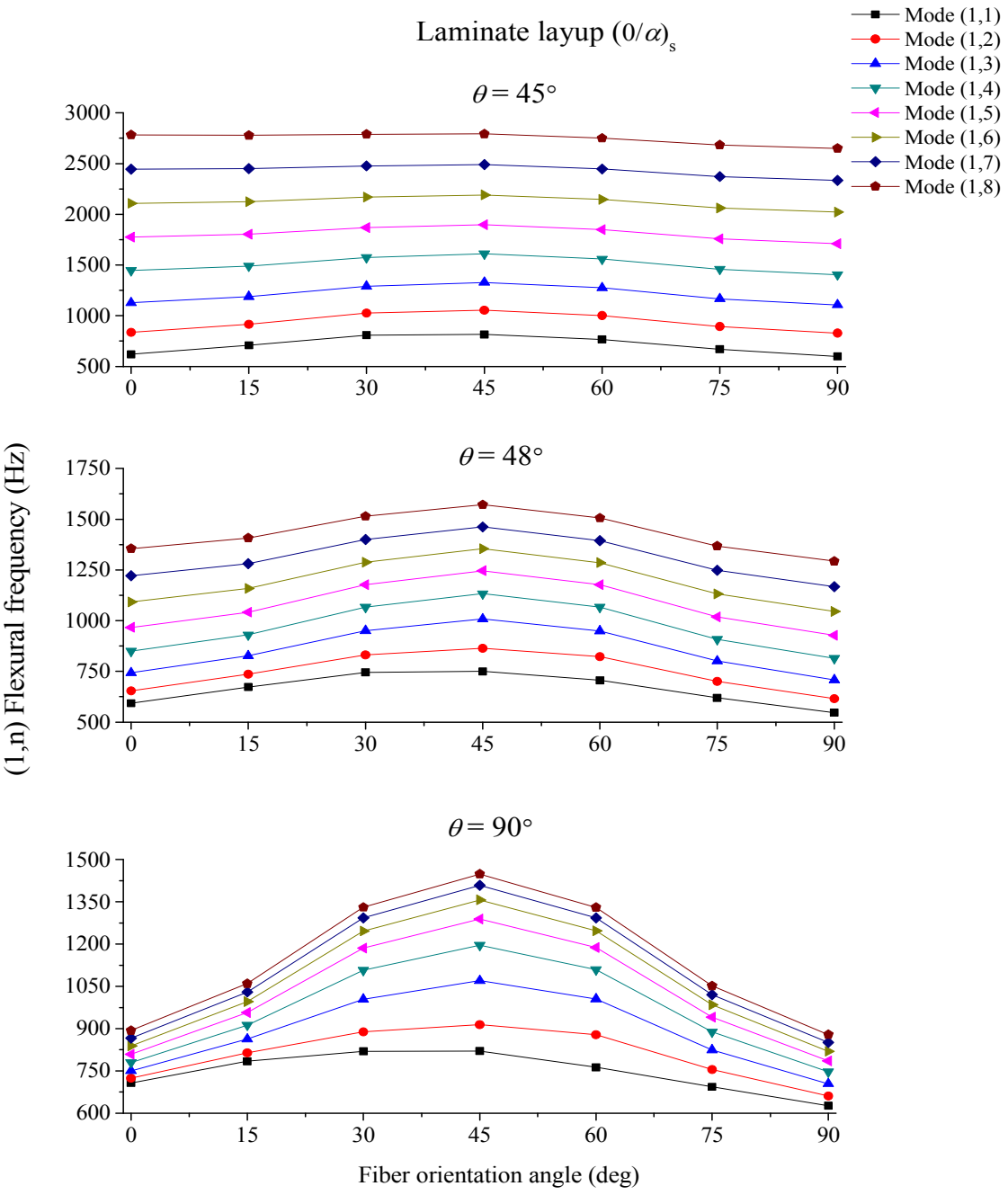

Figure 3.17: Flexural mode (1, n) of sandwich construction with web inclination θ = 45º, 48º and 90º for different fiber orientations

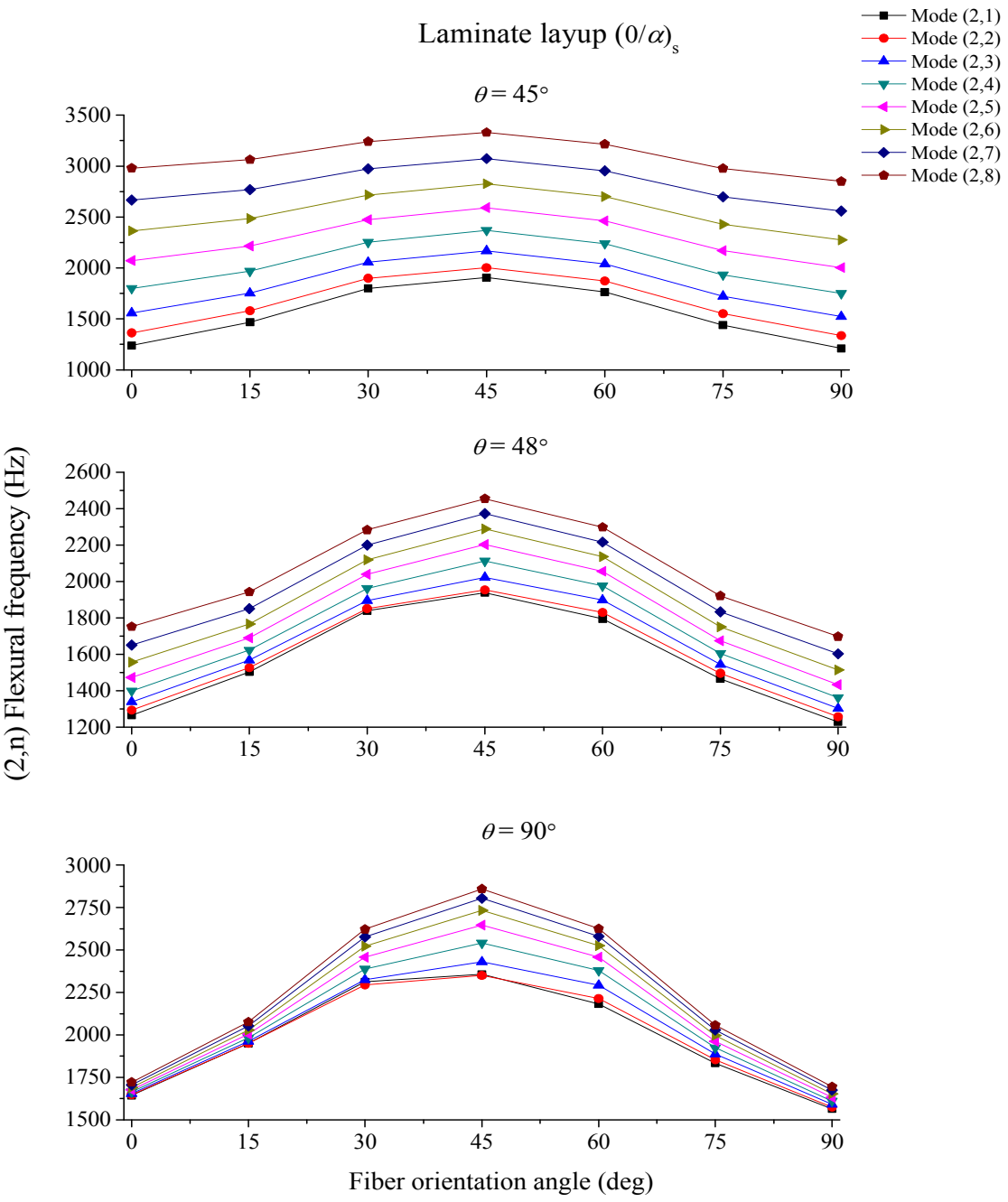

Figure 3.18: (2, n) Flexural frequency of sandwich construction with web inclination θ = 45º, 48º and 90º for different fiber orientations

Figures 3.19 plots the (1,1) flexural natural frequencies of composite sandwich plates in Case Study 1 as a function of fiber orientation angle α for both $(\pm\alpha)_s$ and $(0/\alpha)_s$ laminate constructions. In both cases, natural frequency has a lower value when the web inclination angle θ is 48°. Figure 3.19 also shows that natural frequency first increases

with increasing α, reaches the maximum value at α = 15° with $(\pm\alpha)_s$ laminate construction and α = 30° with $(0/\alpha)_s$ laminate construction and then decreases. After the maximum is reached at α = 15° with $(\pm\alpha)_s$ laminate construction, it decreases rapidly with increasing α and shows the lowest value at α = 90°. With $(0/\alpha)_s$ laminate construction, the effect of α after the maximum value is reached is not as large as with $(\pm\alpha)_s$ laminate construction. Similar observations can be made about the (1,1) natural frequencies of composite sandwich plates in Case Study 2, which are plotted as a function of fiber orientation angle α for both $(\pm\alpha)_s$ and $(0/\alpha)_s$ laminate constructions in Figure 3.20.

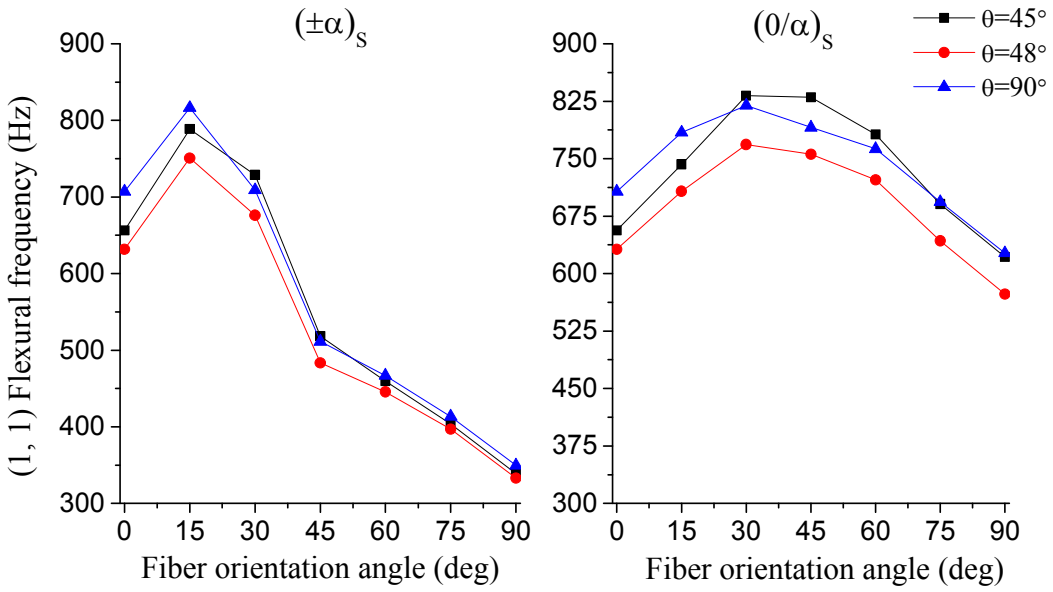

Figure 3.19: Comparison of (1,1) flexural frequencies of sandwich plates with two different laminate constructions, Case study 1 ($t_{TF} = t_{BF} = t_c = t$)

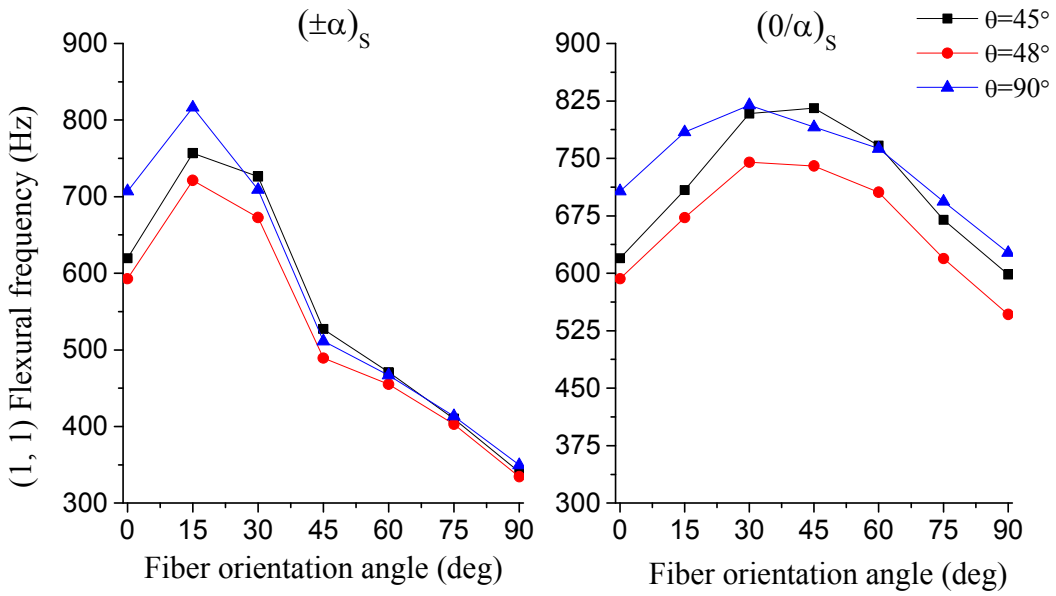

Figure 3.20: Comparison of (1,1) flexural frequencies of sandwich plates with two different laminate constructions, Case study 2 ($t_{TF} = t_{BF} = 1mm$, $t_c = 1mm * \sin\theta$)

3.3.4 Case Study 3: $t_{TF} = t_{BF}$ =1 mm, $t_c \leq 1$ mm, d =80 mm and p =20, 40, 80, 160 and 320 mm

This case study is conducted to examine the effect of pitch ($2p$) on the (1,1) flexural natural frequency of the corrugated-core composite sandwich plates. Two laminate constructions are considered: $(0/90)_s$ and $(\pm 90)_s$. The face thickness is 1 mm and the depth is 80 mm. The pitch is varied from 40 to 640 mm so that p/d = 0.25, 0.5, 1, 2 and 4. The corresponding minimum web inclination angles are 75.96º, 63.5º, 45º, 26.56º and 14.04º. The maximum web inclination angle is 90º. Since the cross-sectional area is maintained constant, the web thickness increases as the web inclination angle is varied from the minimum web inclination angle to the maximum web inclination angle.

The effect of both pitch and web inclination angle on the natural frequency corresponding to flexural mode (1, 1) is shown in Figure 3.21. At all web inclination angles, the natural frequency is significantly higher for the $(0/90)_s$ laminate construction compared to the $(\pm 90)_s$, which is attributed to the presence of the 0º layers in the $(0/90)_s$ construction. It can also be observed in Figure 3.21 that the natural frequency for the 90º

web inclination angle is the same for all *p/d* ratios, and therefore, is independent of pitch. For *p/d* = 0.25, i.e., 40 mm pitch, the highest natural frequency occurs at θ = 75.96º, i.e., with the triangular core, and the lowest natural frequency occurs at θ = 90º, i.e., with the rectangular core. On the other hand, for *p/d* = 4, i.e., 640 mm pitch, the highest natural frequency occurs at θ = 90º, which represents the rectangular core and the lowest natural frequency occurs at θ = 14.04º, which represents a triangular core. For other *p/d* ratios, the lowest natural frequency does not occur at the minimum web inclination angle, but very close to it. It can also be observed in Figure 3.21 that while the natural frequency for the rectangular core does not depend on the pitch, the natural frequency for the triangular core increases with decreasing pitch.

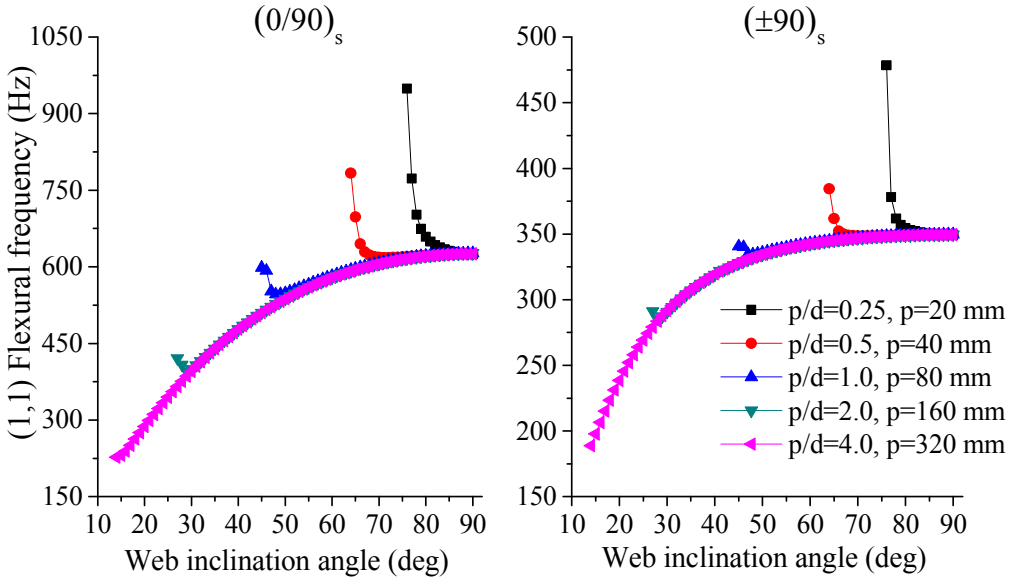

Figure 3.21: (1, 1) Flexural frequencies of sandwich plates with varying web inclination angle and pitch

3.3.5 Case Study 4: $t_{TF} = t_{BF} = 1$ mm, $t_c \leq 1$ mm, $p = 80$ mm and $d = 20, 40, 60, 80$ mm

In this case study, the effect of face center distance (*d*) on the (1,1) natural frequency is considered for corrugated-core composite sandwich plates with $(0/90)_s$ and $(\pm 90)_s$ laminate constructions. The face thickness (t_f) and pitch (*2p*) are maintained constant at 1 mm and 160 mm, respectively. The face center distance *d* is varied from 20 mm to 80 mm in steps of 20 mm. To maintain a constant cross sectional area of 478 mm^2, the web thickness (t_c) is varied as a function of web inclination angle θ for each value of

d. The web thickness as a function of web inclination angle and face center distance is given in Equation (2.22) in Chapter 2. It should be noted that in this case study *p* is a constant; but as *d* is decreased, *p/d* increases, and therefore, the minimum web inclination angle θ_{min} decreases.

The (1,1) natural frequency for sandwich plates with both $(0/90)_s$ and $(\pm 90)_s$ constructions are shown in Figure 3.22. For both laminate constructions, the (1,1) natural frequency increases with increasing depth, which is attributed to increasing bending stiffness. The (1,1) natural frequencies for the $(0/90)_s$ laminate construction is significantly higher than for the $(\pm 90)_s$ laminate construction, which is due to the presence of the 0^o layers in the $(0/90)_s$ laminates. Also shown in Figure 3.22 is the dependency of the (1,1) natural frequencies on the web inclination angle. In all cases, they start with a relatively high value at the minimum web inclination angle, decreases rapidly to the lowest value and then either increases or remains nearly constant at higher web inclination angles. The natural frequency for both the rectangular core and the triangular core increases with increasing face center distance.

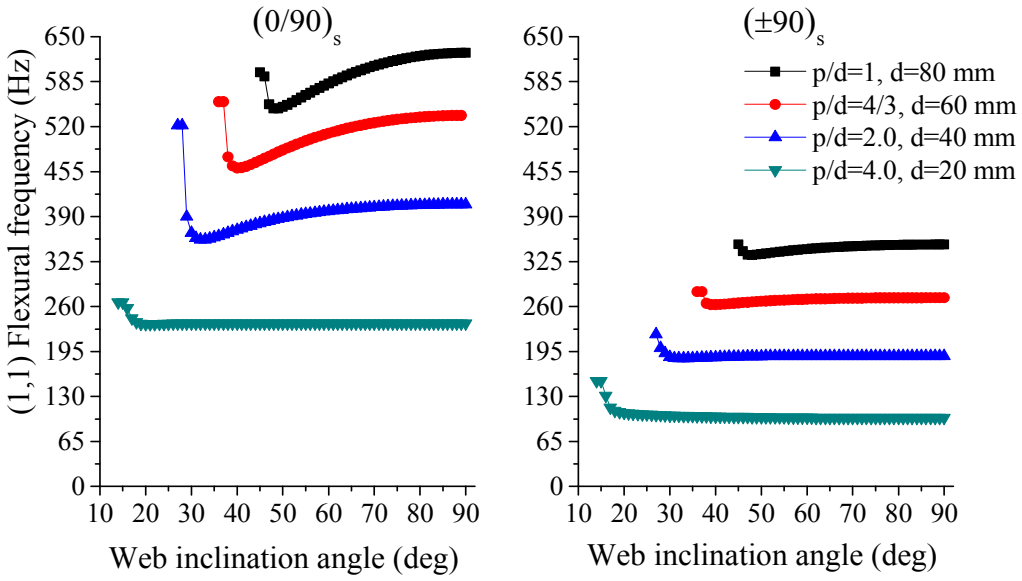

Figure 3.22: (1,1) Flexural frequencies of sandwich plates with varying web inclination angle and face center distance

3.4 EXTENSIONAL MODES

In this section, in-plane extensional mode shapes and natural frequencies of the sandwich plates with corrugated core are presented. The unit cell construction is the same as in Case Study 2 in Section 3.3.3 in which $t_{TF} = t_{BF}$ = 1 mm, p = d = 80 mm, and the web thickness is varied using the relationship $t_c = t_{90^\circ} \sin\theta$ to maintain a constant cross-sectional area of 478 mm^2. Since the laminate construction is symmetric, there is no bending-extension coupling. This has made it possible to separate the extensional vibration modes from the flexural vibration mode. The displacement fields u and v related to the in-plane extension modes are therefore decoupled for the displacement field w, which is related to the flexural mode.

In the following sections, (1,1) in-plane extensional mode shapes and natural frequencies are presented for the corrugated core sandwich plates with $(\pm\alpha)_s$ laminate construction in the faces and webs.

3.4.1 In-plane Extensional Mode Shapes

Global extensional mode shapes for U-dof are shown in Figure 3.23. In the case of fundamental extensional mode with m = 1, n = 1, we can observe a half sine wave in the x-direction and half cosine wave in the y-direction. For m = 1 and n = 2, we can

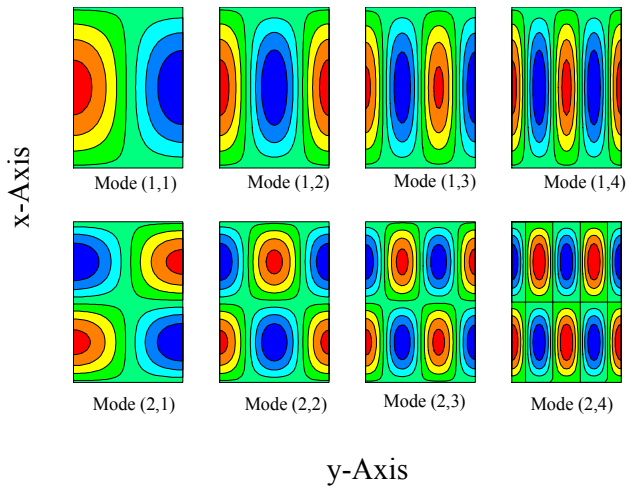

Figure 3.23: Extensional mode shapes for U-dof in the x-direction of corrugated core sandwich plates with $(0/90)_s$ laminate construction in the faces and webs

observe a half sine wave in the x-direction and two half cosine waves in the y-direction. Similarly for higher modes, mode shapes resemble sine and cosine waves, according m and n combinations.

Global extensional mode shapes for V-dof are shown in Figure 3.24. In the case of fundamental extensional mode with m = 1, n = 1, we can observe a half cosine wave in the x-direction and half sine wave in the y-direction. For m =1 and n = 2, we can observe a half cosine wave in the x-direction and two half sine waves in the y-direction. Similarly for higher modes, mode shapes resemble sine and cosine waves, according m and n combinations.

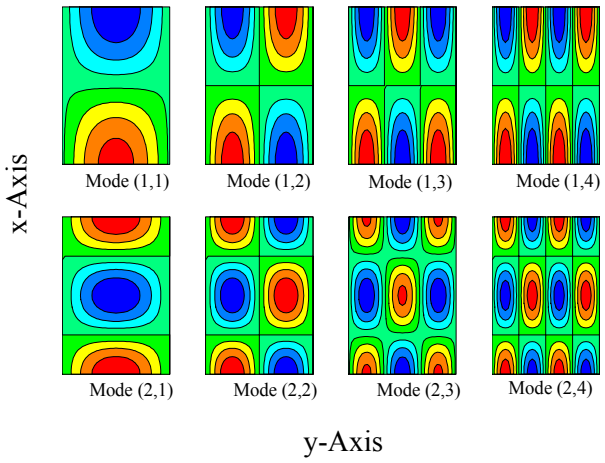

Figure 3.24: Extensional mode shapes for V-dof in the x-direction of corrugated core sandwich plates with $(0/90)_s$ laminate construction in the faces and webs

3.4.2 Natural Frequencies

Natural frequencies in the (1, 1) extensional mode for U-dof of sandwich plates for various web inclination angles and different fiber orientation angles in the laminate construction are given in Figure 3.25. It is observed that the (1,1) natural frequencies change very little with increase in web inclination angle. The fiber orientation angle, however, has a very significant effect on the (1,1) natural frequency. Its maximum and minimum values occur at $\alpha = 0^o$ and $\alpha = 90^o$, respectively. This is a reflection of significantly higher A_{11} value at $\alpha = 0^o$ compared to that at $\alpha = 90^o$.

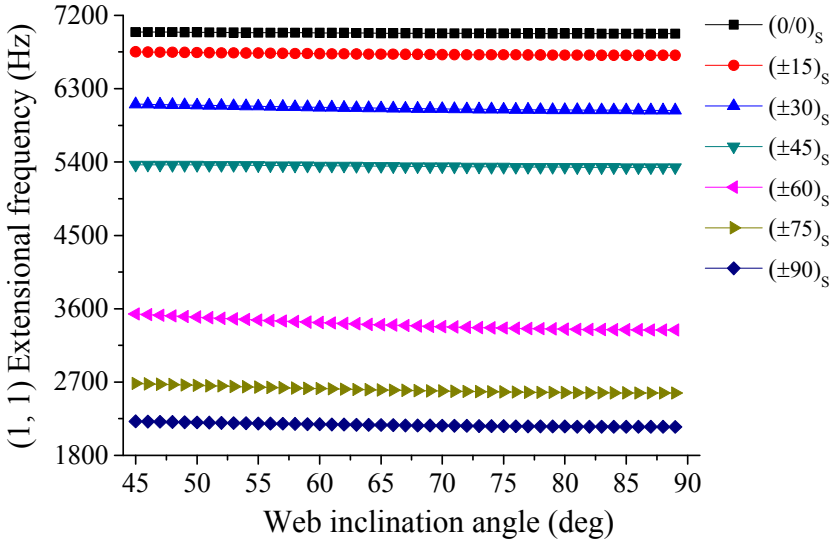

Figure 3.25: (1, 1) Extensional frequencies for U-dof of corrugated core sandwich plates vs. web inclination angle. The laminate construction in the faces and webs is $(\pm\alpha)_s$

Natural frequencies in the (1, 1) extensional mode for V-dof of sandwich construction for various web inclination angles and different fiber orientation angles in the laminate construction are given in Figure 3.26. It is observed that for $\alpha = 0$ to 45°,

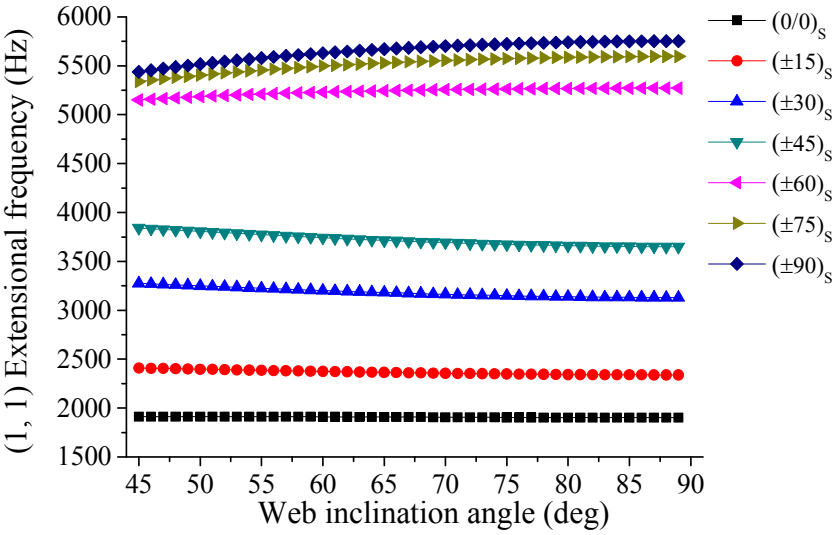

Figure 3.26: (1, 1) Extensional frequencies for V-dof of corrugated core sandwich plates vs. web inclination angle. The laminate construction in the faces and webs is $(\pm\alpha)_s$

the (1,1) natural frequencies have a slightly decreasing trend with increase in web inclination angle. However, for $\alpha = 60$ to $90°$, the (1,1) natural frequencies increase with increase in web inclination angle. As for the effect of fiber orientation angle, the (1,1) natural frequency increases with increase in fiber orientation angle from $\alpha = 0$ to $90°$. The maximum and minimum values in this case occur at $\alpha = 90^o$ and $\alpha = 0^o$, respectively, which is a reflection of significantly higher A_{22} at $\alpha = 90^o$ compared to that at $\alpha = 0^o$.

Figure 3.26 and Figure 3.27 compare the (1,1) natural frequencies of sandwich plates with laminate constructions $(\pm\alpha)_s$ and $(0/\alpha)_s$ in the faces and webs. The web inclination angles selected in these figures are 45, 48 and 90^o. As can be observed in these figures, the (1,1) natural frequencies have similar trends for both $(\pm\alpha)_s$ and $(0/\alpha)_s$ laminate constructions. The x-direction natural frequencies decrease with increasing fiber orientation angle, while the y-direction natural frequencies increase. Another observation that can be made from these figures is that the x-direction natural frequencies are significantly higher with the $(0/\alpha)_s$ laminate construction compared to the $(\pm\alpha)_s$ laminate construction, which is due to higher A_{11} values for the $(0/\alpha)_s$ laminates. On the other hand, the y-direction natural frequencies are higher with the $(\pm\alpha)_s$ laminate construction, which is due to their higher A_{22} values.

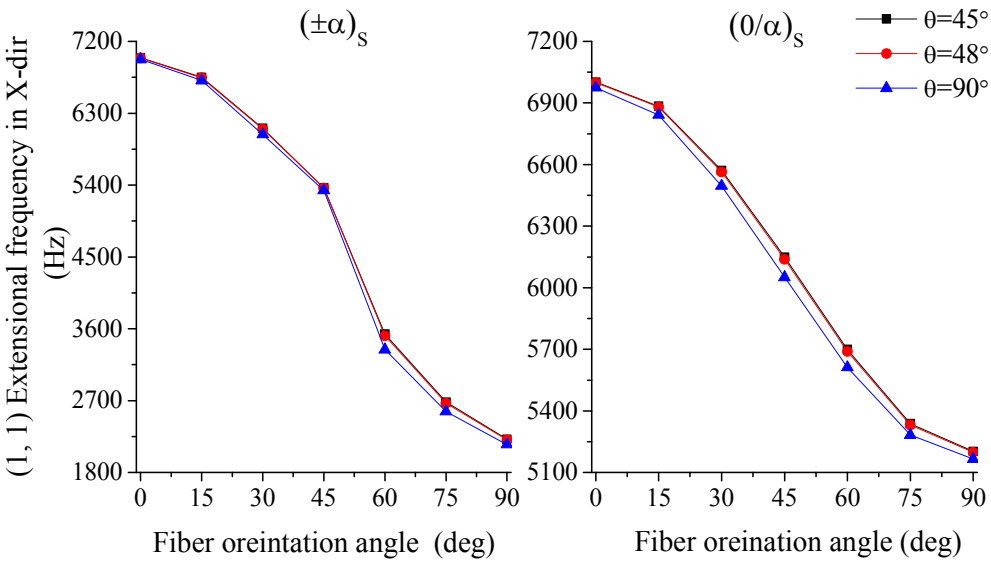

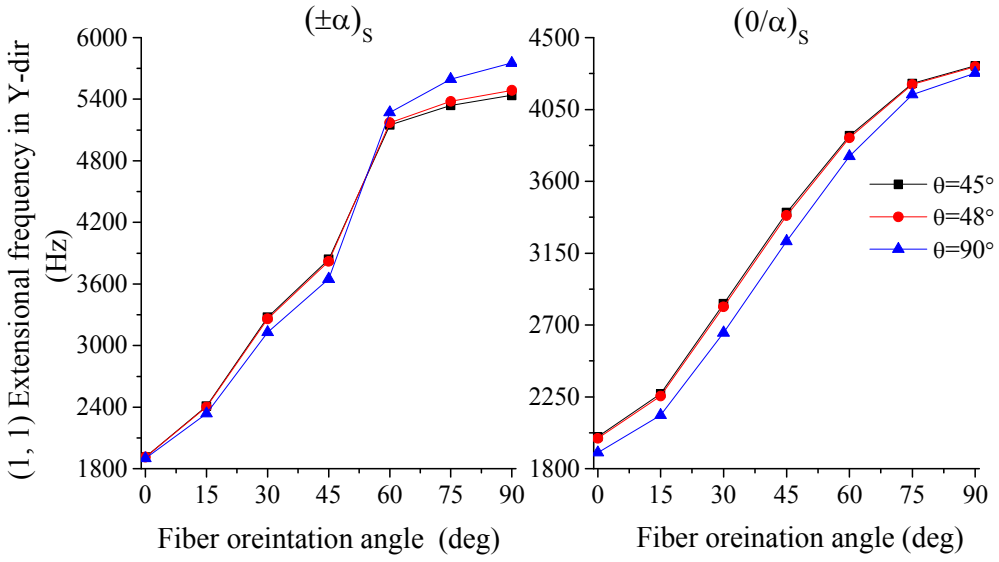

Figure 3.27: Comparison of (1,1) extensional frequencies of corrugated-core sandwich plates with $(\pm\alpha)_s$ and $(0/\alpha)_s$ laminate constructions in the faces and webs

3.5 CONCLUSIONS

This chapter has presented the global vibration response of corrugated-core composite sandwich plates with two different laminate constructions, namely $(\pm\alpha)_s$ and $(0/\alpha)_s$. Both flexural and in-plane extensional modes are considered. The effects of geometric parameters, such as face thickness, web thickness, pitch and face center distance, on the flexural natural frequencies are determined. The effect of web thickness on the extensional natural frequencies is also determined. As the geometric parameters are varied, the web inclination angle is adjusted to maintain a constant volume of the sandwich plates. A range of web shapes ranging from triangular core to rectangular core is considered.

Flexural natural frequency depends strongly on the laminate construction in the faces and webs. For the $(\pm\alpha)_s$ laminates, the peak natural frequency occurs at 15º fiber orientation angle, whereas for the $(0/\alpha)_s$ laminates, the peak natural frequency occurs at 30º fiber orientation angle. After the peak is reached, natural frequencies with the $(0/\alpha)_s$ laminate construction are much higher than with the $(\pm\alpha)_s$ laminate construction. The

web inclination angle, which increases with increasing web thickness to maintain a constant volume of the sandwich plate, also has a significant effect on the natural frequency. For each fiber orientation angle, the natural frequency exhibits the largest value at slightly higher than the minimum web inclination angle.

Flexural natural frequency depends on both the pitch and the face center distance. For the (0/90) and (±90) laminates considered, increasing the pitch increases the natural frequency, the largest effect being observed at the smallest web inclination angle, which corresponds to the triangular core. For the rectangular core, natural frequency is independent of pitch. Increasing the face center distance increases the natural frequency at all web inclination angles.

A comparison of fundamental natural frequencies shows that the extensional mode natural frequencies are much higher than the flexural mode natural frequencies. This is due to the fact the in-plane stiffness of the sandwich plate is higher than the bending stiffness. Also, in the extensional mode, there is no effect of transverse stiffness. As with the flexural natural frequency, the extensional natural frequency shows a strong dependency on fiber orientation angle. The effect of web inclination angle is relatively small.

REFERENCES

[1] Vinson, J.R., "The Behavior of Sandwich Structures of Isotropic and Composite Materials", Technomic Publishing Co., Lancaster, PA, 1999.

[2] Lee, L.J. and Fan, Y.J., "Bending and vibration analysis of composite sandwich plates", *Computers and Structures*, Vol. 60, No. 1, 1993, pp. 103-112.

[3] Frostig, Y. and Thomsen, O.T., "Higher order free vibration of sandwich panels with a soft flexible core", *International Journal of Solids and Structures*, Vol. 41, 2004, pp. 1697-1724.

[4] Wang, T., Sokolinsky, V., Rajaram, S. and Nutt, S.R., "Consistent higher-order free vibration analysis of sandwich plates", *Composite Structures*, Vol. 82, 2008, pp. 609-621.

[5] Liu, Q. and Zhao, Y., "Effect of soft honeycomb core on flexural vibration of sandwich panel using low order and high order shear deformation models", *Journal of Sandwich Structures and Materials*, Vol. 9, 2007, pp. 95-108.

[6] Lok, T. S. and Cheng, Q. H., "Free vibration of clamped orthotropic sandwich panel," *Journal of Sound and Vibration*, Vol. 229, 2000, pp. 311-327.

[7] Lok, T. S. and Cheng, Q. H., "Bending and Forced Vibration Response of a Clamped Orthotropic Thick Plate and Sandwich Panel", *Journal of Sound and Vibration*, Vol. 245, 2001, pp. 63-78.

[8] Lou, J., Ma, L. and Wu, L-Z., "Free vibration analysis of simply supported sandwich beams with lattice truss core", *Materials Science and Engineering B*, Vol. 177, 2012, pp. 1712-1716.

[9] Chandrashekhara, K. Krisnamurthy, K. and Roy, S., "Free vibration of composite beams including rotary inertia and shear deformation", *Composite Structures*, Vol. 14, 1990, pp. 269-279.

[10] Qatu, M. S., "Free vibration of laminated composite rectangular plates", *International Journal of Solids and Structures*, Vol. 28, No. 8, 1991, pp. 941-954.

[11] Narita, Y. and Leissa, A. W., "Frequencies and mode shapes of cantilevered laminated composite plates", *Journal of Sound and Vibration*, Vol. 154, No. 1, 1992, pp. 161-172.

[12] Aydogdu, M. and Timarci, T., "Vibration analysis of cross-ply laminated square plates with general boundary conditions", *Composites Science and Technology*, Vol. 63, 2003, pp. 1061-1070.

[13] Kant, T. and Swaminathan, K., "Free vibration of isotropic, orthotropic, and multilayer plates based on higher order refined theories", *Journal of Sound and Vibration*, Vol. 241, No. 2, 2001, pp. 319-327.

[14] Kant, T. and Swaminathan, K., "Analytical solutions for free vibration of laminated composite and sandwich plates based on a higher-order refined theory", *Composite Structures*, Vol. 53, 2001, pp. 73-85.

[15] Woodcock, R. L., Bhat, R. B. and Stiharu, I. G., "Effect of ply orientation on the in-plane vibration of single-layer composite plates", *Journal of Sound and Vibration*, Vol. 312, 2008, pp. 94-108.

[16] Dozio, L., "In-plane free vibrations of single-layer and symmetrically laminated rectangular composite plates," *Composite Structures*, Vol. 93, 2011, pp. 1787-1800.

CHAPTER 4

LOCAL BENDING RESPONSE OF COMPOSITE SANDWICH PLATES WITH CORRUGATED CORE

4.1 INTRODUCTION

In Chapters 2 and 3, composite sandwich plate with corrugated core is homogenized to an equivalent orthotropic plate for the prediction of global bending and vibration responses. Since both faces and webs in the sandwich plate are constructed of thin composite laminates, there will be local deformations when the sandwich plate is transversely loaded. The local deformations of each member and associated stresses and strains cannot be predicted using the homogenization process. As the transverse load is increased, there will be local failures due to buckling or stress-induced failures, such as fiber fracture, matrix failure, etc. Their predictions are important for structural applications of composite sandwich plates with corrugated core.

Local response of metallic or paperboard sandwich structures with corrugated core has been addressed for several different loading conditions and failure modes. Valdevit et al. [1], [2] structurally optimized metallic sandwich panels with prismatic cores against failure mechanisms of face yielding, face buckling, core yielding and core buckling. Their goal was to find the geometric parameters that minimize weight per unit width subject to a combination of moment and shear forces. Their findings indicated that the corrugated core panel performs best when loaded longitudinally because in this orientation, the performance is limited by plate buckling, rather than beam buckling. Xue and Hutchinson [3], [4] have shown that prismatic core geometries in sandwich construction are nearly optimal for shock resistant and have also indicated that they are

more effective in resisting dynamic shock loading when compared to the conventional construction.

Sek and Kirkpatrick [5] predicted cushioning properties of corrugated board under static and quasi-dynamic compression tests and developed a predictive model of cushioning properties of such boards based on static and quasi-dynamic compression data. Rouillard and Sek [6] analyzed cushioning behavior of multi-layered corrugated board under impact loads.

Nordstrand et al. [7] and Nyman et al. [8] conducted numerical and experimental simulations to predict stability and collapse of corrugated board panels. They developed a procedure for three-dimensional finite element modeling and considered both structural local buckling failure and material failure. Rami et al. [9] presented a refined nonlinear finite element modeling approach for the analysis of corrugated fiberboard material and structural systems. The anisotropic and nonlinear material stress–strain behavior of the linerboards and fluting medium layers of the corrugated fiberboard composite system is modeled using orthotropic material model with Hill's anisotropic plasticity.

In the available literature, research has been carried out in developing analytical models for sandwich construction with corrugated core, where faces and web members are made of isotropic materials. In this chapter, local deformation, buckling and failure are predicted using finite element method. The external load acting on the sandwich plate is a uniform pressure load on its top surface, which is increased in a step-wise fashion. A progressive failure prediction methodology is developed which is used to determine the pressure loads at which the various members of the sandwich plate fails.

4.2 FINITE ELEMENT FORMULATION

4.2.1 Sandwich Plate Geometry

The local analysis is performed with two different unidirectional corrugation geometries, namely a triangular corrugation with web inclination angle of 45º and a rectangular corrugation with web inclination angle of 90º. The sandwich plate size is 640 mm x 640 mm. The pitch ($2p$) and face center distance (d) are 160 mm and 80 mm, respectively. Both top and bottom face thickness (t_f) is 1 mm, and since the volume of the

sandwich plate is maintained the same for both corrugation geometries, the web thickness (t_c) for the triangular core is 0.75 mm and that for the rectangular core is 1 mm. In both cases, there are four unit cells; however, in the case of the triangular core, there is an overhang of 80 mm length on the top face, whereas in the case of the rectangular core, there are overhangs of 40 mm length on both top and bottom faces. Also, to be noted is that in the case of the triangular core, the unsupported length of the faces between the consecutive web connections is 160 mm, whereas that for the rectangular core is only 80 mm. A distributed pressure load is applied on the top surface of the sandwich plate and the plate is simply supported on all four edges.

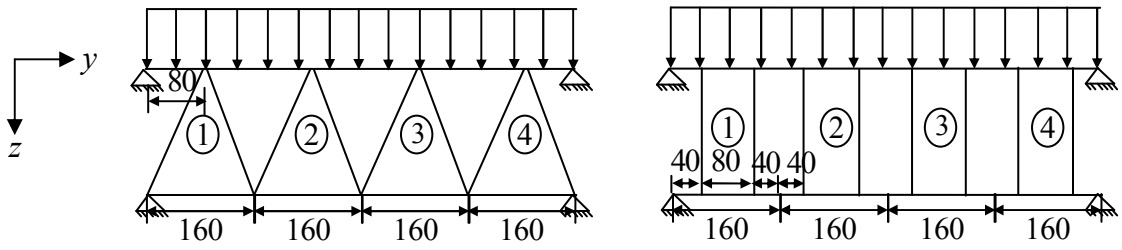

Figure 4.1: Corrugation geometry of the sandwich plates with web inclination angles $\theta = 45^{\circ}$ (left) and 90° (right) (Dimensions are in mm)

4.2.2 Description of Selected Shell Element in ANSYS

In the present study, finite element analysis of composite sandwich plates with corrugated core is performed using Shell 181 element in the ANSYS software. Description of Shell 181 element is given in Figure 4.2. It is a four-noded thin shell element with six degrees of freedom (dof) at each node; they are three translational (UX, UY, UZ) degrees of freedom and three rotational (ROTX, ROTY, ROTZ) degrees of freedom. It is capable of analyzing laminated composite materials with different fiber orientation angles in different laminas and generates strain and stress outputs for each lamina in both global (XYZ) and local (xyz) co-ordinate directions. The local co-ordinate direction, also called the material co-ordinate direction, on the element represents the fiber orientation direction which can vary from lamina to lamina. Stresses and strains in the global co-ordinate directions are transformed into stresses and strains in the local co-ordinate directions using the stress and strain transformation matrices.

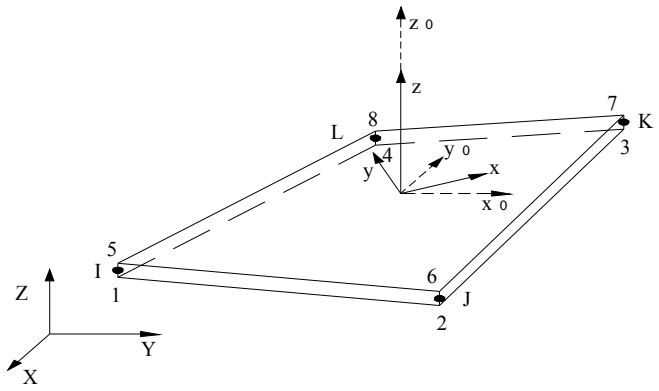

Figure 4.2: Description of SHELL 181 element used for FE-analysis in ANSYS (XYZ is the global coordinate system and xyz is local coordinate system)

4.2.3 Description of Finite Element Model used for Sandwich Plate

The finite element model for the sandwich plates, shown in Figure 4.3, includes a total of 9,600 elements and 10,290 nodes. FE mesh details of individual members in sandwich plates are tabulated in Table 4.1. The webs are connected to the top and bottom faces using coupling (CP) commands in ANSYS, so that all nodes in the faces and the webs in the tolerance of 1E-4 mm are coupled and have equal degrees of freedom. The material of construction of the sandwich plate is a carbon fiber reinforced epoxy laminate containing four laminas of equal thickness. The element thickness is the same as the laminate thickness. Since the laminate thickness for both faces is 1 mm, the lamina thickness in the faces is 0.25 mm. The laminate thickness for the webs in the triangular core is 0.75 mm and that in the rectangular core is 1 mm. The corresponding lamina thicknesses are 0.1875 and 0.25 mm, respectively.

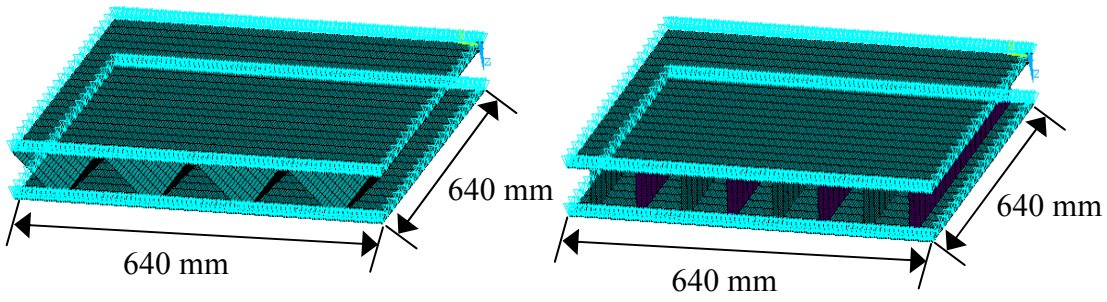

(a) Triangular core ($\theta = 45^{o}$) (b) Rectangular core ($\theta = 90^{o}$)

Figure 4.3: Mesh used for FE-analysis in ANSYS

Table 4.1: Finite element mesh details of individual members in sandwich plate

	Top face	Bottom face	Web	
			$\theta = 45°$	$\theta = 90°$
Number of elements	2,400	2,400	4,800	4,800
Element surface area $\left(mm^2\right)$	170	170	120	85.3

4.2.4 Material Properties used in the Finite Element Model

As in Chapters 2 and 3, the material in the faces and webs is a carbon fiber reinforced epoxy. The basic elastic properties and strength limits of the material in the local material directions 1, 2 and 3 are listed in Table 4.2 and Table 4.3, respectively.

Table 4.2: Elastic properties of carbon fiber reinforced epoxy composite

E_{11} (GPa)	E_{22} (GPa)	G_{12} (GPa)	υ_{12}
138	9	6.9	0.3

Table 4.3: Strength limits of carbon fiber reinforced epoxy composite in MPa [13]

S_{xT}	S_{xC}	S_{yT}	S_{yC}	S_{xy}	S_{xz}	S_{yz}	S_{zT}	S_{zC}
2,250	1,600	64	290	98	98	30	94	290

4.2.5 Load Application and Boundary Conditions

In the sandwich plate, top and bottom faces are simply supported at all edges, i.e. $u_z = 0$ on all four edges, and the top face is subjected to a uniformly distributed surface pressure load p_0 on its top surface. Load transmission into the bottom face occurs through the webs which connect the top face with the bottom face. For the local failure prediction, the load is increased in steps of 3,000 N/m^2 up to a total of 300 load steps, as shown in Figure 4.4. If failure of an element is registered at the end of a load step, the pressure load is reduced by 3,000 N/m^2 and then incremented using a load step of 500 N/m^2 to determine the load at which the element failure has taken place.

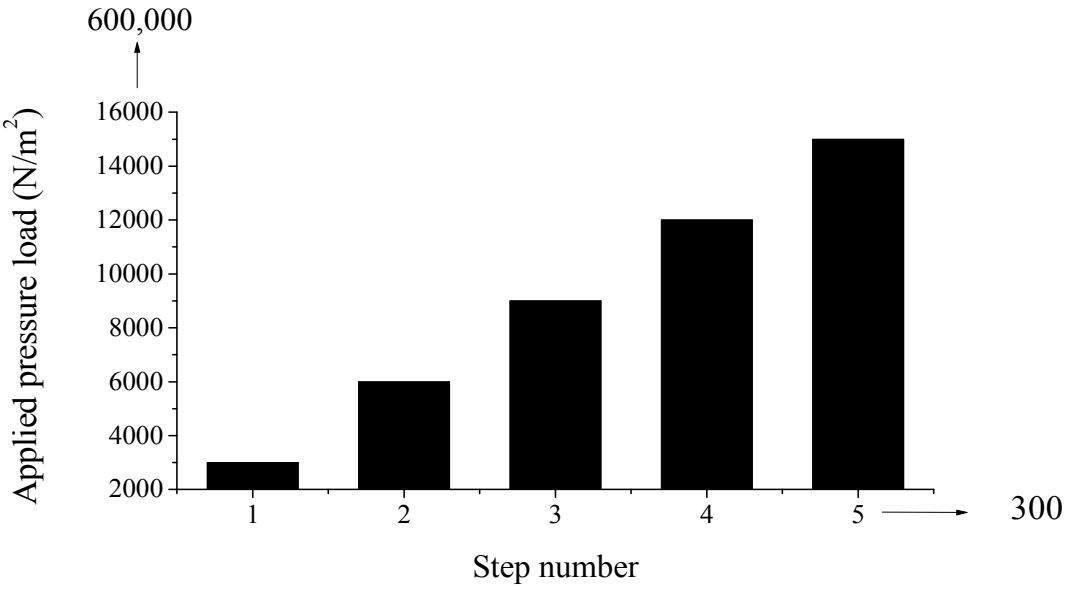

Figure 4.4: Graphical representation of applied pressure load in each step

4.2.6 Finite Element Details

In this section, a detailed description of the finite element formulation used in ANSYS for a four-node laminate shell element and different coordinate systems adopted for modeling composite structures [11], [12] is given.

4.2.6.1 Displacement functions based on Isoparametric formulation

The cartesian coordinate system associated with each nodal point of the shell element has its origin at the shell mid-surface as shown in Figure 4.5. The vector in the n_i direction is constructed from the nodal coordinates of the top and bottom surfaces at node i, so that $n_i = j_i^{top} - j_i^{bot}$, where $j_i = \left[x_i, y_i, z_i\right]^T$ and the vector l_i is perpendicular to m_i and parallel to the global XZ plane, so that $l_i^x = n_i^z$, $l_i^y = 0$ and $l_i^z = -n_i^x$. If n_i is coincident with the y direction, (i.e., $n_i^x = n_i^z = 0$), then $l_i^x = -n_i^y$, $l_i^y = l_i^z = 0$, where the superscripts refer to the vector components in the global coordinate system. The vector m_i is perpendicular to the plane defined by l_i and n_i, so that $m_i = n_i \times l_i$. The unit vectors in the directions l_i, m_i and n_i are represented by $\overline{l}_i$, $\overline{m}_i$ and $\overline{n}_i$, respectively. The vector $\overline{n}_i$ defines the direction of the normal at node i which is not necessarily perpendicular to the

mid surface at i. Vectors $\bar{l}_i$ and $\bar{m}_i$ define the directions of rotations θ_{2i} and θ_{1i}, respectively.

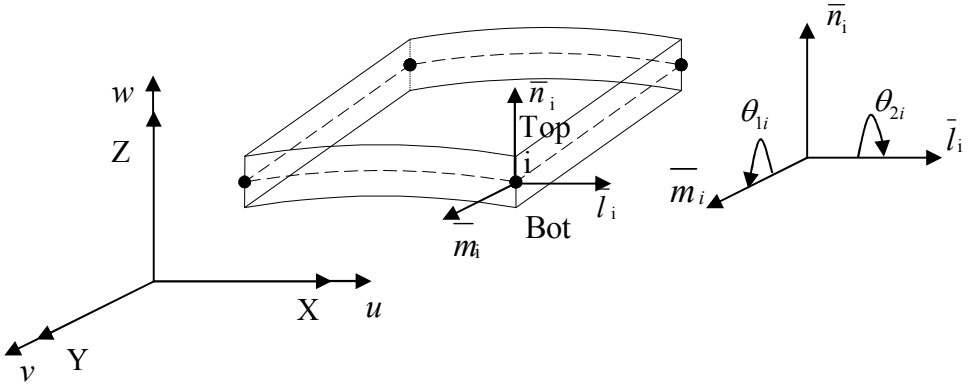

Figure 4.5: Description of general shell element

In the isoparametric formulation, the coordinates of a point within the element are expressed as given in Equations 4.1- 4.3.

$$X=\sum_{i=1}^{4} N_i x_i^{mid} + \sum_{i=1}^{4} N_i h_i \frac{\zeta}{2} \bar{n}_i^x \tag{4.1}$$

$$Y=\sum_{i=1}^{4} N_i y_i^{mid} + \sum_{i=1}^{4} N_i h_i \frac{\zeta}{2} \bar{n}_i^y \tag{4.2}$$

$$Z=\sum_{i=1}^{4} N_i z_i^{mid} + \sum_{i=1}^{4} N_i h_i \frac{\zeta}{2} \bar{n}_i^z \tag{4.3}$$

where, X, Y and Z are the global cartesian coordinates of the nodal point i, $N_i = N_i(\xi,\eta)$ represents the two dimensional shape function corresponding to the surface $\zeta =$ constant. ξ, η and ζ are the normalized co-ordinates for the point under consideration, h_i is the shell thickness at node i and x_i^{mid}, y_i^{mid}, z_i^{mid} are the coordinates at the mid-surface of the shell. The vector $\bar{n}_i$ is constructed from the nodal coordinates of the top and bottom surfaces at node *i*.

The displacement throughout the element, expressed as given in Equation 4.4-4.6, is assumed to be uniquely defined by three cartesian components of the mid-surface

node displacement and two rotations of the nodal vector n_i about orthogonal directions normal to the mid-surface.

$$u = \sum_{i=1}^{4} N_i u_i + \sum_{i=1}^{4} N_i \zeta h_i \left[\overline{l}_i^{\,x} - \overline{m}_i^{\,x} \right] \begin{bmatrix} \theta_{1i} \\ \theta_{2i} \end{bmatrix} \tag{4.4}$$

$$v = \sum_{i=1}^{4} N_i v_i + \sum_{i=1}^{4} N_i \zeta h_i \left[\overline{l}_i^{\,y} - \overline{m}_i^{\,y} \right] \begin{bmatrix} \theta_{1i} \\ \theta_{2i} \end{bmatrix} \tag{4.5}$$

$$w = \sum_{i=1}^{4} N_i w_i + \sum_{i=1}^{4} N_i \zeta h_i \left[\overline{l}_i^{\,z} - \overline{m}_i^{\,z} \right] \begin{bmatrix} \theta_{1i} \\ \theta_{2i} \end{bmatrix} \tag{4.6}$$

where, u , v and w are the displacements in the global X,Y and Z directions respectively and u_i , v_i and w_i are the displacements at node *i*.

4.2.6.2 Strain functions based on strain-displacement relations

Strains are calculated using the strain-displacement relation given in Equation 4.7.

$$\begin{Bmatrix} \varepsilon_x \\ \varepsilon_y \\ \varepsilon_{xy} \\ \varepsilon_{yz} \\ \varepsilon_{xz} \end{Bmatrix} = \begin{Bmatrix} \dfrac{\partial u}{\partial x} \\ \dfrac{\partial v}{\partial y} \\ \dfrac{\partial u}{\partial y} + \dfrac{\partial v}{\partial x} \\ \dfrac{\partial w}{\partial y} + \dfrac{\partial v}{\partial z} \\ \dfrac{\partial u}{\partial z} + \dfrac{\partial w}{\partial x} \end{Bmatrix} \tag{4.7}$$

Expressing the $\{u, v, w\}$ displacements in terms of $\{u_i, v_i, w_i\}$ and $\{\theta_{1i}, \theta_{2i}\}$, strain-displacement relation takes the form of

$$\{\varepsilon\} = [B]\{u\} \tag{4.8}$$

where, $[B]$ is the strain-displacement matrix and $\{u\}^T = \{u_1, v_{1,} w_1, \theta_{11,} \theta_{12,} \ldots\ u_4, v_{4,} w_4, \theta_{41,} \theta_{42,}\}$ is the displacement vector.

The constitutive relationship between the stress and strain components in the local coordinate system can be written as

$$\{\sigma'\} = \left[\overline{C}\right]\{\varepsilon'\} \tag{4.9}$$

where $\left[\overline{C}\right]$ is the constitutive matrix given by $\left[\overline{C}\right] = [T]^T [C][T]$,

$$[\mathrm{C}] = \begin{bmatrix} \mathrm{Q}_{11} & \mathrm{Q}_{12} & \mathrm{Q}_{13} & \mathrm{Q}_{14} & \mathrm{Q}_{15} & \mathrm{Q}_{16} \\ & \mathrm{Q}_{22} & \mathrm{Q}_{23} & \mathrm{Q}_{24} & \mathrm{Q}_{25} & \mathrm{Q}_{26} \\ & & \mathrm{Q}_{33} & \mathrm{Q}_{34} & \mathrm{Q}_{35} & \mathrm{Q}_{36} \\ & & & \mathrm{Q}_{44} & \mathrm{Q}_{45} & \mathrm{Q}_{46} \\ & \mathrm{SYM} & & & \mathrm{Q}_{55} & \mathrm{Q}_{56} \\ & & & & & \mathrm{Q}_{66} \end{bmatrix} \tag{4.10}$$

and $\mathrm{Q}_{11} = \dfrac{\mathrm{E}_{11}}{1 - \upsilon_{12}\upsilon_{21}}$, $\mathrm{Q}_{12} = \upsilon_{21} \times \mathrm{Q}_{11}$, $\mathrm{Q}_{22} = \dfrac{\mathrm{E}_{22}}{1 - \upsilon_{12}\upsilon_{21}}$, $\mathrm{Q}_{44} = \mathrm{G}_{13}$, $\mathrm{Q}_{55} = \mathrm{G}_{23}$, $\mathrm{Q}_{66} = \mathrm{G}_{12}$, E_{11} and E_{22} are the longitudinal and transverse Young's moduli along the respective material axis, υ_{12} and υ_{21} are the major and minor Poisson's ratios, and G_{12}, G_{13} and G_{23} are the shear moduli. $[T]$ is the transformation matrix which transforms the elasticity matrix in the material axis system to the global coordinate system.

4.2.6.3 Layered shell construction

For the layered shell construction as given in Figure 4.6, the laminate constitutive equation can be obtained by integrating the stress components over the thickness, and is written as

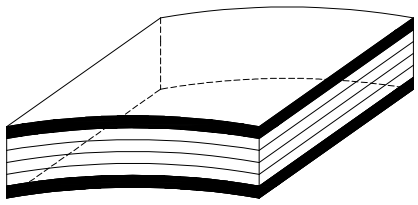

Figure 4.6: Layered shell construction

$$\left\{\begin{matrix}\mathbf{N}\\ \mathbf{M}\end{matrix}\right\}=\left[\begin{array}{c|c}\mathbf{A} & \mathbf{B}\\ \hline \mathbf{B} & \mathbf{D}\end{array}\right]\left\{\begin{matrix}\boldsymbol{\varepsilon}\\ \boldsymbol{\kappa}\end{matrix}\right\} \tag{4.11}$$

where, [A] is the extensional stiffness matrix, [D] is the bending stiffness matrix, and [B] is the extension and bending coupling stiffness matrix.

4.2.6.4 Stiffness evaluation

In the local coordinate system, the total potential energy for the shell is given as

$$\Pi=\frac{1}{2}\int_{\mathrm{v}}\{\varepsilon'\}^{\mathrm{T}}[\mathrm{D}\ ]\{\varepsilon'\}\,\mathrm{dV} \tag{4.12}$$

Minimization of Π with respect to nodal displacements results in the following equation.

$$[K]\{u\}=[F] \tag{4.13}$$

where, [*K*] is the stiffness matrix given by

$$[K]=\int[B^T][\bar{D}][B]dV \tag{4.14}$$

4.2.6.5 Mass matrix

The mass matrix is obtained from the kinetic energy κ of the system and it is given by

$$\kappa=\frac{\rho}{2}\int(\dot{u}+\dot{v}+\dot{w})^2\,dv \tag{4.15}$$

$$\kappa=\frac{1}{2}\{u^T\}[M]\{u\} \tag{4.16}$$

The consistent mass matrix $[M]$ consists of parts corresponding to its translational and rotational DOF. Assuming uniform distribution of mass, the consistent mass matrix is

$$M=\int_v[N]^T[\Gamma][N]dv \tag{4.17}$$

where, [Γ]is the appropriate density matrix and [*N*] is the shape function matrix.

4.2.6.6 Static analysis

After formulating the stiffness matrix, static analysis is carried out with the applied pressure load as given in Equation 4.18.

$$[K]\{\phi\}-\{F\}=0 \tag{4.18}$$

where, $\{\phi\}$ is the displacement vector and $\{F\}$ is the applied load vector

4.2.6.7 Buckling analysis

For local buckling analysis, an eigenvalue approach is used, which is given by Equation 4.19.

$$\left([K]+\lambda_i[S]\right)\{\psi_i\}=\{0\} \tag{4.19}$$

where, $[\mathrm{S}]$ is the stress stiffening matrix, $[\mathrm{K}]$ is stiffness matrix, ψ_i is the eigenvector and λ_i is the eigenvalue.

4.2.6.8 Failure theory

Figure 4.7 shows a lamina in which fibers are oriented in the x direction. In this figure, X, Y and Z are the global coordinate axes and x, y and z are the local material axes.

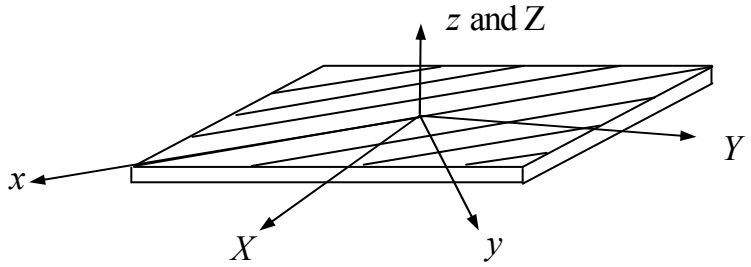

Figure 4.7: Description of lamina principal and global coordinate axes

Several failure theories have been proposed to predict the onset of damage in fiber reinforced composite lamina [10]. The simplest among these theories is the Maximum Stress Failure Theory, which is used in this study and is given by the following conditions. For failure not to occur,

$$\begin{aligned}
&S_{xC} < \sigma_{xx} < S_{xT}\\
&S_{yC} < \sigma_{yy} < S_{yT}\\
&S_{zC} < \sigma_{zz} < S_{zT}\\
&\tau_{xy} < S_{xy}\\
&\tau_{xz} < S_{xz}\\
&\tau_{yz} < S_{yz}
\end{aligned} \tag{4.20}$$

where S_{xT}, S_{yT} and S_{zT} are the tensile strength limits and S_{xC}, S_{yC} and S_{zC} are the compressive strength limits in x, y and z-directions, respectively. Also, S_{xy}, S_{xz} and S_{yz} are the shear strength limits in xy, xz and yz planes. σ_{xx}, σ_{yy} and σ_{zz} are the normal stresses and τ_{xy}, τ_{xz} and τ_{yz} are the shear stresses generated in local material directions (Figure 4.7).

4.3 LOCAL DEFLECTIONS

A uniform pressure load of 1 N/m^2 is applied on the top surface of the sandwich plate to observe the nature of local deflections of the faces and the webs, both with the laminate construction $(0/90)_s$. The local deflection patterns of the sandwich plates with triangular and rectangular cores are shown in Figure 4.8 (a) and (b) respectively. As can be seen in Figure 4.8 (a), there are significant local deflections in the top face of the sandwich plate with the triangular core, but bottom face shows very little deflection. For the sandwich plate with the rectangular core, the bottom face has a lower deflection than the top face, but not as low as the bottom face of the sandwich plate with the triangular core. It is also observed that local deflections of the top faces are higher in the outer unit cells compared to the two middle unit cells. At the junctions of the faces and webs, the deflections are also very low, which is due to the support provided by the webs at these junctions. The maximum local deflections in all four unit cells of the sandwich plates with the triangular core are much higher than the maximum deflections with the rectangular core. This is due to the greater unsupported lengths between the junctions in the case of the triangular core compared to the rectangular core.

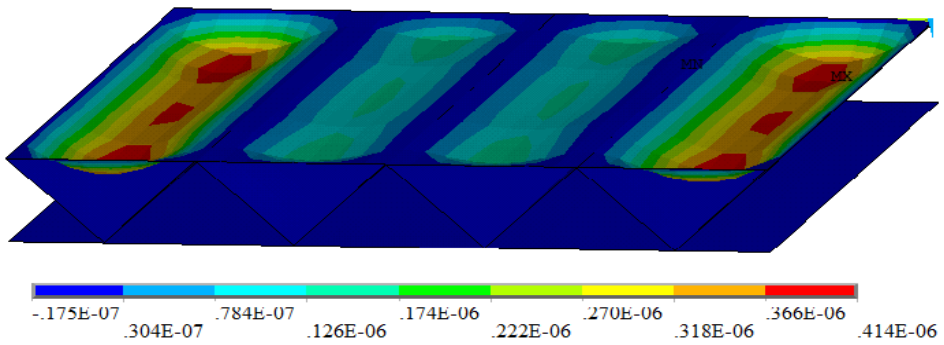

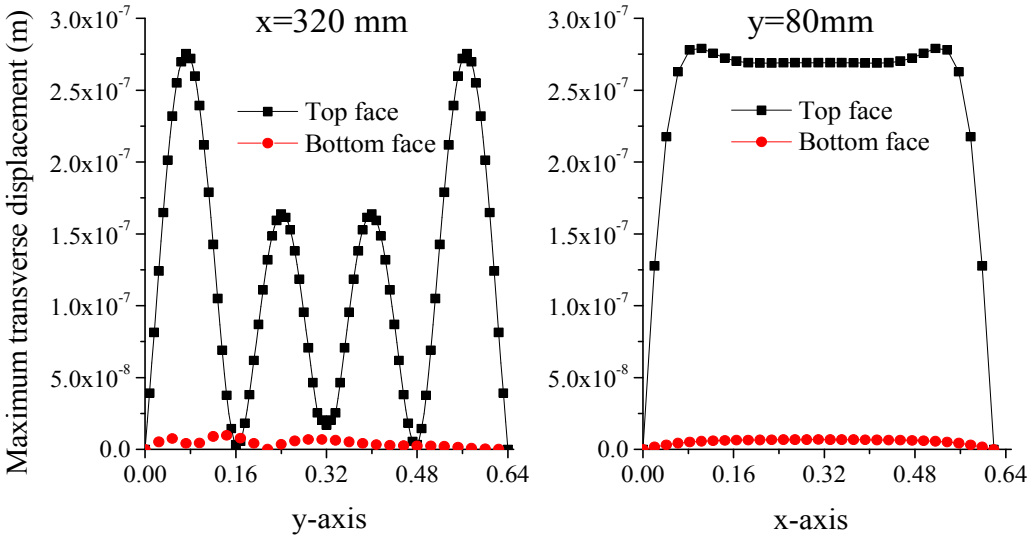

(a) $\theta = 45^{\circ}$ (Triangular Core)

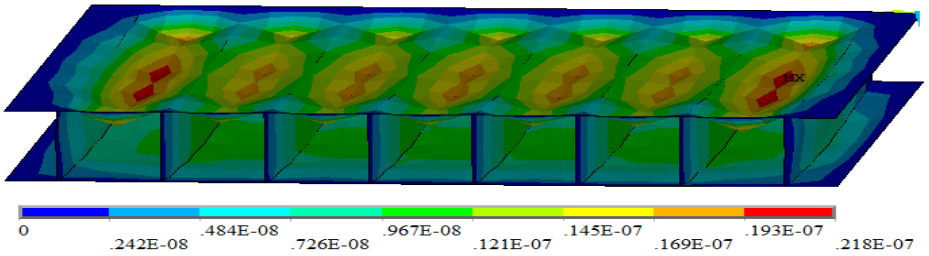

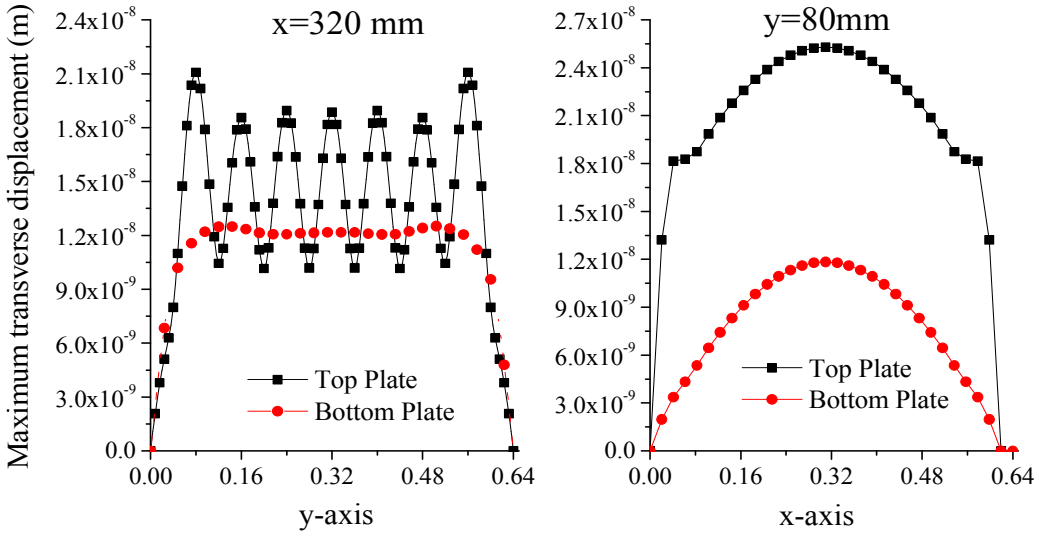

(b) $\theta = 90^{\circ}$ (Rectangular Core)

Figure 4.8: Local deflections of sandwich plates with web inclination angles (a) $\theta = 45^{\circ}$ and (b) $\theta = 90^{\circ}$ subjected to a uniform pressure load of 1 N/m^2

In Figure 4.9, the maximum global deflections of the sandwich plates determined using the homogenization method are compared with the maximum local deflections determined using the FE analysis for three different web inclination angles, $\theta = 45^{\circ}, 48^{\circ}$, and 90º. It is interesting to note that the maximum local deflections are slightly higher than the maximum global deflections for all three web inclination angles, but the trends are similar.

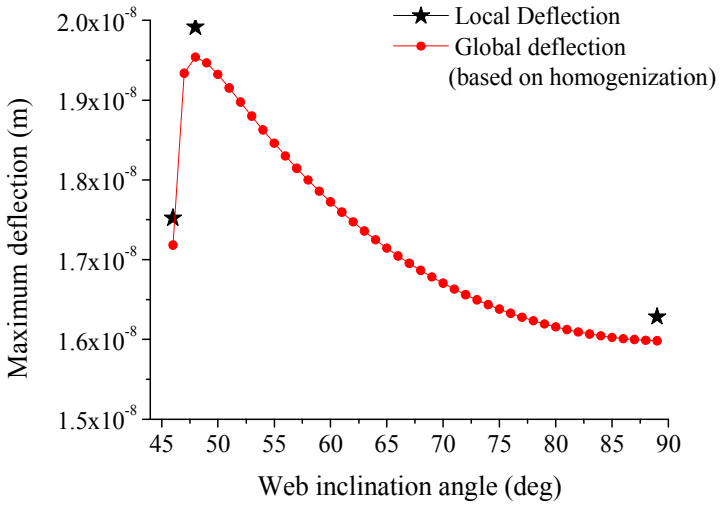

Figure 4.9: Maximum global and local deflections of sandwich plates with various web inclination angles and a uniform pressure load of 1 N/m^2 applied on the top surface

4.4. BUCKLING ANALYSIS

For calculating the critical buckling mode shapes and pressure loads, eigenvalue buckling analysis in ANSYS is used. The laminate constructions in the faces and the webs of the sandwich plates are $(0/\alpha)_s$ and $(\pm\alpha)_s$, in which α is the fiber orientation angle with respect to the x-axis of the plate. The fiber orientation angle is varied between 0 and 90º in steps of 15º. The web inclination angles are 45 and 90º, representing triangular and rectangular cores, respectively.

4.4.1 Buckling Mode Shape

It is observed that the buckling mode shape is highly dependent on the web inclination angle in the sandwich plates and is similar for both laminate constructions.

The first buckling mode shape for the composite sandwich plate with laminate construction $(0/0)_s$ and web inclination angle $\theta = 45°$ is shown in Figure 4.10. The top face on which the pressure load is applied has higher bending displacements compared to the bottom face. The webs have much less bending displacements and even though all inclined webs show evidence of buckling, the second web from each side exhibits the highest bending displacements.

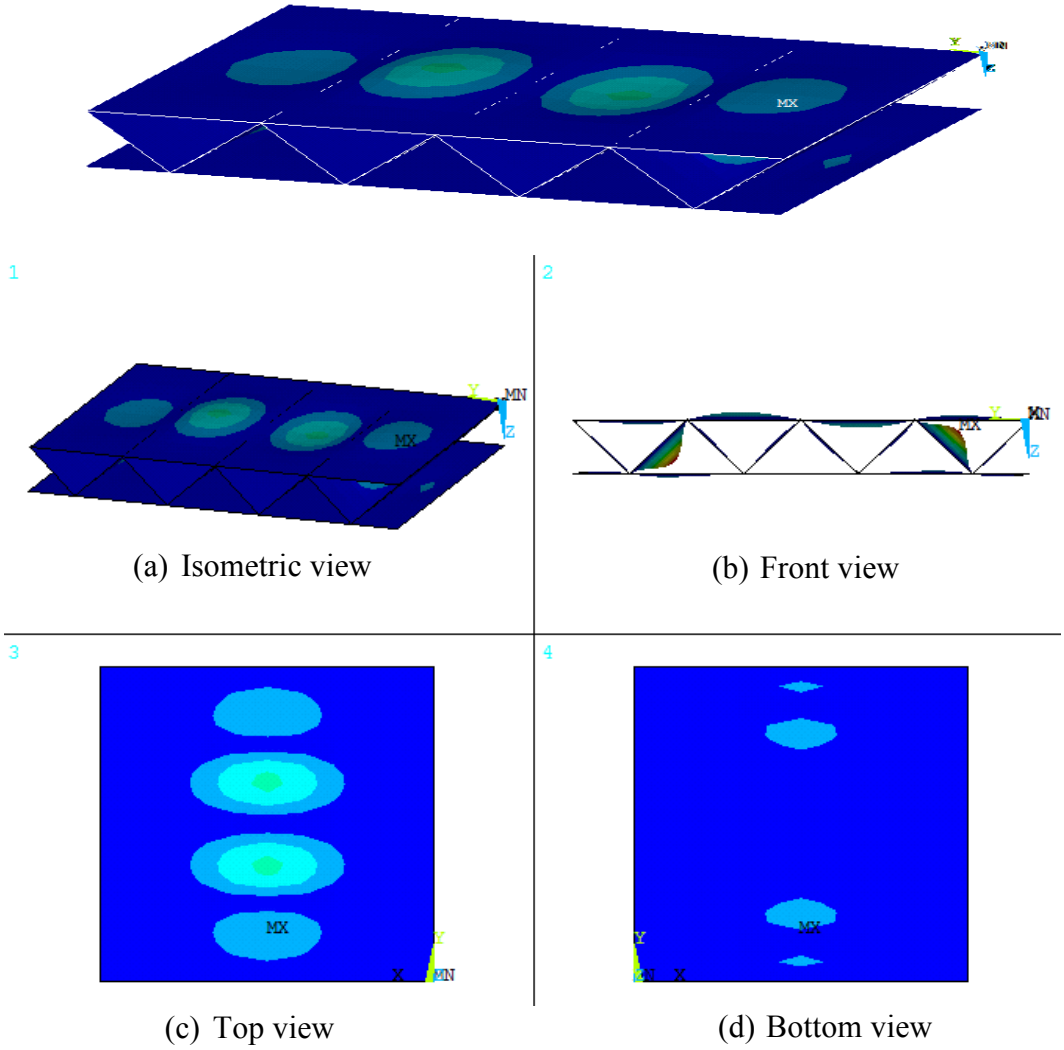

Figure 4.10: Buckling mode shape of composite sandwich plate with laminate construction $(0/0)_s$ and web inclination angle $\theta = 45°$

The first buckling mode shape for the composite sandwich plate with laminate construction $(0/0)_s$ and web inclination angle $\theta = 90°$ is shown in Figure 4.11. The top

face on which the pressure load is applied has less bending displacement compared to the bottom face and all interior webs show much greater bending displacement and different mode shapes than the two outer webs.

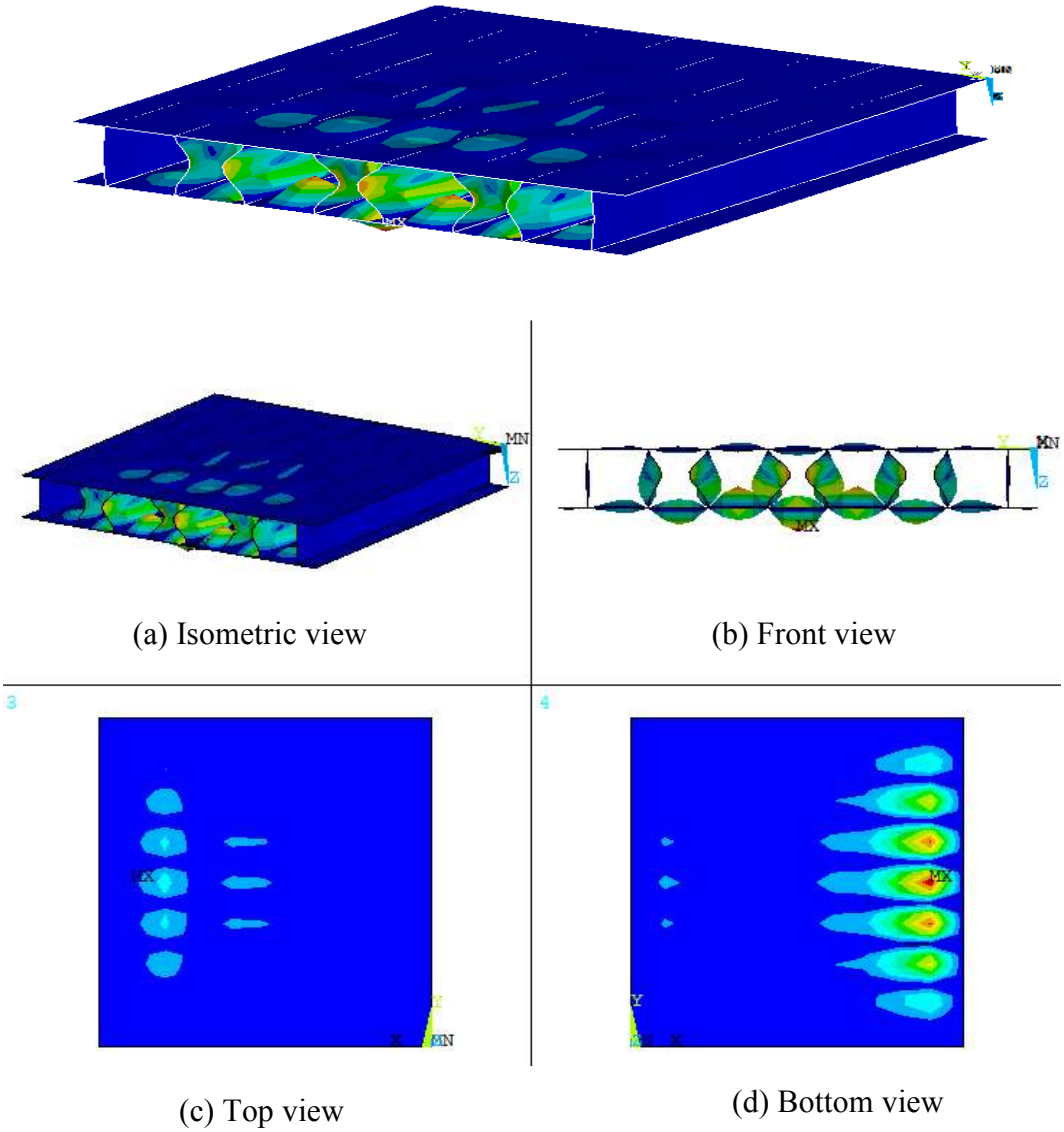

Figure 4.11: Buckling mode shape of composite sandwich plate with laminate construction $(0/0)_s$ and web inclination angle $\theta = 90^o$

4.4.2 Effect of Fiber Orientation Angle on Critical Buckling Pressure Load

The variation of the critical buckling pressure load with fiber orientation angle in the two laminate constructions considered is shown in Figure 4.12 for web inclination angles $\theta = 45°$ and $90°$. The critical buckling pressure load has the highest value when

the fiber orientation angle α = 0º. For all other fiber orientation angles, the critical buckling pressure load is an order of magnitude higher when $\theta = 90°$, i.e, the core is rectangular. When $\theta = 45°$, critical buckling pressure load with the $(0/\alpha)_s$ laminate construction does not change much with increasing α, but it decreases rapidly with increasing α with the $(\pm\alpha)_s$ laminate construction. When $\theta = 90°$, the critical buckling pressure load decreases with increasing α for both laminate constructions. The critical buckling pressure load is higher with the $(0/\alpha)_s$ laminate construction, than with the $(\pm\alpha)_s$ laminate construction. At α = 45º, the critical buckling pressure loads are nearly equal with both laminate constructions.

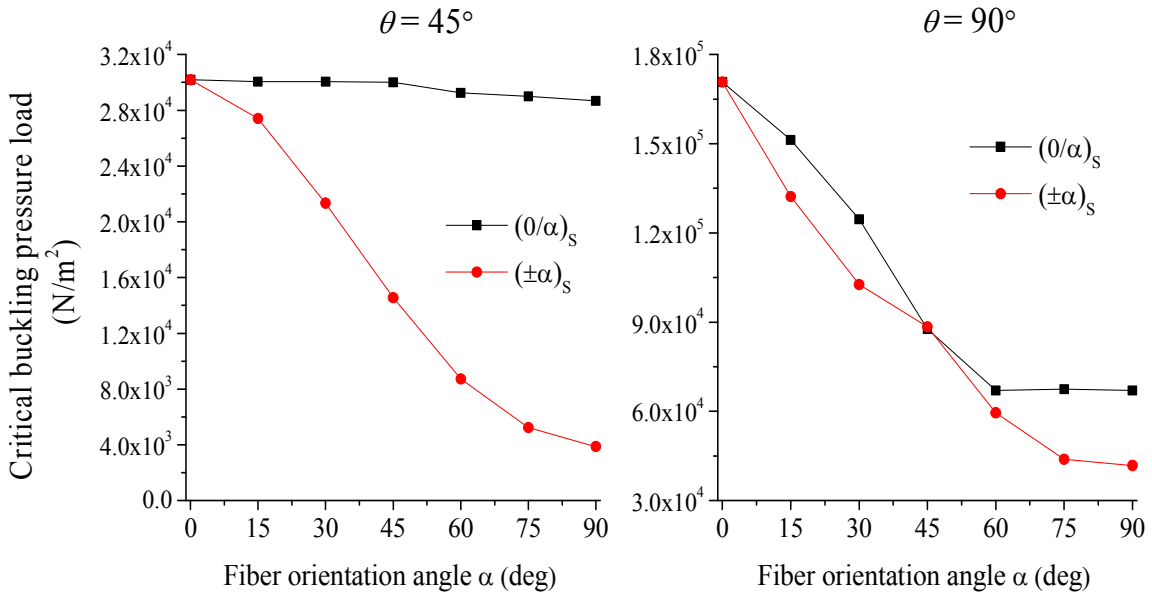

Figure 4.12: Effect of fiber orientation angle α on the critical buckling pressure load for web inclination angles θ = 45º and 90º

4.5 FAILURE ANALYSIS OF COMPOSITE SANDWICH PLATES WITH CORRUGATED CORE

In this section, failure analyses of composite sandwich plates with corrugated core of web inclination angle $\theta = 45°$ and $90°$ are presented. The laminate construction in this section is $(0/0)_s$ for both the faces and webs. The step-wise pressure load application is described in Section 4.2. The LAYER and RSYS commands in the post-processing mode

of ANSYS are used to calculate stresses in each lamina of all 9,600 elements. The maximum stress theory is used as the failure criterion. The elastic properties of the laminas in which stresses exceed the strength limits are degraded by 50% before proceeding to the next load step. A flow chart for failure analysis of composite sandwich plates with corrugated core is given in Figure 4.13.

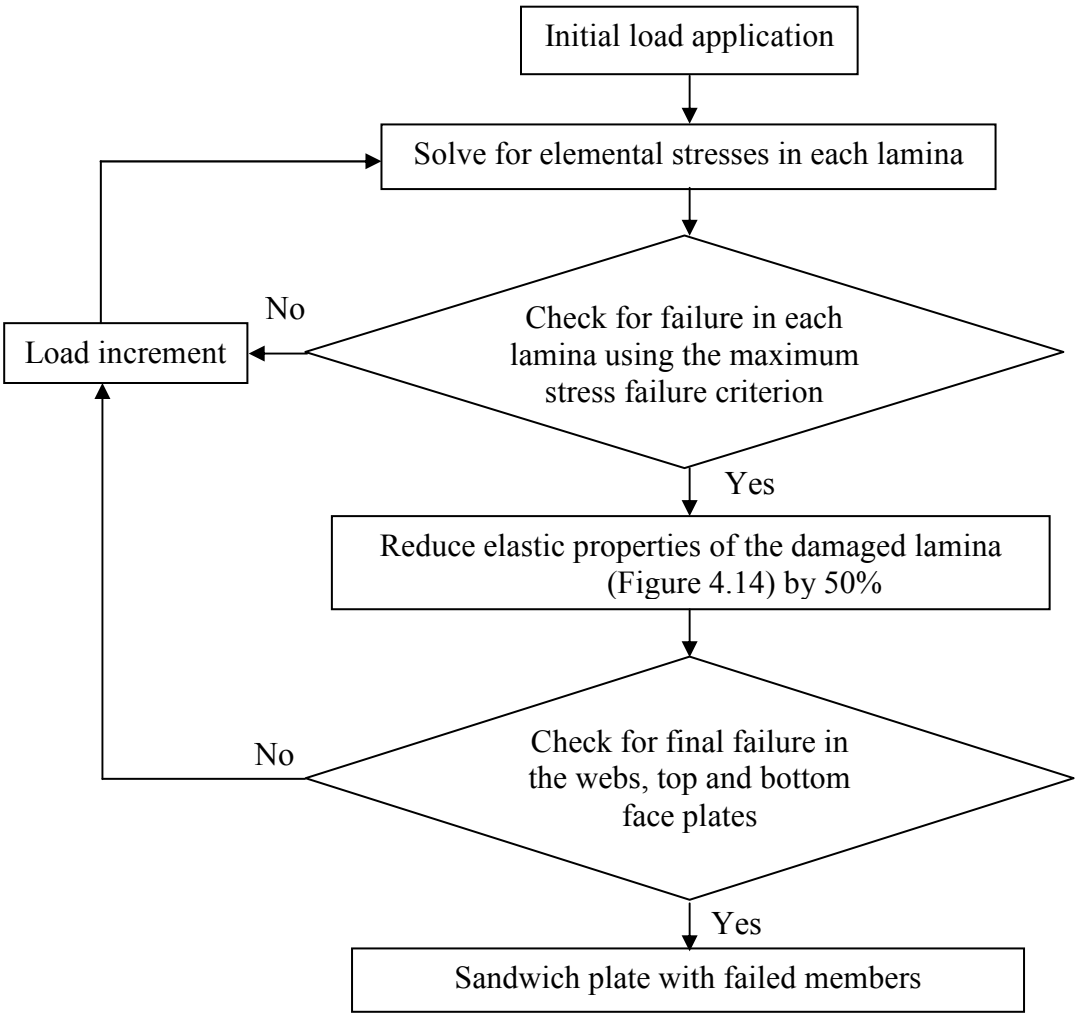

Figure 4.13: Flow chart for failure analysis of composite sandwich plate with corrugated core

Figure 4.14 shows an example of a damaged lamina in one of the elements. The three other laminas in the element are still undamaged. The damage on the top element is due to one or more stresses exceeding the strength limits. The elastic properties of the damaged lamina in this element are reduced by 50% before proceeding with the next pressure load increment.

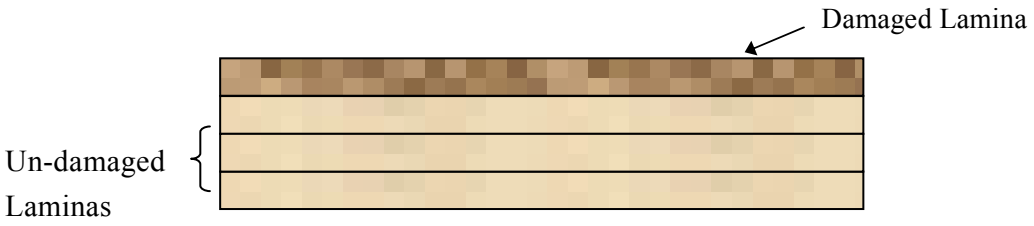

(b) Damaged lamina

Figure 4.14: Example of an element with damaged laminas

The stress zones are indicated by color contours, which are shown in Figure 4.15. The color red indicates the positive maximum zones, the color blue indicates the negative maximum zones and the color green indicates the absolute minimum zones.

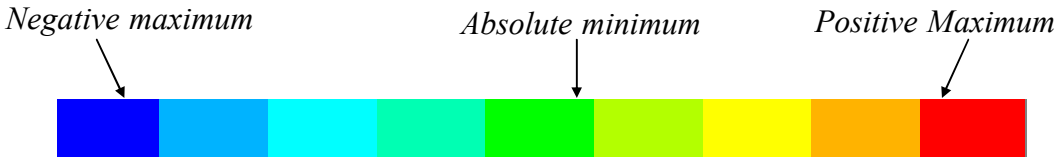

Figure 4.15: Color code used in contour plots of ANSYS in displaying intensity of deflections and stresses

4.5.1 Triangular Core ($\theta = 45^o$)

Normal and shear stress contours in the top face of the composite sandwich plates with web inclination angle θ = 45º and an applied pressure load p_o =1 N/m^2 are plotted in Figure 4.16. Similarly, normal and shear stresses in the bottom face and the web members are shown in Figure 4.17 and Figure 4.18.

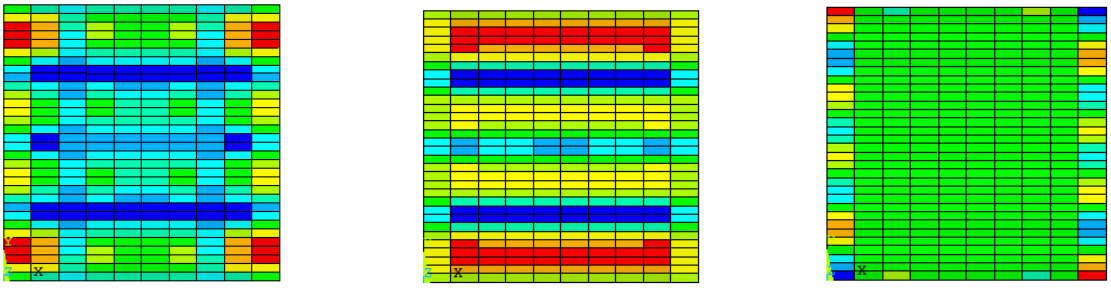

(a) Normal stress σ_x (b) Normal stress σ_y (c) Shear stress τ_{xy}

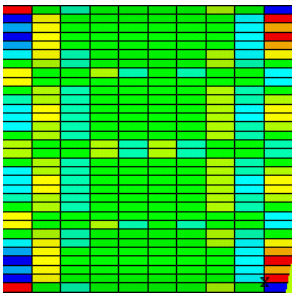

(d) Shear stress τ_{xz}

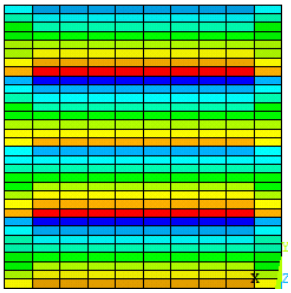

(e) Shear stress τ_{yz}

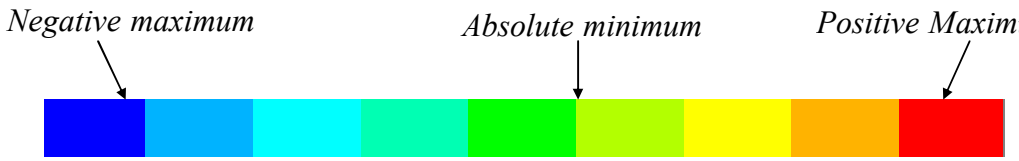

Figure 4.16: Normal and shear stress contours in the top face at p_0=1N/m^2

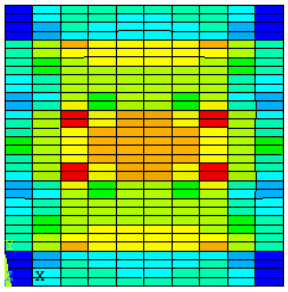

(a) Normal stress σ_x

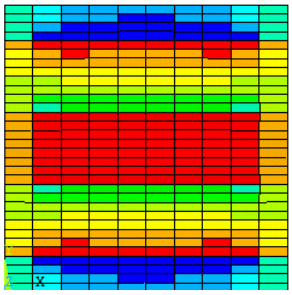

(b) Normal stress σ_y

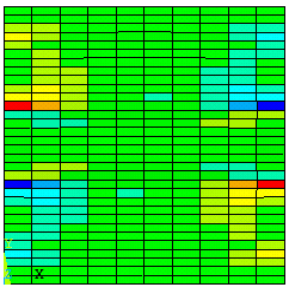

(c) Shear stress τ_{xy}

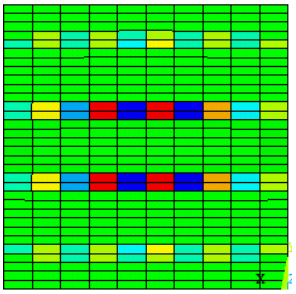

(d) Shear stress τ_{xz}

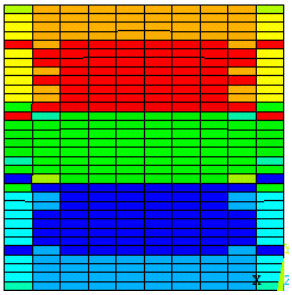

(e) Shear stress τ_{yz}

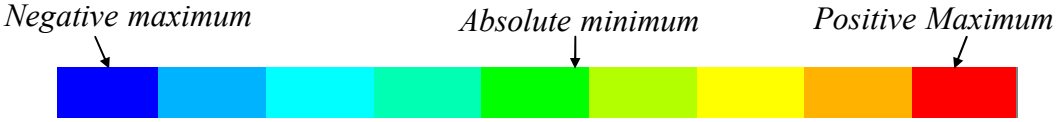

Figure 4.17: Normal and shear stress contours in the bottom face at p_0=1N/m^2

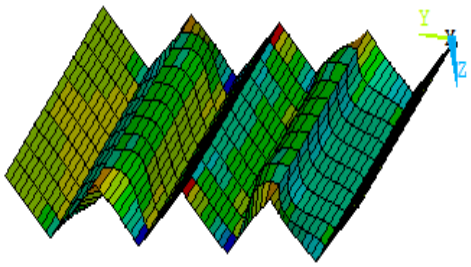

(a) Normal stress σ_x

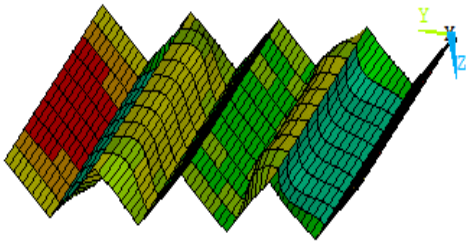

(b) Normal stress σ_y

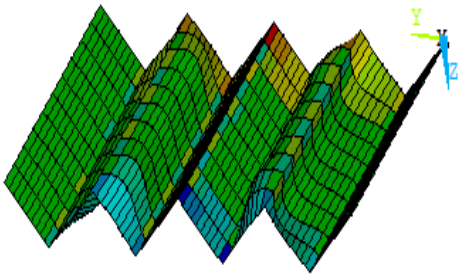

(c) Shear stress τ_{xy}

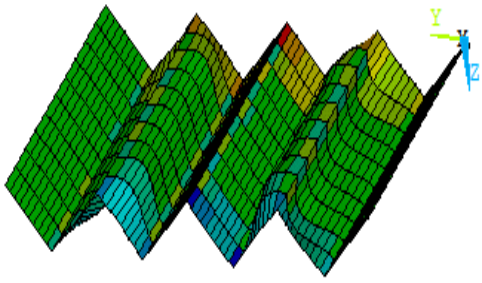

(d) Shear stress τ_{xz}

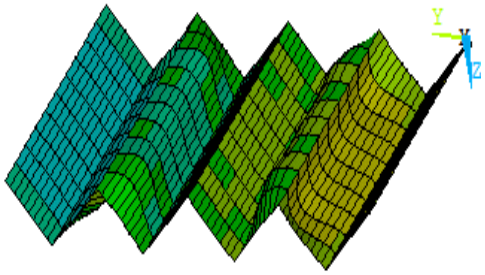

(e) Shear stress τ_{yz}

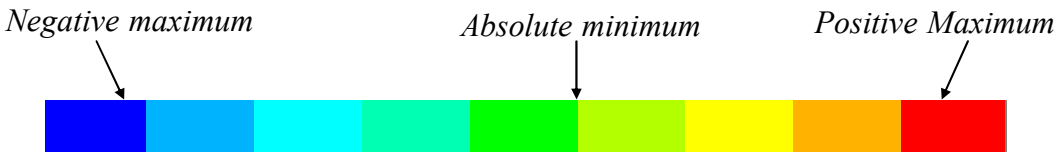

Figure 4.18: Normal and shear stress contours in the web members at p_0=1N/m^2

As the applied pressure load p_0 on the top face of the sandwich plate is increased, local stresses in the elements belonging to the top face, bottom face and web members increase. When one or more of the local stresses in a lamina exceed the corresponding strength limit, the lamina is considered damaged and its elastic properties are reduced by

50% before continuing with the next pressure load application. The damaged elements at 20, 40, 60, 80 and 95% damage levels in the top face, web members and bottom face are shown in Figure 4.19, Figure 4.20 and Figure 4.21. It is noticed that the top face is 95% damaged when damage level in the sandwich plate is only 40%. The bottom face and the web members reach 95% damage at 95% damage level in the sandwich plate.

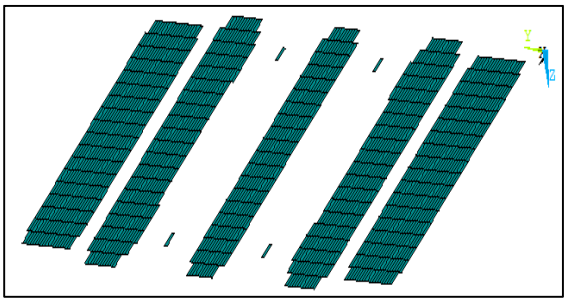

Damage=20%

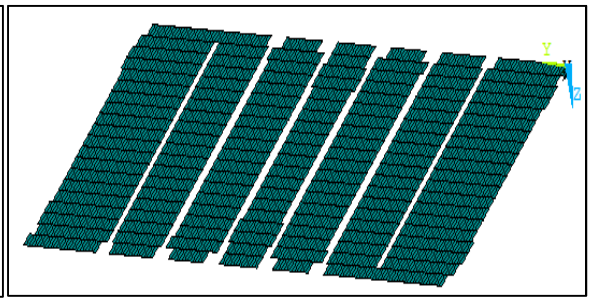

Damage=40%

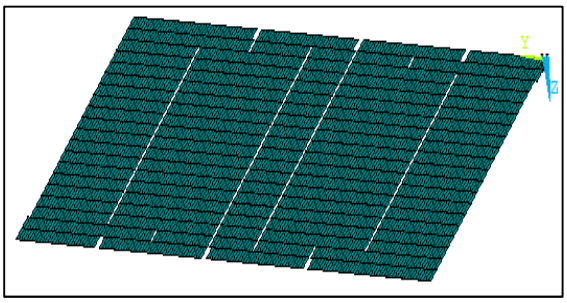

Damage=60%

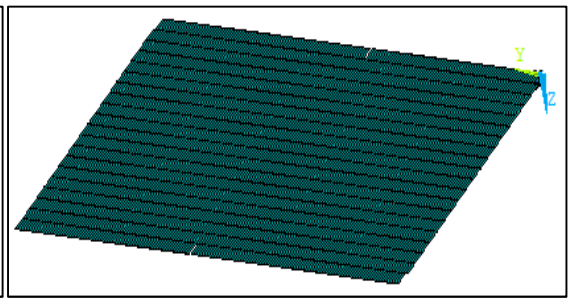

Damage=80%

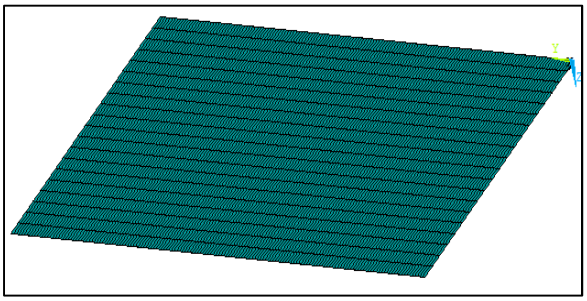

Damage=95%

Figure 4.19: Damaged elements in the top face at 20, 40, 60, 80 and 95 percent damage levels in the sandwich plate with web inclination angle $\theta = 45^{\circ}$

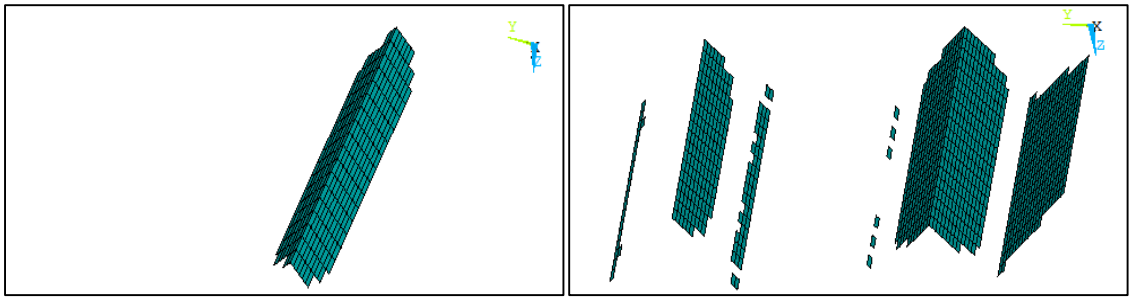

Damage=20% Damage=40%

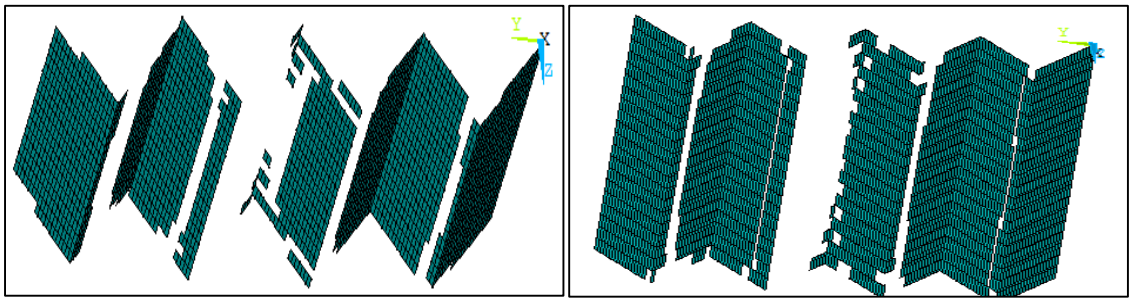

Damage=60% Damage=80%

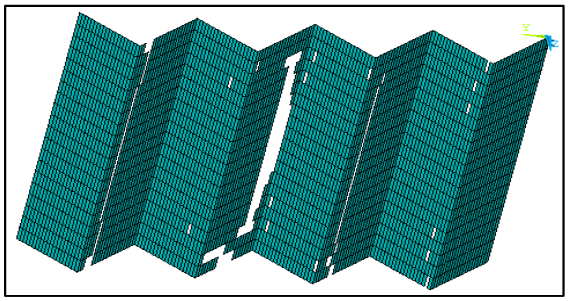

Damage=95%

Figure 4.20: Damaged elements in the web members at 20, 40, 60, 80 and 95 percent damage levels in the sandwich plate with web inclination angle $\theta = 45^{o}$

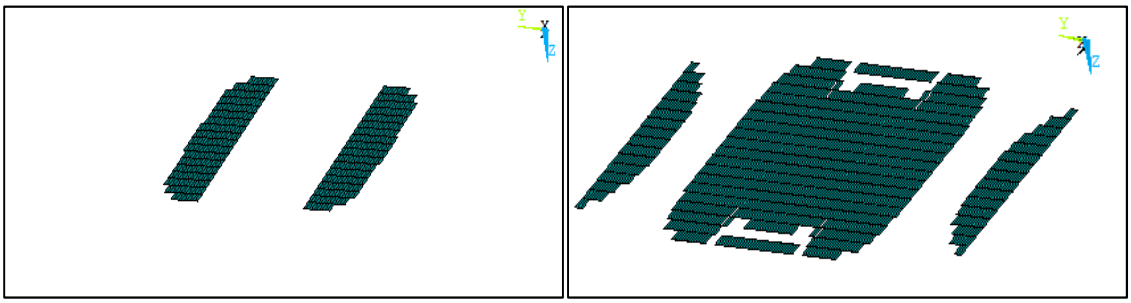

Damage=60% Damage=80%

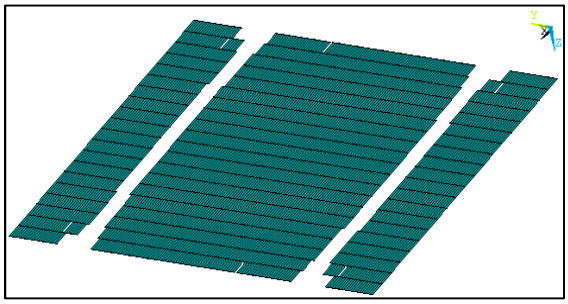

Damage=95%

Figure 4.21: Damaged elements in bottom face at 20, 40, 60, 80 and 95 percent damage levels in the sandwich plate with web inclination angle $\theta = 45^{\circ}$

Maximum stress values in the top face, bottom face and web members with increasing pressure up to a maximum pressure load of 6 x 10^5 N/m^2 are plotted in Figure 4.22 - Figure 4.29. The strength limits are also shown on these figures. It can be observed in Figure 4.22 that the maximum local normal stress in the x-direction σ_x in the top and bottom faces does not exceed the strength limits S_{xt} and S_{xc}. Similar observations can be made about several other stress components. The first damage occurs at p_0 = 5,000 N due to the maximum local stress in the y-direction σ_y on the top face exceeding the strength limit S_{yt}. Pressures (in N/m^2) at which stresses in the top face, bottom face and web members exceed the failure strength limits are tabulated in Table 4.4. It is observed that failure is initiated in the top face, followed by the web members and the bottom face. Pressure loads at 20, 40, 60, 80 and 95% damage levels in the sandwich plate and the corresponding damage levels in the top face, bottom face and web members are listed in Table 4.5. The pressure load at which 20% of the sandwich plate is damaged is 43,000 N/m^2 and the pressure load at which 95% of the sandwich plate is damaged is 553,000 N/m^2.

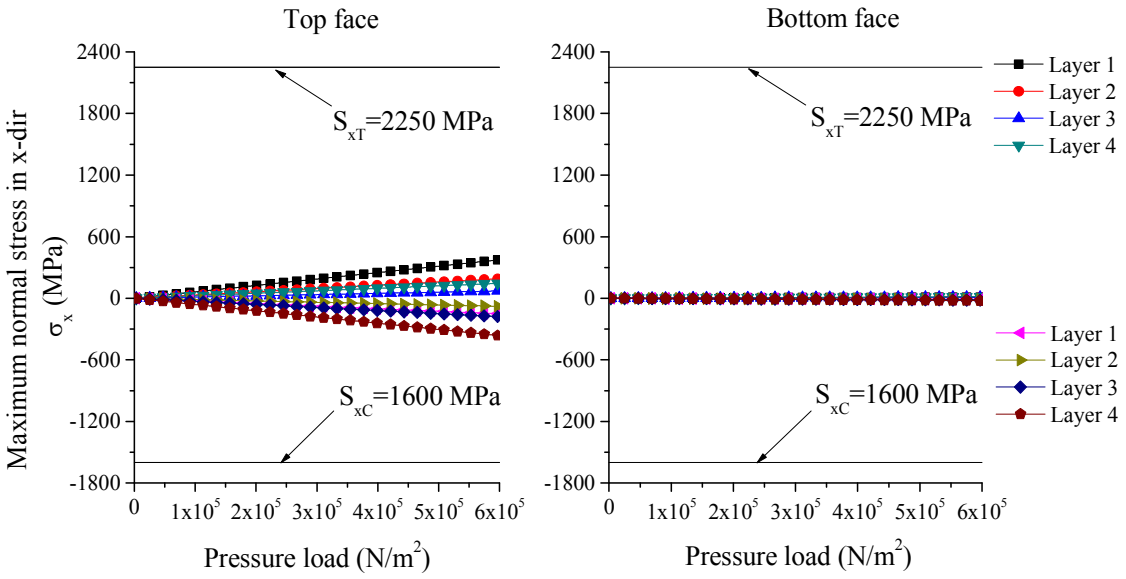

Figure 4.22: Maximum normal stress σ_x in the top and bottom faces of the composite sandwich plate with web inclination angle $\theta = 45°$

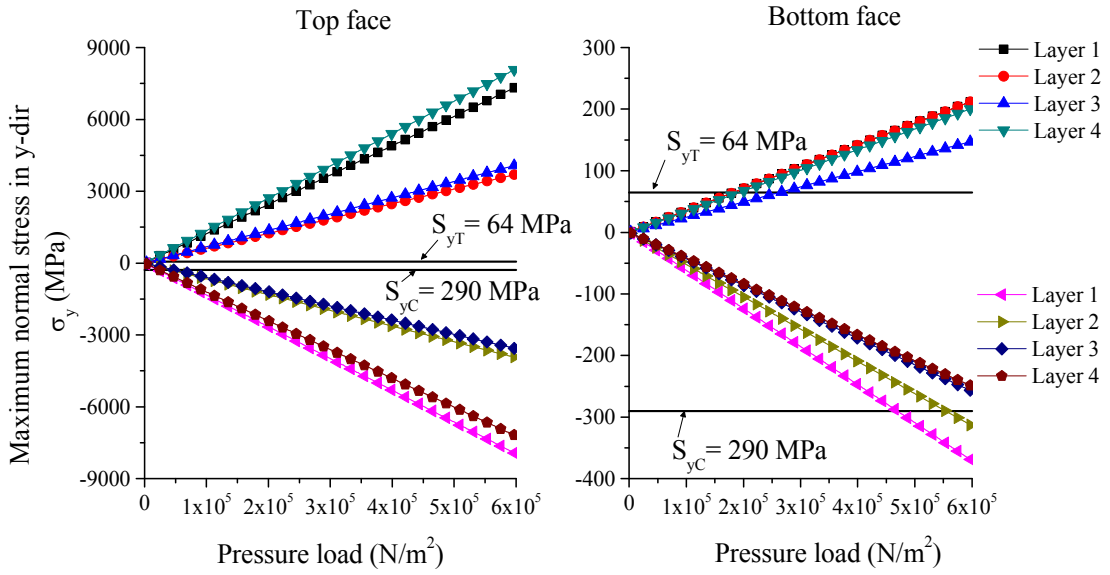

Figure 4.23: Maximum normal stress σ_y in the top and bottom faces of the composite sandwich plate with web inclination angle $\theta = 45°$

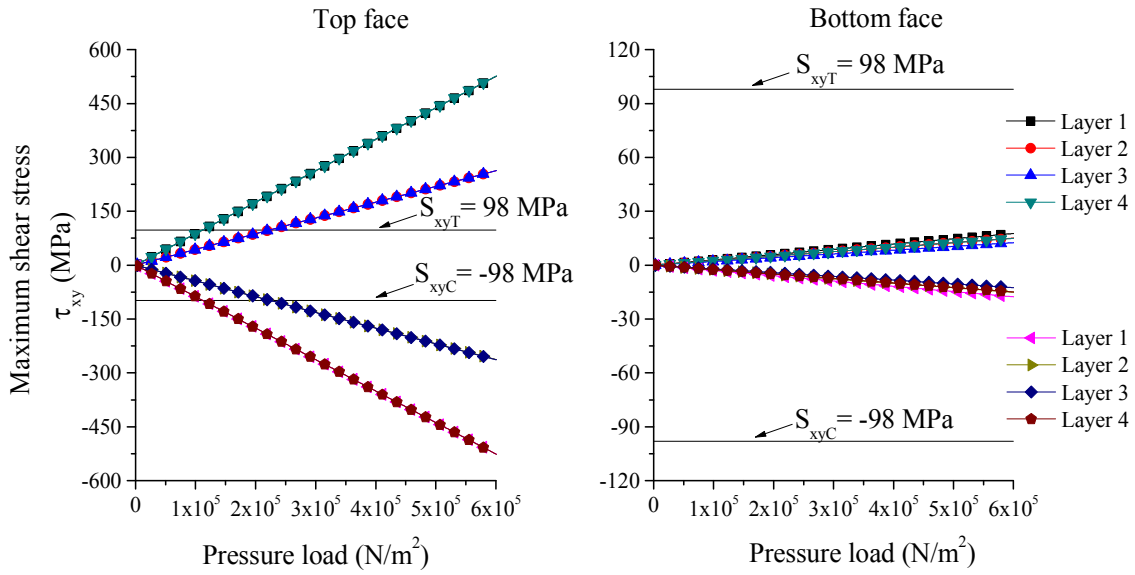

Figure 4.24: Maximum shear stress τ_{xy} in the top and bottom faces of the composite sandwich plate with web inclination angle θ= 45º

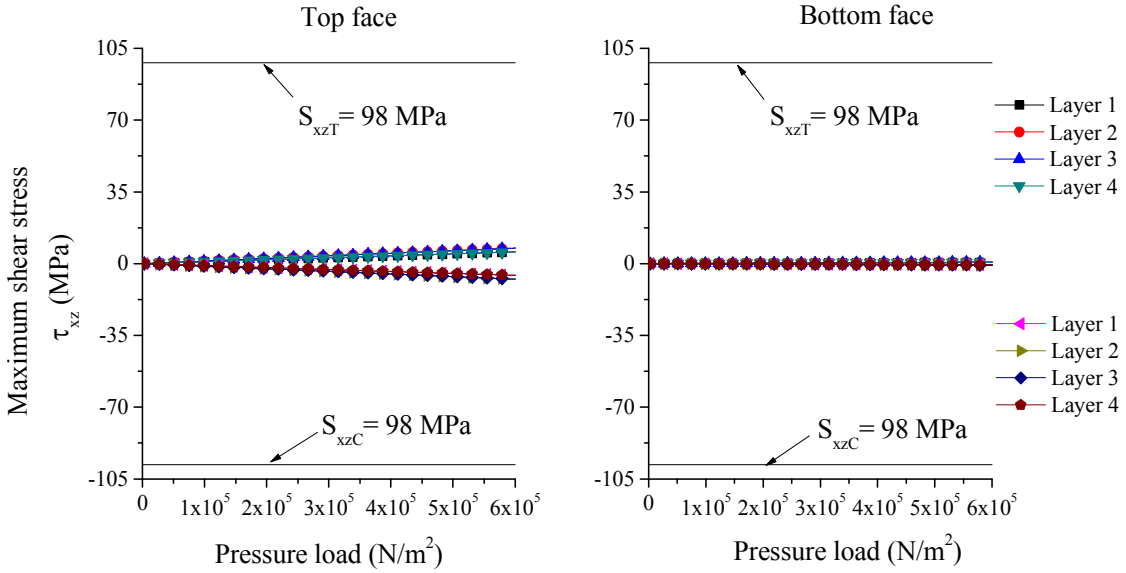

Figure 4.25: Maximum shear stress τ_{xz} in the top and bottom faces of the composite sandwich plate with web inclination angle θ = 45º

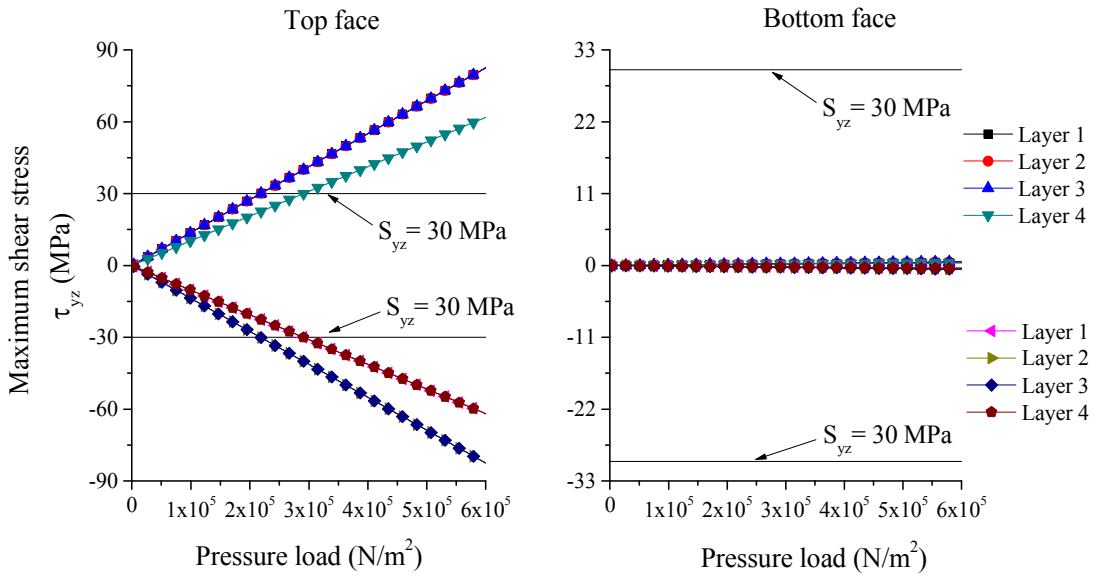

Figure 4.26: Maximum shear stress τ_{yz} in the top and bottom faces of the composite sandwich plate with web inclination angle $\theta = 45°$

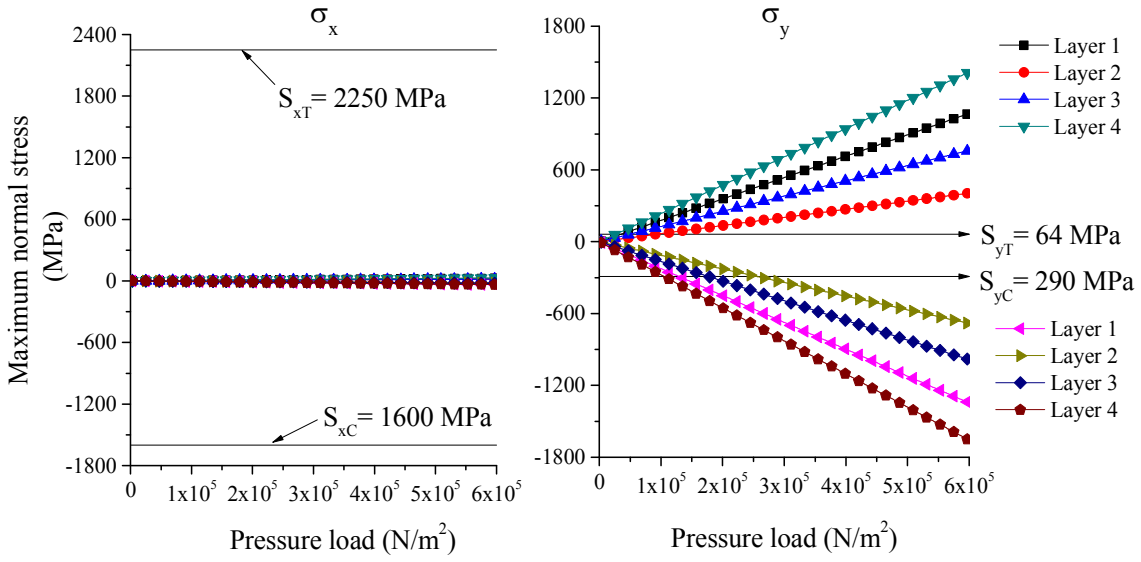

Figure 4.27: Maximum stress normal σ_x and σ_y, in one of the web members of the composite sandwich plate with web inclination angle $\theta = 45°$

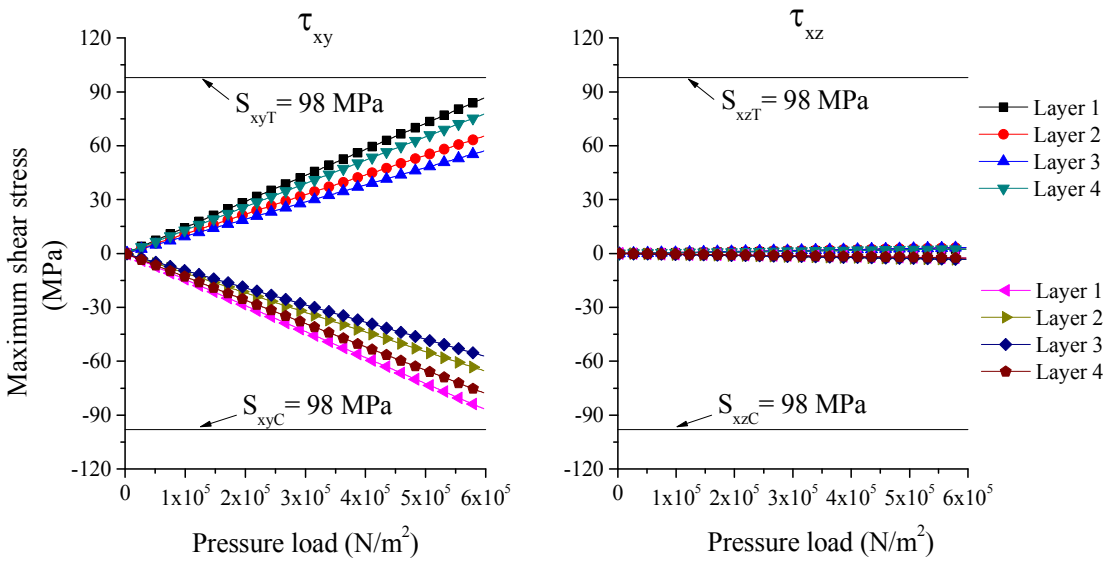

Figure 4.28: Maximum shear stress τ_{xy} and τ_{xz} in one of the web members of the composite sandwich plate with web inclination angle $\theta = 45^{o}$

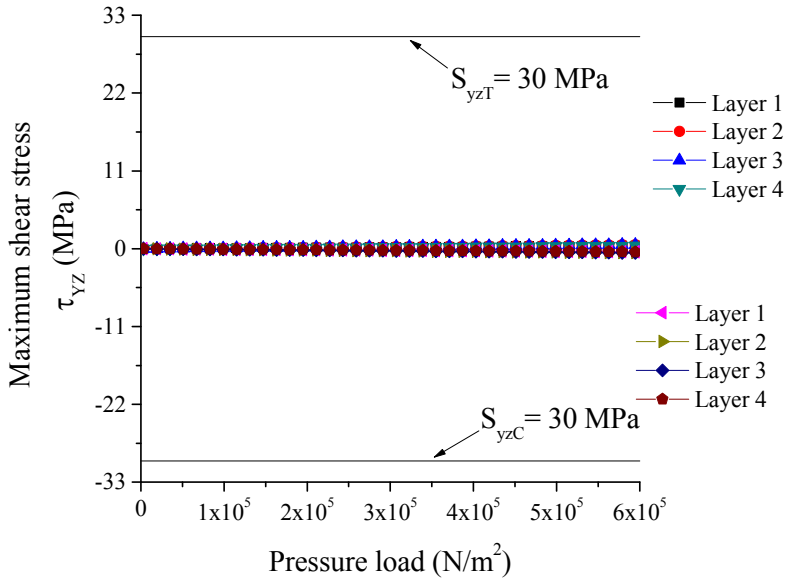

Figure 4.29: Maximum shear stress τ_{yz} in one of the web members of the composite sandwich plate with web inclination angle $\theta = 45^{o}$

Table 4.4: Applied pressure load (in N/m^2) at which stresses exceed the failure strength limit

Stress	Failure mode	Pressure load (N/m^2)		
		Top	Bottom	web
σ_x	Tensile failure	--	--	--
	Compressive failure	--	--	--
σ_y	Tensile failure	5,000	180,000	10,000
	Compressive failure	23,000	470,000	103,000
τ_{xy}	Shear failure	113,000	--	--

Table 4.5: Damage in top and bottom faces and web members at different damage levels in the sandwich plate with web inclination angle $\theta = 45^o$

Damage in the sandwich plate (%)	Pressure load (N/m^2)	Damage in top and bottom faces and web members (%)		
		Top face	Bottom face	Web members
20	43,000	49	0	12
40	103,000	94	0	30
60	323,000	99	16	65
80	423,000	99	61	78
95	553,000	100	90	94

4.5.2 Rectangular Core ($\theta = 90^o$)

Normal and shear stress contours in the top face of the composite sandwich plates with web inclination angle $\theta = 90^o$ and an applied pressure load $p_o = 1 N/m^2$ are plotted in Figure 4.30. Similarly, normal and shear stress components in the bottom face and the web members are shown in Figure 4.31 and Figure 4.32.

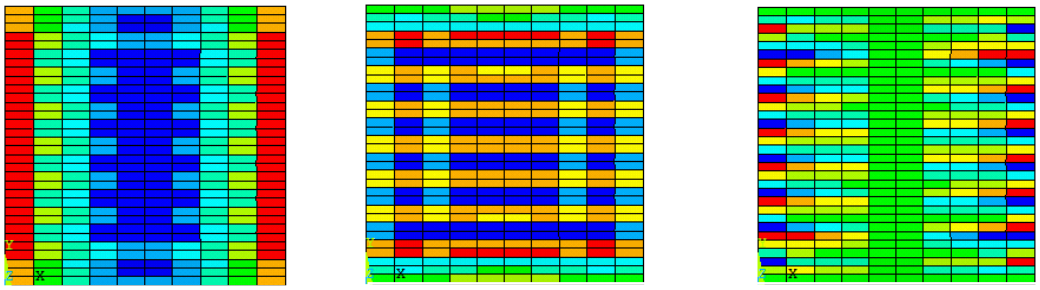

(a) Normal stress σ_x (b) Normal stress σ_y (c) Shear stress τ_{xy}

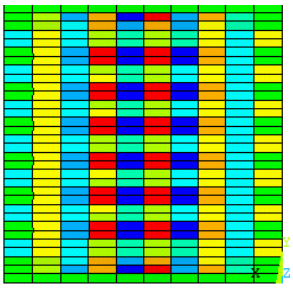

(d) Shear stress τ_{xz}

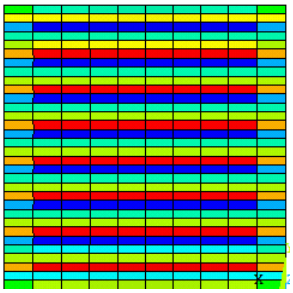

(e) Shear stress τ_{yz}

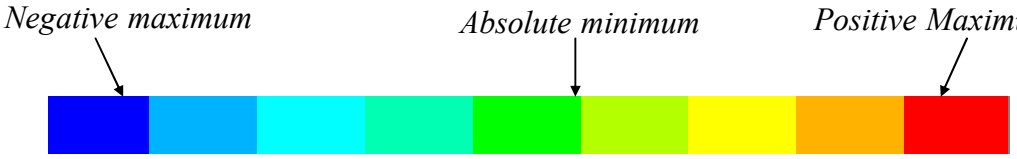

Figure 4.30: Normal and shear stress contours on the top face at p_0=1N/m^2

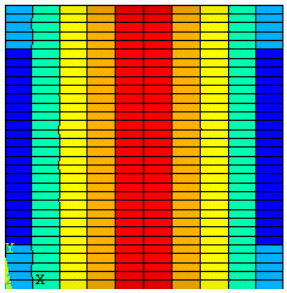

(a) Normal stress σ_x

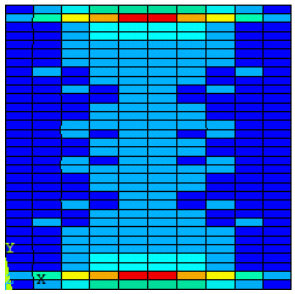

(b) Normal stress σ_y

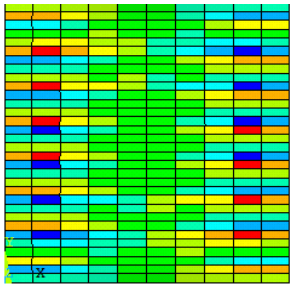

(c) Shear stress τ_{xy}

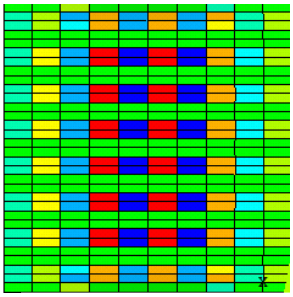

(d) Shear stress τ_{xz}

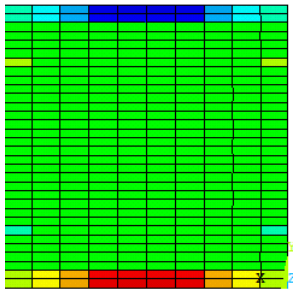

(e) Shear stress τ_{yz}

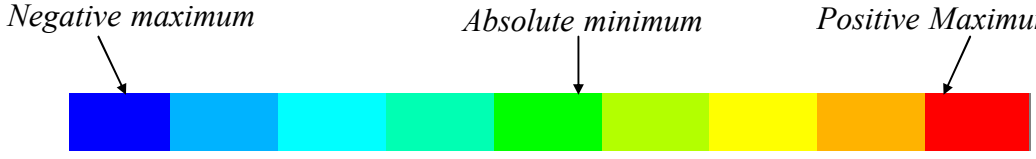

Figure 4.31: Normal and shear stress contours on the bottom face at p_0=1N/m^2

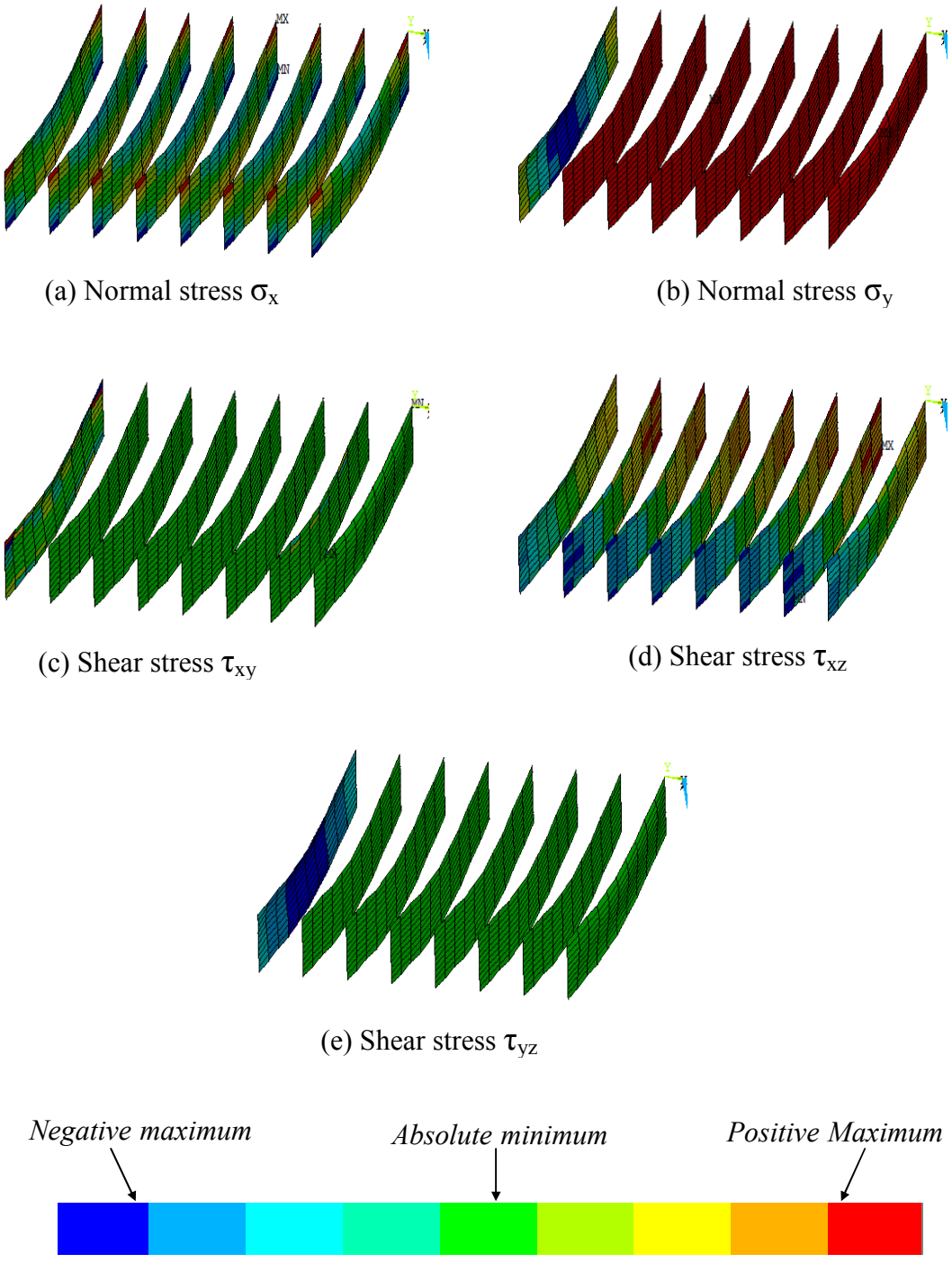

Figure 4.32: Normal and shear stress contours on the web members at p_0=1N/m^2

The damaged elements in the top face, bottom face and web members at 20, 40, 60, 80 and 95% damage levels in the sandwich plate are shown in Figure 4.33 - Figure 4.35. Maximum stress values are plotted in Figure 4.36 - Figure 4.43 as a function of

increasing pressure. As with the triangular core, several stress components do not exceed the corresponding strength limits. The stress component that causes the first damage is σ_y in the top face which exceeds S_{yt} when the applied pressure load reaches 33,000 N/m^2. This pressure load is five times higher than the pressure load at which the first damage appears in the sandwich plate with triangular core. The pressure loads at which the other strength limits are exceeded are given in Table 4.6. In Table 4.7 it is noticed that the top face on which the pressure load is applied is completely damaged (i.e., 99 percent) at the 60 percent damage level in sandwich plate. Complete damage of the bottom face and the web members occurs simultaneously with complete damage (i.e., 95 percent) of the sandwich plate. The pressure load at which 20% of the sandwich plate is damaged is 175,000 N/m^2 and the pressure load at which 95% of the sandwich plate is damaged is 600,000 N/m^2. Both these loads are significantly higher than the corresponding loads for sandwich plates with triangular core.

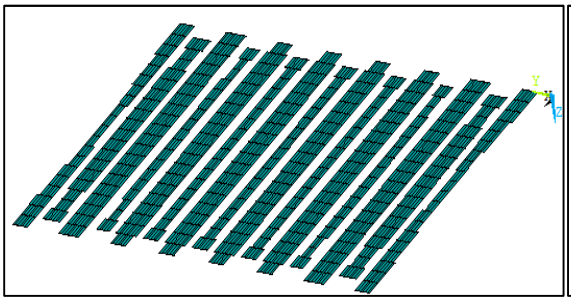

Damage=20%

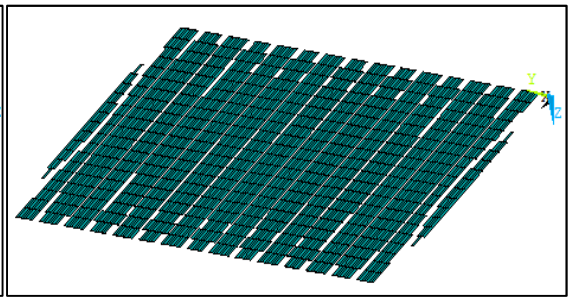

Damage=40%

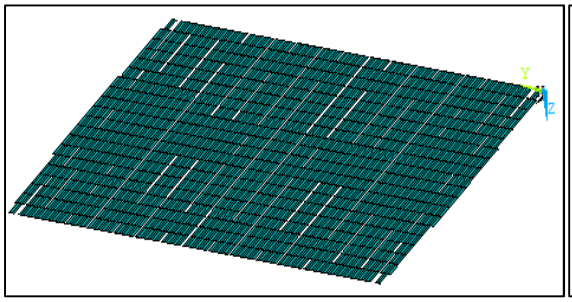

Damage=60%

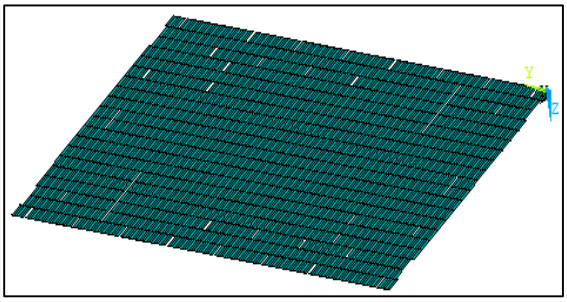

Damage=80%

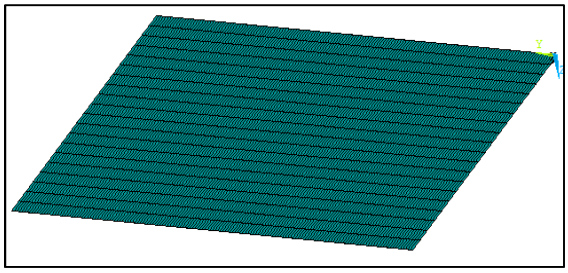

Damage=95%

Figure 4.33: Damaged elements in the top face at 20, 40, 60, 80 and 95 percent damage in the sandwich plate with web inclination angle $\theta = 90^{o}$

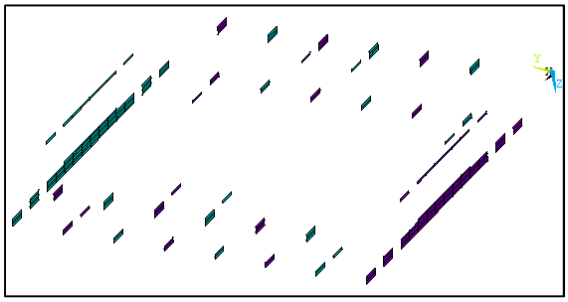

Damage=20%

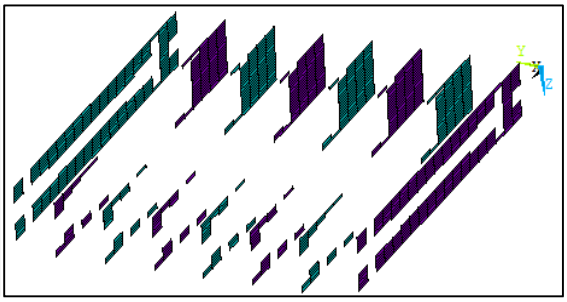

Damage=40%

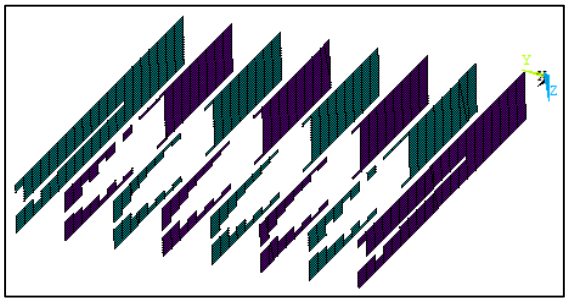

Damage=60%

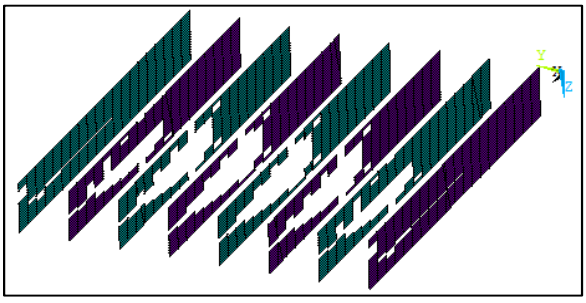

Damage=80%

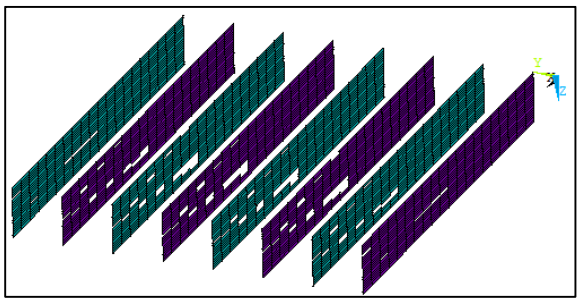

Damage=95%

Figure 4.34: Damaged elements in the web members at 20, 40, 60, 80 and 95 percent damage in sandwich plate with web inclination angle $\theta = 90^{o}$

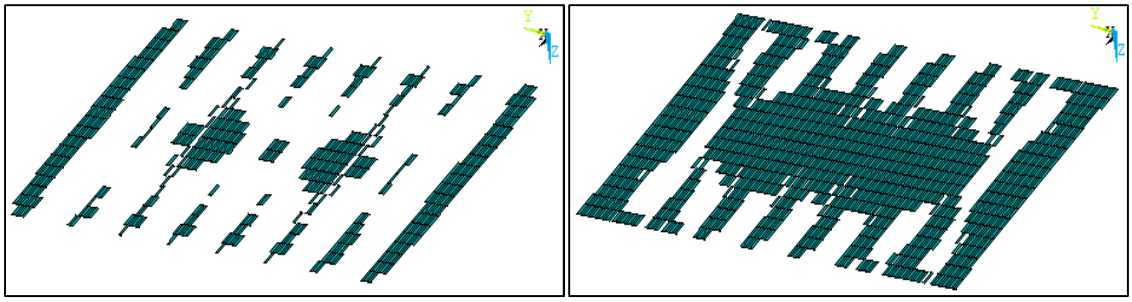

Damage=60%

Damage=80%

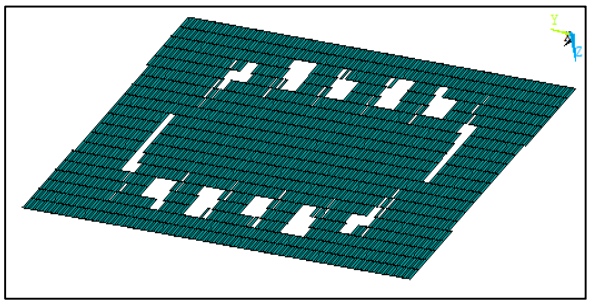

Damage=95%

Figure 4.35: Damaged elements in the bottom face at 20, 40, 60, 80 and 95 percent damage in sandwich plate with web inclination angle $\theta = 90^{o}$

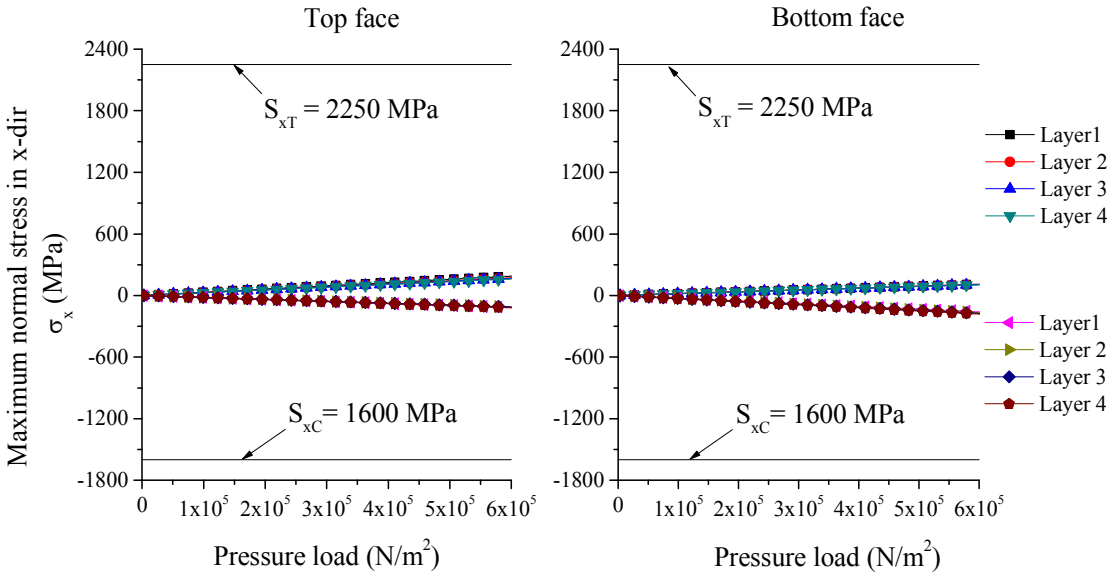

Figure 4.36: Maximum stress σ_x, in top and bottom faces of the composite sandwich plate with web inclination angle $\theta = 90^{o}$

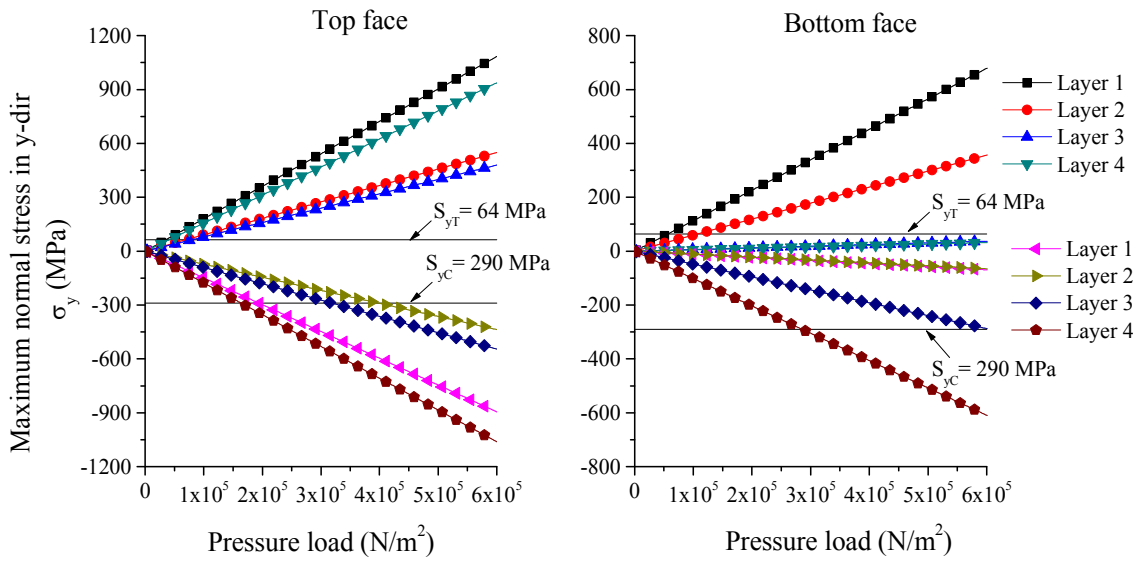

Figure 4.37: Maximum stress σ_y, in top and bottom faces of the composite sandwich plate with web inclination angle $\theta = 90^o$

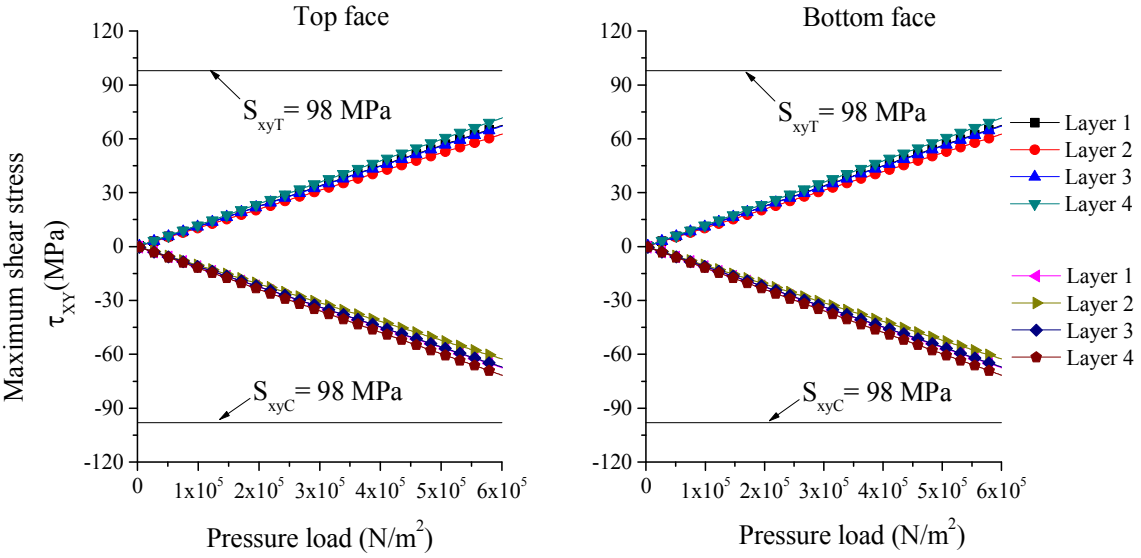

Figure 4.38: Maximum shear stress τ_{xy}, in the top and bottom faces of the composite sandwich plate with web inclination angle $\theta = 90^o$

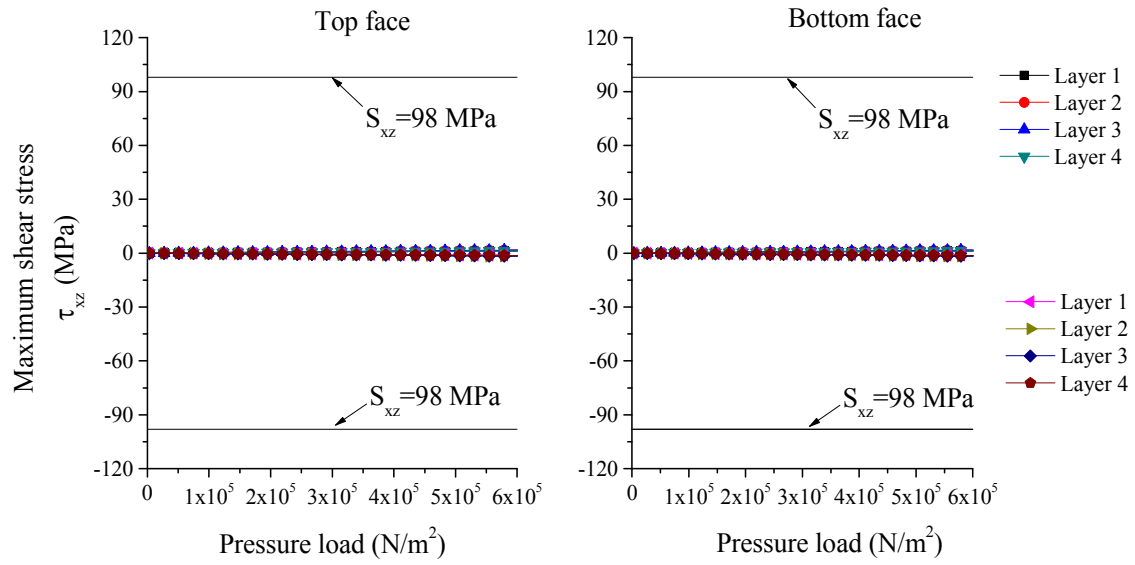

Figure 4.39: Maximum shear stress τ_{xz}, in the top and bottom faces of the composite sandwich plate with web inclination angle $\theta = 90^{o}$

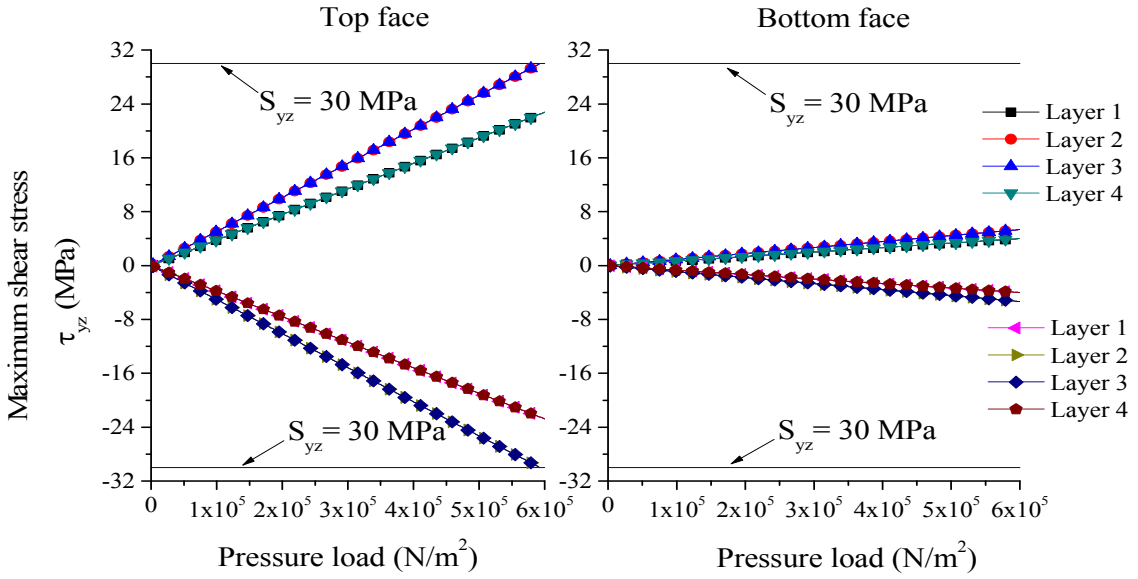

Figure 4.40: Maximum shear stress τ_{yz}, in the top and bottom faces of the composite sandwich plate with web inclination angle $\theta = 90^{o}$

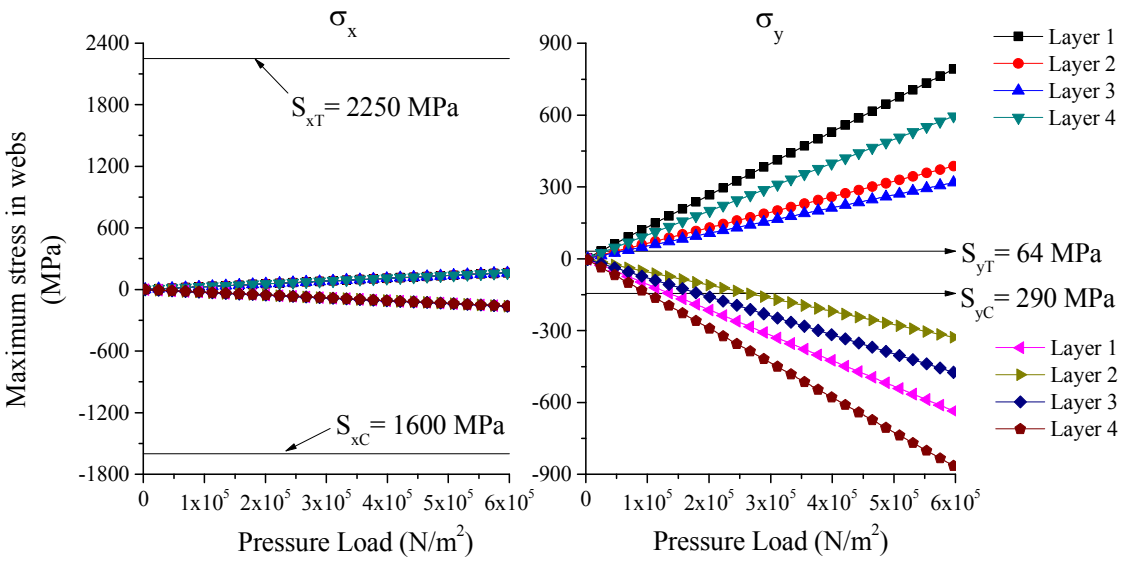

Figure 4.41: Maximum normal stresses σ_x and σ_y in one of the web members of the composite sandwich plate with web inclination angle $\theta = 90^o$

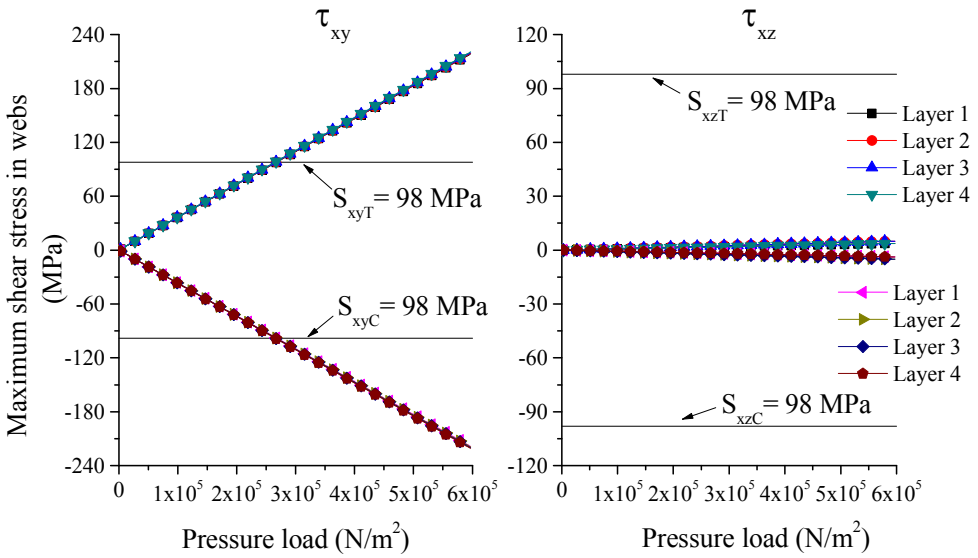

Figure 4.42: Maximum shear stress τ_{xy} and τ_{yz} in one of the web members of the composite sandwich plate with web inclination angle $\theta = 90^o$

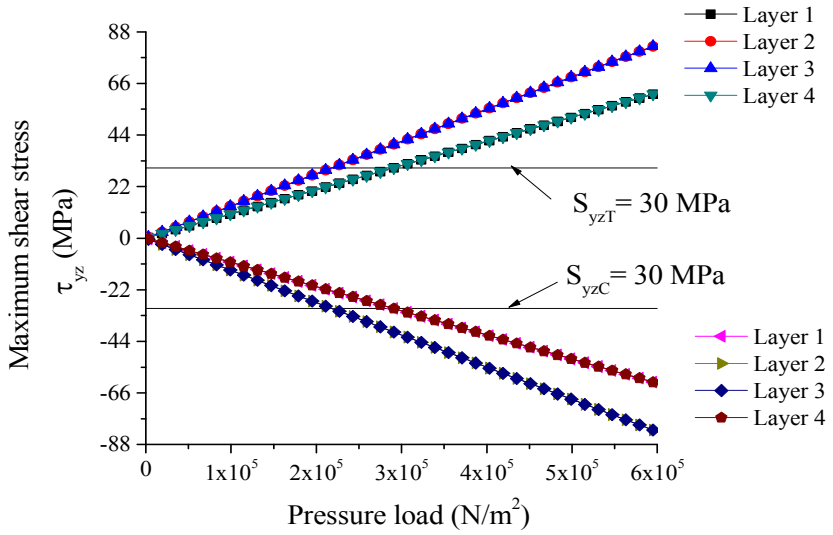

Figure 4.43: Maximum shear stress τ_{yz} in one of the web members of the composite sandwich plate with web inclination angle $\theta = 90^{o}$

Table 4.6: Applied pressure load (in N/m^2) at which stresses exceed the failure strength limit

Stress	Failure mode	$\theta = 90^{o}$		
		Top	Bottom	Web
σ_x	Tensile failure	--	--	--
	Compressive failure	--	--	
σ_y	Tensile failure	33,000	63,000	53,000
	Compressive failure	203,000	303,000	203,000
τ_{xy}	Shear failure	--	--	269,000

Table 4.7: Damage in top and bottom faces and web members at different damage levels in the sandwich plate with web inclination angle $\theta = 90^{o}$

Damage in the sandwich plate (%)	Applied pressure load (N/m^2)	Damage in top and bottom faces and web members (%)		
		Top face	Bottom face	Web
20	175,000	55	0	8
40	373,000	87	0	40
60	470,000	99	20	60
80	520,000	100	70	74
95	600,000	100	88	97

4.6 CONCLUSIONS

In this chapter, local failure of composite sandwich plates with corrugated core is studied in terms of local buckling failure and material failure. Finite element models of sandwich plates with web inclination angles θ = 45º, 48º and 90º are developed using Shell 181 element in ANSYS.

Critical buckling pressure loads of sandwich plates with web inclination angles θ = 45º and 90º and different fiber orientation angles in laminate constructions $(0/\alpha)_s$ and $(\pm\alpha)_s$ are compared. Critical buckling pressure loads for $\theta = 90°$ is higher when compared to $\theta = 45°$. In the case of web inclination angle θ = 45º, the top face buckles more compared to the bottom faces and only a few web members are buckle. In the case of web inclination angle $\theta = 90°$, the bottom face buckles more compared to top face and almost all web members are buckled. Critical buckling pressure load of sandwich plates with laminate construction $(0/\alpha)_s$ is higher compared to laminate construction $(\pm\alpha)_s$. It is observed that as the fiber orientation angle is increased from $\alpha = 0$ to $90°$, critical buckling pressure load value is decreased from a maximum value at $\alpha = 0°$ to a minimum value at $\alpha = 90°$. Similar trend is observed in both web inclination angles $\theta = 45°$ and $90°$.

Composite sandwich plates with corrugated core of web inclination angle $\theta = 45°$ and $90°$ and $(0/0)_s$ laminate construction are analyzed for local material failure. A progressively increasing uniformly distributed pressure load is applied on the top face. The maximum stress failure criterion is used to determine the occurrence of failure in each lamina.

Failure initiation in the sandwich plates occurs in top the face due to σ_y exceeding tensile strength limit normal to the fiber direction. Failure initiation in the web members and the bottom face occurs at higher pressure loads than the top face. The maximum pressure load at which the composite sandwich plate reaches 95% damage level is higher for the 90° web inclination angle than for the 45° web inclination angle.

REFERENCES

[1] Valdevit, L., Hutchinson, J.W. and Evans, A.G., "Structurally optimized sandwich panels with prismatic cores," *International Journal of Solids and Structures*, Vol. 41,2004, pp. 5105-5124.

[2] Valdevit, L., Wei, Z., Mercer, C., Zok, F.W. and Evans, AG., "Structural performance of near optimal sandwich panels with corrugated cores," *International Journal of Solids and Structures*, Vol. 43, 2006, pp. 4888-4905.

[3] Z. Xue and J. W. Hutchinson, "Preliminary assessment of sandwich plates subject to blast loads", *International Journal of Mechanical Sciences*, Vol.45, 2003, pp. 687–705.

[4] Z. Xue and J. W. Hutchinson, "A comparative study of impulse-resistant metallic sandwich plates", *International Journal of Impact Engineering*, Vol. 30, 2004, pp.1283–1305.

[5] Sek, M. and Kirkpatrick, J., "Prediction of the cushioning properties of corrugated fiberboard from static and quasi dynamic compression data," *Packaging Technology and Science*, Vol. 10, 1997, pp. 87-94.

[6] Rouillard, V. and Sek, M. A., "Behaviour of multi-layered corrugated paperboard cushioning systems under impact loads,"*Strain*, Vol. 43, 2007, pp. 345–347.

[7] Nordstrand, T. and Allansson, A., "Stability and collapse of corrugated board panels, numerical and experimental analysis," *Proceedings of 6th International Conference on Sandwich Structures*, Florida, USA, 2003, pp. 202 -210.

[8] Nyman, U. and Gustafsson, P.J., "Material and structural failure criterion of corrugated board facings," *Composite. Structures*, Vol. 50, 2000, pp. 79-83.

[9] Rami, H. A., Choi, J., Wei, B. S., Popil, R., and Schaepe, M. , "Refined nonlinear finite element models for corrugated fiberboards," *Composite Structures*, Vol. 87, 2009, pp. 321-333.

[10] Mallick, P. K., Fiber-Reinforced Composites, 3rd Edition, CRC Press, Boca Raton, FL, 2009.

[11] ANSYS, Inc, ANSYS Theory Reference, release 5.7, http://www.ansys.com

[12] Cook, R. D., Concepts and Applications of Finite Element Analysis, Second Edition, John Wiley and Sons, New York, 1981.

[13] Tserpes, K.I., Labeas,G., Papanikos, P. and Kermanidis, Th., “Strength prediction of bolted joints in graphite/epoxy composite laminates”, *Composites*: *Part B*, Vol. 33, 2002, pp. 521–529.

CHAPTER 5

VIBRO-ACOUSTIC RESPONSE OF COMPOSITE SANDWICH PLATES WITH CORRUGATED CORE

5.1 INTRODUCTION

Sandwich plates with corrugated core construction have the potential for reducing vibration and sound transmission; however, there have been only a limited number of studies exploring these potentials. El-Raheb [1] studied the vibration frequency response of two-dimensional truss-like periodic panel using an analytical approach. Later, El-Raheb and Wagner [2], [3] developed a hybrid analytical method to predict the sound transmission across similar panels. In Ref. [1], the corrugation was in the shape of a right-angled triangular core and was oriented in the width direction of the panel. The material of the panel was a polymer with a relatively low modulus and the panel was simply supported at its ends. El-Raheb observed that in such panels, intracell resonances occur at relatively low frequencies due to low stiffness of the cell members and the panel response modes can be approximated using an equivalent homogeneous model. However, at high frequencies, as flexural vibration of the cell members becomes dominant, equivalent homogenization process fails.

Ruzzene [4] analyzed the vibration and sound radiation from sandwich beams with a core of hexagonal honeycomb pattern in the thickness direction and compared them with core construction similar to El-Raheb's [1]. Here also the corrugation was parallel to the beam's width direction. Elements of the honeycomb core were modeled as beams assembled to form a frame structure. The analysis was conducted using spectral element method which utilizes frequency domain instead of time domain to formulate the dynamic shape function. Ruzzene observed that the unit cell resonance peaks also appear

in the whole beam resonance peaks; hence, the analysis of a unit cell can be used to predict the characteristics of the entire beam assembled from the unit cells. He also observed that hexagonal honeycomb core undergoes resonances at higher frequencies compared to the core construction of right-angled triangular type. The sound transmission loss is also higher with the hexagonal honeycomb core.

In previous studies, vibration and sound transmission analysis in corrugated-core sandwich construction was carried out using either an analytical approach or spectral finite elements. In the current study, a combination of finite element method (FEM) and boundary element method (BEM) is used. In the process of calculating vibro-acoustic response, first the vibration response which contains displacements of sandwich plates subjected to surface pressure loads is calculated using FEM, which are then imported to BEM for prediction of radiated sound pressure, power levels and radiation efficiencies. Several studies relating to the sound radiation have been proposed based on these methods.

Raveendra and his coworkers [5], [6] developed an indirect boundary element formulation and also demonstrated the applicability of this procedure for prediction of sound radiation characteristics of a realistic engineering problem. They also calculated sound radiation characteristics of complex structures by developing an algorithm which automatically updated the boundary element model with complexities like multiple connections and free edge constraints. Seybert et al. [7] calculated structural vibration and radiated noise levels using finite element and boundary element methods and also verified numerical simulation results by conducting experiments. Zhao et al. [8] proposed a method to calculate the sound radiation efficiency of arbitrary structures by combining BEM and general eigenvalue decomposition. The surface pressure of the structure was calculated using BEM, and as the impedance matrix is positive definite and the mean square velocity is real symmetric and also positive definite, the sound radiation can be decoupled using general eigenvalue decomposition. The method was validated with the prediction for sound radiation efficiencies of a pulsating sphere and a radiating cube. Nolte and Gaul [9] investigated the sound radiation from a vibrating structure in water. The pressure field in the fluid domain and the velocity field were determined by using

BEM with input data of surface velocities obtained from a FEM-based modal analysis. The sound radiation can be identified by determining the intensity vector in the acoustic near field. For comparison, the sound radiation calculated using BEM was compared with the results obtained by a superposition of monopole sources (pulsating spheres). Boorle et al. [10], [11] conducted vibro-acoustic analysis of composite discs, where radiation efficiencies, sound pressure and power level were predicted and analyzed using BEM.

5.2 DYNAMIC ANALYSIS OF SANDWICH PLATE

After completion of static analysis, the sandwich plate with damaged layers is taken to subsequent dynamic analysis, such as modal analysis and harmonic response. The equations of motion for modal and harmonic analyses are given by Equations 5.1 and 5.2, respectively.

$$[M]\{\ddot{u}\}+([K]+[S])\{u\}=0 \tag{5.1}$$

$$[M]\{\ddot{u}\}+[C]\{\dot{u}\}+([K]+[S])\{u\}=F_0(\omega) \tag{5.2}$$

where $[M]$, $[C]$ and $[\mathrm{K}]$ are mass, damping co-efficient and stiffness matrix respectively. $[\mathrm{S}]$ is the stress stiffening matrix, $F_0(\omega)$ is a harmonic excitation, and u is the displacement function which is assumed as $u_0(\omega)$. Structural damping for composite structures is higher compared to structures made up of isotropic materials, such as steel and aluminum. Kyriazoglou and Gould [12] determined damping of composite structures both experimentally and numerically and found that for simple orthotropic structures, the damping co-efficient is close to 1%. For the current research, a damping co-efficient of 1% is considered.

5.3 BOUNDARY ELEMENT FORMULATION FOR ACOUSTIC ANALYSIS

The formulation and details of indirect BEM (I-BEM) for acoustic analysis are given in References [13] and [14] and are briefly described in the following sections.

5.3.1 Description of Acoustic Domain used for I-BEM

The governing differential equation for periodic acoustic domain Ω, as shown in Figure 5.1, is written in the form of Helmholtz wave equation as given in Equation 5.3.

$$\nabla^2 p + k^2 p = 0 \tag{5.3}$$

where, $k = \omega/c$ is the wave number, p = acoustic pressure, ω = circular frequency, c = speed of sound, and Ω is the acoustic domain.

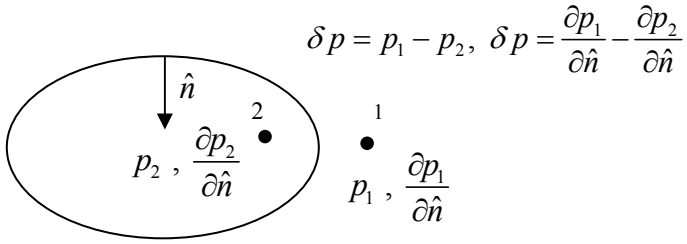

Figure 5.1: Description of Indirect BEM

The acoustic velocity vector $\vec{v}$ on the surface of the boundary element model is related to the acoustic pressure through Equation 5.4.

$$\vec{v} = -\frac{1}{j\rho_f \omega}\frac{\partial p}{\partial \hat{n}} \tag{5.4}$$

where, ρ_f = density of the acoustic medium, $j = \sqrt{-1}$ and $\hat{n}$ is the unit normal vector.

The Helmholtz/ Kirchoff integral equation for acoustic pressure at a data recovery point $\vec{r}$ within the acoustic domain Ω is:

$$C(\vec{r})\,p(\vec{r}) = \int_{S_\gamma}\left(G(\vec{r},\vec{r}_\gamma)\frac{\partial p(\vec{r})}{\partial \hat{n}_\gamma} - \frac{\partial G(\vec{r},\vec{r}_\gamma)}{\partial \hat{n}_\gamma}\,p(\vec{r}_\gamma)\right) dS_\gamma \tag{5.5}$$

where S_γ =surface of the boundary element model, γ indicates a source point on the boundary element surface, $\vec{r}$ =position vector for the data recovery point, $\vec{r}_\gamma$ = position vector of a source point on the surface of the model, $\hat{n}_\gamma$ = unit normal at the location of

the source point directing away from the direction of the acoustic domain, $C(\vec{r})$= integration constant, and $G(\vec{r},\vec{r}_\gamma)=\frac{1}{4\pi|\vec{r}-\vec{r}_\gamma|}e^{-j|\vec{r}-\vec{r}_\gamma|}$ is the Green function. The direction of the unit normal specifies the side of the model on which the primary variables, namely acoustic pressure $p(\vec{r}_\gamma)$ and acoustic pressure gradient $\frac{\partial p(\vec{r}_\gamma)}{\partial \hat{n}_\gamma}$ are defined. The primary variables must be on the same side with the corresponding acoustic domain Ω for which the analysis is being performed. Therefore, if a sound radiation problem is to be solved, the unit normal must point away from the acoustic domain (toward the interior), and the primary acoustic variables are defined on the outer side of the boundary element model. The opposite must hold for an interior acoustic problem.

5.3.2 Applying Acoustic Velocity as Boundary Condition

In the current study, acoustic velocity is defined on the surface of the boundary element model. The prescribed velocity can be stated as $v(\vec{r}_{X_1})=-v(\vec{r}_{X_2})=\overline{v}(\vec{r}_X)\Rightarrow \delta dp(\vec{r}_X)=0$ on S_γ. It should be noted that when the acoustic velocity is prescribed, the motion on both sides of the model is the same. Due to the opposite direction of the unit normal associated with the definition of the acoustic velocity on each side of the model, the velocities on each side will have the same magnitude, but opposite algebraic signs.

In order to achieve a numerical solution, the unknown functions of the primary variables on the surface of the boundary element model are expressed as a product between the unknown nodal values of the primary variables at nodes of boundary element model and the element shape functions. This is shown in Equation 5.6.

$$\begin{aligned}\delta dp(\vec{r}_X)&=\{N_i\}^T\{\delta dp_i\}\\ \delta p(\vec{r}_X)&=\{N_i\}^T\{\delta p_i\}\end{aligned} \tag{5.6}$$

where, $\{\delta dp_i\}$ and $\{\delta p_i\}$ are column vectors of nodal values of the primary variables at the nodes of the i^{th} element. Spatial derivatives of the primary variables can also be expressed in terms of the nodal values of the primary variables and the spatial derivatives of the

shape functions. It leads to a system of equations given by Equation (5.7).

$$[A]\{q\} = \{f\} \tag{5.7}$$

where, $[A]$= the system matrix which is a square and symmetric matrix, $\{q\}$ =vector of unknown primary variables on the surface of the boundary element model, and $\{f\}$ = vector representing the excitation, derived from the velocity boundary condition. Equation (5.7) can also be written as

$$[H(\omega)]\{\mu\} = [G(\omega)]\{\sigma\}$$

where $[H(\omega)]$ and $[G(\omega)]$ are frequency dependent BEM global matrices, $\{\sigma\}$ and $\{\mu\}$ are unknown primary variables, i.e., single layer and double layer potentials on the mesh.

5.3.3 Implementing Free Edge and Multiple Connection Boundary Conditions

Due to the definition of the primary variables in the I-BEM, the acoustic medium is accounted on both sides of the model. Thus, it is possible to include openings and multiple connections in the model as shown in Figure 5.2.

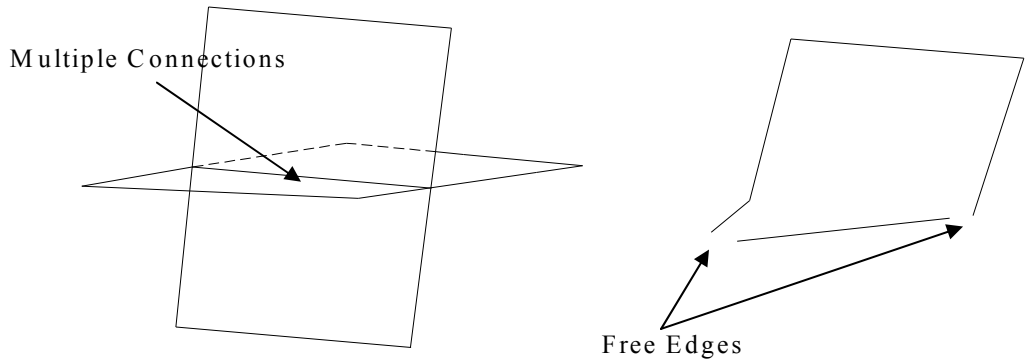

Figure 5.2: Multiple connections and free edges in the structures

There are two issues associated with modeling these geometric complexities. At a free edge of an opening the acoustic pressure is the same for both sides of the model and this must be accounted properly when defining the primary variables at the nodes residing along the free edges. Further, along the common edge of a multiple connection,

the number of the defined acoustic sub-spaces equals the number of panels connected along the same edge. This creates an inconsistency in the definition of the primary variables. These two issues are accounted properly in the numerical solution of the IBEM by imposing constraint conditions on the appropriate primary variables in the boundary element system of equations. Free edge constraints are imposed in order to take into account the openings and multiple connection constraints are imposed in order to take into account the presence of multiple connections.

The physical phenomenon along a free edge is the continuity of the acoustic pressure between the acoustic spaces from both sides of the model. The implication in the primary variables is that the difference in the pressure δp along a free edge has to be zero: $\delta p_k = 0$, k=1,...,K where δp_k is the nodal value of the primary variable δp on a node along a free edge, and K is the total number of nodes along the free edges in the boundary element model. The values of the primary variables δp_k corresponding to the free edge nodes can be enforced to become equal to zero during the solution of the boundary element system by a penalty method. Specifically, if k is one of the nodes on a free edge, then in the primary system of equations, a penalty term with a large value is added to the corresponding diagonal term.

5.4 VARIOUS ACOUSTIC MEASURES

5.4.1 Sound Power

The sound power W through an area S is

$$W = \int_S I_n \, dS \tag{5.8}$$

where, I_n is the component of the acoustic intensity normal to S. If S is a closed surface that is also the boundary of a vibrating object, the radiation efficiency σ is defined as

$$\sigma = \frac{W}{\rho_f c S \left\langle V_n^2 \right\rangle_{t,s}} \tag{5.9}$$

where, ρ_f is the density of the acoustic medium, c is the speed of sound, and $\left\langle V_n^2 \right\rangle_{t,s}$ is

the space-time mean square velocity of the normal component of the velocity of the surface over a time period, i.e.,

$$\left\langle V_n^2 \right\rangle_{t,s} = \frac{1}{S}\int_S \left[\frac{1}{T}\int_0^T V_n^2(S,t)\,dt \right] dS \tag{5.10}$$

For harmonic motion, $V_n(S,t) = V_n(S)\cos\omega t$; therefore the quantity inside the brackets in Equation 5.10 becomes $V_n^2(S)/2$ at each point on the surface S.

$$\left\langle V_n^2 \right\rangle_{t,s} = \frac{1}{2}\left[\frac{1}{S}\int_S V_n^2(S)\,dS \right] \tag{5.11}$$

The quantity in the brackets in Equation 5.11 is the space mean-square velocity.

5.4.2 Radiation Efficiency

The radiation efficiency is a useful way to explain the typical radiation characteristics of structures. For vibrating structures, it is given as a ratio of radiated sound energy and vibrational energy. For example, a loudspeaker of area S in a cabinet (infinite baffle) radiates sound at low frequencies much like a uniformly pulsating sphere. The radiation efficiency of a sphere of area S is $\sigma_{sphere} = k^2S/4\pi$, where $k = \omega/c$ is called the wave number.

5.4.3 Decibel Scales

The sound pressure level L_p (in decibels, dB) is defined by

$$L_p = 10\ \log_{10}\frac{P^2_{rms}}{P^2_{ref}} \tag{5.12}$$

where, P_{rms} is the root-mean square (RMS) or effective pressure given by

$$P_{rms} = \left[\frac{1}{T}\int_0^T P^2(t)\,dt \right]^{1/2} \tag{5.13}$$

and P_{ref} is the reference pressure (equal to 20μ Pa for air). Similarly, the sound power level L_w (in decibels, dB) is defined by

$$L_w = 10 \log_{10} \frac{W}{W_{ref}} \tag{5.14}$$

where, W is the sound power defined in Equation 5.8 and W_{ref} is the reference sound power, equal to 10^{-12} W.

5.5 METHODOLOGY FOR VIBRO-ACOUSTIC ANALYSIS

For vibro-acoustic analysis of sandwich plates with corrugated core, initially vibration analysis is performed using finite element model developed in ANSYS, which is then submitted to boundary element model in LMS SYSNOISE, where sound radiation is calculated.

The boundary element (BE) mesh for vibro-acoustic analysis is created by directly using finite element mesh described in Chapter 4. The corrugated-core composite sandwich plates are 640 mm x 640 mm in length and width, with $p = d = 80$ mm, and has either a triangular core with web inclination angle $\theta = 45°$or a rectangular core with web inclination angle $\theta = 90°$. The BE mesh contains 9,600 elements and 10,290 nodes and is shown in Figure 5.3. The details of the elements in individual members are tabulated in Table 5.1. Because of discontinuity in BE-mesh on the periphery (i.e. outer edges of the sandwich plate) and connection points (i.e. where webs are connected to the top and bottom faces), free edge boundary conditions are imposed, i.e., pressure jump $\partial p/\partial n = 0$ is equal to zero.

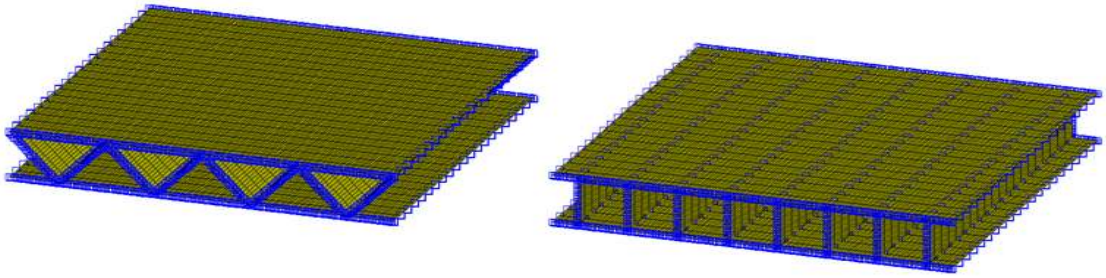

Figure 5.3: Boundary mesh used for vibro-acoustic analysis

Table 5.1: Boundary element mesh details of individual members in sandwich plate

Member	Top face	Bottom face	Webs
Elements	2,400	2,400	4,800

For sound radiation calculation, an acoustic domain of dimensions 2.64 m in length, 2.64 m in width and 2.08 m in height is created around the BE mesh (Figure 5.4) with 125,000 acoustic elements. The density of air $\rho = 1$ kg/m^3 and the speed of sound in air is $c = 456$ m/s. After calculating surface potentials on the BE mesh, radiation efficiency, sound pressure and power levels are calculated as given in Section 5.4 and plotted in the following sections.

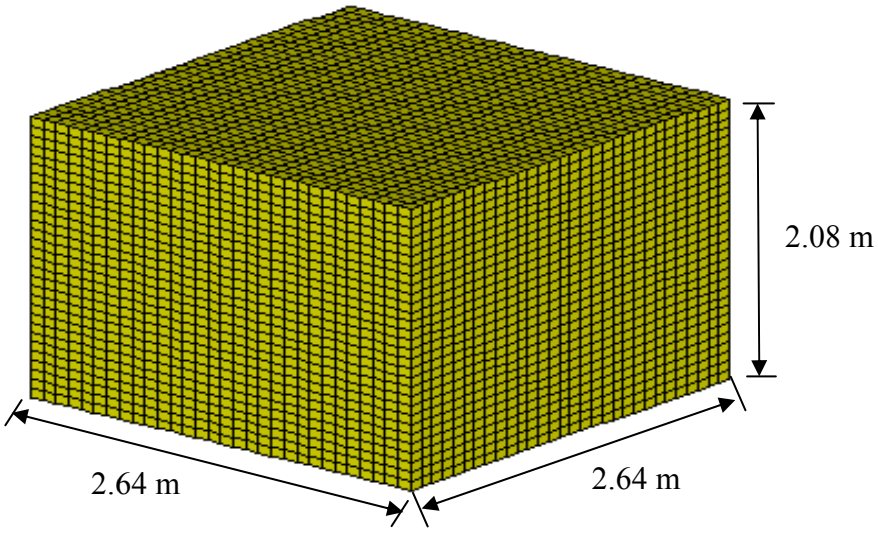

Figure 5.4: Acoustic domain used for vibro-acoustic analysis

5.6 VIBRO-ACOUSTIC ANALYSIS OF UNDAMAGED SANDWICH PLATES

In this section, vibro-acoustic analysis is carried out for an undamaged sandwich plate in the frequency range of 0 to 1000 Hz. A pressure load of amplitude $p_0 = 1\,\mathrm{N/m^2}$ is applied on the top face of the sandwich plate and both normal velocity and radiated sound power levels are calculated. Two web configurations are considered: triangular core with web inclination angle $\theta = 45°$ and rectangular core with web inclination angle $\theta = 90°$. The laminate construction in both faces and webs is $(0/0)_s$.

5.6.1 Triangular Core (Web Inclination Angle θ = 45º)

Figure 5.5 shows the resonance peaks for both normal velocity level and sound power level for the undamaged sandwich plate with triangular core. It is noticed that the fundamental mode at $f_n = 210$ Hz has higher normal velocity and radiated sound power

level than at higher frequencies. All natural frequency peaks in the normal velocity level response curve have corresponding peaks in the radiated sound power level response curve, which implies that all natural frequencies of the sandwich plate radiate sound.

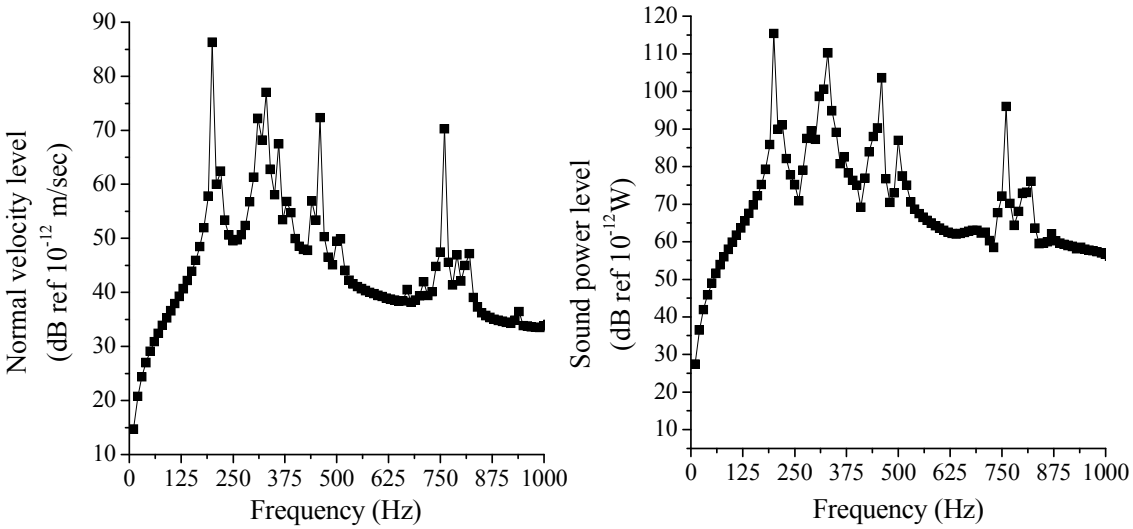

Figure 5.5: Normal velocity level and radiated sound power level of an undamaged sandwich plate with web inclination angle $\theta = 45^{o}$

In structural noise and vibration analysis, usually the fundamental mode, which corresponds to the lowest natural frequency, is the critical mode when compared to other natural frequencies. Fundamental structural and acoustic mode shape of the undamaged sandwich plate with corrugated core of web inclination angle $\theta = 45^{o}$, i.e., at frequency $f_n = 210\ \text{Hz}$ is shown in Figure 5.6. In the case of fundamental structural mode, it is observed that the top face and all webs in the sandwich plate have resonances, while the bottom face does not experience resonance. It appears that local resonances occur before global vibration of sandwich structure. In the case of fundamental acoustic mode, intensity of radiated sound pressure level is much higher at $y = 0$ and 0.64 m, i.e., the left and right edges of the sandwich plate. Also, it appears that resonance of the webs leads to greater noise generation compared to the top face. It is noticed that the sound wave generated due to the resonance of webs (which is noticed from structural mode shape) is circular in shape.

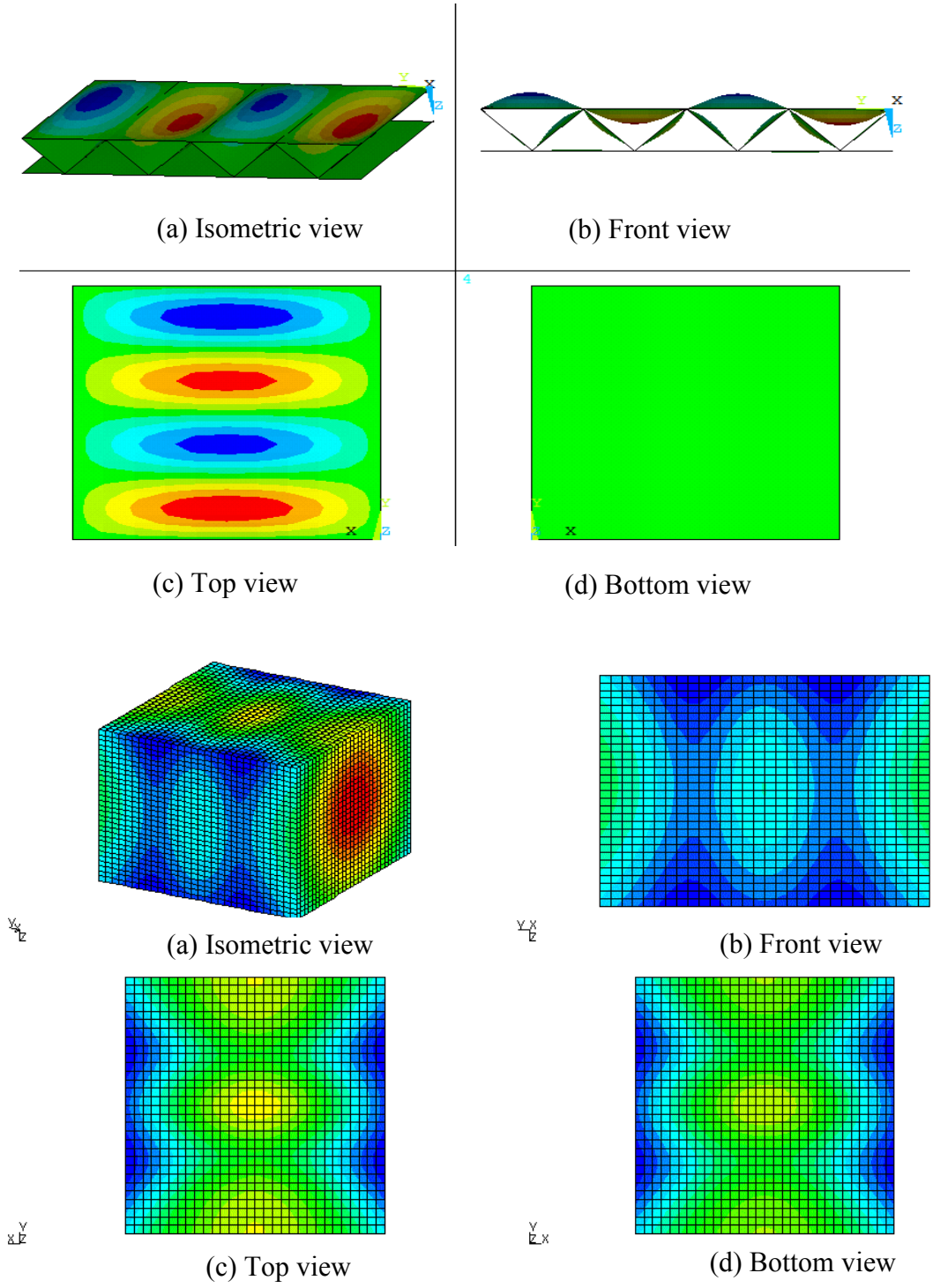

Figure 5.6: Structural and acoustic mode shapes of an undamaged sandwich plate with corrugated core of web inclination angle θ= 45º

5.6.2 Rectangular Core (Web Inclination Angle $\theta = 90^{o}$)

Figure 5.7 shows normal velocity and radiated sound power level peaks for the sandwich plate in which the web inclination angle is 90^{o}. The fundamental mode in this case occurs at a frequency of 540 Hz. As with the 45^{o} web inclination angle, all peaks of natural frequencies in normal velocity level response curve have corresponding peaks in radiated sound power level response curve, which implies that the sandwich plate radiates sound at all natural frequencies. It is also observed that the normal velocity level and radiated sound power level are higher for the web inclination angle $\theta = 90°$ compared to when the web inclination angle is $\theta = 45°$, which is due to higher overall stiffness of the former.

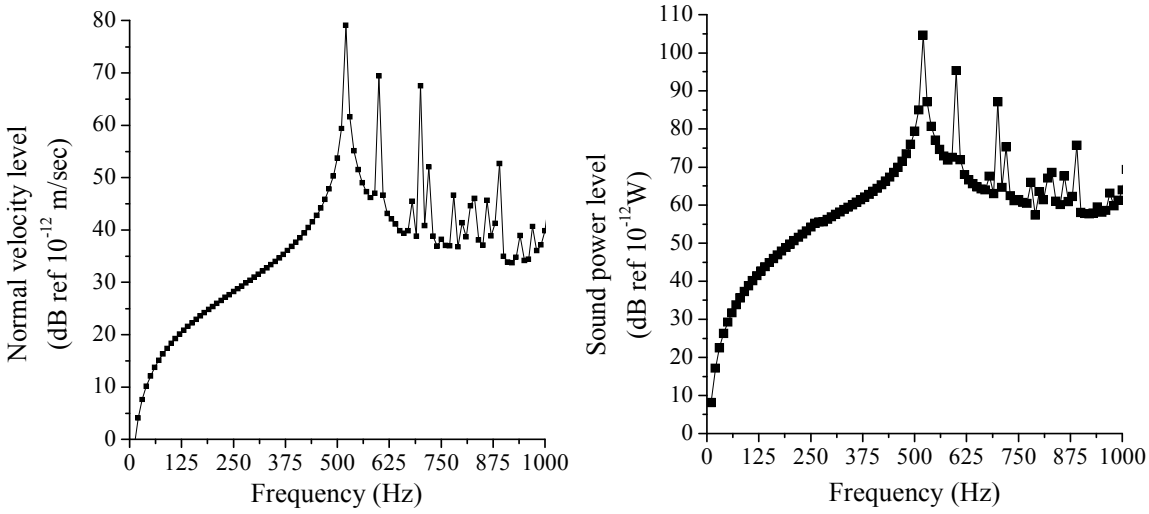

Figure 5.7: Normal velocity level and radiated sound power level of an undamaged sandwich plate with web inclination angle $\theta = 90^{o}$

Fundamental structural and acoustic mode shapes of undamaged sandwich plate with corrugated core of web inclination angle $\theta = 90^{o}$ i.e. at frequency f_n = 540 Hz are shown in Figure 5.8. In the case of fundamental structural mode, it is observed that both top and bottom faces have resonances, but the webs do not have any kind of resonance. It appears that the local resonances occur in the faces before global vibration of the sandwich plate. In the case of fundamental acoustic mode, intensity of radiated sound

pressure level is much higher at the center of the sandwich plate, i.e., above the top and bottom faces, and it appears that resonance of both top and bottom faces generates noise. It is noticed that the sound wave generated from the faces is circular in shape.

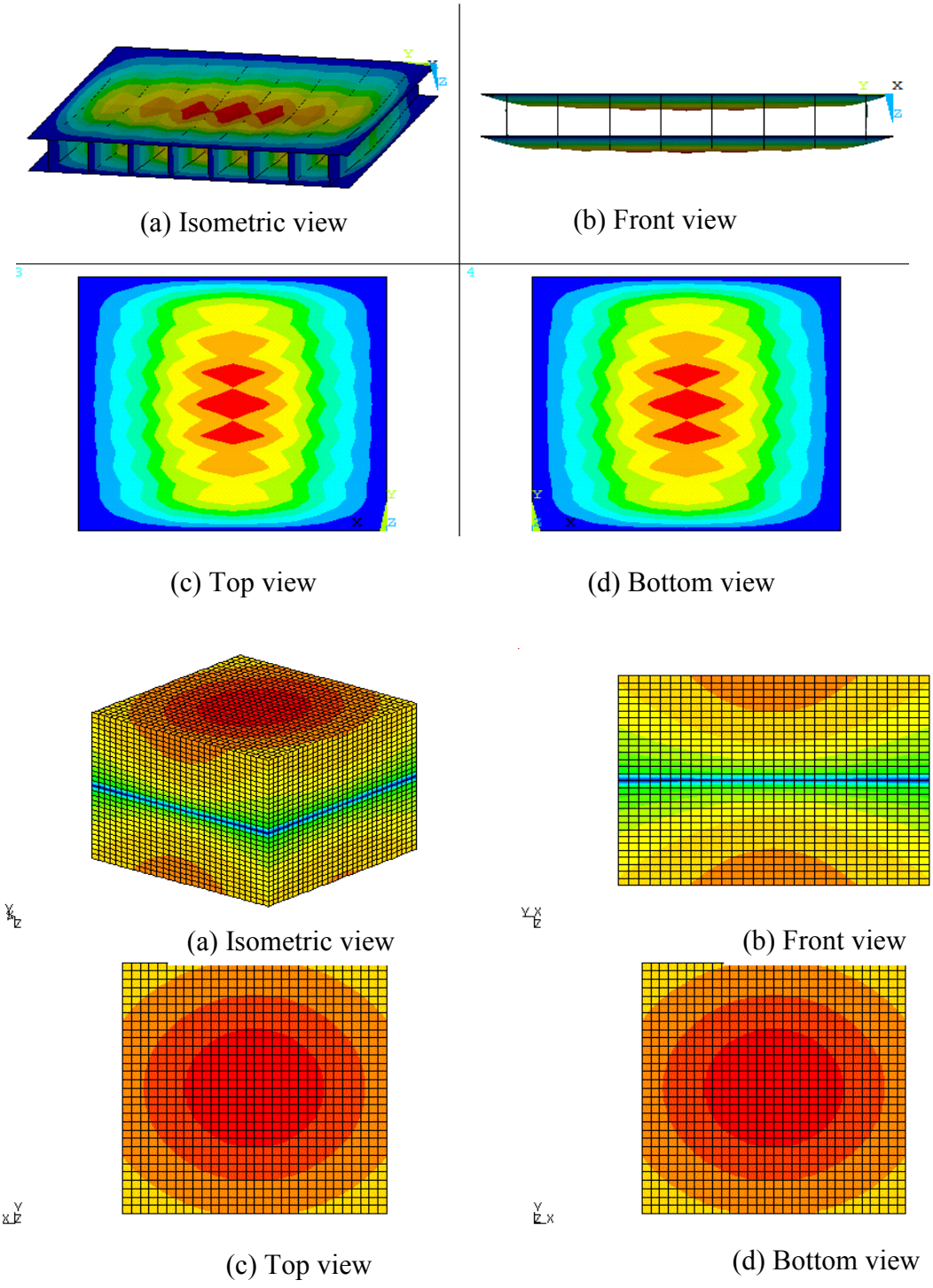

Figure 5.8: Structural and acoustic mode shapes of an undamaged sandwich plate with corrugated core of web inclination angle $\theta = 90^{o}$

5.7 FUNDAMENTAL VIBRATION FREQUENCY OF PRE-STRESSED SANDWICH PLATES

In this section, free vibration analysis is performed to determine the fundamental frequency of the sandwich plate pre-stressed with a surface pressure load acting on its top face. The pressure load is increased in steps of 3,000 N/m^2 until it becomes equal to the critical buckling pressure load, which is determined in Chapter 4 as 30,185 N/m^2 for the triangular core (θ = 45º) and 170,770 N/m^2 for the rectangular core (θ = 90º). The stress-stiffening effect due to pre-stressing is taken into account. As the pressure load is increased, the sandwich plate undergoes damage, which affects the fundamental vibration frequency of the sandwich plate.

The flow chart in Figure 5.9 shows the procedure used in the vibration analysis of pre-stressed sandwich plates with corrugated core. Initially, the finite element model is subjected to a step by step progressively increasing surface pressure load and a static analysis is carried out to calculate the stresses in each element in its local coordinate system. The maximum stress failure theory is used to determine the laminas that are damaged due to any of the stresses acting on these elements exceeding the strength limit. The elastic properties of the damaged laminas are reduced by 50% before proceeding with the vibration analysis.

Fundamental frequencies of pre-stressed sandwich plates with web inclination angles $\theta = 45°$ and $90°$ are plotted in Figure 5.10 as a function of increasing surface pressure load. In the case of web inclination angle $\theta = 45°$, as the pressure load increases, there is a decrease in the fundamental frequency. When the pressure load is equal to the critical buckling pressure load, the fundamental frequency becomes zero. In the case of web inclination angle $\theta = 90°$, as the pressure load increases, the fundamental frequency remains the same up to a pressure load $p_0 = 85,000\, N/m^2$; with further increase in the pressure load, the fundamental frequency decreases and becomes zero when it becomes equal to the critical buckling pressure load.

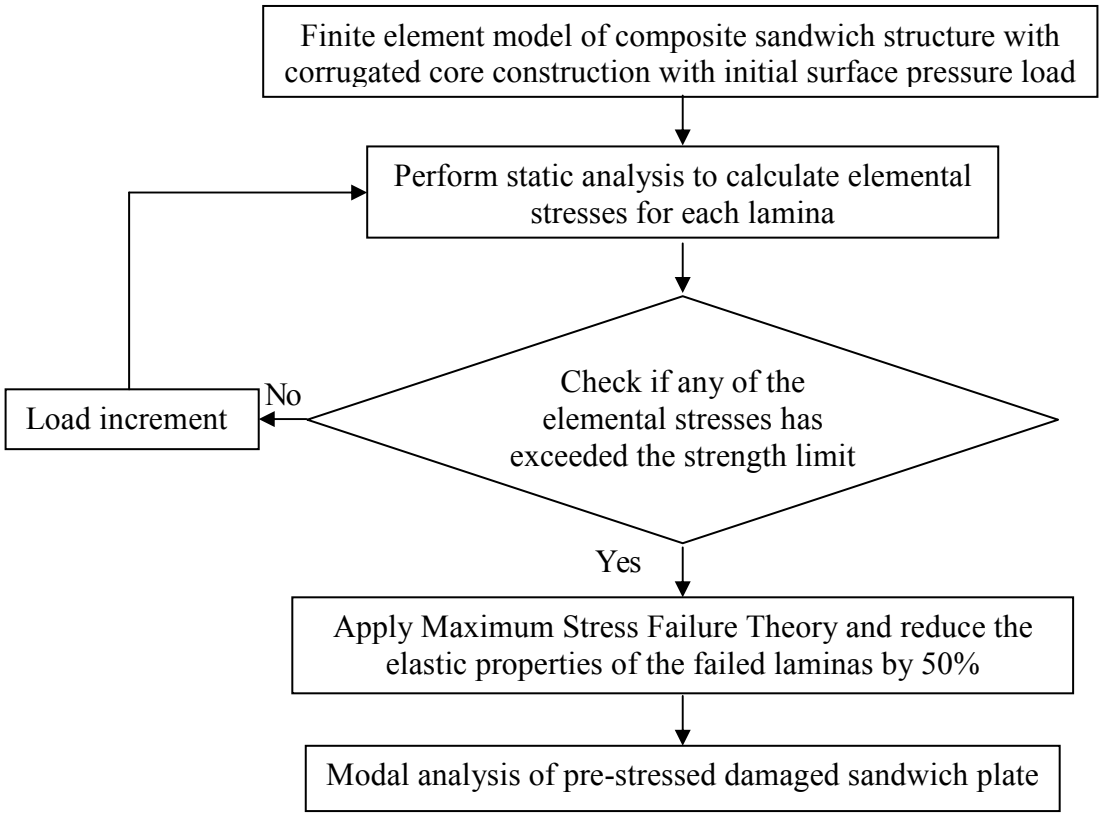

Figure 5.9: Flow chart for modal analysis of composite sandwich plate with corrugated core

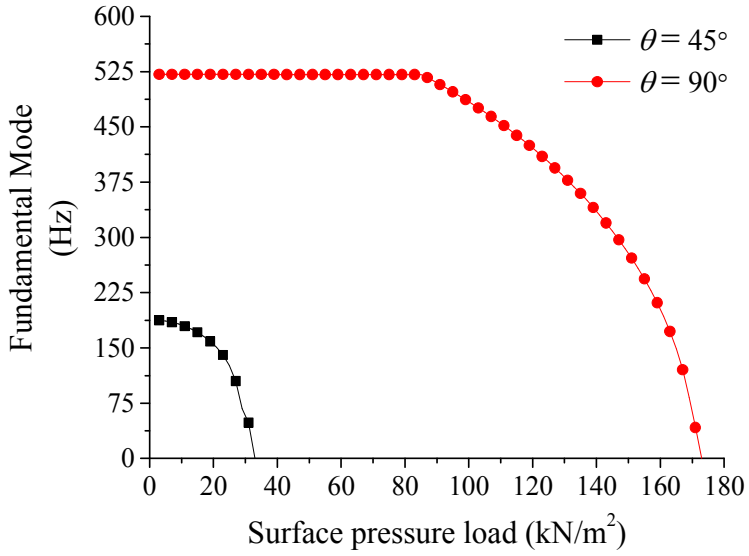

Figure 5.10: Fundamental mode of sandwich plate with web inclination angles θ = 45º and 90º and pre-stressed due to increasing pressure load

5.8 VIBRO-ACOUSTIC ANALYSIS OF DAMAGED SANDWICH PLATES WITH CORRUGATED CORE

The flow chart for the vibro-acoustic analysis of damaged sandwich plates with corrugated core is shown in Figure 5.11. To predict the vibro-acoustic response, initially the finite element model is subjected to a step by step progressively increasing surface pressure load and static analysis is carried out. At the end of each step increase in pressure load, LAYER and RSYS commands in the post-processing mode of ANSYS are used to calculate stresses in each element in its local coordinate system. The maximum stress failure theory is then used to determine the laminas that have exceeded the strength limits and the elastic properties of the damaged laminas are reduced by 50% before proceeding to the next load step. This procedure is repeated to determine the damaged conditions and the pressure loads corresponding to approximately 20, 40, 60, 80 and 95 percent damage in the elements on the top face. The pressure load values and the extent of damage on the top face in all elements of the sandwich plates are listed in Table 5.2. When the damage level reaches 20, 40, 60, 80 or 90 percent, the pressure load is removed and vibro-acoustic performance of the damaged sandwich plate models is determined using BEM. A unit pressure load $p_0 = 1\,\mathrm{N/m^2}$ is applied on the top face during the BEM analysis. The outputs of the BEM analysis are normal velocity, radiated sound power level and radiation efficiency.

Table 5.2: Fundamental frequency values of damaged sandwich plates due to applied pressure load (determined by FEM)

Approximate damage on the top face [1] (%)	$\theta = 45^\circ$		$\theta = 90^\circ$	
	Pressure Load (N/m^2)	Frequency(Hz)	Pressure Load (N/m^2)	Frequency (Hz)
Undamaged	1	210	1	540
20	23,000	180	103,000	500
40	33,000	160	203,000	310
60	43,000	120	303,000	340
80	63,000	100	403,000	190
95	103,000	50	453,000	160

(1) As determined by damaged element count

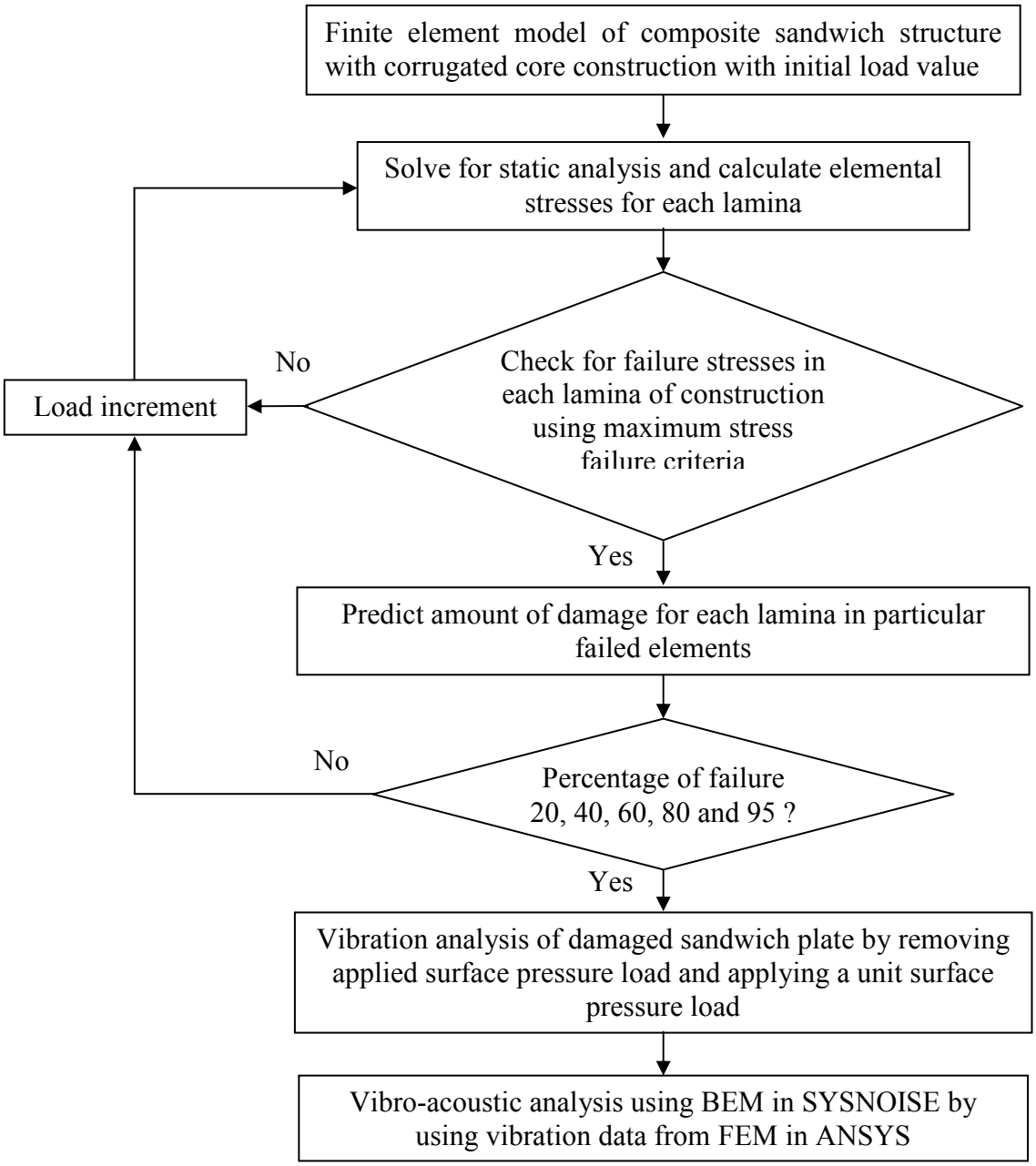

Figure 5.11: Flow chart for vibro-acoustic analysis of composite sandwich plates with corrugated core

5.8.1 Triangular Core (Web Inclination Angle $\theta = 45^{o}$)

Normal velocity and radiated sound power level of damaged sandwich plates with web inclination angle $\theta = 45^{o}$ in the frequency range $f = 0$ - 270 Hz are shown in Figure 5.12. It is observed that as damage increases, there is an increase in normal velocity and radiated sound power levels, and also frequency response curve shifts toward the lower

frequency zone.

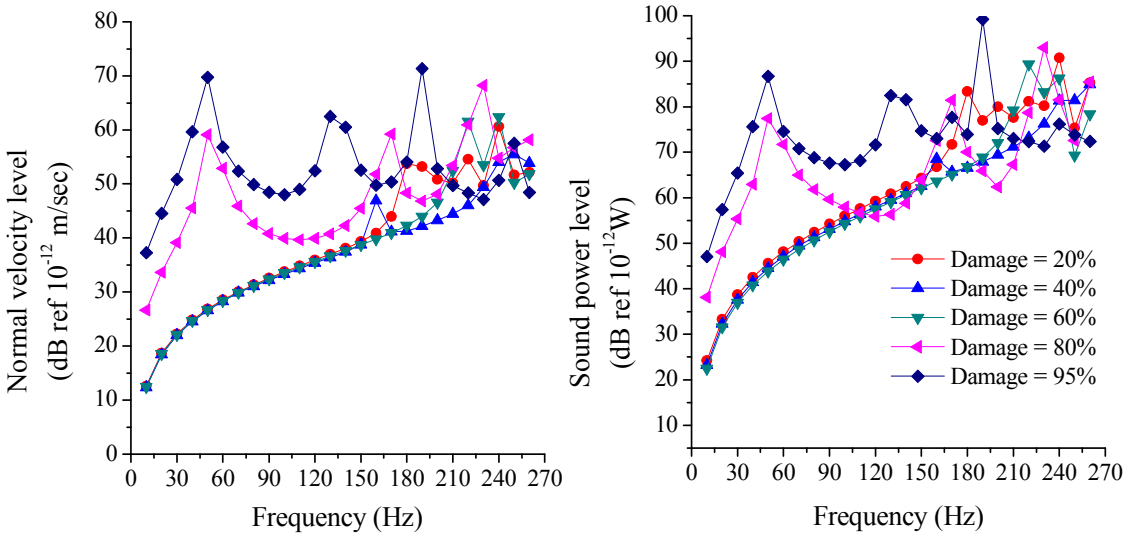

Figure 5.12: Normal velocity and radiated sound power level of a damaged sandwich plate with web inclination angle $\theta = 45^{\circ}$ and different damage levels on the top face

The radiation efficiency, which indicates distribution of input energy due to external loads into vibrational energy and radiated sound power, is shown in Figure 5.13 for the composite sandwich plate with web inclination angle $\theta = 45^{\circ}$ at increasing damage

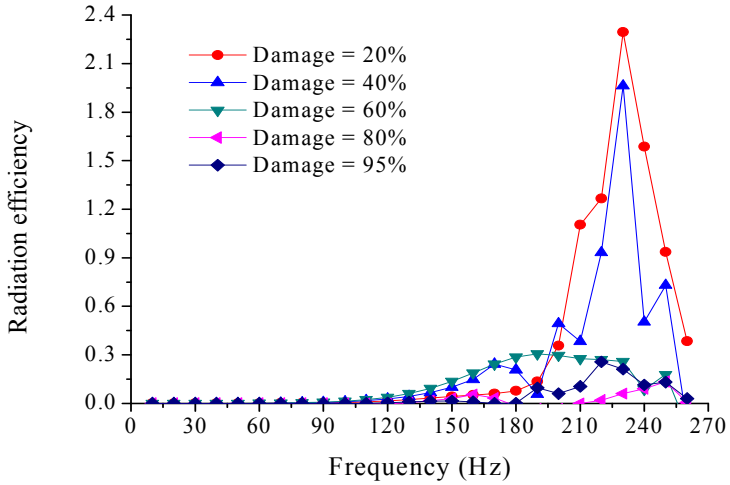

Figure 5.13: Radiation efficiency of a damaged sandwich plate with web inclination angle $\theta = 45^{\circ}$ and different damage levels on the top face

levels on the top face. It is observed that radiation efficiency decreases as the damage increases. For 20 and 40 percent damaged models, it has values higher than unity in the operating frequency zone of $f = 210 - 250$ Hz, which indicates that more input energy is converted to sound energy than vibration energy at this higher frequency zone.

Fundamental structural and acoustic mode shapes for completely damaged top face in sandwich with corrugated core of web inclination angle $\theta = 45°$, i.e., at frequency $f_n = 50$ Hz is given in Figure 5.14. In the case of fundamental structural mode, it is observed that only the top face has achieved resonance, and both webs and the bottom face do not have any kind of resonance. In the case of fundamental acoustic mode, intensity of radiated sound pressure level is much higher at the center of the sandwich plate. It appears that resonance of the top and bottom faces generate more noise. It is noticed that the sound wave generated from the top face has an elliptic shape with x-axis as the major axis and y-axis as the minor axis. The sound wave generated from the bottom face also has an elliptic shape, but with x-axis as the minor axis and y-axis as the major axis.

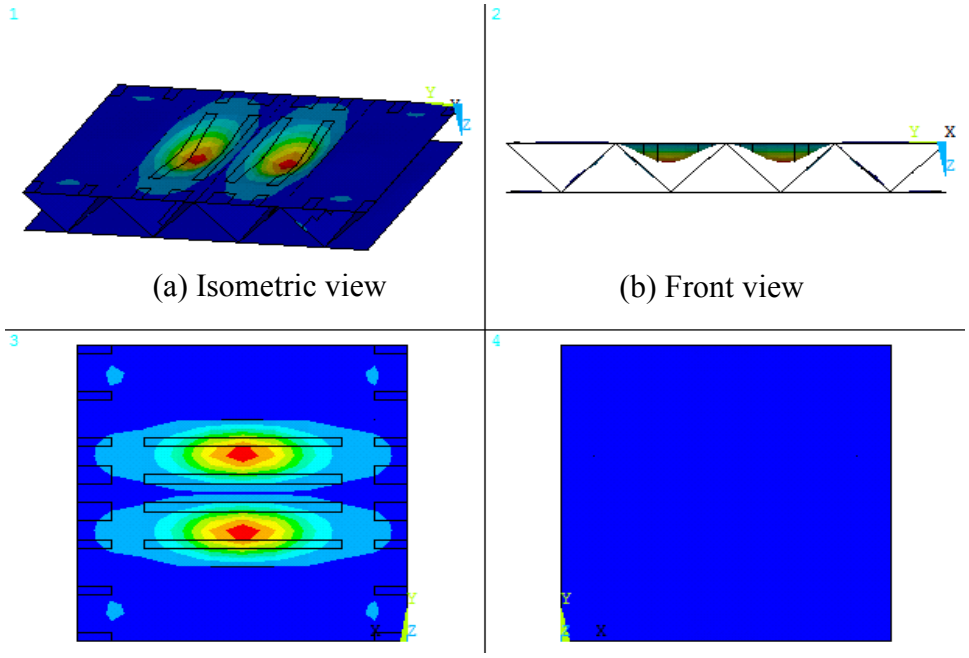

(a) Isometric view (b) Front view

(c) Top view (d) Bottom view

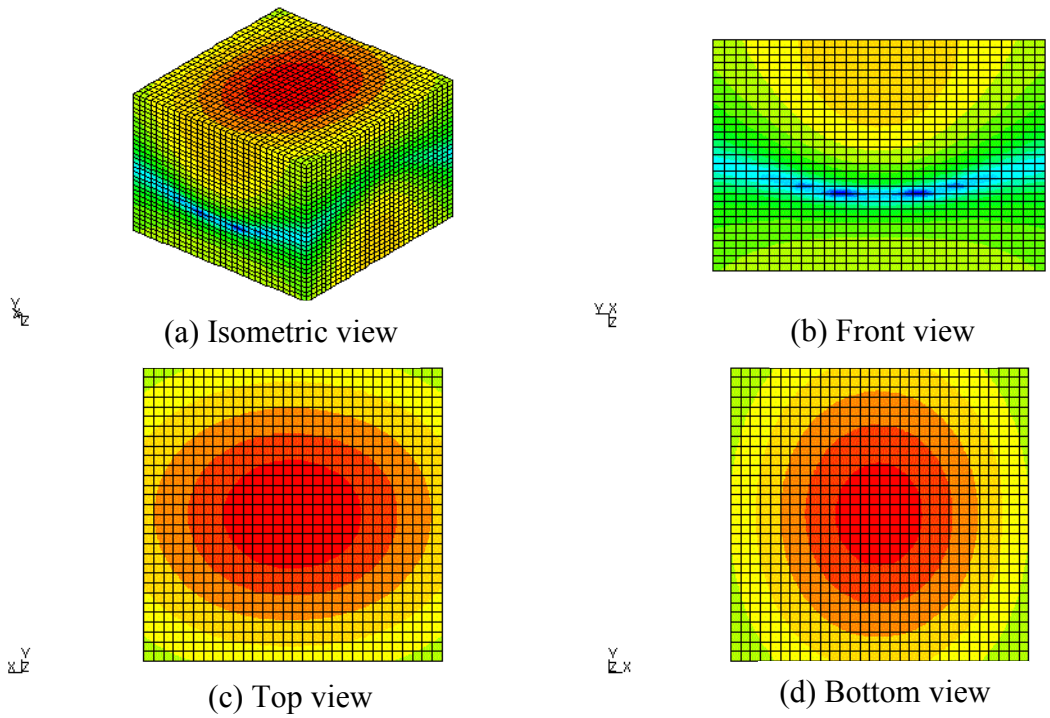

Figure 5.14: Structural and acoustic mode shapes of a completely damaged sandwich plate with corrugated core of web inclination angle θ =45º

5.8.2 Rectangular Core (Web Inclination Angle θ = 90º)

Figure 5.15 shows normal velocity and sound power response level of the composite sandwich plate with web inclination angle $\theta = 90°$ at different damage levels in the frequency range $f = 0 - 640 Hz$. Both normal velocity and radiated sound power levels increase with increasing damage level, and also frequency response curve shift toward the lower frequency zone.

In the frequency range $f = 0 - 640$ Hz, radiation efficiency of the composite sandwich plate with web inclination angle $\theta = 90°$ for increasing damage level is given in Figure 5.16. It is observed that radiation efficiency decreases as the damage level increases; with 20 and 40 percent damaged levels, it has values higher than unity in the operating frequency zone of $f = 300 - 570 Hz$, which indicates that more input energy is converted to sound energy than vibration energy in this frequency zone.

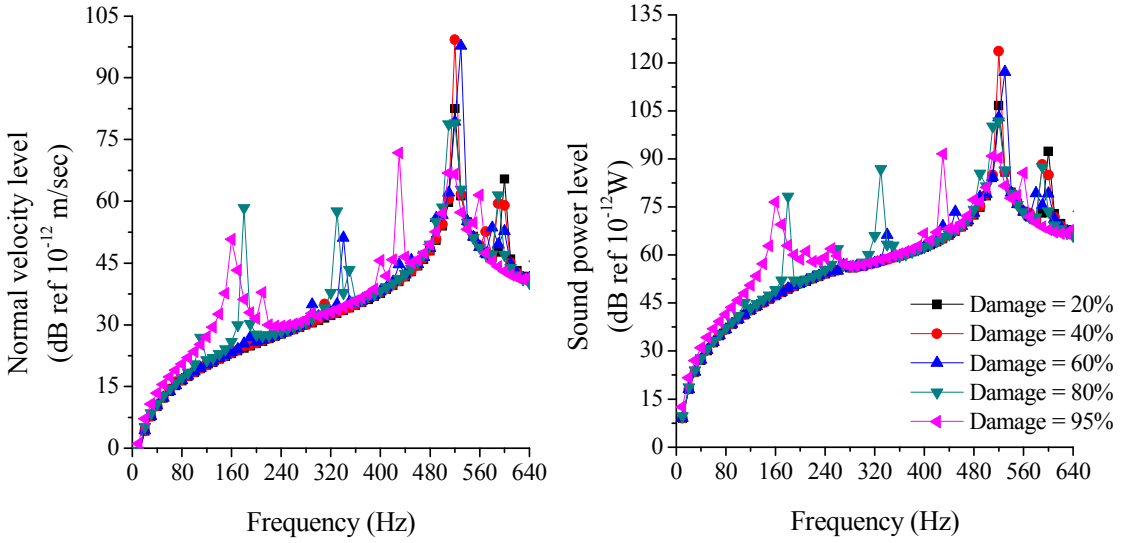

Figure 5.15: Normal velocity and radiated sound power level of a damaged sandwich plate with web inclination angle $\theta = 90^{o}$ and different damage levels on its top face

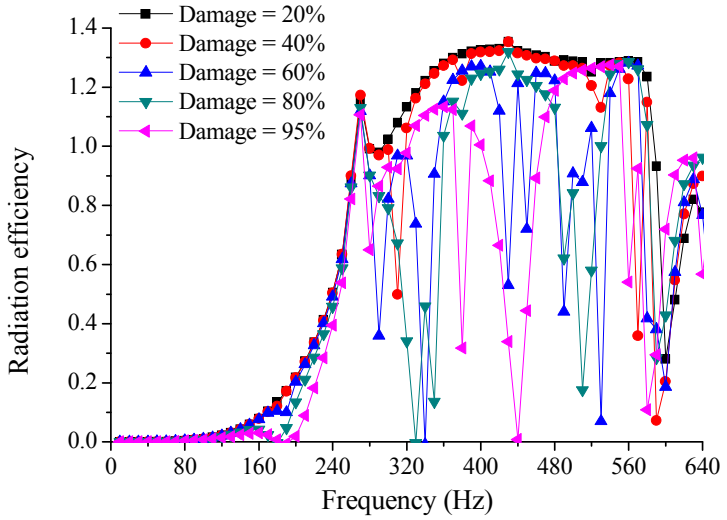

Figure 5.16: Radiation efficiency of a damaged sandwich plate with web inclination angle $\theta = 90^{o}$ and different damage levels on its top face

Fundamental structural and acoustic mode shapes for completely damaged top face in the sandwich plate with corrugated core of web inclination angle $\theta = 90^{o}$ at a frequency $f_n = 160Hz$ are shown in Figure 5.17. In the case of fundamental structural

mode, it is observed that the top face has reached resonance, but the bottom face and the webs have not reached resonance.

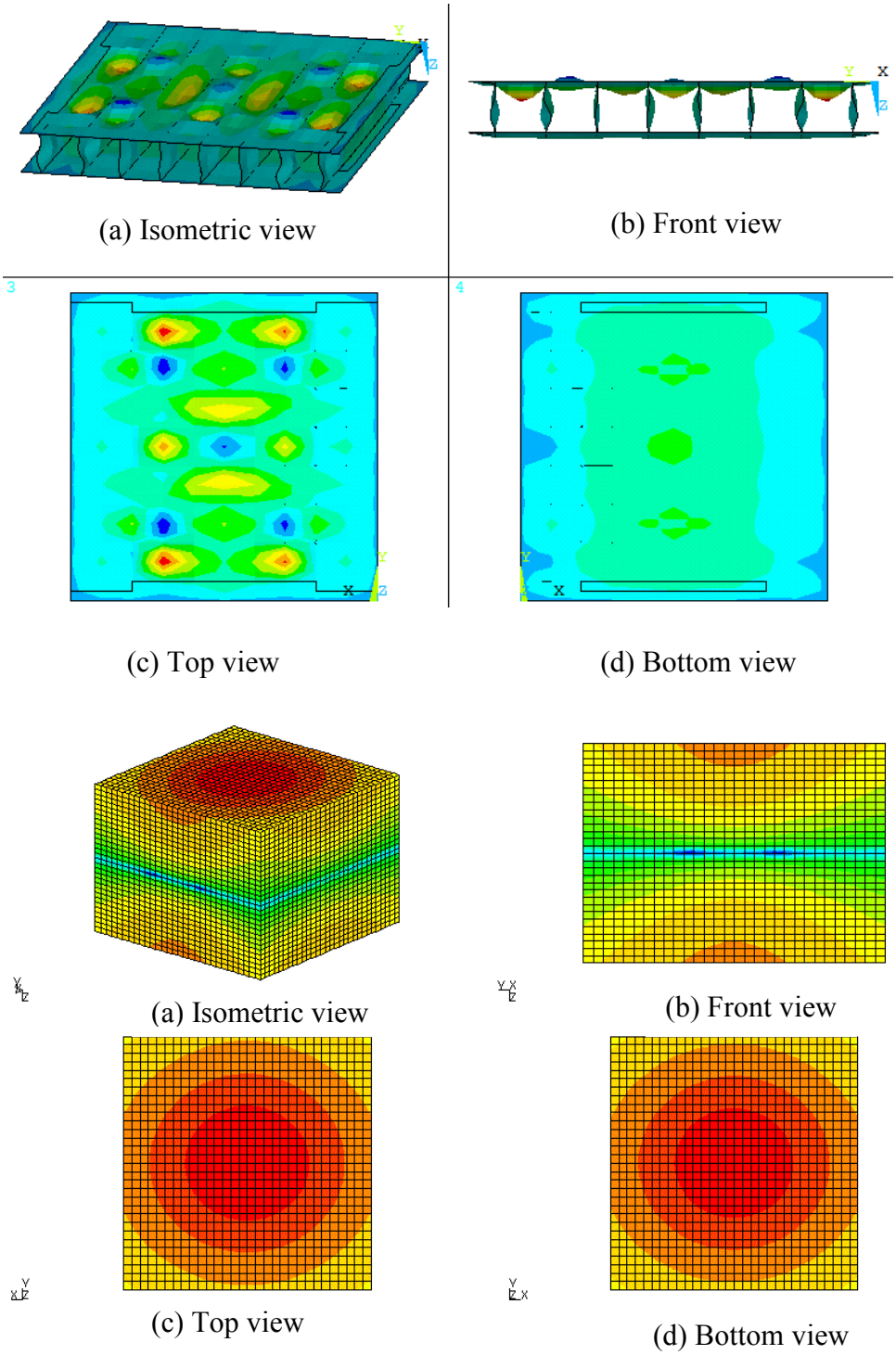

Figure 5.17: Structural and acoustic mode shapes of a completely damaged sandwich plate with corrugated core of web inclination angle θ = 90º

In the case of fundamental acoustic mode, intensity of radiated sound pressure level is much higher at the center of the sandwich plate. It appears that resonance of the top and bottom faces generates more noise than the webs. It is noticed that sound wave generated from the top and bottom faces is circular in shape.

5.9 CONCLUSIONS

Vibro-acoustic analysis of composite sandwich plates with triangular ($\theta = 45°$) and rectangular ($\theta = 90º$) corrugated cores is conducted in this chapter. Both undamaged and damaged sandwich plates are considered. The damage is created by applying transverse pressure load in increasing steps on the top face of the sandwich plate. From the structural and acoustic mode shapes, normal velocities, radiated sound power levels and radiation efficiency plots, the following principal conclusions are made.

At the fundamental natural frequency, the top face and the webs of the undamaged sandwich plate with triangular core undergo resonances, while the bottom face remains resonance free. Fundamental acoustic mode indicates that the intensity of noise generated due to the resonance of the webs is higher compared to that of the top face. With the rectangular core, both top and bottom faces undergo resonance, while the webs remain resonance free.

For the sandwich plate with triangular corrugated core, the fundamental structural frequency of pre-stressed and progressively damaged sandwich plates starts to decrease as it is pre-stressed and damaged with increasing applied pressure load. For the sandwich plate with rectangular core, the fundamental structural frequency does not change until a damage level of 2% (approximate damage of 6% in top face plate)) is reached. With both corrugations, the fundamental structural frequency becomes zero at the critical buckling load.

For the undamaged sandwich plates, the fundamental resonance frequencies for both normal velocity and sound pressure level are significantly higher when the core has a rectangular shape. On the other hand, normal velocity and sound power level peaks at resonance frequencies are higher when the core has a triangular shape. As damage increases due to increasing transverse pressure load on the top face, both normal velocity

and radiated sound pressure levels increase, and the frequency response curve starts to shift toward lower frequency. The radiation efficiency also decreases with increasing damage in the sandwich plates.

REFERENCES

[1] El-Raheb, M. "Frequency response of a two-dimensional truss like periodic panel," *Journal of the Acoustical Society of America*, Vol. 101, No. 6, 1997, pp. 3457-3465.

[2] El-Raheb, M. and Wagner, P., "Transmission of sound across a truss like periodic panel: 2-D analysis," *Journal of the Acoustical Society of America*, Vol. 102, No. 4, 1997, pp. 2176-2183.

[3] El-Raheb, M. and Wagner, P., "Effects of end cap and aspect ratio on transmission of sound across a truss-like periodic double panel," *Journal of Sound and Vibrations*, Vol. 250, No. 2, 2002, pp. 299-322.

[4] Ruzzene, M, "Vibration and sound radiation of sandwich beams with honeycomb truss core," *Journal of Sound and Vibration*, Vol. 277, 2004, pp. 741–763.

[5] Raveendra,S. T., Vlahopoulos, N. and A. Glaves, "An indirect boundary element formulation for multi-valued impedance simulation in structural acoustics", *Applied Mathematical Modelling,* Vol. 22, 1998, pp. 379-393.

[6] Vlahopoulos, N. and Raveendra, S. T., "Formulation, implementation, and validation of multiple connection and free edge constraints in an indirect boundary element formulation", *Journal of Sound and Vibration*, Vol. 210, No. 1, 1998, pp. 137-152.

[7] Seybert. A.F, Wu, T.W. and Wu, X.F., Experimental Validation of Finite Element and Boundary Element Methods for Predicting Structural Vibration and Radiated Noise. *NASA Grant NAG3-912,* January 1994.

[8] Zhao, Z.G., Huang, Q. B. and He, Z., "Calculation of sound radiant efficiency and sound radiant modes of arbitrary shape structures by BEM and general Eigenvalue decomposition", *Applied Acoustics*, Vol. 69, No. 9, 2008, pp. 796-803.

[9] Nolte, B. and Gaul, L., "Sound energy flow in the acoustic near field of a vibrating plate," *Mechanical Systems and Signal Processing*, Vol. 10, No. 3, 1996, pp. 351–364.

[10] Boorle, R. K., Ganesan, N. and Sethuraman, R., "Vibro-acoustic analysis of composite circular disc with various orthotropic properties under thermal environment", *International Journal of Vehicle Noise and Vibration,* Vol. 4, No. 1, 2008, pp. 35–69.

[11] Boorle, R. K., Ganesan, N. and Sethuraman, R., "Vibro-acoustic analysis of functionally graded circular disc under thermal environment". *International Journal of Vehicle Noise and Vibration,* Vol. 4, No. 2, 2008, pp. 123–149.

[12] Kyriazoglou, C., and Guild, F. J., "Finite element prediction of damping of composite GFRP and CFRP laminates- a hybrid formulation- vibration damping experiments and Rayleigh damping. *Composites Science and Technology*, Vol. 66, 2006, pp. 487- 498.

[13] O. von Estorff, Boundary Elements in Acoustics: Advances and Applications, WIT Press, Southampton, 2000.

[14] Wu, T.W. (ed.), Boundary Element Acoustics: Fundamentals and Computer Codes, WIT Press, Boston, 2000.

CHAPTER 6

CONCLUSIONS

The current research deals with the global and local responses of composite sandwich plates with unidirectional corrugated core subjected to transversely applied uniform pressure load. The global response is analyzed in Chapters 2 and 3 and the local response is analyzed in Chapters 4 and 5. Even though conclusions are given at the end of each chapter, the major conclusions are summarized here. Recommendations for future work are also made.

6.1 SUMMARY

6.1.1 Global Analysis

Global analysis of the sandwich plates, which includes both static bending and free vibration modes, is conducted by transforming the sandwich plate into a homogeneous orthotropic plate and then using the energy approach. For the static bending mode, global deflection and internal loads, such as bending moments and shear forces, are calculated. For the vibration mode, flexural and longitudinal resonant frequencies are determined. For the static bending analysis, effects of geometric parameters, such as face plate thickness (t_{TF} and t_{BF}), web plate thickness (t_C), web inclination angle (θ), pitch (p) and face center distance (d_c), on the global response of the sandwich plates with $[0/90°]_s$ laminates in the faces and the webs are systematically determined. The effects of laminate construction on the global response are also determined for two different laminate constructions, namely $[0/\alpha]_s$ and $[\pm\alpha]_s$, for the faces and the webs. The fiber orientation angle α in the laminates is varied between 0 and 90^o. In all cases, the cross-sectional area, and therefore the mass is maintained at a

constant value so that direct comparison can be made between the effects of various geometric parameters and laminate constructions.

The following conclusions are made regarding the effects of geometric parameters and laminate construction.

- The maximum deflection of the sandwich plates depends on the web inclination angle with its largest value occurring at a web inclination angle at or closer to the triangular core. The maximum deflection has the lowest value at web inclination angle of 90^o, i.e., for the rectangular core.
- The maximum deflection depends on the core thickness relative to the face thickness; however, the effect of core thickness is greater that the effect of face thickness. The maximum deflection is higher when the core thickness is lower than the face thickness compared to when both core and face thicknesses are the same.
- The maximum deflection decreases with increasing pitch. Pitch influences the highest maximum deflection, which occurs at or near the web inclination angle close to that of a triangular core. The lowest maximum deflection which occurs with a rectangular core is not influenced by the pitch, since increase in pitch is accompanied with increase in core thickness.
- The maximum deflection decreases with increasing face center distance, which is principally due to the increase in the flexural stiffness components.
- The maximum transverse deflection of the sandwich plates is significantly higher with $[\pm\alpha]_s$ laminate construction than with $[0/\alpha]_s$ laminate construction at fiber orientations angles higher than 30^o. The largest difference in maximum deflections occurs at fiber orientation angle of 90^o. For the $[\pm\alpha]_s$ laminate construction, the lowest maximum deflection occurs at a fiber orientation angle of 15^o, i.e., with the $[\pm15]_s$ laminate. For the $[0/\alpha]_s$ laminate construction , the lowest maximum deflection occurs at a fiber orientation angle of 30^o, i.e., with the $[0/30]_s$ laminate. The difference in maximum deflections of the two types of laminate construction can be attributed mainly to the transverse normal rotation influenced by the transverse shear stiffness A_{55}.

- The fiber orientation angle α has a relatively small effect on bending moments and shear forces in the sandwich plates with the $[0/\alpha]_s$ laminate construction; but its influence is significant with the $[\pm\alpha]_s$ laminate construction.

Global vibration response of corrugated core composite sandwich plates with two different laminate constructions, namely $(\pm\alpha)_s$ and $(0/\alpha)_s$, is analyzed. Both flexural and in-plane extensional modes are considered. The effects of geometric parameters, such as face thickness, web thickness, pitch and face center distance, on the flexural natural frequencies are determined. The effect of web thickness on the extensional natural frequencies is also determined. As the geometric parameters are varied, the web inclination angle is adjusted to maintain a constant mass of the sandwich plates. A range of web shapes ranging from triangular core to rectangular core is considered.

Flexural natural frequency depends strongly on the laminate construction in the faces and the webs. For the $(\pm\alpha)_s$ laminates, the peak natural frequency occurs at 15º fiber orientation angle, whereas for the $(0/\alpha)_s$ laminates, the peak natural frequency occurs at 30º fiber orientation angle. After the peak is reached, natural frequencies with the $(0/\alpha)_s$ laminate construction are much higher than with the $(\pm\alpha)_s$ laminate construction. The web inclination angle, which increases with increasing web thickness to maintain a constant mass of the sandwich plate, also has a significant effect on the natural frequency. For each fiber orientation angle, the natural frequency exhibits the largest value at slightly higher than the minimum web inclination angle.

Flexural natural frequency depends on both the pitch and the face center distance. For the (0/90) and (±90) laminates considered, increasing the pitch increases the natural frequency, the largest effect being observed at the smallest web inclination angle, which corresponds to the triangular core. For the rectangular core, natural frequency is independent of pitch. Increasing the face center distance increases the natural frequency at all web inclination angles.

A comparison of fundamental natural frequencies shows that the extensional mode natural frequencies are much higher than the flexural mode natural frequencies.

This is due to the fact the in-plane stiffness of the sandwich plate is higher than the bending stiffness. Also, in the extensional mode, there is no effect of transverse stiffness. As with the flexural natural frequency, the extensional natural frequency shows a strong dependency on the fiber orientation angle. The effect of web inclination angle is relatively small.

6.1.2 Local Analysis

Local failure analysis of composite sandwich plates with triangular and rectangular corrugated cores is studied in terms of critical buckling and local structural failures using a finite element code. The critical buckling failure is studied using the eigenvalue approach and the local structural failure is predicted using the maximum stress failure criterion. A systematic procedure is developed for the analysis of local structural failure.

- Critical buckling pressure load is higher for the rectangular core than for the triangular core.
- Critical buckling pressure load of sandwich plates with laminate construction $(0/\alpha)_s$ is higher compared to that with laminate construction $(\pm\alpha)_s$. It was observed that as the fiber orientation angle α is increased from $0°$ to $90°$, critical buckling pressure load value is decreased from a maximum value at $\alpha = 0°$ to a minimum value at $\alpha = 90°$. Similar trend is observed in both triangular and rectangular cores.

For local failure prediction, the laminate construction in the top and bottom faces as well as web members is $(0/0)_s$. For both triangular and rectangular core sandwich plates, damage initiation occurs in the top face due to the maximum local stress in the y-direction (normal to the fiber which is also corrugation direction) in the top face exceeding the transverse tensile strength limit. The damage initiation and complete structural failure loads are higher for the rectangular core sandwich plates.

The vibro-acoustic response of sandwich plates is analyzed using a combination of finite element code and boundary element code. Both undamaged and damaged

sandwich plates are considered. The damage is created by applying transverse pressure load in increasing steps on the top face of the sandwich plate. At the fundamental natural frequency, the top face and the webs of the undamaged sandwich plate with triangular core undergo resonances, while the bottom face remains resonance free. Fundamental acoustic mode indicates that the intensity of noise generated due to the resonance of webs is higher compared to that of the top face. With the rectangular core, both top and bottom face undergo resonances, while the webs remain resonance free.

For the sandwich plate with triangular corrugated core, the fundamental structural frequency of pre-stressed and progressively damaged sandwich plates starts to decrease as it is pre-stressed and damaged with increasing applied pressure load. For the sandwich plate with rectangular core, the fundamental structural frequency does not change until a damage level of 2% (approximate damage of 6% in top face) is reached. With both corrugations, the fundamental structural frequency becomes zero at the critical buckling load.

For the undamaged sandwich plates, the fundamental resonance frequencies for both normal velocity and sound pressure level are significantly higher when the core has a rectangular shape. On the other hand, normal velocity and sound power level peaks at resonance frequencies are higher when the core has a triangular shape. As damage increases due to increasing transverse pressure load on the top face, both normal velocity and radiated sound pressure levels increase, and the frequency response curve starts to shift toward lower frequency. The radiation efficiency also decreases with increasing damage in the sandwich plates.

6.2 CONCLUSIONS

Conclusions and original contributions based on the current research study are as follows.

6.2.1 Part 1: Global Response

The global analysis based on homogenization process has provided systematic information on the important geometric and laminate construction parameters on the stiffness parameters needed for the design of composite sandwich plates with a

unidirectional corrugated core. The face center distance, web thickness and web inclination angle have the largest influence to the global maximum deflection of the sandwich plates. The pitch and face thickness have much lower influence to the global maximum deflection. The influence of the web inclination angle is principally due to the effect of the transverse shear stiffness components, while the influence of the face center distance and web thickness is principally due to the bending stiffness components. Among the two laminate constructions considered, the global maximum deflection is lower with the $[0/\alpha]_s$ laminates than with the $[\pm\alpha]_s$ laminates, which is due to higher bending stiffness of the $[0/\alpha]_s$ laminates.

Global vibration response of composite sandwich plates with unidirectional core is studied in terms of the flexural and extensional frequencies. Both frequencies depend strongly on the laminate construction and also on the fiber orientation angle. The flexural natural frequency is strongly influenced by the face center distance, web thickness and web inclination angle. The web inclination angle has a much lower influence on the extensional natural frequency.

6.2.1 Part 2: Local Analysis

A finite element based methodology is developed to predict the buckling and structural failure of individual members in composite sandwich plates with unidirectional corrugated core. Buckling failure mode of the sandwich plates with triangular core is different from that with rectangular core. The critical buckling load is significantly lower for the sandwich plates with triangular core than with rectangular core. The critical buckling load also depends on the laminate construction and decreases with increasing fiber orientation angle. Material failure with increasing pressure load initiates first in the top face and later in the webs and bottom face. The maximum failure load is higher for sandwich plates with rectangular core than with triangular core.

A boundary element based methodology is developed to predict the vibro-acoustic response with both undamaged and damaged sandwich plates with corrugated core. The damage level on the top face is increased by applying increasing pressure load on the top face of the sandwich plates. As damage percentage increases, both normal velocity and

radiated sound pressure levels increase, and the frequency response curve starts to shift toward lower frequency.

6.3 RECOMMENDATIONS FOR FUTURE WORK

This research deals only with the theoretical analyses of the global and local responses of composite sandwich plates with unidirectional corrugated core. The theoretical predictions are not verified with experimental data, since such data are not currently available. An experimental program can be developed where the validity of the theoretical predictions can be checked. This will require manufacturing the composite sandwich plates with different core geometries and carefully conducting experiments to determine flexural deflections, resonance frequencies and sound radiation.

Another area of research will be the optimization of laminate construction and core geometry which will produce the structural performance required for different applications. For example, if such sandwich constructions are considered for weight reduction in automotive body structures and panels, the total thickness of the sandwich panel may not be greater than 2 mm. The sandwich construction must then be optimized to provide stiffness and/or crush resistance under such total thickness constraint.

The manufacturing process development for composite sandwich plates with corrugated core is also a challenging area of research. The manufacturing process for corrugated core paperboard is well developed. Similar techniques may not apply to composite sandwich panels because of the difference in the processing behaviour of composites and fiberboards.

APPENDIX A

MATLAB CODES

A1. UNIT CELL STIFFNESS CALCULATION

```
%UNIT CELL DIMENSIONS
NL=4;                          % NUMBER OF LAYERS IN LAMINATE
LAYUP=[0 1 1 0];
%PRE PROCESSING VARIABLES
A11=zeros(50,50,50,50);
A12=zeros(50,50,50,50);
A16=zeros(50,50,50,50);
A22=zeros(50,50,50,50);
A26=zeros(50,50,50,50);
A66=zeros(50,50,50,50);
A44=zeros(50,50,50,50);
A55=zeros(50,50,50,50);
B11=zeros(50,50,50,50);
B12=zeros(50,50,50,50);
B16=zeros(50,50,50,50);
B22=zeros(50,50,50,50);
B26=zeros(50,50,50,50);
B66=zeros(50,50,50,50);
D11=zeros(50,50,50,50);
D12=zeros(50,50,50,50);
D16=zeros(50,50,50,50);
D22=zeros(50,50,50,50);
D26=zeros(50,50,50,50);
D66=zeros(50,50,50,50);
%POST PROCESSING DATA VARIABLES
DEFR=zeros(50,50,50,50);
DEFR_GDE=zeros(50,50,50,50);
AREA=zeros(50,50,50,50);
U=zeros(50,50,50,50);
V=zeros(50,50,50,50);
W=zeros(50,50,50,50);
RTX=zeros(50,50,50,50);
RTY=zeros(50,50,50,50);
NX=zeros(50,50,50,50);
NY=zeros(50,50,50,50);
NXY=zeros(50,50,50,50);
MX=zeros(50,50,50,50);
MY=zeros(50,50,50,50);
MXY=zeros(50,50,50,50);
QX=zeros(50,50,50,50);
QY=zeros(50,50,50,50);
MATT=1;
RHO=1800;
G=6.9E9;
% % PLATE DIMENSIONS
a=0.64;
b=0.64;
% % UNIT CELL DIMENSIONS
RT1=[1.0 1.25 1.5 1.75 2.0 2.25 2.5 2.75 3.0]' ;
TT=1E-3;
BFP=TT*2./(1+RT1);
TFP=RT1.*BFP;
RT2=[1]';
THT=[45 48 50 60 70 80 90]';
```

```
for l=1:7
LTHETA=LAYUP*15*(l-1);

for i=1:1
TF2=BFP(i);
TF1=TFP(i);
for j=1:1
P=80E-3;
DU=P*RT2(j);
syms Y YY real;
for k=7:7
KKT1=zeros(6,6);
KKT2=zeros(6,6);
KKT3=zeros(6,6);
KKT4=zeros(6,6);
KK3=zeros(6,6);
KK4=zeros(6,6);
KKCT=zeros(6,6);
KKCB=zeros(6,6);
THETA(k,1)=THT(k,1)*(pi/180);
CX=cos(THETA(k,1));
SX=sin(THETA(k,1));
DC=DU-(TF1/2)-(TF2/2);
% WEB THICKNESS FOR CONSTANT MASS
TK=1E-3*SX;
TCK(k,1)=TK;
TC=TK;
F=(1/2*(P-(DC/(SX/CX))));
S=DC/SX;
DCU=(DC-TC);
ZZTF=TF2+DC+TF1/2;
ZZBF=TF2/2;
ZZW=TF2+DC/2;
ZT=TF1+TF2+DC;
NW=b/P;
ATF=b*TF1;
ABF=b*TF2;
AW=S*TC/SX;
ZSC=((ATF*ZZTF)+(ABF*ZZBF)+NW*(AW*ZZW))/(ATF+ABF+NW*AW);
%%TRANSFORMATION MATRIX FOR TOP FACE PLATE
T1=[1 0 0 (ZZTF-ZSC) 0 0;0 1 0 0 (ZZTF-ZSC) 0;0 0 1 0 0 (ZZTF-ZSC);0 0
0 1 0 0;0 0 0 0 1 0;0 0 0 0 0 1];
[A B D]=LAMINATE_STIFFNESS(NL,LTHETA,TF1,1);
KKT1=T1'*[A B;B D]*T1;
%TRANSFORMATION MATRIX FOR BOTTOM FACE PLATE
T2=[1 0 0 -(ZSC-ZZBF) 0 0;0 1 0 0 -(ZSC-ZZBF) 0;0 0 1 0 0 -(ZSC-ZZBF);0
0 0 1 0 0;0 0 0 0 1 0;0 0 0 0 0 1];
[A B D]=LAMINATE_STIFFNESS(NL,LTHETA,TF2,1);
KKT2=T2'*[A B;B D]*T2;
% LIMITS OF INTEGRATION FOR WEBS
Y0=0;
Y1=S;
%%TRANSFORMATION MATRIX FOR LEFT WEB
T3=[1  0 0 ((ZT-TF1-ZSC)-Y*SX) 0 0;0 0 0 0 ((CX^2)*((ZT-TF1-ZSC)-Y*SX))
0;0 0 -CX 0 0 (-CX*((ZT-TF1-ZSC)-Y*SX));0 0 0 -CX 0 0;0 0 0 0 (-(CX^3)-
2*CX*SX^2) 0;0 0 0 0 0 1];
[A B D]=LAMINATE_STIFFNESS(NL,LTHETA,TC,1);
```

```
KKT3=T3'*[A B;B D]*T3;
KK3=int(KKT3,Y,Y0,Y1);
%%TRANSFORMATION MATRIX FOR RIGHT WEB
T4=[1   0  0  ((ZT-TF1-ZSC)-YY*SX)  0  0;0  0  0  0  ((CX^2)*((ZT-TF1-ZSC)-
YY*SX))  0;0  0  CX  0  0  (CX*((ZT-TF1-ZSC)-YY*SX));0  0  0  CX  0  0;0  0  0  0
((CX^3)+2*CX*SX^2)  0;0  0  0  0  0  1];
%%[A B D]=LAMINATE_STIFFNESS(NL,LTHETA,TC,1);
KKT4=T4'*[A B;B D]*T4;
KK4=int(KKT4,YY,Y0,Y1);
KKL=((((KKT1+KKT2)))+((KK3+KK4)/(2*P)));
for ii=1:3
    for jj=1:3
        AAU(ii,jj)=KKL(ii,jj);
        BBU(ii,jj)=KKL(ii+3,jj);
        DDU(ii,jj)=KKL(ii+3,jj+3);
    end
end
%EXTENSIONAL STIFFNESS MATRIX TERMS
A11(i,j,k,l)=KKL(1,1);
A12(i,j,k,l)=KKL(1,2);
A22(i,j,k,l)=KKL(2,2);
A66(i,j,k,l)=KKL(3,3);
%EXTENSIONAL AND FLEXURAL COUPLING MATRIX TERMS
B11(i,j,k,l)=KKL(4,1);
B12(i,j,k,l)=KKL(4,2);
B13(i,j,k,l)=KKL(4,3);
B21(i,j,k,l)=KKL(5,1);
B22(i,j,k,l)=KKL(5,2);
B66(i,j,k,l)=KKL(6,3);
%FLEXURAL STIFFNESS MATRIX TERMS
D11(i,j,k,l)=KKL(4,4);
D12(i,j,k,l)=KKL(4,5);
D22(i,j,k,l)=KKL(5,5);
D66(i,j,k,l)=KKL(6,6);
%TRANSVERSE SHEAR STIFFNESS TERMS
[C1 C2]=TRA44(NL,SX,CX,LTHETA,TF1,TF2,TC,P,F,DU,S,b,a,MATT);
[C3 C4]=TRA55(NL,SX,CX,LTHETA,TF1,TF2,TC,P,F,DU,DC,S,b,a,MATT,KKL,DDU);
A44(i,j,k,l)=abs(C1);
A44C(i,j,k,l)=abs(C2);
A55(i,j,k,l)=C3;
A55C(i,j,k,l)=C4;
end                 %END FOR STIFFNESS CALCULATION
end                 %END FOR VARYING P/D VARIATION
end                 %END FOR VARYING TC/TF VARIATION
end                 %END OF DIFFERENT COMPOSITE LAYUPS
```

```
%A44 CALCULATION

function[A44 A44C]=TRA44(NL,SX,CX,LTHETA,TF1,TF2,TC,P,F,DU,S,b,a,MATT)
[A B D]=LAMINATE_STIFFNESS(NL,LTHETA,TF1,MATT);
ID1=inv(D);
[A B D]=LAMINATE_STIFFNESS(NL,LTHETA,TF2,MATT);
ID2=inv(D);
[A B D]=LAMINATE_STIFFNESS(NL,LTHETA,TW,MATT);
ID3=inv(D);

syms PF RF FF PD Y YY;

%TOP PLATE
M1=Y*FF;
%M2=(Y-(P-F))*PF;
M2=PF*Y;
%BOTTOM PLATE
M3=(1-FF)*Y-(PF+RF)*P+PD*DU;
%M4=(Y-F)*RF;
M4=RF*Y;
%WEB PLATE
M5=((((P-F)*PF)+(F*FF))-(((PD*SX)+((PF-FF)*CX))*YY));

% LIMITS OF INTEGRATION FOR WEBS
Y0=0;
Y1=F;
Y00=0;
Y11=P-F;
YY0=0;
YY1=S;

%BENDING STRAIN ENERGY
US=(((1/2)*ID1(1,1))*((int((M1)^2,Y,Y0,Y1))+(int((M2)^2,Y,Y00,Y11))))+(
((1/2)*ID2(1,1))*((int((M3)^2,Y,Y00,Y11))+(int((M4)^2,Y,Y0,Y1))))+((((1
/2)*ID3(1,1))*(int((M5)^2,YY,YY0,YY1))));
US1=diff(US,'FF');
US2=diff(US,'PF');
US3=diff(US,'RF');
US4=diff(US,'PD');
DF1=subs((subs(US1,PD,(P/DU))),PF,1-RF);
DF2=subs((subs(US2,PD,(P/DU))),PF,1-RF);
DF3=subs((subs(US3,PD,(P/DU))),PF,1-RF);
DF3=(subs(US3,PF,1-RF));
DF4=subs((subs(US4,PD,(P/DU))),PF,1-RF);
TEMP=DF2-DF3;
FRS=solve(DF1,TEMP,FF,RF);
DEF1=subs((subs(DF1,RF,FRS.RF)),FF,FRS.FF);
DEF2=subs((subs(DF2,RF,FRS.RF)),FF,FRS.FF);
DEF3=subs((subs(DF3,RF,FRS.RF)),FF,FRS.FF);
DEF4=subs((subs(DF4,RF,FRS.RF)),FF,FRS.FF);
DEF5=(1/2)*ID2(1,1)*(DU*(1-FRS.FF)*(P-F)^2);
A44=1/(((DEF4+DEF5)/DU)+(DEF2/P));
A44C=1/(((DEF4+DEF5)/DU)+(DEF3/P));
end             %end of calculation
```

```
%A55 CALCULATION

function[A55]=TRA55(NL,SX,CX,LTHETA,TF1,TF2,TC,P,F,DU,DC,S,b,a,MATT,KKL
,DDU)
syms MX QX X Y real;
MX=QX*X;
ZZTF=TF2+DC+TF1/2;
ZZBF=TF2/2;
ZZW=TF2+DC/2;
ZT=TF1+TF2+DC;
NW=b/P;
ATF=b*TF1;
ABF=b*TF2;
AW=S*TC/SX;
ZSC=((ATF*ZZTF)+(ABF*ZZBF)+NW*(AW*ZZW))/(ATF+ABF+NW*AW);
%%TRANSFORMATION MATRIX FOR TOP FACE PLATE
T1=[1 0 0 (ZZTF-ZSC) 0 0;0 1 0 0 (ZZTF-ZSC) 0;0 0 1 0 0 (ZZTF-ZSC);0 0
0 1 0 0;0 0 0 0 1 0;0 0 0 0 0 1];
T3=[1  0 0 ((ZT-TF1-ZSC)-Y*SX) 0 0;0 0 0 0 ((CX^2)*((ZT-TF1-ZSC)-Y*SX))
0;0 0 -CX 0 0 (-CX*((ZT-TF1-ZSC)-Y*SX));0 0 0 -CX 0 0;0 0 0 0 (-(CX^3)-
2*CX*SX^2) 0;0 0 0 0 0 1];
%FICTIOUS APPLIED LOADS
NMU=[0 0 0 MX 0 0]';
[A B D]=LAMINATE_STIFFNESS(NL,LTHETA,TF1,1);
NMT=[A B;B D]*T1*inv(KKL)*NMU;
DI=inv(DDU);
FF1=(2*P)*A(1,1)*(DU/2)*DI(1,1)*MX;
[A B D]=LAMINATE_STIFFNESS(NL,LTHETA,TC,1);
NMW=[A B;B D]*T3*inv(double(KKL))*NMU;
NMWW=int(NMW,Y);     %INTEGRATE WITHOUT SUBSTITUTING LIMITS
FF2=(2*DI(1,1)*MX*(A(1,1)*int(((DC/2)-Y*SX),Y)));
% LIMITS OF INTEGRATION FOR WEBS
Y0=0;
Y1=S;
G=(A(3,3)/TC);
TUXYC=(diff((FF1+FF2),'X'))*DU/(2*TC*S*SX);
A55IC=(2/(QX)^2)*(TC/(2*P))*int((TUXYC)^2,Y,Y0,Y1)/G;
A55C=(A55IC)^-1;
TUXY=(diff(((NMT(1,1)*2*P)+(2*NMWW(1,1))),'X'))*DU/(2*TC*S*SX);
%MODIFIED WITH LENGTH OF THE WEB
A55I=(2/(QX)^2)*(TC/(2*P))*int(((TUXY)^2),Y,Y0,Y1)/G;
A55=vpa((A55I)^-1);
end           %END OF CALCULATION
```

A2. GLOBAL BENDING RESPONSE CALCULATION

```
function [WW UOU VOV WOW RTOX RTOY NOX NOY NOXY MOX MOY MOXY QOX
QOY]=DEFLECTION_ENERGY_APPROACH(KKL,C1,C3,a,b,i)
A=zeros(6,6);
B=zeros(6,6);
D=zeros(6,6);
WW=zeros(20,20);
A(1,1)=KKL(1,1);
A(1,2)=KKL(1,2);
A(1,6)=KKL(1,3);
A(6,1)=A(1,6);
A(2,1)=A(1,2);
A(2,2)=KKL(2,2);
A(2,6)=KKL(2,3);
A(6,2)=A(2,6);
A(4,4)=C1;
A(5,5)=C3;
A(6,6)=KKL(3,3);
TR=[A(4,4) 0;0 A(5,5)];
%FLEXURAL STIFFNESS MATRIX TERMS
D(1,1)=KKL(4,4);
D(1,2)=KKL(4,5);
D(2,1)=D(1,2);
D(1,6)=KKL(4,6);
D(6,1)=D(1,6);
D(2,2)=KKL(5,5);
D(2,6)=KKL(5,6);
D(6,2)=D(2,6);
D(6,6)=KKL(6,6);
for ii=1:3
for jj=1:3
DD(ii,jj)=KKL(ii+3,jj+3);
end
end
%FLEXURAL AND EXTENSIONAL STIFFNESS MATRIX TERMS
B(1,1)=KKL(1,4);
B(1,2)=KKL(1,5);
B(2,1)=B(1,2);
B(1,6)=KKL(1,6);
B(6,1)=B(1,6);
B(2,2)=KKL(2,5);
B(2,6)=KKL(2,6);
B(6,2)=B(2,6);
B(6,6)=KKL(3,6);
syms X Y T UMN VMN WMN RTXMN RTYMN PMN PP0 ppi p0 real
U0=0;
V0=0;
W0=0;
RTX0=0;
RTY0=0;
P0=0;
PX=0;
PY=0;
X0=0;
Y0=0;
X1=a;
```

```
Y1=b;
M=20;
N=40;
FCUMN=sym(zeros(M,N));
FCVMN=sym(zeros(M,N));
FCWMN=sym(zeros(M,N));
FCRTXMN=sym(zeros(M,N));
FCRTYMN=sym(zeros(M,N));
FCPMN=sym(zeros(M,N));
for m=1:M
for n=1:N
syms UMN VMN WMN RTXMN RTYMN PMN ppi real
U=(UMN*sin(ppi*(m/a)*X)*cos(ppi*(n/b)*Y));
V=(VMN*cos(ppi*(m/a)*X)*sin(ppi*(n/b)*Y));
W=(WMN*sin(ppi*(m/a)*X)*sin(ppi*(n/b)*Y));
RTX=(RTXMN*cos(ppi*(m/a)*X)*sin(ppi*(n/b)*Y));
RTY=(RTYMN*sin(ppi*(m/a)*X)*cos(ppi*(n/b)*Y));
%FORCE
if mod(m,2)==1
if mod(n,2)==1
PMN=((16*p0)/(m*n*ppi^2));
else
PMN=0;
end
else
PMN=0;
end
P=(PMN*sin(ppi*(m/a)*X)*sin(ppi*(n/b)*Y));
%Partial differential Equation
%Strecthing
US=(1/2)*((A(1,1)*(diff(U,'X'))^2)+(2*A(1,2)*(diff(U,'X'))*(diff(V,'Y')
))+(2*A(1,6)*(diff(U,'X'))*((diff(V,'X'))+(diff(U,'Y'))))+(A(2,2)*(diff
(V,'Y'))^2)+(2*A(2,6)*(diff(V,'Y'))*((diff(V,'X'))+(diff(U,'Y'))))+(A(6
,6)*(diff(V,'X')+diff(U,'X'))^2));
%Bending
UB=(1/2)*((D(1,1)*(diff(RTX,'X'))^2)+(2*D(1,2)*(diff(RTX,'X'))*(diff(RT
Y,'Y')))+(D(2,2)*(diff(RTY,'Y'))^2)+(D(6,6)*(diff(RTX,'Y')+diff(RTY,'X'
))^2)+(2*D(1,6)*(diff(RTX,'X')*((diff(RTX,'Y')+diff(RTY,'X')))))+(2*D(2
,6)*(diff(RTY,'Y')*(diff(RTX,'Y')+diff(RTY,'X')))));
%Bending - Strecthing coupling
UBS=((B(1,1)*diff(U,'X')*diff(RTX,'X'))+(B(1,2)*((diff(U,'X')*diff(RTY,
'Y'))+(diff(V,'Y')*diff(RTX,'X'))))+(B(1,6)*((diff(U,'X')*(diff(RTX,'Y'
)+diff(RTY,'X')))+((diff(U,'Y')+diff(V,'X'))*diff(RTX,'X'))))+(B(2,2)*d
iff(V,'Y')*diff(RTY,'Y'))+(B(2,6)*((diff(V,'Y')*(diff(RTX,'Y')+diff(RTY
,'X')))+((diff(U,'Y')+diff(V,'X'))*diff(RTY,'Y'))))+(B(6,6)*(diff(RTX,'
Y')+diff(RTY,'X'))*(diff(U,'Y')+diff(V,'X'))));
%Transverse shear
UTS=(1/2)*((A(5,5)*(diff(W,'X')+RTX)^2)+(A(4,4)*(diff(W,'Y')+RTY)^2)+(2
*A(4,5)*(RTY+diff(W,'Y'))*(RTX-diff(W,'X'))));
SE=int((int((US+UB+UBS+UTS-(P*W)),X,X0,X1)),Y,Y0,Y1);
SE=(subs(SE,ppi,3.1416));
SE1=simplify(diff(SE,'UMN'));
SE2=simplify(diff(SE,'VMN'));
SE3=simplify(diff(SE,'WMN'));
SE4=simplify(diff(SE,'RTXMN'));
SE5=simplify(diff(SE,'RTYMN'));
FC=solve(SE1,SE2,SE3,SE4,SE5,UMN,VMN,WMN,RTXMN,RTYMN);
```

```
UMN=FC.UMN;
VMN=FC.VMN;
WMN=FC.WMN;
RTXMN=FC.RTXMN;
RTYMN=FC.RTYMN;
%STORING FOURIER COEFFICIENTS
if mod(m,2)==1
if mod(n,2)==1
FCPMN(m,n)=((16*p0)/(m*n*ppi^2));
else
FCPMN(m,n)=0;
end
else
FCPMN(m,n)=0;
end
FCUMN(m,n)=subs(UMN,p0,1);
FCVMN(m,n)=subs(VMN,p0,1);
FCWMN(m,n)=subs(WMN,p0,1);
FCRTXMN(m,n)=subs(RTXMN,p0,1);
FCRTYMN(m,n)=subs(RTYMN,p0,1);
U0=U0+(FCUMN(m,n)*sin(ppi*(m/a)*X)*cos(ppi*(n/b)*Y));
V0=V0+(FCVMN(m,n)*cos(ppi*(m/a)*X)*sin(ppi*(n/b)*Y));
W0=W0+(FCWMN(m,n)*sin(ppi*(m/a)*X)*sin(ppi*(n/b)*Y));
RTX0=RTX0+(FCRTXMN(m,n)*cos(ppi*(m/a)*X)*sin(ppi*(n/b)*Y));
RTY0=RTY0+(FCRTYMN(m,n)*sin(ppi*(m/a)*X)*cos(ppi*(n/b)*Y));
P0=P0+(FCPMN(m,n)*sin(ppi*(m/a)*X)*sin(ppi*(n/b)*Y));
syms UMN VMN WMN RTXMN RTYMN PMN unreal
end
end
%MOMENT MX, MY
STRAIN=[diff(U0,'X')       diff(V0,'Y')       (diff(U0,'Y')+diff(V0,'X'))
diff(RTX0,'X')       diff(RTY0,'Y')       (diff(RTX0,'Y')+diff(RTY0,'X'))
(RTY0+diff(W0,'Y')) (RTX0+diff(W0,'X'))]';
STIFFNESS=[KKL zeros(6,2); zeros(2,6) TR];
M=STIFFNESS*STRAIN;
%FOR ALL LOCATIONS IN PLATE
for ii=1:41
PX=(ii-1)*a/40;
for jj=1:41
PY=(jj-1)*b/40;
UOU(ii,jj)=subs(subs(subs(U0,ppi,pi),X,PX),Y,PY);
VOV(ii,jj)=subs(subs(subs(V0,ppi,pi),X,PX),Y,PY);
WOW(ii,jj)=subs(subs(subs(W0,ppi,pi),X,PX),Y,PY);
RTOX(ii,jj)=subs(subs(subs(RTX0,ppi,pi),X,PX),Y,PY);
RTOY(ii,jj)=subs(subs(subs(RTY0,ppi,pi),X,PX),Y,PY);
NOX(ii,jj)=(subs(subs(subs(M(1,1),ppi,3.1416),X,PX),Y,PY));
NOY(ii,jj)=(subs(subs(subs(M(2,1),ppi,3.1416),X,PX),Y,PY));
NOXY(ii,jj)=(subs(subs(subs(M(3,1),ppi,3.1416),X,PX),Y,PY));
MOX(ii,jj)=(subs(subs(subs(M(4,1),ppi,3.1416),X,PX),Y,PY));
MOY(ii,jj)=(subs(subs(subs(M(5,1),ppi,3.1416),X,PX),Y,PY));
MOXY(ii,jj)=(subs(subs(subs(M(6,1),ppi,3.1416),X,PX),Y,PY));
QOY(ii,jj)=(subs(subs(subs(M(7,1),ppi,3.1416),X,PX),Y,PY));
QOX(ii,jj)=(subs(subs(subs(M(8,1),ppi,3.1416),X,PX),Y,PY));
end
end
end %end of function
```

A3. GLOBAL VIBRATION RESPONSE CALCULATION

```
function
[BUCK,FREQQ,FREQQ1,FREQQ12,FREQQ_GDE,FREQQ_GDE1]=ENERGY_APPROACH_EIGENV
ALUE_ANALYSIS(KKL,A44,A55,a,b,P,DC,TF1,TF2,TC,THETA,RHO,M,N)
A=zeros(6,6);
B=zeros(6,6);
D=zeros(6,6);
WW=zeros(20,20);
A(1,1)=KKL(1,1);
A(1,2)=KKL(1,2);
A(1,6)=KKL(1,3);
A(6,1)=A(1,6);
A(2,1)=A(1,2);
A(2,2)=KKL(2,2);
A(2,6)=KKL(2,3);
A(6,2)=A(2,6);
A(4,4)=A44;
A(5,5)=A55;
A(6,6)=KKL(3,3);
%FLEXURAL STIFFNESS MATRIX TERMS
D(1,1)=KKL(4,4);
D(1,2)=KKL(4,5);
D(2,1)=D(1,2);
D(1,6)=KKL(4,6);
D(6,1)=D(1,6);
D(2,2)=KKL(5,5);
D(2,6)=KKL(5,6);
D(6,2)=D(2,6);
D(6,6)=KKL(6,6);
%FLEXURAL AND EXTENSIONAL STIFFNESS MATRIX TERMS
B(1,1)=KKL(1,4);
B(1,2)=KKL(1,5);
B(2,1)=B(1,2);
B(1,6)=KKL(1,6);
B(6,1)=B(1,6);
B(2,2)=KKL(2,5);
B(2,6)=KKL(2,6);
B(6,2)=B(2,6);
B(6,6)=KKL(3,6);
% INERTIA TERMS FOR KINETIC ENERGY
SX=sin(THETA);
CX=cos(THETA);
S=DC/SX;
F=(1/2*(P-(DC/(SX/CX))));
NW=(b/P);
%NORMAL INERTIA
PNI=RHO*(TF1+TF2+(NW*S*TC/b));
%ROTARY INERTIA OF FACE PLATES
JX=(PNI/DC)*DC^3/12;
JY=(PNI/DC)*DC^3/12;
RX=0;
RY=0;
syms X Y OMG OMGG T UMN VMN WMN RTXMN RTYMN PMN PP0 ppi p0 real
U0=0;
V0=0;
W0=0;
```

```
RTX0=0;
RTY0=0;
P0=0;
PX=0;
PY=0;
X0=0;
Y0=0;
X1=a;
Y1=b;
YY0=0;
YY1=F;
FCUMN=sym(zeros(M,N));
FCVMN=sym(zeros(M,N));
FCWMN=sym(zeros(M,N));
FCRTXMN=sym(zeros(M,N));
FCRTYMN=sym(zeros(M,N));
FCPMN=sym(zeros(M,N));

for m=1:M
for n=1:N
syms UMN VMN WMN RTXMN RTYMN PMN ppi real
i=sqrt(-1);
%S-S-S-S BOUNDARY CONDITION
U=(UMN*sin(ppi*(m/a)*X)*cos(ppi*(n/b)*Y)*exp(i*OMG*T));
V=(VMN*cos(ppi*(m/a)*X)*sin(ppi*(n/b)*Y)*exp(i*OMG*T));
W=(WMN*sin(ppi*(m/a)*X)*sin(ppi*(n/b)*Y)*exp(i*OMG*T));
RTX=(RTXMN*cos(ppi*(m/a)*X)*sin(ppi*(n/b)*Y)*exp(i*OMG*T));
RTY=(RTYMN*sin(ppi*(m/a)*X)*cos(ppi*(n/b)*Y)*exp(i*OMG*T));
%Partial differential Equation
%Strecthing
US=(1/2)*((A(1,1)*(diff(U,'X'))^2)+(2*A(1,2)*(diff(U,'X'))*(diff(V,'Y')
))+(2*A(1,6)*(diff(U,'X'))*((diff(V,'X'))+(diff(U,'Y'))))+(A(2,2)*(diff
(V,'Y'))^2)+(2*A(2,6)*(diff(V,'Y'))*((diff(V,'X'))+(diff(U,'Y'))))+(A(6
,6)*(diff(V,'X')+diff(U,'X'))^2));
%Bending
UB=(1/2)*((D(1,1)*(diff(RTX,'X'))^2)+(2*D(1,2)*(diff(RTX,'X'))*(diff(RT
Y,'Y')))+(D(2,2)*(diff(RTY,'Y'))^2)+(D(6,6)*(diff(RTX,'Y')+diff(RTY,'X'
))^2)+(2*D(1,6)*(diff(RTX,'X')*((diff(RTX,'Y')+diff(RTY,'X')))))+(2*D(2
,6)*(diff(RTY,'Y')*(diff(RTX,'Y')+diff(RTY,'X')))));
%Bending - Strecthing coupling
UBS=((B(1,1)*diff(U,'X')*diff(RTX,'X'))+(B(1,2)*((diff(U,'X')*diff(RTY,
'Y'))+(diff(V,'Y')*diff(RTX,'X'))))+(B(1,6)*((diff(U,'X')*(diff(RTX,'Y'
)+diff(RTY,'X')))+((diff(U,'Y')+diff(V,'X'))*diff(RTX,'X'))))+(B(2,2)*d
iff(V,'Y')*diff(RTY,'Y'))+(B(2,6)*((diff(V,'Y')*(diff(RTX,'Y')+diff(RTY
,'X')))+((diff(U,'Y')+diff(V,'X'))*diff(RTY,'Y'))))+(B(6,6)*(diff(RTX,'
Y')+diff(RTY,'X'))*(diff(U,'Y')+diff(V,'X'))));
%Transverse shear
UTS=(1/2)*((A(5,5)*(diff(W,'X')+RTX)^2)+(A(4,4)*(diff(W,'Y')+RTY)^2)+(2
*A(4,5)*(RTY+diff(W,'Y'))*(RTX-diff(W,'X'))));
%Inertia terms
TT=((1/2)*simplify((PNI*(((diff(U,T))^2)+((diff(V,T))^2)+((diff(W,T))^2
)))+(JX*((diff(RTX,T))^2))+(JY*((diff(RTY,T))^2))+(2*RX*(diff(RTX,T)*di
ff(U,T)))+(2*RY*(diff(RTY,T)*diff(V,T)))));
%KE=simplify(int((int((TT),X,X0,X1)),Y,Y0,Y1));
KE=int((int((TT),X,X0,X1)),Y,Y0,Y1);
%TOTAL STRAIN ENERGY
SE1=simplify(int((int((US+UBS+UB+UTS),X,X0,X1)),Y,Y0,Y1));
```

```
%TOTAL ENERGY
SE=SE1+KE;
SE=vpa(subs(SE,T,0));
SE=vpa(subs(SE,ppi,3.1416));
SE1=simplify(diff(SE,'UMN'));
SE2=simplify(diff(SE,'VMN'));
SE3=simplify(diff(SE,'WMN'));
SE4=simplify(diff(SE,'RTXMN'));
SE5=simplify(diff(SE,'RTYMN'));
%FIRST ROW IN DYNAMIC STIFFNESS MATRIX
DYNSTIFF(1,1)=subs(subs(subs(subs(subs(SE1,UMN,1),VMN,0),WMN,0),RTXMN,0
),RTYMN,0);
DYNSTIFF(1,2)=subs(subs(subs(subs(subs(SE1,UMN,0),VMN,1),WMN,0),RTXMN,0
),RTYMN,0);
DYNSTIFF(1,3)=subs(subs(subs(subs(subs(SE1,UMN,0),VMN,0),WMN,1),RTXMN,0
),RTYMN,0);
DYNSTIFF(1,4)=subs(subs(subs(subs(subs(SE1,UMN,0),VMN,0),WMN,0),RTXMN,1
),RTYMN,0);
DYNSTIFF(1,5)=subs(subs(subs(subs(subs(SE1,UMN,0),VMN,0),WMN,0),RTXMN,0
),RTYMN,1);
%SECOND ROW IN DYNAMIC STIFFNESS MATRIX
DYNSTIFF(2,1)=subs(subs(subs(subs(subs(SE2,UMN,1),VMN,0),WMN,0),RTXMN,0
),RTYMN,0);
DYNSTIFF(2,2)=subs(subs(subs(subs(subs(SE2,UMN,0),VMN,1),WMN,0),RTXMN,0
),RTYMN,0);
DYNSTIFF(2,3)=subs(subs(subs(subs(subs(SE2,UMN,0),VMN,0),WMN,1),RTXMN,0
),RTYMN,0);
DYNSTIFF(2,4)=subs(subs(subs(subs(subs(SE2,UMN,0),VMN,0),WMN,0),RTXMN,1
),RTYMN,0);
DYNSTIFF(2,5)=subs(subs(subs(subs(subs(SE2,UMN,0),VMN,0),WMN,0),RTXMN,0
),RTYMN,1);
%THIRD ROW IN DYNAMIC STIFFNESS MATRIX
DYNSTIFF(3,1)=subs(subs(subs(subs(subs(SE3,UMN,1),VMN,0),WMN,0),RTXMN,0
),RTYMN,0);
DYNSTIFF(3,2)=subs(subs(subs(subs(subs(SE3,UMN,0),VMN,1),WMN,0),RTXMN,0
),RTYMN,0);
DYNSTIFF(3,3)=subs(subs(subs(subs(subs(SE3,UMN,0),VMN,0),WMN,1),RTXMN,0
),RTYMN,0);
DYNSTIFF(3,4)=subs(subs(subs(subs(subs(SE3,UMN,0),VMN,0),WMN,0),RTXMN,1
),RTYMN,0);
DYNSTIFF(3,5)=subs(subs(subs(subs(subs(SE3,UMN,0),VMN,0),WMN,0),RTXMN,0
),RTYMN,1);
%FOURTH ROW IN DYNAMIC STIFFNESS MATRIX
DYNSTIFF(4,1)=subs(subs(subs(subs(subs(SE4,UMN,1),VMN,0),WMN,0),RTXMN,0
),RTYMN,0);
DYNSTIFF(4,2)=subs(subs(subs(subs(subs(SE4,UMN,0),VMN,1),WMN,0),RTXMN,0
),RTYMN,0);
DYNSTIFF(4,3)=subs(subs(subs(subs(subs(SE4,UMN,0),VMN,0),WMN,1),RTXMN,0
),RTYMN,0);
DYNSTIFF(4,4)=subs(subs(subs(subs(subs(SE4,UMN,0),VMN,0),WMN,0),RTXMN,1
),RTYMN,0);
DYNSTIFF(4,5)=subs(subs(subs(subs(subs(SE4,UMN,0),VMN,0),WMN,0),RTXMN,0
),RTYMN,1);
%FIFTH ROW IN DYNAMIC STIFFNESS MATRIX
DYNSTIFF(5,1)=subs(subs(subs(subs(subs(SE5,UMN,1),VMN,0),WMN,0),RTXMN,0
),RTYMN,0);
```

```
DYNSTIFF(5,2)=subs(subs(subs(subs(subs(SE5,UMN,0),VMN,1),WMN,0),RTXMN,0
),RTYMN,0);
DYNSTIFF(5,3)=subs(subs(subs(subs(subs(SE5,UMN,0),VMN,0),WMN,1),RTXMN,0
),RTYMN,0);
DYNSTIFF(5,4)=subs(subs(subs(subs(subs(SE5,UMN,0),VMN,0),WMN,0),RTXMN,1
),RTYMN,0);
DYNSTIFF(5,5)=subs(subs(subs(subs(subs(SE5,UMN,0),VMN,0),WMN,0),RTXMN,0
),RTYMN,1);
%MASS AND STIFFNESS MATRICES
STIFF=subs(DYNSTIFF,OMG,0);
MASS=subs((DYNSTIFF-STIFF),OMG,1);
% FREE VIBRATION ANALYSIS
% CALCULATION OF NATURAL FREQUENCIES
[EV,FRE]=eig(STIFF,MASS);
FRE1=inv(EV)*(inv(MASS)*STIFF)*EV;
FRE12=zeros(5,5);
TFRE=(abs(FRE));
for ii=1:5
FFRE(ii)=TFRE(ii,ii);
end
FFRE=sort(FFRE);
for ii=1:5
FREQ(m,n,ii)=FFRE(ii);
FREQ1(m,n,ii)=FRE1(ii,ii);
FREQ12(m,n,ii)=FRE12(ii,ii);
end
FREQQ=sqrt(abs(FREQ))/(2*pi);
FREQQ1=sqrt(abs(FREQ1))/(2*pi);
FREQQ12=sqrt(abs(FREQ12))/(2*pi);
% GOVERNING DIFFERENTIAL EQUATION
DYNSTIFF_GDE=[((D(1,1)*(m*pi/a)^2)+(D(6,6)*(n*pi/b)^2)+A(5,5))-
JY*OMGG^2                                ((D(1,2)+D(6,6))*(m*n*pi^2/(a*b)))
(A(5,5)*(m*pi/a));((D(1,2)+D(6,6))*(m*n*pi^2/(a*b)))
((D(2,2)*(n*pi/b)^2)+(D(6,6)*(m*pi/a)^2)+A(4,4))-JX*OMGG^2
(A(4,4)*(n*pi/b));(A(5,5)*(m*pi/a))                          (A(4,4)*(n*pi/b))
((A(5,5)*(m*pi/a)^2)+(A(4,4)*(n*pi/b)^2))-PNI*OMGG^2];
STIFF_GDE=subs(DYNSTIFF_GDE,OMGG,0);
MASS_GDE=subs((DYNSTIFF_GDE-STIFF_GDE),OMGG,1);
% CALCULATION OF NATURAL FREQUENCIES BY GDE
[EV_GDE,FRE_GDE]=eig(STIFF_GDE,MASS_GDE);
FFRE_GDE=inv(EV_GDE)*STIFF_GDE*EV_GDE;
for ii=1:3
FREQ_GDE(m,n,ii)=(FRE_GDE(ii,ii));
FREQ_GDE1(m,n,ii)=(FFRE_GDE(ii,ii));
end
FREQQ_GDE=sqrt(abs(FREQ_GDE))/(2*pi);
FREQQ_GDE1=sqrt(abs(FREQ_GDE1))/(2*pi);
%MODE SHAPE FACTORS
for ii=1:5
SSE1=subs(subs(SE1,OMG,FRE(ii,ii)),WMN,1);
SSE2=subs(subs(SE2,OMG,FRE(ii,ii)),WMN,1);
SSE3=subs(subs(SE3,OMG,FRE(ii,ii)),WMN,1);
SSE4=subs(subs(SE4,OMG,FRE(ii,ii)),WMN,1);
SSE5=subs(subs(SE5,OMG,FRE(ii,ii)),WMN,1);
MFC=solve(SSE1,SSE2,SSE4,SSE5,UMN,VMN,RTXMN,RTYMN);
MFACUMN(m,n,ii)=MFC.UMN;
MFACVMN(m,n,ii)=MFC.VMN;
```

```
MFACWMN(m,n,ii)=1;
MFACRTXMN(m,n,ii)=MFC.RTXMN;
MFACRTYMN(m,n,ii)=MFC.RTYMN;
end
syms UMN VMN WMN RTXMN RTYMN PMN unreal
end
end
end %end of function
```